Fall 12-14-2018

Development of The University of New Mexico Spectrometer for High-Resolution Fission Product Yield Data

Richard Emery Blakeley
University of New Mexico - Main Campus

Richard Emery Blakeley

Candidate

Nuclear Engineering

Department

This dissertation is approved, and it is acceptable in quality and form for publication:

Approved by the Dissertation Committee:

Adam Hecht, Ph.D, Chairperson

Gary Cooper, Ph.D.

Cassiano de Oliveira, Ph.D.

Fredrik Tovesson, Ph.D.

Development of The University of New Mexico Spectrometer for High-Resolution Fission Product Yield Data

By

Richard Blakeley

B.S. Nuclear Engineering, University of New Mexico, 2009

M.S. Nuclear Engineering, University of New Mexico, 2013

DISSERTATION

Submitted in Partial Fulfillment of the Requirements for the Degree of

DOCTOR OF PHILOSOPHY

Engineering

University of New Mexico

Albuquerque, New Mexico

December, 2018

Development of The University of New Mexico Spectrometer for High-Resolution Fission Product Yield Data

By

Richard Blakeley

B.S. Nuclear Engineering, University of New Mexico, 2009

M.S. Nuclear Engineering, University of New Mexico, 2013

Ph.D. Engineering. University of New Mexico, 2018

ABSTRACT

Well-defined fission product yield data has been of increasing interest in various applications within the nuclear industry. With this need in mind, a fission fragment mass spectroscopy system was designed and developed at the University of New Mexico in collaboration with the Los Alamos National Laboratories with a stated goal of attaining a mass resolution of ≤ 1 % (FWHM/centroid) for light fragments and near 1 % for heavy fragments. The mass spectrometer utilized in this work consists of a transmission time-of-flight detection system to measure fission product velocity and an axial ionization chamber to measure the fission product energy, with measurements giving quasi-prompt (~50 - 100 ns) fission data. With these measured quantities of velocity and energy, the fission product mass can be calculated. As an additional feature, the ionization chamber was designed to serve as a time projection chamber, providing information regarding the fission product depth of penetration in the ionization gas, and thus information on the stopping power and the fission product atomic number, Z.

Measurements of mass and Z using the UNM spectrometer were performed on a ^{252}Cf spontaneous fission source at UNM and ^{235}U(n_{th}, f)X at the LANSCE Lujan Center neutron

beamline facility located at Los Alamos National Laboratory. The results of the experimental mass and Z measurements for both fission parent nuclides are compared to ENDF/B-VII fission product yield data files for analysis and discussion. An assessment of statistical and mass related uncertainties and their contributors is also presented for ^{252}Cf and ^{235}U measurements. Finally, remaining issues and ideas for future work are identified and possible solutions proposed.

Table of Contents

Table of Figures

List of Tables

Chapter 1: Introduction

1.1 Motivation

The primary purpose for the experimental work performed regarding fission product detection and identification is to is to improve fission product yield (FPY) empirical data by further advancing physical detection techniques, materials and analysis. Reducing uncertainty that currently exists within evaluated FPY data is of great interest in many applications throughout the nuclear industry, from understanding fundamental fission theory to advanced reactor design. Our detection system has been developed to provide high-precision, event-by-event fission product measurements to aid in filling in the gaps in currently existing FPY data.

1.2 Overview

Interest in precision FPY data within the nuclear industry has increased in recent years. Within the nuclear power community, FPY data is important for calculating fission product inventories at various stages of the fuel cycle for safe storage, handling and reactor operation [1]. Reactor operators use FPY data for important criticality and reactivity calculations for more efficient core management plans as well as burnup calculations for efficient fuel use. In reprocessing and fuel management, decay heat removal and radiation hazards to workers are of primary concern. FPY data in even the most well-known fissioning systems (e.g., $^{235}U + n_{th}$ fission) there exists high relative uncertainties, upwards of 40% exist in the "tails" and "valleys" and as much as 10% in the most abundant masses of the fission product distribution within ENDF/B-VII evaluated dataset [2]. A reactor modelling evaluation on the uncertainty propagation of nuclear data as it pertains to burnup calculations found that uncertainties in FPY data had a primary impact on reactivity, inventory and toxicity results [3].

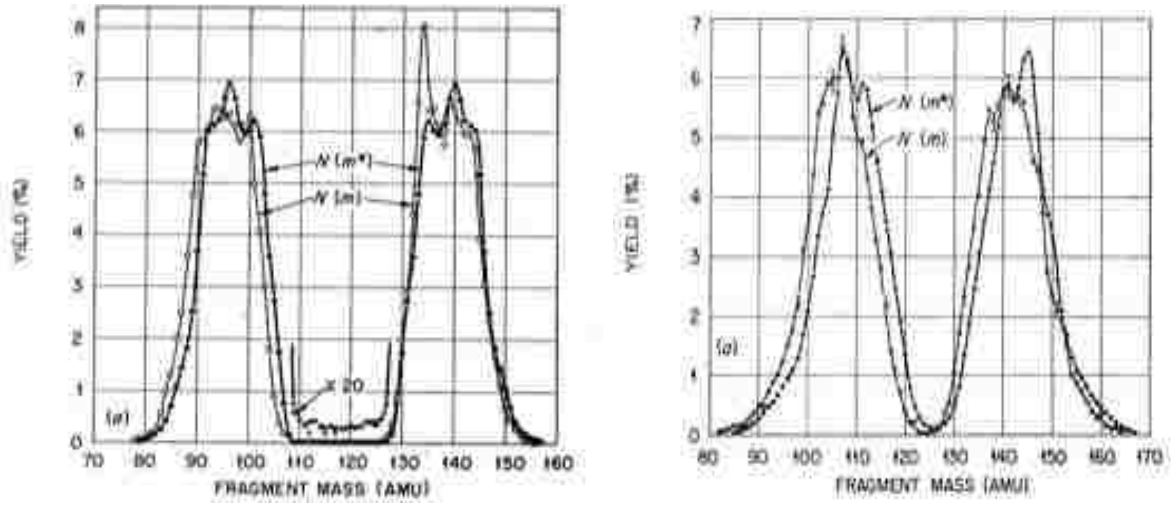

Figure 1: FPY distributions for $^{235}U(n_{thermal}, f)$ and ^{252}Cf(s.f.) from Schmitt *et al*. [4].

FPY data is of increasing importance in modelling future, more complex systems such as Accelerator Driven Systems (ADS), which suffer from a complete lack of empirical FPY data for actinide systems [5]. Reducing uncertainty in the FPY data is important to improving fission systematics, such as the multi-Gaussian representation done by A.C. Wahl [6] which already suffer an uncertainty of upwards of 15% on the highest yields where empirical data is abundant [7].

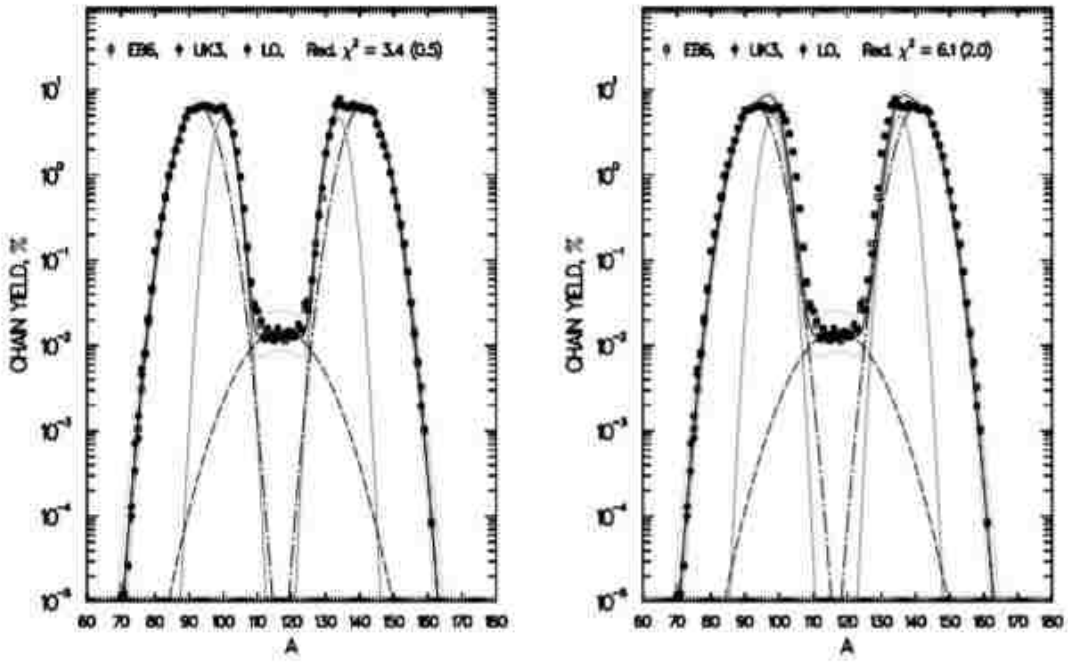

Figure 2: Wahl fission systematics for $^{235}U(n_{thermal},f)$ [6].

The systematics developed by Wahl are the cornerstone of predictive fission product and Z yield modeling for fissioning systems absent of empirical data. Uncertainties propagated through interpolation of theory could lead to unforeseen consequences in more advanced systems.

In addition to just mass yields, correlated measurements relating to physical quantities observed in the fission process is of great importance to theorists who develop predictive fission models. Knowing the relations between fission product mass, Z, kinetic energy, average neutron number released and total kinetic energy in the compound nucleus provides a better fundamental understanding of the fission process and improves modeling of more difficult to measure systems.

National security interests are another application where improved empirical FPY data, particularly Z yields correlated with mass, A, would prove useful. The Department of Homeland

Security has been studying improved cargo container screening for special nuclear material (SNM) by means of active interrogation via neutron bombardment. In theory, if SNM is present, the neutrons will induce fission and the SNM would be identified by the delayed gamma signature of the emitted fission products. Having a well-defined A and Z distribution for typical SNM would decrease the uncertainty in the expected gamma signal, leading to faster more accurate identification. These same principles also apply to other defense related applications such as post-detonation forensics and deterrence management and maintenance.

1.3 Problem Description & Research Goals

Many methods have been devised for measuring the mass and Z distributions in fissioning systems since the 1940's. As technology has improved, the quality of the data has also improved. However, while great advancements in materials and experimental techniques have led to very sharp mass resolutions (~0.5 amu) for light mass products, heavy fragment mass resolution still suffer broader mass resolutions (~2-3 amu) [8]. The primary goal of this work is to measure light masses to better than 1 amu resolution, and heavy masses to near 1 amu resolution, FWHM. This would allow the individual masses to be discerned in the total yield mass plots.

In physical methods (discussed in more detail in section 2.2), the mass of each product is determined through the classical kinetic energy equation $E = {}^1/_2\, mv^2$, restated as

.

$$M = 2\frac{E}{v^2} = 2\frac{E}{\left[\frac{l}{\Delta t}\right]^2} \qquad \text{[Eq. 1]}$$

where M, *E*, *v*, *l*, and *t* correspond to the mass, energy, velocity, length of the TOF path, and TOF measurement respectively. Extracted values for velocity and mass are functions of energy, length, and time.

The uncertainty in the mass measurements is then a function of the uncertainty in the timing, energy and length.

$$\frac{\delta M}{M} = \sqrt{\left(\frac{\delta E}{E}\right)^2 + \left(\frac{2\delta l}{l}\right)^2 + \left(\frac{2\delta t}{t}\right)^2} \qquad \text{[Eq. 2]}$$

where

$$\frac{\delta M}{M} * 100 = Mass\ Resolution\ (\%) \quad \text{[Eq. 3]}$$

For our purposes we are using FWHM for the uncertainty, δ. The uncertainty in length is due to placement of the electrostatic mirrors, the length, however, is constant and the error contribution is systematic rather than random. Using alpha particle measurements, the length can be calibrated to where the length has minimal contribution to the overall mass uncertainty when compared to energy and time. A more detailed description of the length calibration can be found in the master's work performed by Shelby Fellow [9]. The uncertainty analysis here will instead be focused on energy and time.

Here we use results from similar previous work for energy resolution (510 keV for heavy products) [7], as well as our results from time-of-flight measurements utilizing 50 μg/cm^2 carbon foils (~282 ps FWHM for α-particles) to determine the feasibility of obtaining necessary energy and timing resolution to reach the goal of 1 amu mass resolution. As an example, the published mean mass from the light and heavy peak of $^{235}U + n_{th}$ fission reaction, or A= 96 and 139 [10] and so 1 amu resolution corresponds to 1.04% for light products and 0.72% for heavy products.

We find that the square root of the sum of squares for the energy and time resolution needs to be less than or equal to 0.01 to achieve a ≤ 1% mass resolution.

$$0.01 = \sqrt{\left(\frac{\delta E}{E}\right)^2 + \left(\frac{2\delta t}{t}\right)^2} \qquad \text{[Eq. 4]}$$

The uncertainty in length is minimal, and is systematic rather than random, so length is not considered in the uncertainty accounting. Using the expected values from previous and current work we find for mean ^{235}U light products, at a length of 50 cm:

$$\left(\frac{\delta E}{E}\right) = \left(\frac{385\ keV}{101{,}560\ keV}\right) = 0.00379 \qquad \text{[Eq. 5]}$$

$$\left(\frac{2\delta t}{t}\right) = \left(\frac{2*282\ ps}{36{,}053\ ps}\right) = 0.01564 \qquad \text{[Eq. 6]}$$

which gives the final mass resolution of 1.61%,

$$\frac{\delta M}{M} = \sqrt{\left(\frac{\delta E}{E}\right)^2 + \left(\frac{2\delta t}{t}\right)^2} = \sqrt{(0.00379)^2 + (0.01564)^2} = 0.016 * 100 = 1.61\%. \quad \text{[Eq. 7]}$$

For mean heavy products:

$$\left(\frac{\delta E}{E}\right) = \left(\frac{510\ keV}{70340\ keV}\right) = 0.00725 \qquad \text{[Eq. 8]}$$

$$\left(\frac{2\delta t}{t}\right) = \left(\frac{2*282\ ps}{52{,}182\ ps}\right) = 0.01081 \qquad \text{[Eq. 9]}$$

which gives the final mass resolution of 1.3%,

$$\frac{\delta M}{M} = \sqrt{\left(\frac{\delta E}{E}\right)^2 + \left(\frac{2\delta t}{t}\right)^2} = \sqrt{(0.00725)^2 + (0.01081)^2} = 0.013 * 100 = 1.3\%. \quad \text{[Eq. 10]}$$

A goal of ≤ 1% mass resolution for heavy products is achievable, given small improvements in either the energy or timing resolution or an increase of spectrometer length, though 0.72% is more difficult, and near 1% for light fragments would give 1 amu resolution.

Much of the FPY data that exists is not from time of collection spectrometry but rather delayed yield, gathered by chemical separation [8]. This method produces sharp mass values as most fission daughters decay along the isobar line except for known beta delayed neutron branching, but the Z distributions have to be reconstructed by models.

Aside from the primary goal of achieving a mass resolution near 1 amu for fission product mass distributions, we also investigated methods for determining independent Z yields correlated particle-by-particle with A yields. Radiochemical methods have produced very accurate cumulative Z yields, however the inherent deficiencies in the methodology prohibits the dissemination of independent yields [8]. The physical methods employed in the current work will provide a means to determine the independent Z distributions through details of the energy detector constructed for this work.

In this work we measure time-of-flight and kinetic energy for each particle. The time-of-flight measurement is made by two measurements of the fission fragment by two different timing detectors, which are compared for the time of flight. The energy is determined by a gas filled ionization chamber (IC), in which the amount of ionization is proportional to the kinetic energy of the entering particle. Utilizing a gas-filled IC, there are several techniques used to obtain Z information. Bragg curve spectroscopy offers one method for determination of light products; however, heavy products do not produce a Bragg peak due to their low kinetic energy per nucleon [8, 11]. Since heavy product Z is also important to our measurement, a method

developed by Tyukavkin *et al* utilizing a time-of-flight method based on the product range in the ion chamber [12].

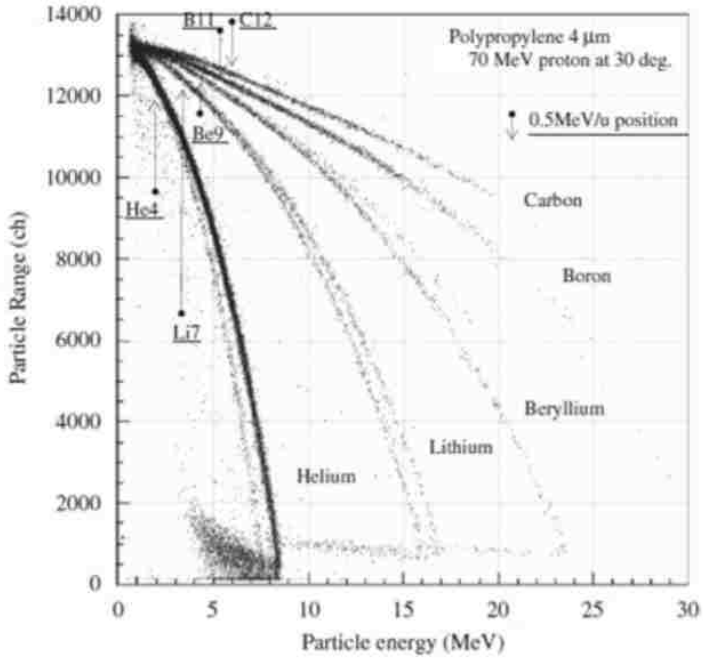

Figure 3: Measurement of heavy ion range as a function of energy [11], which shows a difference in behavior based on Z.

The context of this work is presented through discussion of prior work in in chapter 2. The methods our spectrometer technique employs will be discussed further in chapter 3. The end goal of this work will be to provide high-precision, correlated mass, energy and Z measurements for ^{252}Cf spontaneous fission (s.f.) and ^{235}U thermal neutron induced fission (n_{th}, f) in an aim to improve current independent FPY data. Mass measurements are presented in chapter 4, while Z determination work based on particle range in the ion chamber is presented in chapter 5. Finally, conclusions are presented in chapter 6 and future work in chapter 7.

Chapter 2: Background

2.1 A Brief History of the Fission Process

After the discovery of the neutron by James Chadwick in 1932, Enrico Fermi postulated that the neutral particle would make for an interesting projectile for investigations into nuclear reactions. Initially, the ambitious scientists believed that by adding neutrons they were creating heavier and heavier transuranic elements. It wasn't until 1939 that chemists Hahn and Strassmann [13] and Meitner and Frisch [14] revealed that those "transuranic elements" were, in fact, radioactive lighter elements. These revelations led first to the development of the liquid-drop model and eventually the nuclear shell model [8].

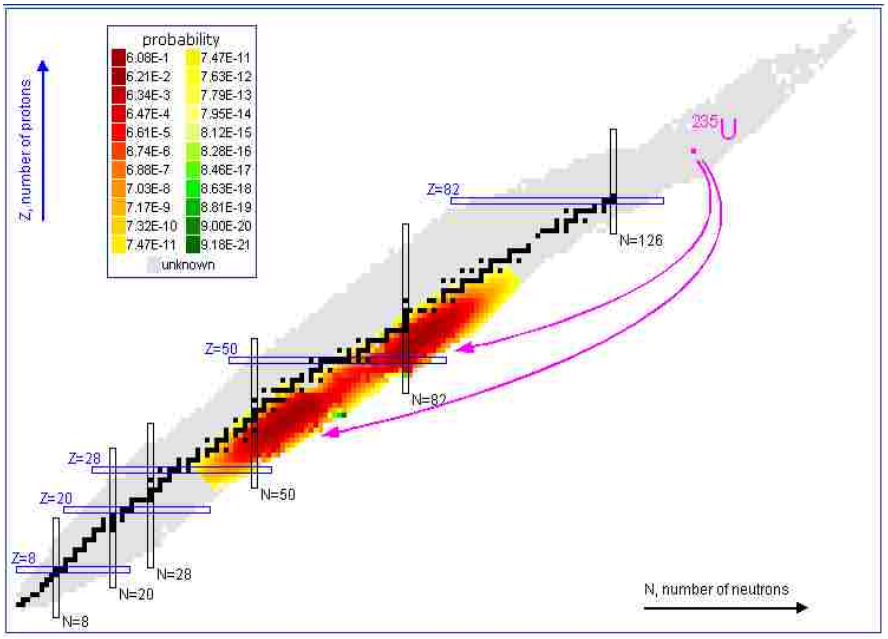

Figure 4: A, Z fission product probability distribution [15].

In this work we study fission of heavy elements, emphasizing well studied elements to understand our spectrometer. For this work, asymmetric spontaneous fission of ^{252}Cf and thermal neutron-induced fission of ^{235}U will be the focus for benchmarking purposes. In typical

fission, an unstable or excited heavy nucleus is split into two asymmetric lower mass elements, these are fission fragments. In a short time after the splitting of the nucleus (scission), ~10^{-15} s, typically from 0-7 neutrons can be released, leaving behind fission products which can be measured by physical and radiochemical methods [8]. This excited state of the parent nucleus may be caused by an incident neutron, excitation of the parent with a photon, called photofission, or other processes. The parent nucleus may also fission by tunneling, called spontaneous fission, which is the case for radioactive sources such as Cf-252. When the two heavy products are different masses this is called asymmetric fission. If the parent nucleus is very excited, such as with high the incident neutron energy, the fission product distribution becomes more symmetric.

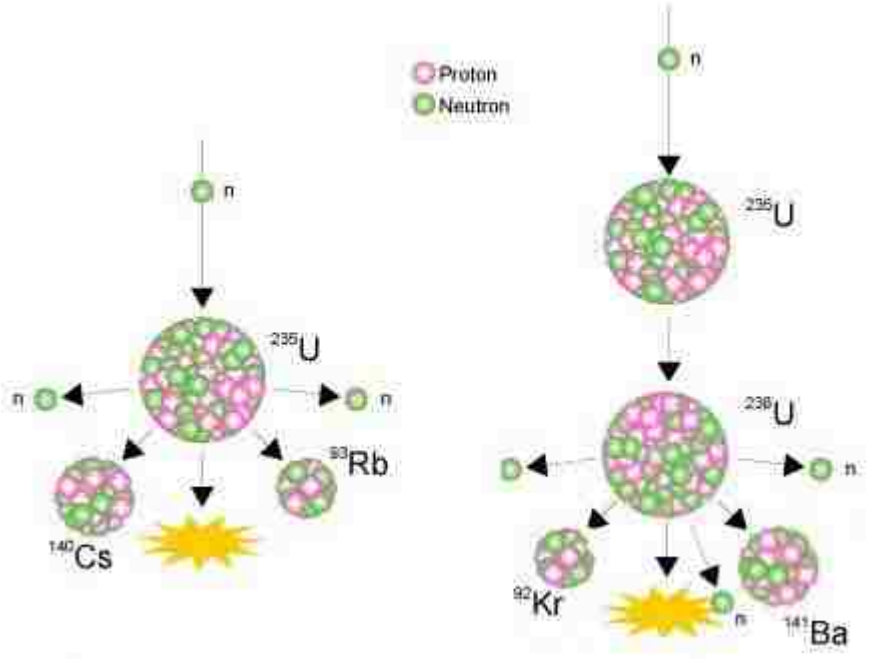

Figure 5: Basic diagram of the fission process. [16]

2.2 Experimental Methods & Previous Experiments

2.2.1 Radiochemical Methods

Chemical separation methods have been used extensively to determine cumulative yields of fission fragment inventories. The process for detection generally involves the use of a fission chamber with separation post irradiation. Following separation, gamma and beta counts are taken. This method has an overall accuracy of 2-5% [17] and produces some independent yield data measured shortly after irradiation or cumulative yield data through the collection of integral fission events via long irradiation and counting times. Theory can be adjusted to match these results, and some information about the pre-fission mass surface can be extracted. However, as these are a measure of single fission products and there is no measured correlation between both fragments from each fission, they cannot be used well to directly develop relationships to reconstruct the scission event. Methods of measurement with different correlations between variables are presented below.

2.2.2 2E Method

Methods for directly or indirectly measuring fission observables can be broken down into two categories; physical methods and chemical methods [8]. Both methodologies suffer from uncertainties either inherent or technological in nature. Physical methods potentially offer a wide variety of information related to various fission observables in a real-time environment; e.g., mass (A), atomic number (Z), total kinetic energy (TKE), average prompt neutrons (ν).

The most widely used physical method has been 2E measurements, utilizing gas-filled ion chambers, typically back-to-back electrodes in the same gas volume, or solid-state detectors. This method allows measurement of two important quantities, mass, and TKE, with potentially some Z information. In the 2E detector scheme, TKE is measured by the simple relation:

$$TKE = E_L + E_H \qquad \text{[Eq. 11]}$$

Where E_L and E_H are the kinetic energies of the light and heavy product respectively. If prompt neutron emission is neglected, the determination of the mass is straightforward.

$$M = M_L^* + M_H^* \qquad \text{[Eq. 12]}$$

M^*_L and M^*_H are the mass of the primary fragments and the total mass M is the mass of the fission parent which is known. Using momentum conservation in the center-of-mass frame, the relation between the light and heavy fragments becomes, for absolute values of momentum:

$$P_L = M_L^* V_L^* = P_H = M_H^* V_H^* \qquad \text{[Eq. 13]}$$

where V^*_L and V^*_H are the velocities of the fission fragments. Substituting further using $E=p^2/2m$, we find:

$$E_L^*/E_H^* = M_H^*/M_L^* \qquad \text{[Eq. 14]}$$

Combining equations 12 and 14, the masses can be easily determined from the energy measurements. However, as stated earlier, this neglects the prompt neutron emission, which leads to a shift and broadening in the resulting energy spectrum.

Another way to measure energies is with solid state detectors. One type of solid state detectors, a thin silicon surface barrier detectors (SSB), is manufactured in a way where a very thin p-type electrode layer is deposited on a thicker, low dopant density, n-type layer. As voltage is applied, a depletion layer where detection occurs is created thick enough that the fission products are fully stopped within the depletion layer. These detectors are easy to use and widely available at relatively low cost. However, these detectors suffer from a large pulse height defect, particularly for heavier products, due to charge recombination for these densely ionizing

particles. They also have an inferior energy resolution to an ionization chamber for heavy particles (δE~1 – 2 MeV) [8]. However, surface barrier detectors have the advantage of an absolute calibration method for fission products developed by Schmitt *et al* [10]. The 2E method utilizing solid-state detectors produce a mass resolution of δM ~ 4 – 5 amu [8].

In an ionization chamber based system, fission products deposit their kinetic energy in the ionization gas with the resulting electron motion generating an induced voltage signal on the anode and cathode. Ion chambers have the advantage over solid state devices, as an IC does not suffer from radiation damage, and has a smaller pulse height defect due to more spread out charge deposition, and has improved resolution for heavy ions. The disadvantage of utilizing an ion chamber for physical measurements is the inherent lack of absolute calibration systematics. For absolute calibration, a heavy ion beam with well-known mass is necessary. In recent years, ion chambers have become the detectors of choice due to their improved resolution, minimal pulse height defect, and design customization.

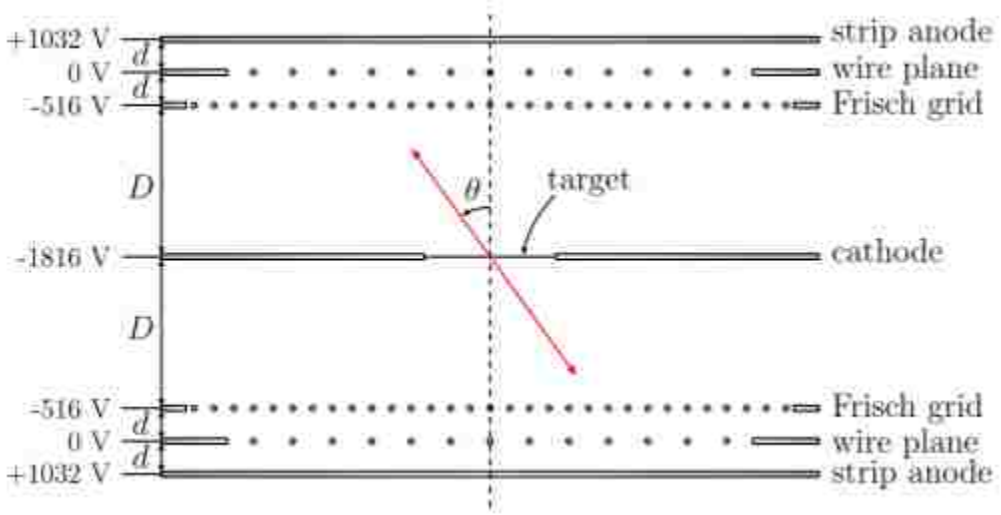

Figure 6: Schematic of a 2E, back-to-back ion chamber [18].

2.2.3 1v – 1E, 2v – 2E Method

A second method, which will be employed in this work, is the v-E method, use as 1v – 1E and 2v – 2E. A brief discussion of this method is covered in this section, with a more rigorous description given in Chapter 3. The 1v – 1E method uses a transmission time-of-flight measurement with heavy ions passing through thin foils and ejecting electrons. These secondary electrons can be reflected toward timing detectors, often microchannel plate detectors, via electrostatic mirrors, to produce start and stop timing signals, and the foils are a known distance apart, giving a velocity. The ion energy is then fully deposited in an energy detector, and either solid-state or ion chambers are typically used. The product mass is then easily determined based on the classical kinetic energy equation:

$$E = \frac{1}{2}Mv^2 \qquad \text{[Eq. 15]}$$

Simply rearranging to solve for mass we have

$$M = 2\frac{E}{v^2} = 2\frac{E}{\left[\frac{l}{\Delta t}\right]^2} \qquad \text{[Eq. 16]}$$

where M, E and v are the mass, kinetic energy and velocity of the ion, respectively. Figure 7 gives a simplified illustration of the 1v – 1E measurement technique; where t_1 is the start time detector, t_2 is the stop time detector, l the length and E the energy detector.

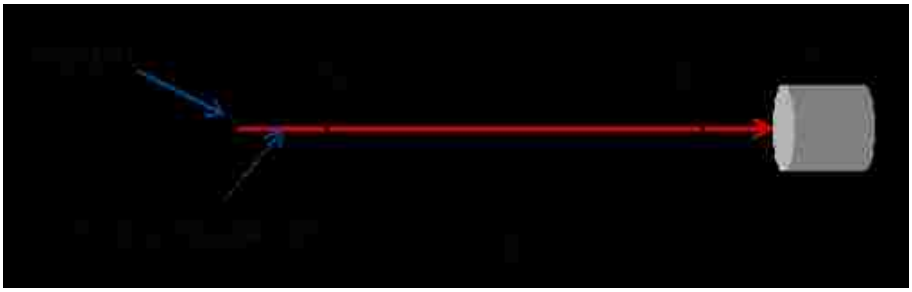

Figure 7: Simplified 1v – 1E detector system.

This method employs fast timing detectors with timing resolution superior to the ionization chamber in the 2E systems, resulting in uncertainties of a few hundred picoseconds (FWHM) [8]. Increasing the distance and thus increasing the time of flight decreases the proportional uncertainty in the time-of-flight measurement, $\delta t/t$, however geometric efficiency into the energy detector suffers, thus a compromise must be made. The largest inherent drawback of the 1v – 1E technique has historically been low detection efficiency, with the TOF-E correlated efficiency of ~0.01% in work by Boucheneb et al. [19]. For fission product detection, the 1v – 1E method provides correlated information on single product mass, kinetic energy and velocity. If an axial ion chamber is used as the energy detector, it can be modified to provide further information about the fission product range and Z [12].

The 2v – 2E method is simply two 1v – 1E detectors typically oriented about 180^{o} from each other around the target for low recoil beam reactions, as shown below in Figure 8. This 2E-2V detector configuration is optimal for event-by-event fission product detection. Paired fission product detection can be correlated by time stamping data to reveal unique information about the fundamental fission process. This method has the additional value of providing information on total kinetic energy and prompt neutron release, as well as correlated measurements of the fission product mass, energy, range and Z, on an event-by-event basis. Due to the wealth of information

this method provides, a v – E detection system has been designed and developed for the experimental work, with a single arm and with the eventual intended addition of a second arm.

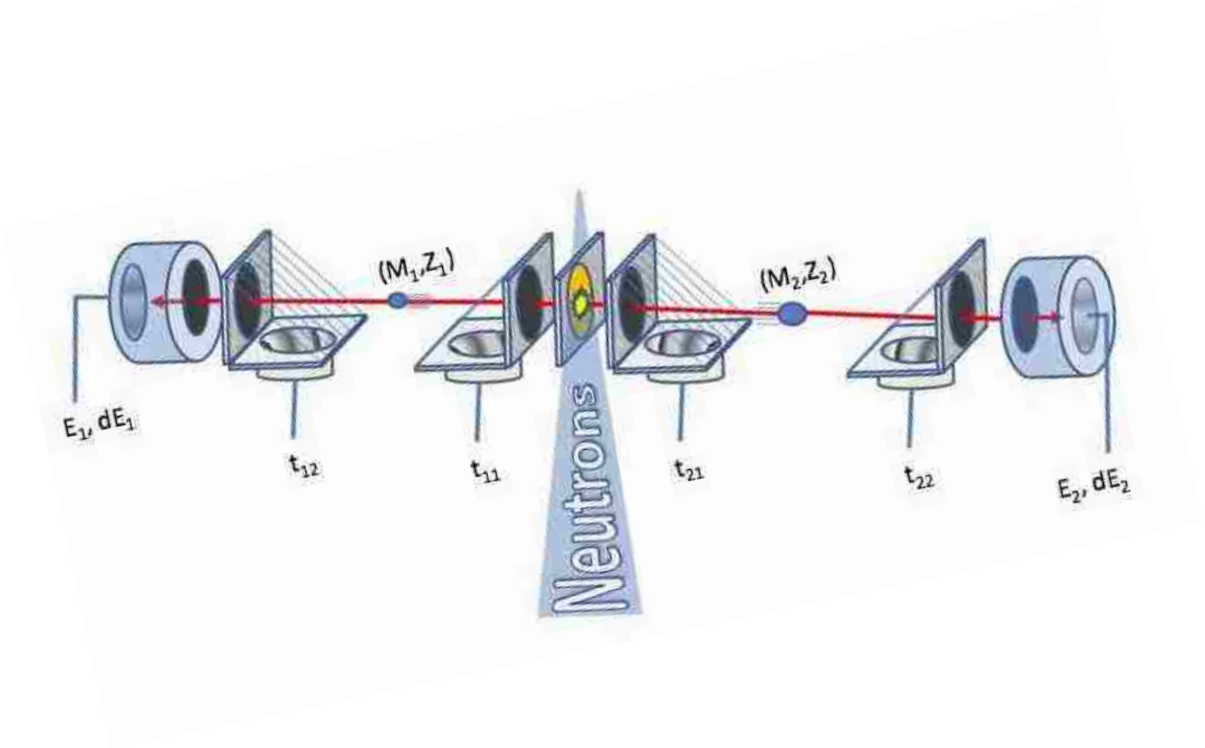

Figure 8: Depiction of a typical 2v – 2E spectrometer [20].

2.2.4 Previous Experiments

2.2.4.1 2E Method

The 2E method, as discussed in section 2.2.2, has been extensively used in fission product mass measurements [10, 21, 22]. This is typically done with two solid-state silicon detectors [10,21] or a single gas volume with back-to-back ion chamber electrodes around the fission source [22]. While the 2E method is relatively simple to design and construct, especially the solid-state version, the measurements lack the mass resolution for our stated purpose. However, due to the access to absolute calibration methods with solid-state devices, we considered using the calibration method presented by Schmitt *et al* for heavy ion energy loss

measurements for experimental confirmation of energy correction methodology performed on the 1v – 1E data. This is covered in detail in Chapter 5: Future Work. Recent work utilizing the 2E technique was performed by D. Duke [23] to investigate mass and TKE relationships for the ^{238}U(n, f) reaction as a function of various neutron energies, En, see Figure 9.

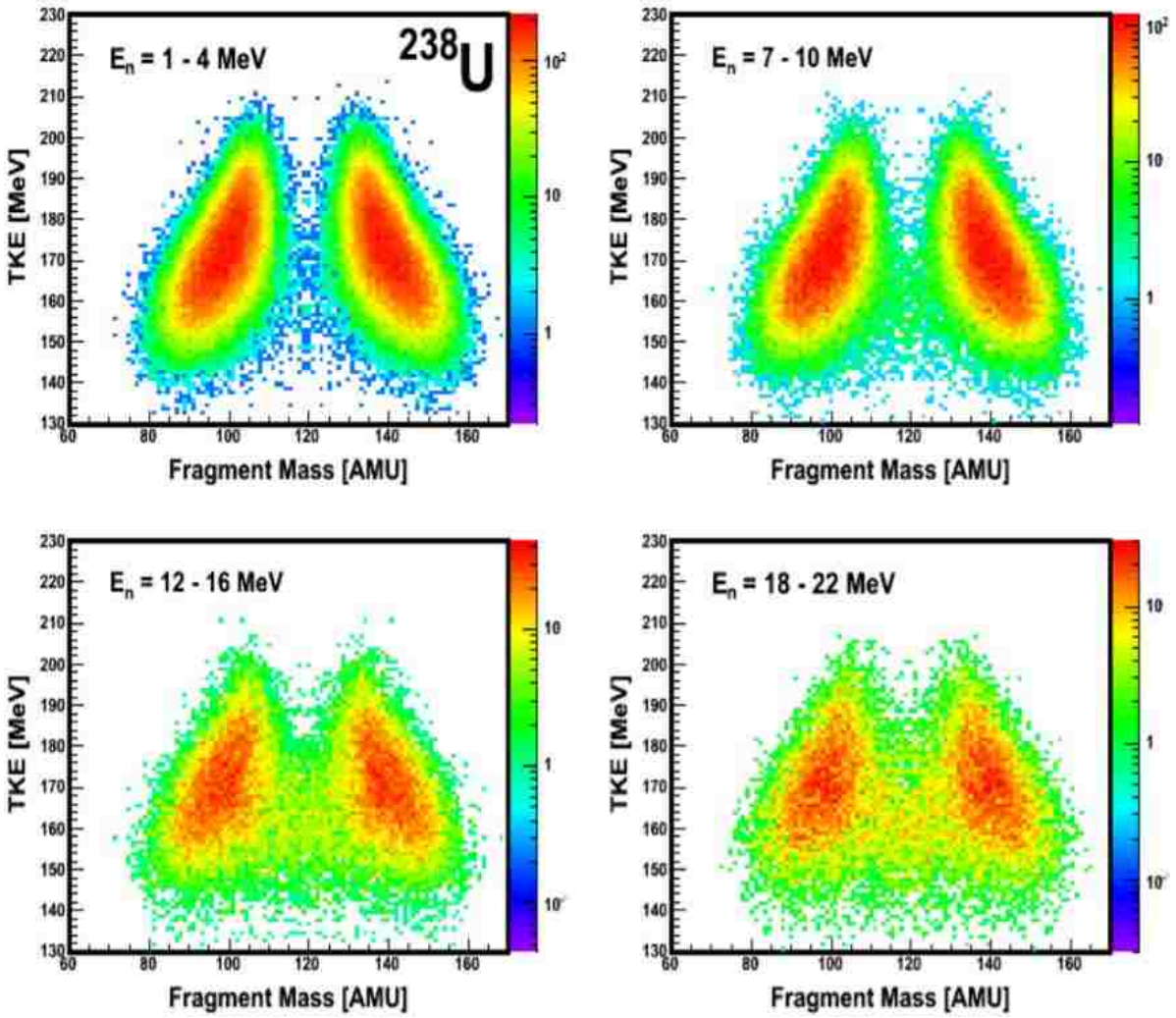

Figure 9: Measured TKE as a function of fragment mass [23]

These measurements confirmed a decrease in TKE of the compound nucleus with increased symmetry. Mass yields as a function of neutron energy were also measured previously,

[23] see Figure 10, though the mass resolution in that experiment was found to be ~ 4 amu, typical for a 2E measurement system.

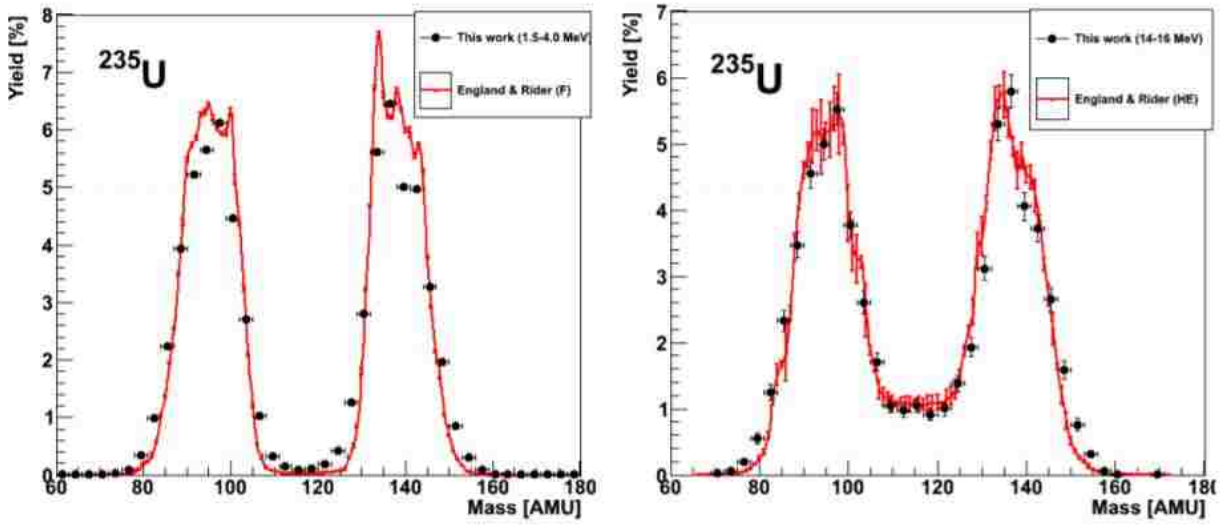

Figure 10: ^{235}U FPY evaluation at different neutron energies using 2E method [23].

2.2.4.2 Mass Separation for Unslowed Fission Products at Lohengrin

The Lohengrin spectrometer at the Institut Laue-Langevin (ILL) is the current high resolution standard in event-by-event fission fragment measurement, and is used coupled to the Grenoble high flux reactor [24]. The Lohengrin detector utilizes recoil mass spectrometry to separate the products of differing mass. An actinide sample is placed near the reactor core and subject to a flux of 5.3 x 10^{14} n cm^{-2} s^{-1}. The fission products that travel down the beam pipe are mass selected (A/Q) by a magnetic field and momentum selected (p/Q) by an electric field, Q being the fragment charge. Products of a single mass are then collected and analyzed using various techniques [25]. The selection is very precise, but this makes the acceptance extremely low. Figure 11 gives a schematic of the Lohengrin spectrometer.

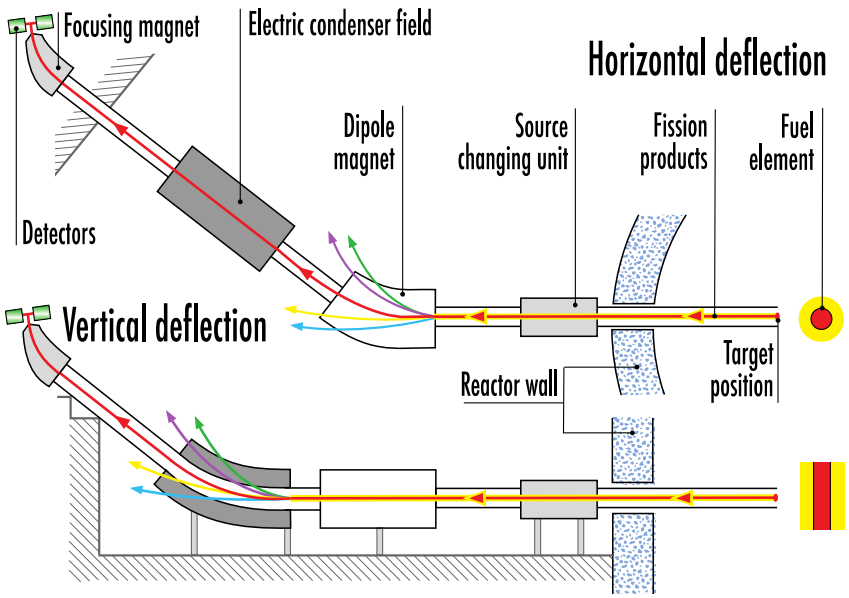

Figure 11: Lohengrin detector principles and operation [24].

The Lohengrin spectrometer has a typical mass resolving power of $A/\Delta A \sim 1500$, and an energy resolution of $E/\Delta E \sim 100$ to 1000 for thermal neutron energy induced fission [25]. One limitation of the Lohengrin spectrometer stems from the large use of "beam time" and its dependence on careful measurement of fragment charge state, as it directly influences the results. Intrinsically, Lohengrin cannot distinguish between "multiplets", fission products possessing the same A/q value, e.g., $A/q = 100/25 = 96/24 = 4$. This has been remedied through the inclusion of a surface barrier detector or ionization chamber to collect atomic number information, Z [25]. This spectrometer has been used successfully to measure fission products from the $^{235}U(n_{thermal},f)$ reaction and is a primary source of fission product data contained within current nuclear data libraries [17]. To remedy the extremely low acceptance, another spectrometer, COSI FAN TUTE, a 1v – 1E mass spectrometer, was developed and extensively studied at the Lohengrin facility.

2.2.4.3 COSI FAN TUTTE

The COSI FAN TUTTE spectrometer yielded a mass resolution of 1-2 amu for light products in the $^{229}Th(n_{thermal}, f)$, $^{239}Pu(n_{thermal}, f)$, and $^{233,235}U(n_{thermal}, f)$ reactions [19]. Though COSI FAN TUTTE was originally proposed to measure energy and velocity of both fission products (2v - 2E), no values were published and, through private communication, the issue appeared to be low efficiency which made simultaneous back-to-back measurements rare. Thus, COSI FAN TUTTE was essentially operated as a 1v - 1E detector, shown in Figure 12.

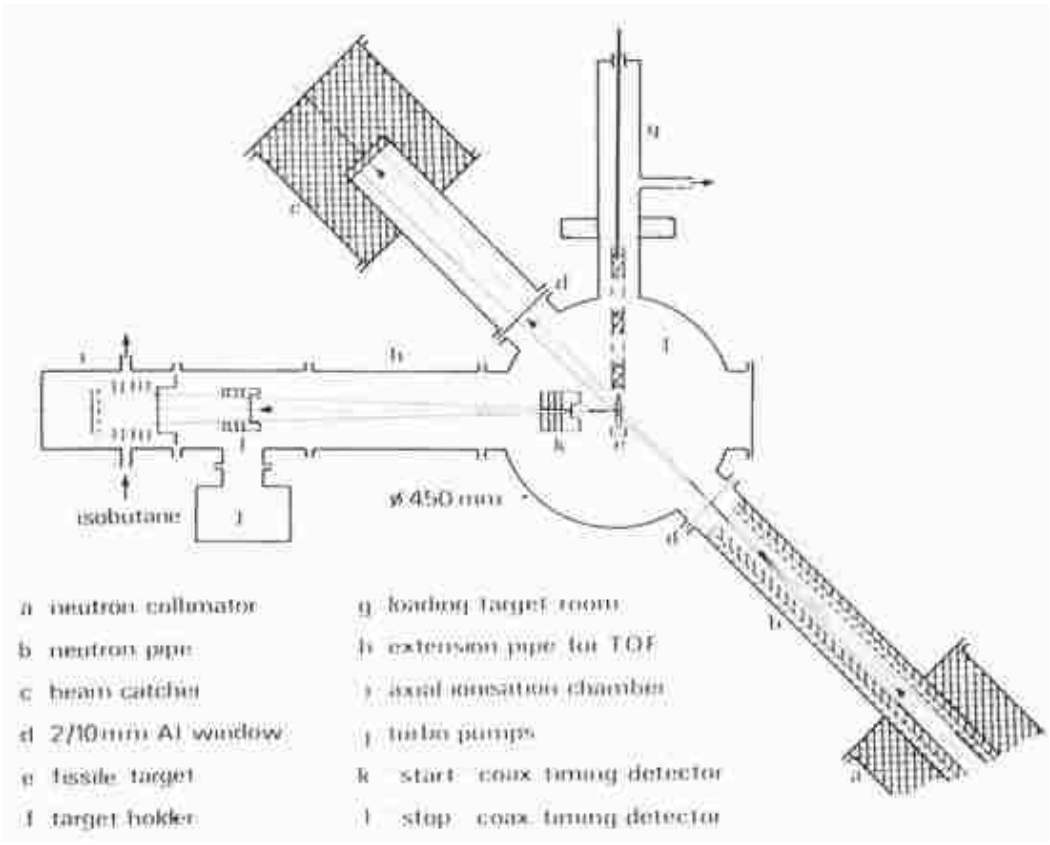

Figure 12: COSI-FAN-TUTTE experimental setup [19].

The fission cross-section drops strongly with increased neutron energy [19, 26], and so the inherent low geometric efficiency (0.01%) of COSI FAN TUTTE limits the feasibility of fission product measurements for incident neutron energies outside of the thermal region. By

setting a coincide window on a small section of the raw time-of-flight and energy data, clear mass lines develop. Figure 13 shows the coincidence windows set on the time-of-flight and energy distributions.

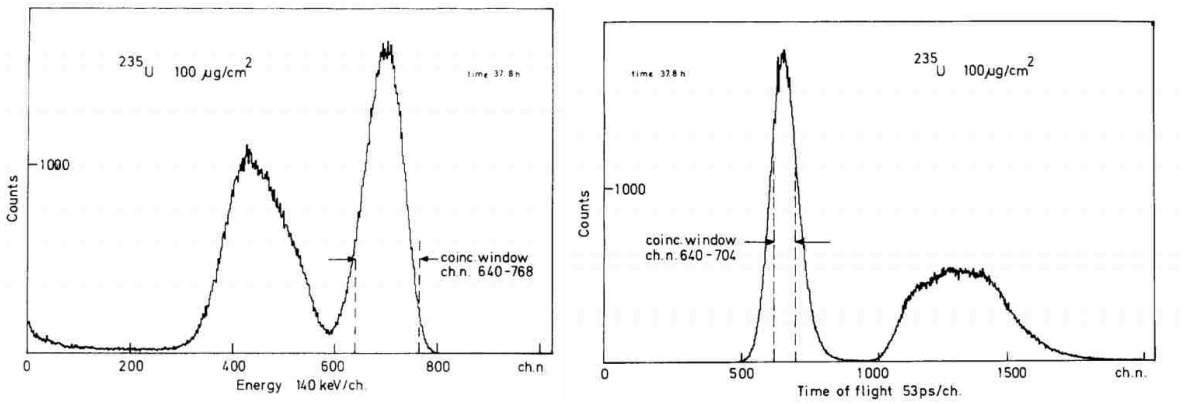

Figure 13: Calibrated energy (left) and time-of-flight (right) data in a 1v – 1E detector [27].

The results for light products shown in Figure 14 were promising, particularly in the separation seen in the time-of-flight and pulse height correlations in the coincidence region. The time resolution for this experiment was found to be $\delta t \approx 100$ ps [27].

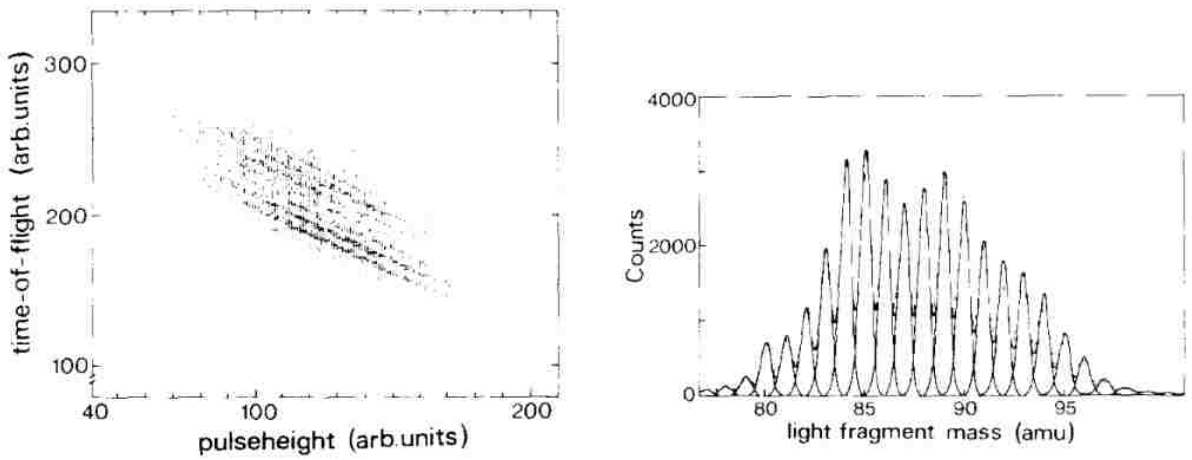

Figure 14: Results for coincidence window correlations [27] The image on the right is a fit to the extracted masses using Gaussians at each mass.

One benefit of fielding COSI FAN TUTTE at the Lohengrin facility is the access to the charge separator for absolute energy calibration and uncertainty analysis of ions at typical fission product energies as seen in Figure 15. [7]

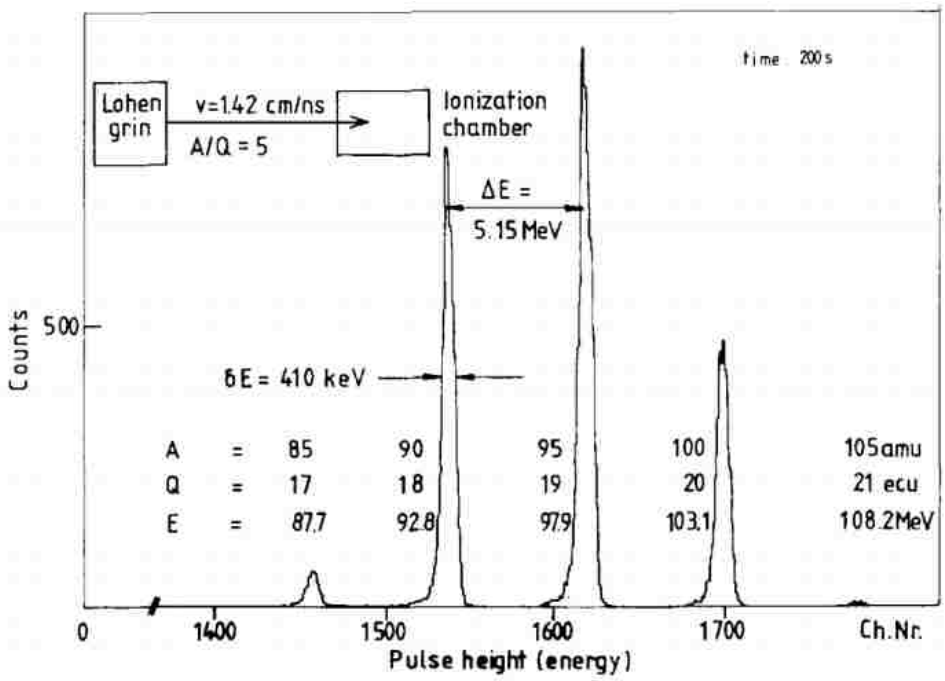

Figure 15: Heavy ion energy resolution measured at the Lohengrin facility. [7]

The energy resolution of the COSI FAN TUTTE spectrometer was assessed to be δE_L = 385 keV and δE_H = 510 keV for light and heavy products, respectively, after correcting for straggling in the beam. Utilizing advancements in time resolution seen in fast-timing MCP, improved energy resolution in ion chambers, digital data acquisition electronics and thin, silicon nitride ion chamber entrance windows, we set forth to improve light and heavy fission products mass resolution with higher efficiency [26].

2.3 Current Collaboration: Spectrometer for Ion Detection in Fission Research (SPIDER)

The detector currently being developed and tested at UNM, is in direct support of the SPIDER project, working closely with our collaboration partners within Los Alamos National Laboratories P-division. The SPIDER collaboration is an ambitious project following the proposed 2v - 2E method of the COSI FAN TUTTE detector.

The UNM role in the collaboration is mainly focused on detector and technique development, developing and fielding as single arm spectrometer. This development is described in detail in this dissertation. The development on the UNM spectrometer feeds into understanding and improvements of the LANL spectrometer, and contributions to the LANL spectrometer are described below.

For context, the LANL role in the collaboration is primarily interested in increased efficiency for measurements of lower cross section reactions, such as fission yields at higher neutron energies. The SPIDER project aims to increase the efficiency and mass resolution by implementing an array of 16 back-to-back V - E detectors or 8 full 2V - 2E arm pairs as shown in Figure 16.

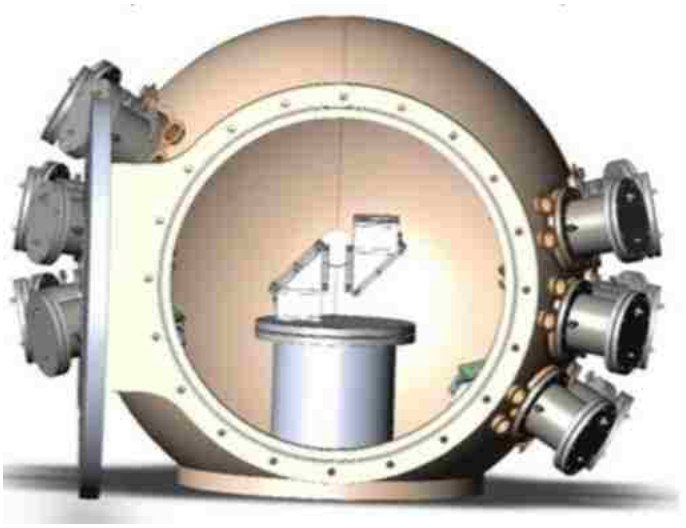

Figure 16: Proposed SPIDER multi-arm, 2v -2E chamber.

The single arm pair 2v – 2E system is currently installed at Flight Path 12 in the LANSCE Lujan Center thermal neutron facility, Figure 17. Thus far, initial $^{239}Pu(n_{thermal}, f)$, $^{235}U(n_{thermal}, f)$ and $^{252}Cf(s.f.)$ measurements have been made to test the feasibility of the device before the construction and expansion to the "8 arm" configuration.

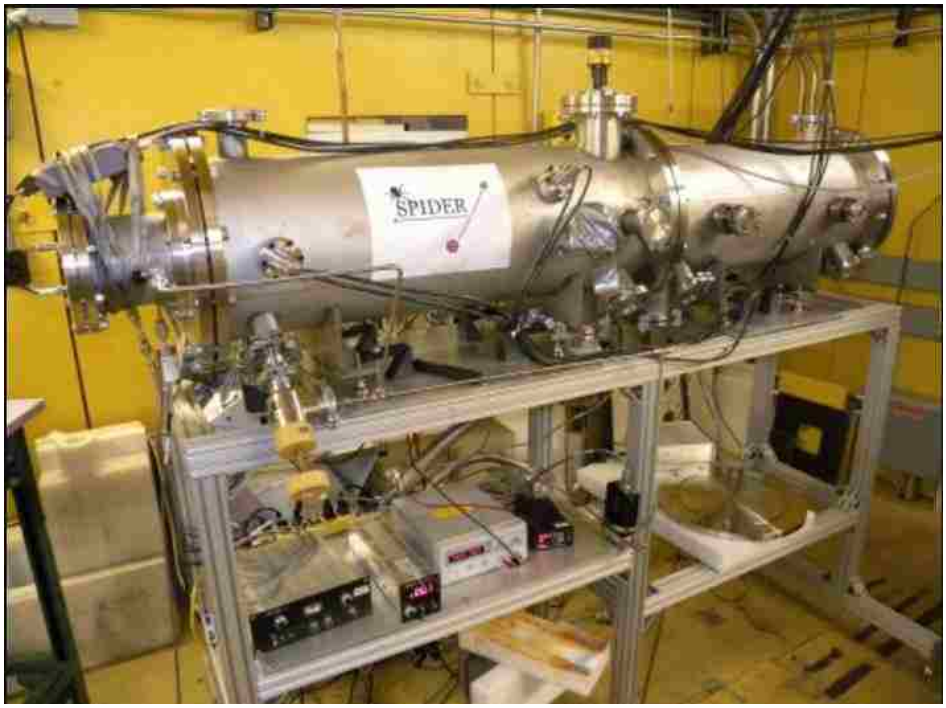

Figure 17: Current LANL SPIDER 2v -2E chamber, the target is in the center.

Preliminary FPY data is shown in Figure 18. FPY for ^{252}Cf(s.f.) has shown to be comparable to previous work done by Schmitt [10]. However, initial analysis of the ^{235}U($n_{thermal}$, f) has proven difficult, particularly in the heavy mass peak. Various analysis methods are still being investigated. Work by our collaboration with SPIDER yielded several publications [28,29,30,31]

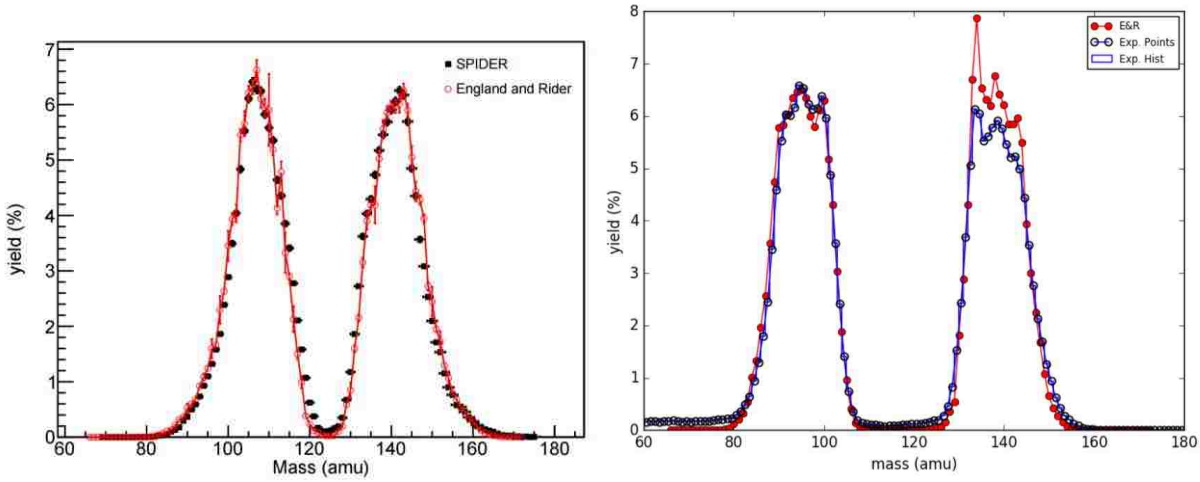

Figure 18: Initial FPY results for (left) ^{252}Cf(s.f.) and (right) ^{235}U($n_{thermal}$, f) [20].

2.3.1 UNM development in support of the SPIDER fission project

At UNM we have developed instruments and techniques in support of the LANL led SPIDER effort. We developed the ionization chamber, based on Oed et al [7, 27], that is in use on SPIDER, and characterized response as a function of particle lateral position and gas pressure, and examined both P-10 (10% methane in Ar) and isobutane ionization gasses. We examined the TOF detector system timing and detection efficiency as a function of particle position. We developed ionization chamber structure, based on the active cathode work of Sanami et al. [11] which they applied to light particles near carbon, to allow independent cathode pulses for cathode vs. anode timing and thus range and Z determination for fission fragments. We further developed and applied this work in this dissertation. We also developed an independent ionization chamber window setup different from LANL to allow individual small window replacement when needed, rather than a full, larger window replacement. This prior work by our group is detailed in the thesis work of Shelby Fellows [9], Lena Heffern [32], Drew Mader [33], James Cole [34] and the current author Rick Blakeley [35].

Chapter 3: Detection Methods

3.1 Detector Description & Resolution Tests

The UNM spectrometer was developed with an eye on improving mass resolution and extracting any additional correlated data available, including Z information. Since the LANL effort was on increased efficiency, in designing the UNM spectrometer the efficiency requirement was just to have sufficient statistics. Details of the UNM spectrometer developed here are presented in the current chapter.

3.1.1 Timing Detectors

The two time-of-flight module each consist of a carbon conversion foils from which electrons are ejected by the ion passing through, an electrostatic mirror to reflect the electrons to the detector, and a Hammamatsu 9890-11 microchannel plate detector [36] (MCP). The carbon conversion foils used were 20 to 100 micrograms/cm^2 mass thickness. The electrostatic mirror is composed of thin wires with a very low geometric cross section to allow the ions to pass through, though with a strong enough field to deflect the much lighter electrons with only minor perturbation to the ions. The MCP detectors provide sharp time 1 (start) and time 2 (stop) signals to determine the time of flight of a given particle. The modules are spaced by 50 cm or 1 m, foil to foil, depending on efficiency and resolution tradeoffs. Figure 19 provides a detailed schematic of an individual conversion foil/electrostatic mirror/MCP module.

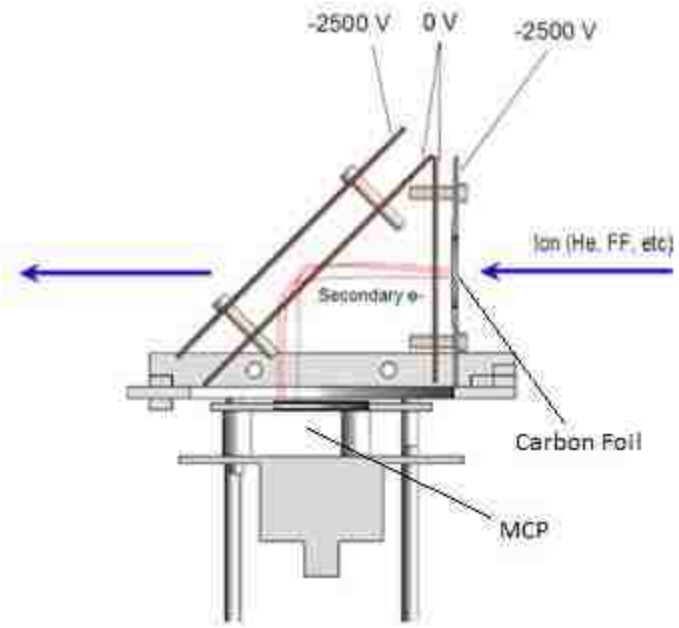

Figure 19: Single time-of-flight measurement setup.

Particles under investigation pass through the first carbon foil, emitting secondary electrons from the foil, and continue to the second conversion foil where the electron ejection is repeated. The secondary electrons ejected from the foils are accelerated and reflected toward the MCP surface where they are detected and provide a sharp timing signal (~2 ns FWHM for the 9890-11 MCPs) which, when the two MCP signals are compared through a constant fraction discriminator, can produce a much sharper TOF signal.

3.1.2 Microchannel Plate Detector

At the heart of the microchannel plate detector are the microchannel plates used for charge multiplication. Unlike photomultiplier tubes, the microchannel plate consists of an array of millions of very small (6 to 25 μm in diameter, 0.24 to 1 mm in length [36]), individual cylindrical glass capillaries fused together at an angle in the shape of a thin disc, as in Figure 20, or rectangular plate to supply the charge amplification. These detectors are primarily used for charged particle detection; however, they are also sensitive to UV and X-ray radiation.

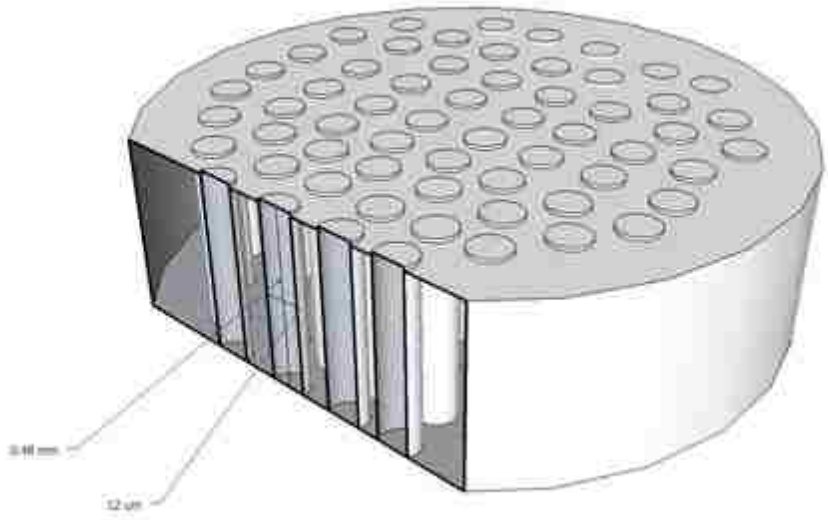

Figure 20: Illustrates a simplified MCP. [35]

MCP detectors have a very desirable timing resolution due to the short pulse width (to ~100 ps) as well as a well-defined 1 and 2-dimensional spatial resolution utilizing discrete multiple anodes or phosphor screen imaging (~40 to 120 μm) [36]. Project collaborators on the related SPIDER project at LANL use large area MCPs employing spatial resolution by edge electrode comparison to correct for differences in travel length for different lateral positions, though the MCPs in this work do not employ position sensitivity as we have a smaller MCPs and thus lower position uncertainty. The high electron sensitivity and fast pulse makes MCP ideal for high-resolution TOF measurements in fission fragment identification.

3.1.2.1 MCP Construction and Operating Principles

The channels of the MCP are constructed individually and bundled together to form a dense hexagonal array of millions of separately insulated lead glass channels. Each channel acts as an individual charge multiplier. There is a strong field between the MCP faces, with 1 kV potential across the ~1 mm thick plates in the MCPs used in our work. The channels are at a slight angle to the normal of the plate face. The incoming, primary radiation strikes the interior surface of an individual channel, releasing secondary electrons from the channel surface based on the energy of the primary radiation. The secondary electrons are accelerated by the field to the next impact point in the channel where they release more electrons, as in Figure 21, and so on for high charge multiplication. Ni-Cr or Inconel depositions on the input and output surfaces of the MCP serve as the electrodes to accelerate the secondary electrons along a parabolic path produced by the primary radiation to induce further secondary electron emission as it interacts with the channel walls [36, 37].

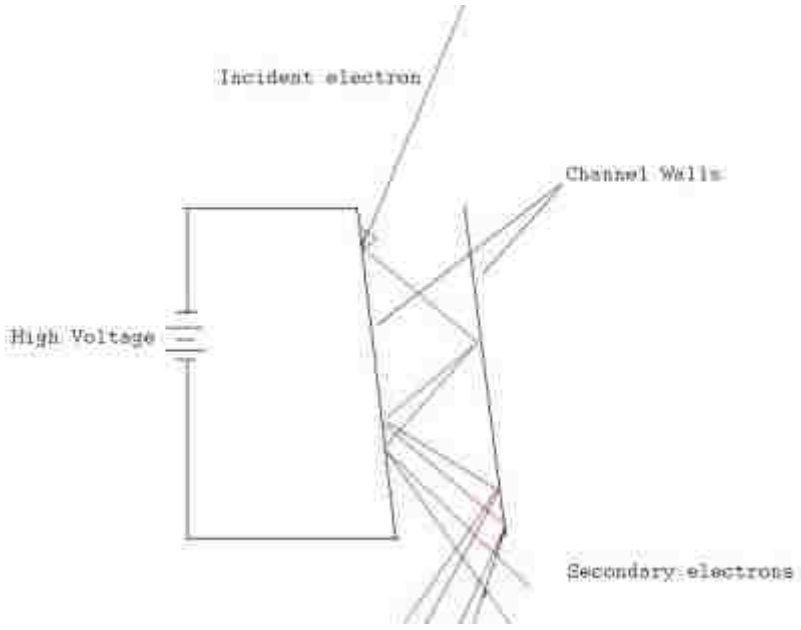

Figure 21: Charge multiplication within a single channel of the MCP. [35]

The overall gain, *g*, of the MCP can be written as a function of both the secondary emission characteristics of the channel wall material called the gain factor, G (~0.3-0.5), and the length-to-diameter ratio, α, of the channel (α = *l*/*d*) given by [36, 37]:

$$g = \exp(G * \alpha) \qquad \text{[Eq. 17]}$$

Gain characteristics for MCPs as a function of applied voltage is shown in Figure 22 for various length-to-diameter ratios.

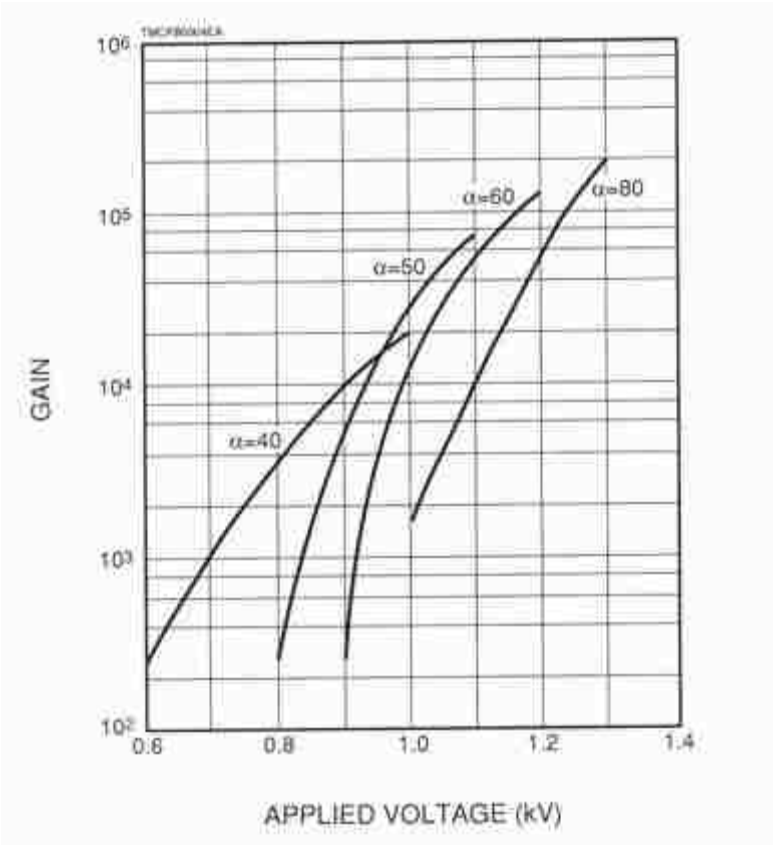

Figure 22: MCP gain as a function of voltage for various length-to-diameter values [36].

Manufactured length-to-diameter ratios vary from 40 – 100 producing a gain of 10^3 – 10^5 for a single plate with an applied voltage of 1000V. Gains larger than 10^4 suffer from an increase

in noise due to ion feedback [36]. The ion feedback, an undesired effect for this application, arises from the high charge density near the channel output producing positive ions when electrons collide with residual gas molecules. These positive ions then cause further secondary electron emission that leads to ion after pulses [38]. These repeated signals must be avoided as we are interested in the MCP detectors for timing.

When a higher gain is required, multiple MCPs can be placed in series to achieve gains greater than 10^4. The placement of two MCPs in series, typically separated by 50-200 μm, is often referred to as the "Chevron" or two-stage MCP configuration, and was used in this work, for an individual plate gain of about 1,000 and for the pair a total of 1,000,000. 3 MCPs in an alternating direction series is referred to as a "Z-stack" or three-stage MCP configuration. Figure 23 illustrates a typical Chevron configuration of MCPs.

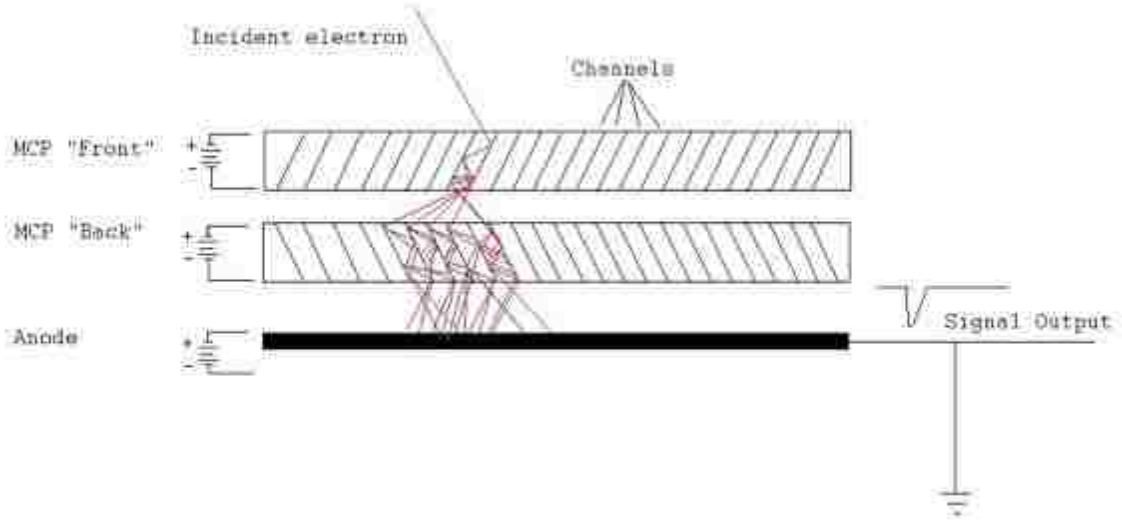

Figure 23: Chevron configuration of two MCPs placed in series [37].

In the Chevron configuration, the channels are typically biased at an angle of 5^{o}-15^{o} from the normal of the plate face in an attempt to limit ion feedback as well as increasing sensitivity to the incident radiation normal to the MCP surface [36].

Ion feedback in the chevron configuration is diminished due to the large bias prohibiting positive ions created near proximity of the exit of the first plate from impacting the entrance of the second plate [39]. Chevron configured MCPs also exhibit charge saturation at gain values of $\sim 10^{7}$. This is primarily due to the inter-plate bias voltage preventing the radial spread of the space-charge cloud exiting the single excited channel, which results in fewer channels being excited in the second plate. As a result, the excited channels experience an increase in the probability of space-charge saturation due to the increased electron impact energy [39]. This is a desirable effect as it narrows the pulse height distribution FWHM, to as much as 60% for a 3-stage MCP. Figure 24 shows the gain characteristics of a single stage MCP, Chevron configured MCPs and Z-stack MCPs as well as the peaked pulse height distributions from Chevron and Z-stack configured MCPs.

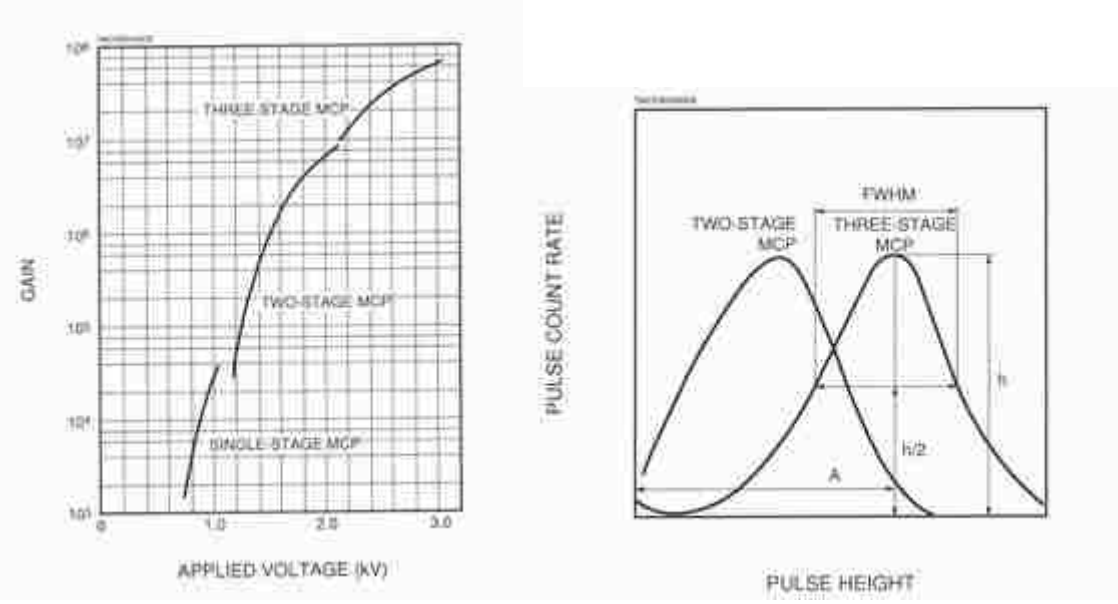

a) b)

Figure 24: (left) Gain characteristics of single and multi-stage MCP configurations and (right) pulse height distributions [36] for different stage MCPs.

Many pulse processing methods benefit from consistent pulse amplitudes, such as decreasing discriminator walk. Table 1 shows the expected pulse height distribution (FWHM), gain characteristics of single and multi-stage MCPs with varying length-to-diameter ratios and maximum applied voltage. The FWHM% is simply the ratio of the FWHM/peak-position channel ratio.

Table 1: MCP gain characteristics as a function of l/d and applied voltage [39]

Configuration	*l/d* ratio	Maximum Voltage (V)	Gain	Pulse Height (FWHM%)
Single-stage	40	1000	$> 4 \times 10^3$	N/A
	60	1200	$> 1 \times 10^4$	N/A
Chevron	40	2000	$> 4 \times 10^6$	< 175%
	60	2400	$> 1 \times 10^7$	< 100%
Z-Stack	40	3000	$> 3 \times 10^7$	< 120%
	60	3600	$> 2 \times 10^8$	< 60%

3.1.2.2 Gain Limiting Mechanisms

At gains higher than 10^8, the pulse height distribution changes from a negative exponential distribution to a quasi-Gaussian shape with a full-width-half-maximum (FWHM) of 50% or better [40], as in Figure 24 (right). This phenomenon is primarily the result of space-charge effects near the exit of the multiplier channel. Space-charge effects on gain limitations in straight channel multipliers were investigated extensively by Adams and Manely at the Bendix Corporation in the U.K. [38]. Their work focused on the relation between space charge density and the electron transit time. When the gain reaches a high value, the space-charge density near the channel exit becomes large enough to decrease the kinetic energy of the electrons impacting the channel wall. This causes the secondary electron emission coefficient, δ, to drop below one and electron multiplication ceases to occur. The space-charge density is a dynamic quantity and as the multiplication drops below unity, the space-charge density also decreases, causing an increase in the impacting electron kinetic energy, increasing the δ value [40]. This feedback allows for a state of equilibrium or charge saturation to occur at gains approaching 10^8. Operating the MCP in charge saturated mode leads to desirable effects on the current pulses for

pulse processing schemes seen in the experiments performed by Schmidt and Hendee [40]. MCPs suffer from discriminator walk due to the large amplitude differences in pulse output. Operating in charge saturation mode helps to lessen discriminator walk that leads to inaccuracies in timing measurements, though this reduces the differences between alpha and fission product signals and increases the risk of arcing, and was not used in the current work.

3.1.2.3 MCP Detection Efficiency

MCP detectors have been used in a multitude of scientific applications. This is primarily due to their stable performance and reliability [37], and it is also due to the MCP being sensitive to various types of radiation. Table 2 gives MCP detection efficiencies for various types of radiation. The reported efficiencies are not absolute as the efficiency is also a function of the angle of the incident radiation normal to the surface of the MCP.

Table 2: MCP detection efficiencies for different radiation [37].

Radiation Type	Energy/Wavelength	Detection Efficiency (%)
Electron	0.2 keV to 2 keV	50 - 85
	2 keV to 50 keV	10 - 60
Ion	0.5 keV to 2 keV	5 - 58
	2 keV to 50 keV	60 - 85
	50 keV to 200 keV	4 - 60
UV	300 Å to 1100 Å	5 - 15
	1100 Å to 1500 Å	1 - 5
X-Ray	0.12 Å to 0.2 Å	up to 1
	2 Å to 50 Å	5 - 15
High E Particles (ρ,π)	1 GeV to 10 GeV	up to 95
Neutron	2.5 MeV to 14 MeV	0.14 - 0.64

For this work, the primary concern is how the MCP responds to electrons. Electron detection efficiency reaches a maximum (~60-80%) with input electron energy around 500 eV to 1 keV [36]. Figure 25 shows a plot of the MCP detection efficiency as a function of input electron energy. With electrons striking the MCP at low energy, the efficiency is roughly equivalent to the Open Area Ratio (OAR), which is the ratio of the effective detection area and the total area of the MCP face. Typically, the OAR value is manufactured to be around 60%, however, the OAR can be increased to 70% to 80% by etching the glass channel walls on the input side of the MCP plate [36].

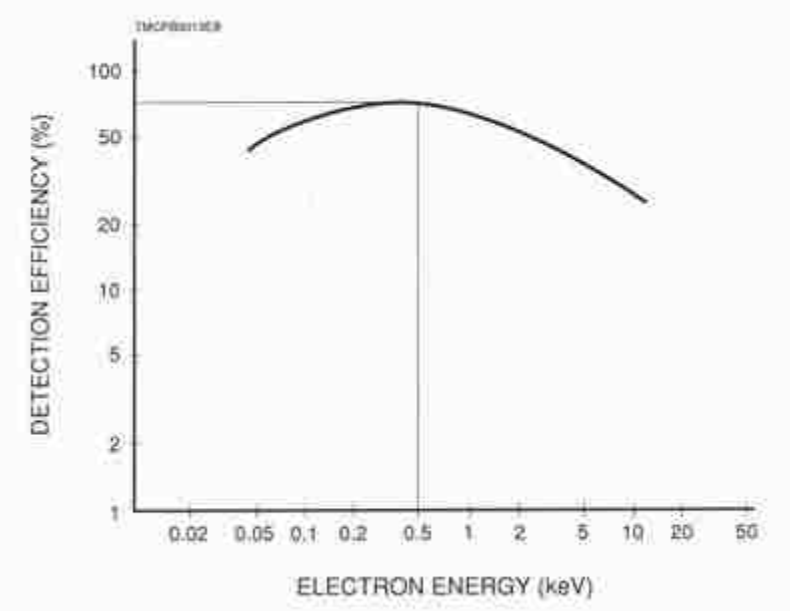

Figure 25: Electron detection efficiency as a function of energy [36].

Another variable to consider in the efficiency calculation is the MCP sensitivity to the angle of the primary electron. At lower energies, 500 eV to 1 keV, the optimum angle measured normal to the MCP surface was found to be ~13° [36] and so MCP channels are set to about 13 degrees (depending on specific model) from the surface normal, maximizing efficiency for electrons coming straight down. An angular spread in electrons to the MCP thus decreases

efficiency. Figure 26 shows a plot of the probability of interaction of primary electrons, in the 500 eV to 1 keV energy range, as a function of the incident electron angle to the MCP channel. As the input angle becomes very sharp, the probability of interaction within the channel drops sharply as the electrons traverse parallel to the channel axis. With electron energies greater than 1 keV, the incident angle has less of an effect as the electrons striking the MCP face have an increased probability of creating secondary electrons that can, in turn, excite the neighboring channels [39].

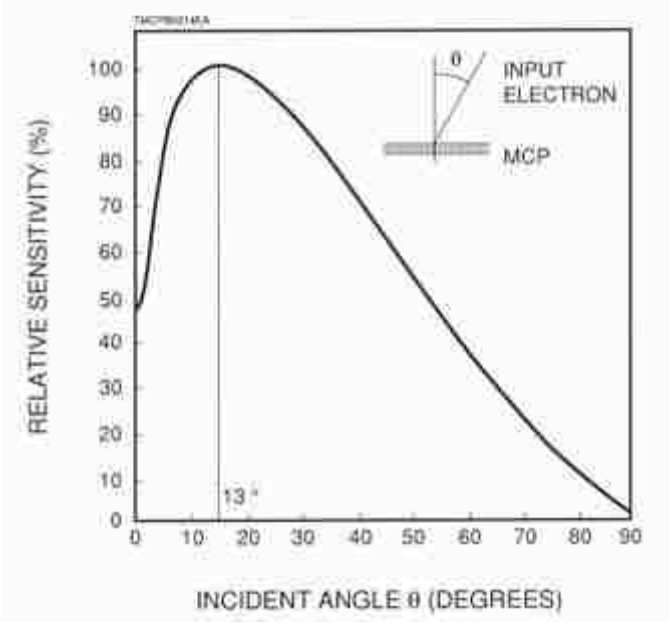

Figure 26: MCP sensitivity to 500 eV to 1 keV primary electrons as a function of incident electron and channel [36].

3.1.2.4 Single Timing Module Efficiency Measurements

Experimental efficiency measurements were performed using a PIPS detector for alpha detection in coincidence with the MCP for secondary electron detection. The dimensions for the MCP efficiency measurement are given in Figure 27. Dimensions were measured within the chamber after installation using a digital micrometer. In this setup the electrons are ejected from

the conversion grid by alphas from the ^{241}Am source on the far right. The grid and electrode voltages are listed, and electrons are accelerated from the conversion foil at -2500 V to the grid at +300 V; the inner diagonal grid, the inner vertical grid, and the MCP, all at +300 V, create a field free region within the setup; and the potential between the diagonal grids reflects the electrons emitted from the conversion foil.

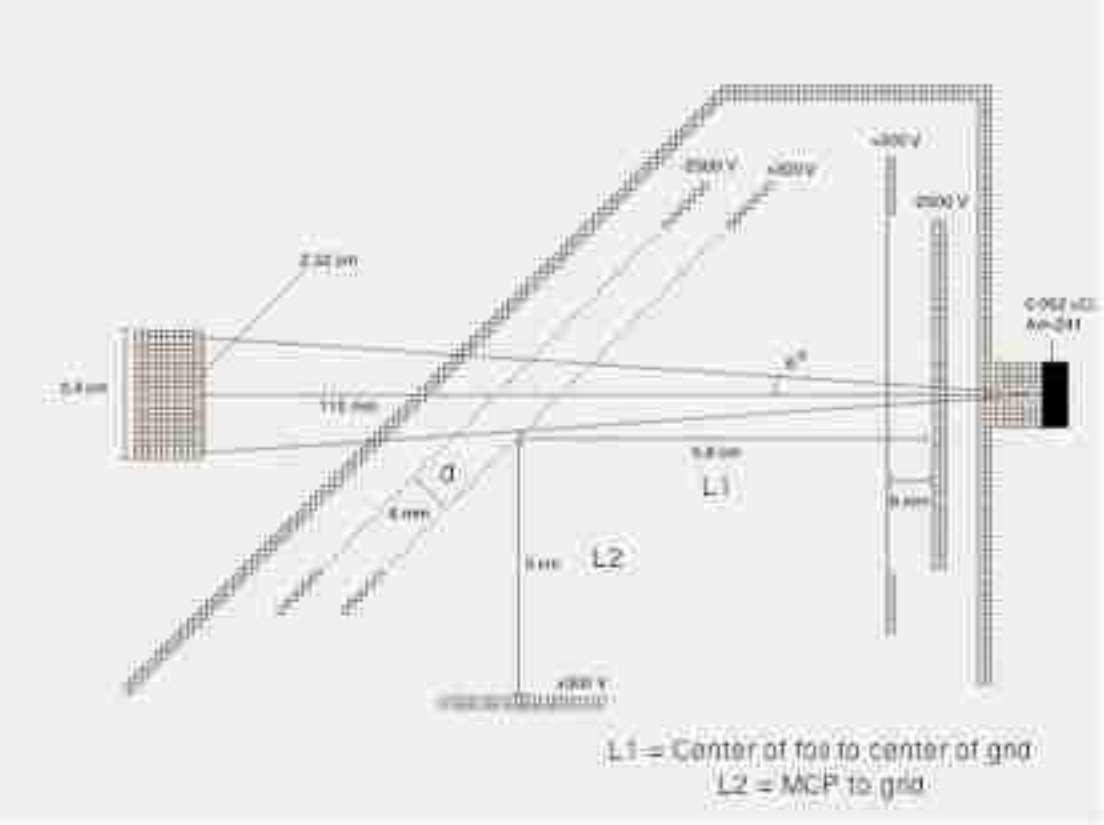

Figure 27: Final dimensions used for efficiency/timing measurements. [35]

A block diagram of the analog NIM electronics utilized for the efficiency measurement is given in Figure 28 below.

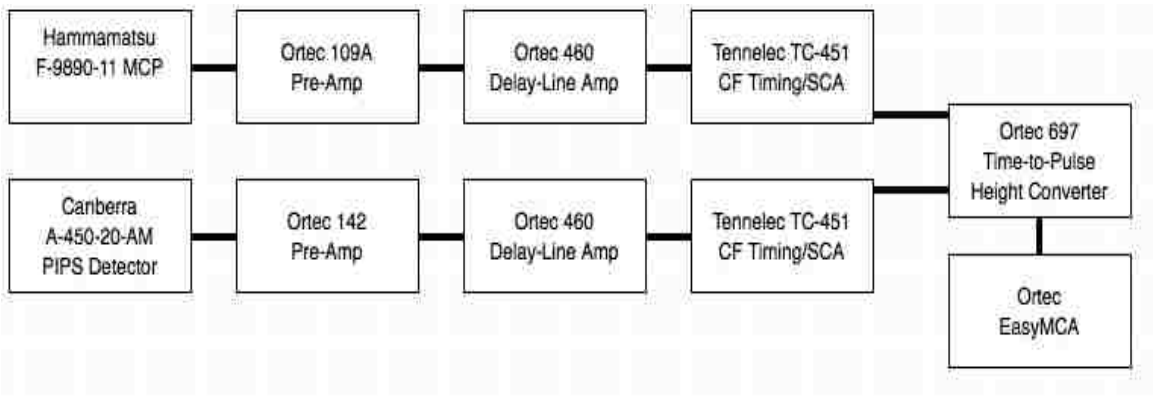

Figure 28: Experimental setup for the coincidence efficiency measurements. [35]

A downstream PIPS detector was used to detect alpha particles, producing a logic gate that was a requirement for accepting signals in the EasyMCA from the timing module MCP detector. The PIPS detector was extremely clean, producing no signals when no alpha source was present, giving confidence to this method. A gate signal width of 50 ns was used since a small gate width decreases accidental coincidences [41]. This is expressed mathematically as:

$$Accidental\ Coincidence = N1 * N2 * \sigma \qquad \text{[Eq. 18]}$$

Where *N1* and *N2* are the count rates for the MCP and PIPS detector and σ is the gate width. The accidental count rate is low for this work as the count rates above the trigger threshold are less than 10 Hz for the MCP and ~ 0.10 Hz for the gating PIPS detector.

To set the discriminator on the PIPS detector, a pulse height distribution was taken in real time as the discriminator was adjusted. The pulse height discriminator was set to 2 V as this effectively cuts out any infrequent low energy pulses not attributed to the alpha particles being investigated, which were centered tightly around 4 V. The discriminator on the MCP is carried out by the ADC in the EasyMCA and is set at channel 20 rather than on the lowest level to omit low-level noise in the MCP circuit. A 0.052 uCi ^{241}Am source provided alpha particles. The

primary alpha particle energy (84.8% branching) used was 5.485 MeV. The alphas were collimated to 6° half angle with a solid angle slightly smaller than the PIPS detector at the detector distance.

For the initial measurements, the distance from the foil to the reflector, L_1, and the distance from the reflector to the MCP, L_2, as shown in Figure 27, were configured to 5.8 cm and 6.5 cm, respectively. This returned consistent experimental coincidence efficiency results of ~ 15 - 20% with a counting time of 10 hours for sufficient statistics. The experimental efficiency was found by taking the ratio of the number of MCP pulses in coincidence with the PIPS based gate to the total number of times the PIPS detector fired.

SIMION [42] electric field based simulations show that the hit efficiency improves by shifting the single module unit forward relative to the MCP surface by 1.5 cm as shown in Figure 29. These adjustments were made to the single module unit, resulting in the final dimensions that were presented in Figure 27.

SIMION simulations also show the electron angular distribution being coned down towards the reflector and thus the MCP with increasing accelerating voltage. This was borne out experimentally. The results of efficiency as a function of acceleration potential are presented in Figure 30 with a saturated efficiency ~68 - 70%.

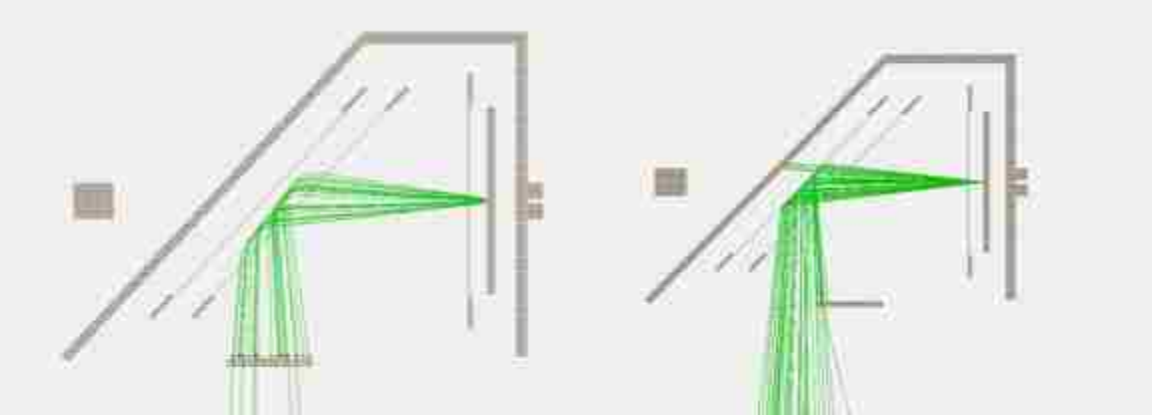

a) b)

Figure 29: a) Simulated SE flight path with the single module shifted forward by 1.5 cm, hit efficiency = 70-80%. b) Initial MCP position, hit efficiency = 5-10%. [35]

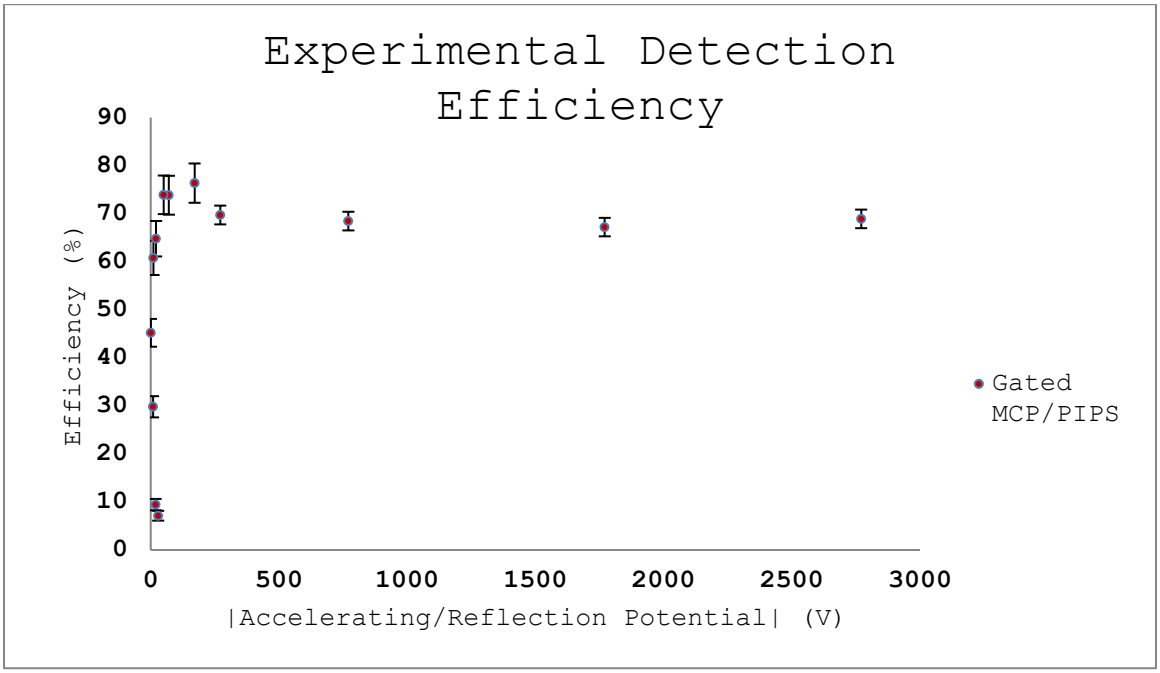

Figure 30: Efficiency of the single module coincidence unit. [35]

These results are in good agreement with previous efficiency measurements performed on similar SE reflection experiments by D'Erasmo *et al* (74% ± 0.7 %) [43]. The main difference in experiments performed by D'Erasmo *et al* being the reflection potential was kept constant

while adjusting the acceleration potential. For this work, the carbon foil and reflection grid voltages are supplied by the same voltage source keeping the ratio of reflection to acceleration potentials equal to or greater than 1. A condition on the potential ratio such that the SEs experience reflection is given by Nankov *et al* [44],

$$\frac{\Delta V_r}{\Delta V_f} \geq 0.5 \qquad \text{[Eq. 19]}$$

The steep drop in efficiency at low potentials could be due to keeping the ratio in equation 24 equal to or greater than 1. The steep slope in efficiency at low accelerating potentials resembles another SE reflection experiment by Kosev where an efficiency of ~25% was achieved for alpha particles with energy 5.8 MeV, however, the reflection potential used in that work is not reported [45]. In the D'Erasmo experiment, in which the reflection potential is held constant, the efficiency begins to decrease at an accelerating voltage of 1000 V. SIMION simulations suggest that if that ratio of Equation 19 is brought too much above 1, the SEs experience too much reflection and subsequent angular spread, such as in Figure 31, which effectively lowers the hit efficiency as is presented in Figure 32. This ratio becomes important to the optimization of timing measurements discussed in the following section.

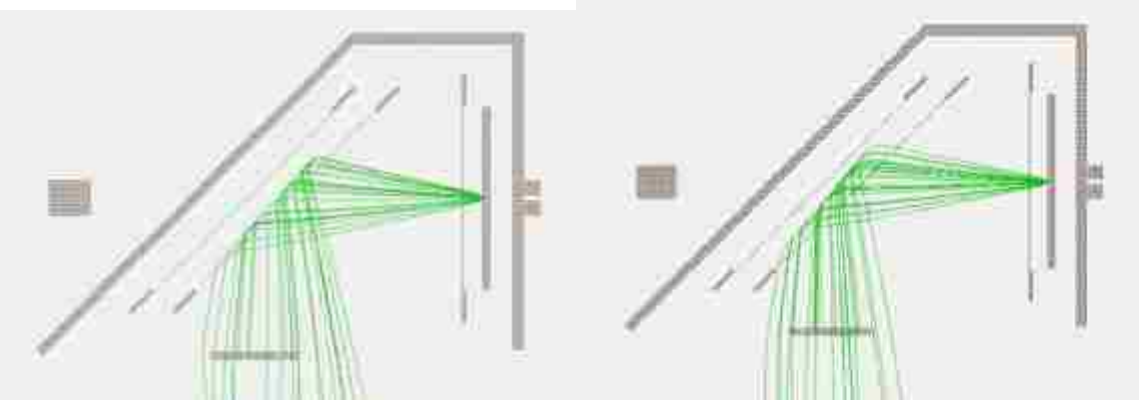

a) b)

Figure 31: a) Reflection potential at 2500 V, acceleration potential at 1000 V (lower efficiency) and b) Reflection potential at 1000V, acceleration potential at 1000 V (higher efficiency). [35]

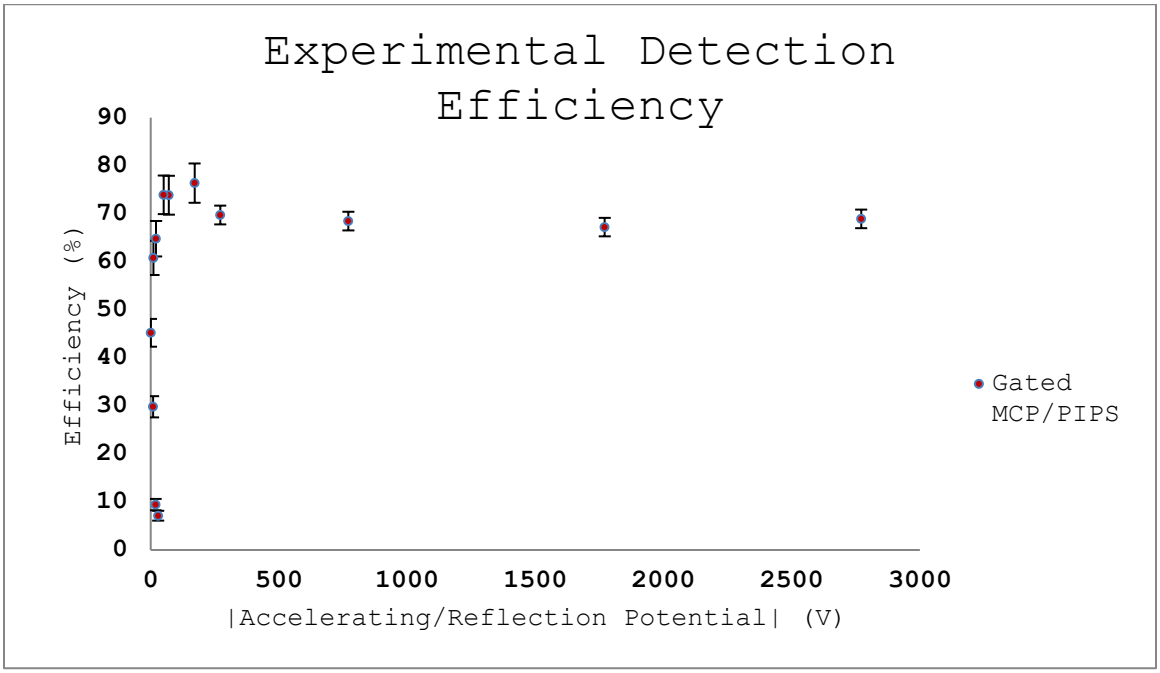

Figure 32: Efficiency of the single module coincidence unit as a function of the ratio of the accelerating potential to the reflection potential. [35]

3.1.2.4 MCP Time Response

The sharp timing characteristics exhibited by an MCP are primarily due to the short electron transit time in the very small channel volume compared to transit between discrete dynodes utilized in the more conventional photomultiplier tube (PMT). The signal transit time is proportional to the channel diameter; improvement in time resolution can be obtained as the diameter of the channel decreases [36]. Figure 33 illustrates a typical signal from a Hamamatsu F-9890-12 fast response MCP.

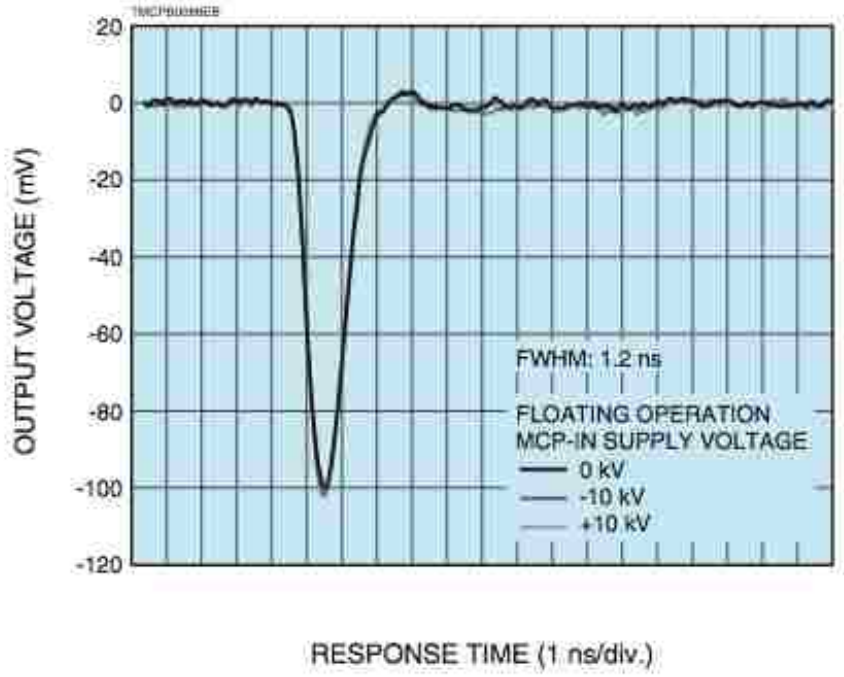

Figure 33: Typical output signal from a fast response MCP [36].

The Hamamatsu F-9890-12 MCP has a similar configuration to the F-9890-11 used in this work. The F-9890-12 has a channel diameter of 6 μm giving a signal width of 1.2 ns FWHM. We are using the F-9890-11 with a channel diameter of 12 microns.

3.1.2.5 Hamamatsu F-9890-11

The Hamamatsu F-9890-11 MCP utilized in the single module coincidence experiments is a fast-timing, non-position sensitive MCP, ideal for time-of-flight measurements. Table 3 gives the specifications for the Hamamatsu F9890-11.

Table 3: Specifications for the Hamamatsu F-9890-11.

Parameter	Quantity	Unit
Channel Diameter	12	µm
Bias Angle	12	degree
Effective Diameter	27	mm
Number of MCPs	2	-
Gain	1×10^6	-
Plate Resistance	10 to 40	MΩ
Dark Count	3	$s^{-1}\,cm^{-2}$
Pulse Width (FWHM)	0.9	ns
ΔV Between Plates	2	kV
ΔV MCP-Out & Anode	0.5	kV
Max MCP-In Bias	10	kV
Operating Pressure	$< 1 \times 10^{-3}$	mTorr

3.1.2.6 F-9890-11 Set-up & Installation

The F-9890-11 MCP was installed affixed to the vacuum side of an 8-inch ConFlat flange and supported by four 8-32, steel threaded rods. The MCP is held in place by nuts and lock washers measured equidistant from the surface of the ConFlat flange. Small slits were cut on the sides of the steel threaded rods near the ends to prevent “virtual leaks” of trapped gas from the

tapped holes below the rods. Figure 34 a & b shows the MCP support structure on the ConFlat flange and installation in the six-way cross.

a) b)

Figure 34: a) MCP support setup b) MCP installed on its side, inside the six-way cross. [35]

For precautionary reasons, the flange holding the MCP is installed on a side port of the six-way cross to avoid any accidental damage to the thin glass MCP due to falling objects during installation (washers, nuts, screws etc.).

The ConFlat flange used to support the MCP has been modified to provide bias and signal feedthroughs. The voltage supply and signal feedthroughs go through two, 2.75 inch half-nipples welded to an 8-inch ConFlat flange flat. The bias feedthrough consists of four pins, with each pin having a voltage rating of 5 kV and an amperage rating of 1 A. The signal feedthrough is a grounded, double-ended BNC connection type. Figure 35 shows an external view of the MCP experimental setup.

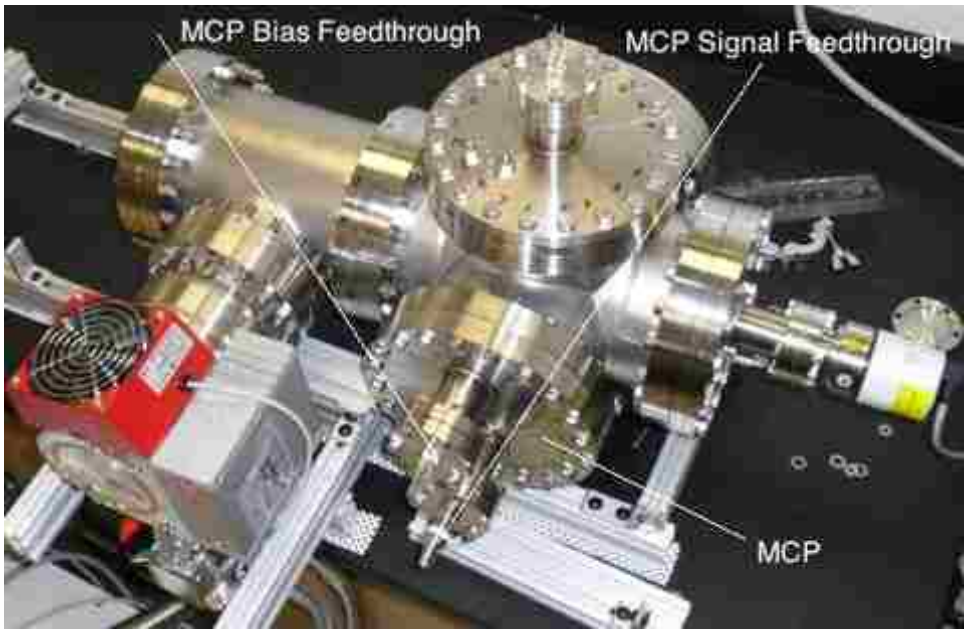

Figure 35: External view of the MCP experimental setup. [35]

Voltage is supplied to the MCP via an ORTEC 456 power supply rated for ± 3 kV, 0-10 mA. A voltage divider circuit provides bias to each MCP stage, defined as "MCP Front or MCP-in" and "MCP Back or MCP-out", and the anode by a simple voltage division circuit. See Figure 23 as a visualization of voltage application to the MCP. MCP-in voltage is applied to the top of the diagram, MCP-out to the bottom of the lowest MCP plate, and anode voltage to the top of the anode. The output is tied near ground by a resistor (not shown) and is connected to the anode via a capacitor (not shown).

After sealing the ConFlat, the chamber is brought to appropriate vacuum conditions, ~7.5 x 10^{-5} mtorr, with a Pfeiffer Hi-Cube pumping station of a turbo pump backed by a roughing pump and held for roughly 24 hours before applying voltage to the MCP [36]. Table 4 gives typical operating voltages for each charged component based on incident particle type.

Table 4: MCP suggested voltage for ion/photon & electron detection modes [46].

Component	Ion or Photon	Electron Detection	This Work
MCP-In	- 2400 V	+ 300 V	+ 271 V
MCP-Out	0 V	+ 2700 V	+ 1938 V
Anode	+ 150 V	+ 2850 V	+ 2200 V

The Hamamatsu F-9890-11 has a limit of 2 kV difference between MCP-in and MCP-out and a limit of 500 V between MCP-out, from which the signal is read, and the collection anode. MCP-out is connected to the anode via a capacitor to allow flexibility in anode biasing. Great care must be taken to ensure these limits are not exceeded as an electrical discharge within the plates can result in permanent damage to the MCP. This was the primary reason behind initially operating with a voltage difference of 1667 V between MCP-in/MCP-out and 262 V between MCP-out and anode rather than closer to the manufacturer listed limits.

3.1.3.7 F-9890-11 Characterization

Before installing the acceleration and reflection grids, the electron optics, for the coincidence measurements, it is useful to determine the operating characteristics of the MCP. Starting from a conservative bias voltage of 2200 V, the bias was increased at 100 V intervals up to 2600 V to analyze the F-9890-11 raw signal time characteristics and pulse height distribution. Table 5 gives a synopsis of the bias voltages, voltage to each component of the MCP and voltage potential between components for several test runs.

Table 5: Test operating voltages for the F-9890-11 MCP.

Bias Voltage	MCP-In	MCP-Out	Anode	ΔV MCP-in/MCP-out	ΔV MCP-out/Anode
+ 2200 V	+ 271 V	+ 1938 V	+ 2200 V	1667 V	262 V
+ 2300 V	+ 283 V	+ 2016 V	+ 2300 V	1733 V	284 V
+ 2400 V	+ 296 V	+ 2103 V	+ 2400 V	1807 V	297 V
+ 2500 V	+ 308 V	+ 2191 V	+ 2500 V	1883 V	309 V
+ 2600 V	+ 320 V	+ 2279 V	+ 2600 V	1959 V	321 V

3.1.2.8 F-9890-11 Time Response

A Techtronix TDS 2024B 200 MHz 2 GS/s 4-channel oscilloscope was utilized to analyze the raw signal from the MCP. The MCP signal time characteristics are expected to be unchanged with varying voltage potentials. The time characteristics are primarily governed by the diameter of the individual channel multipliers. Figure 36 shows that the time characteristics of the output pulse remain relatively unaffected by changes in the voltage potentials.

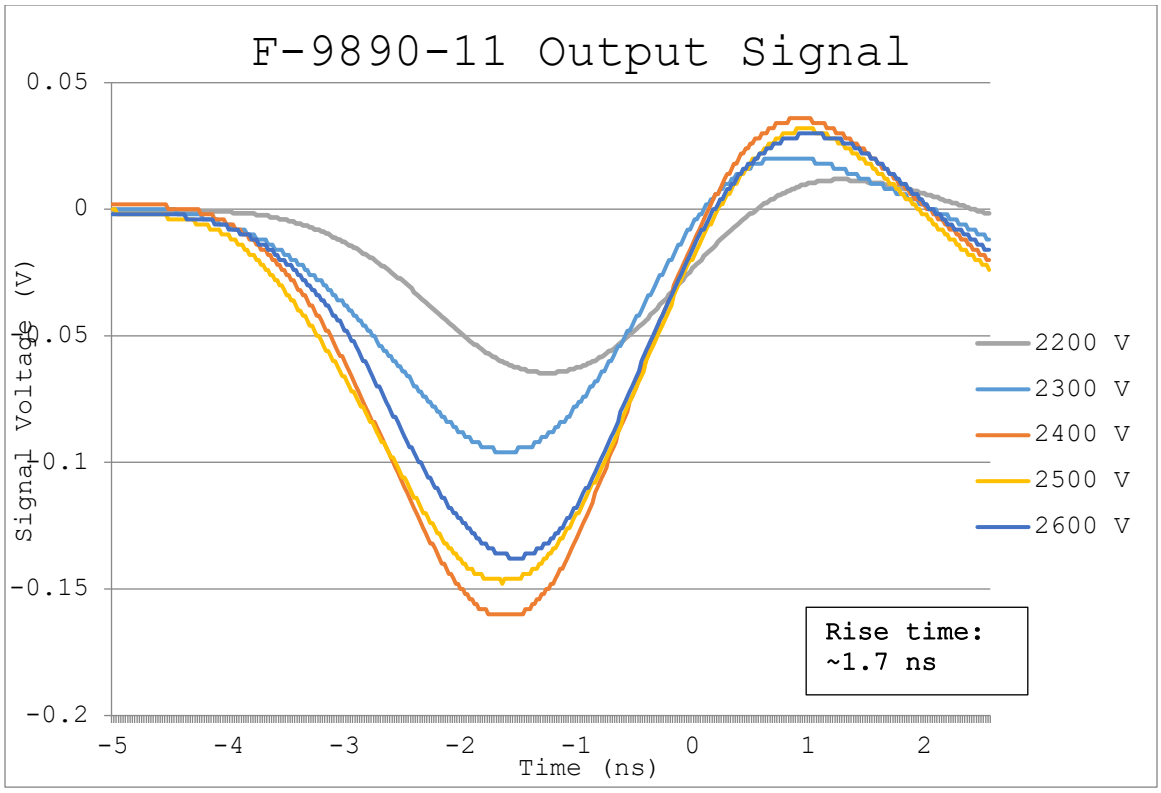

Figure 36: MCP output signal at varied voltage potentials. [35]

The signal rise time and fall time was calculated by subtracting the time measured at 90% maximum signal peak height from the time measured at 10% maximum peak height. The F-9890-11 output signal, regardless of voltage potentials, has a characteristic rise time of 1.7 ns, fall time of 1.1 ns and FWHM of 2.2 ns. There is significant ringing in the raw signal, which may be due to impedance mismatch, however the amplitude of the signal ring is roughly 20% of the peak height of the original signal and can be discriminated out to eliminate the false triggering in a pulse-processing scheme. The signal to the oscilloscope used a 50 ohm terminator to reduce viewed ringing, and all feedthroughs and coaxial cables matched this, so we are unsure of the source of the mismatch. The signal settling time is found to be roughly 35 ns. Figure 37 shows an example of the ringing experienced with the F-9890-11

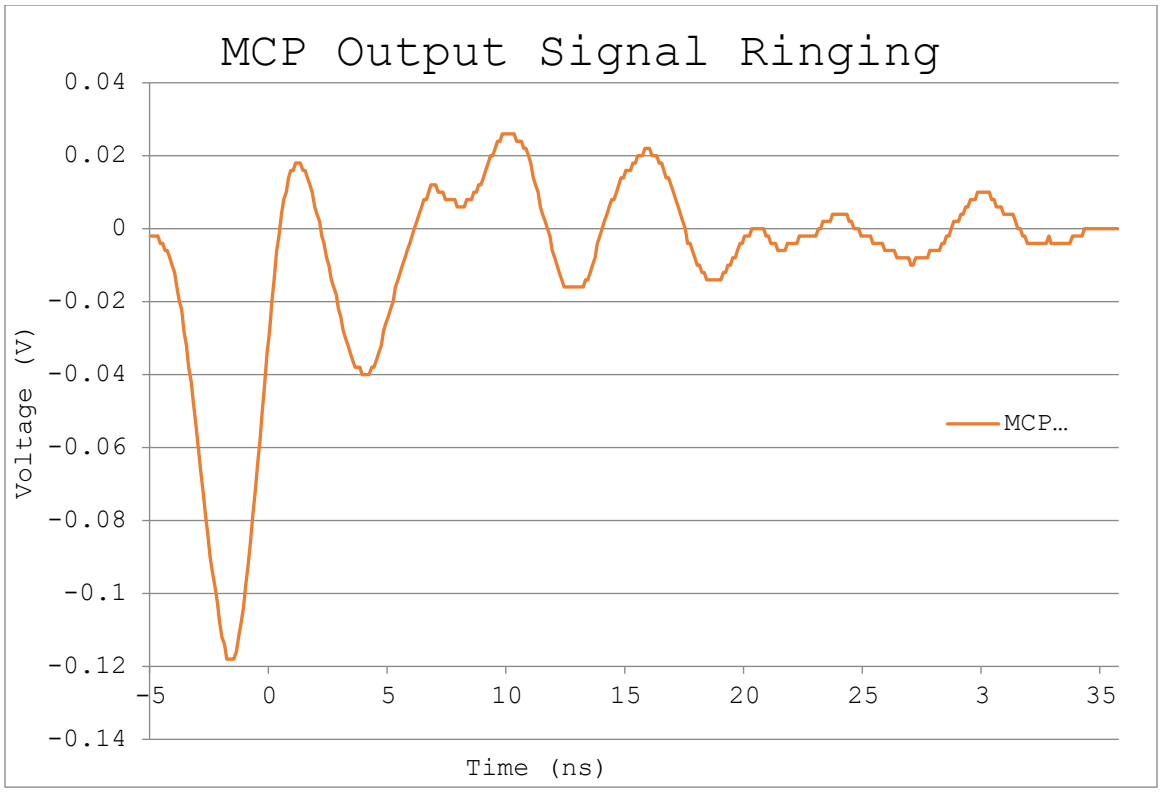

Figure 37: F-9890-11 output signal at a bias voltage of 2200V. The output pulse settles to baseline after ~35 ns. [35]

3.1.2.9 F-9890-11 Pulse Height Distribution & Charge Saturation

The pulse height distribution of the MCP becomes important for discriminator settings in coincidence measurements. It is often beneficial to operate the MCP in charge saturation mode as a threshold discriminator can be used to filter out low-level noise. Measurements for the pulse height distributions were performed at the same bias voltages as the time response measurements in the previous section. The F-9890-11 output signal is pre-amplified by the ORTEC 109PC charge-sensitive pre-amplifier with further amplification utilizing the ORTEC 590A amplifier. The amplified analog signal is then converted to digital in the analog-to-digital converter (ADC) of the ORTEC EasyMCA multichannel analyzer to histogram the pulse height distribution.

Viewing the signal up to the pre-amplifier, the ringing phenomenon in the raw signal is discriminated out by means of a low-pass filter in the pulse shaping stage of the pre-amplifier. The signal is inverted to provide the multichannel analyzer with a positive input signal. The pre-amplifier signal experiences overshoot due to amplifier characteristics as the pre-amplifier is set to return to baseline quickly to allow for high rates. This fast pulse is to be used for sharp timing measurements. For pulse height distribution characterization, a slower, ORTEC 590A amplifier is used on the pre-amplified signal to provide a semi-Gaussian signal to the multichannel analyzer to lower the signal-to-noise ratio and allow easy digitization. Unipolar, semi-Gaussian pulse-shaping amplifiers are normally the optimum choice for energy spectroscopy [47]. Figure 38 a and b shows the output pulses from the 109PC pre-amplifier and 590A amplifier.

a) b)

Figure 38: a) 109PC pre-amplifier signal and b) 590A amplifier signal.

Even though the MCP pulse height does not give any energy information about the incident electrons, it is useful to analyze the pulse height distribution to determine the optimum threshold discrimination threshold to remove random events from electrons originating in the MCP itself. As mentioned in section 4.2.1.2, for coincidence measurements and pulse-processing schemes it is often beneficial to operate the MCP in charge saturated mode to be able to better

discriminate the real signal from the noise in the system. The pulse height distribution was obtained for the F-9890-11 utilizing the same 100 V increments on the operating bias used in the time response analysis from 2200 V to 2600 V. Figure 39 shows the results of the pulse height distribution at the various bias voltages.

Figure 39: Pulse height distribution for the Hamamatsu F-9890-11 MCP. [35]

From Figure 39, charge saturation of the MCPs begins to occur at a bias voltage of 2400 V. As the bias voltage increases past 2400 V, the FWHM of the pulse height distribution begin to increase. Operating the MCP at a bias voltage of 2200-2400 V should allow for proper threshold discrimination for timing measurements to decrease inaccuracies due to discriminator walk.

3.1.2.10 Time-of-flight Resolution Test

A collimated 1.67 Ci ^{239}Pu particle source is utilized to measure the TOF between the two MCP detectors as seen in Figure 40.

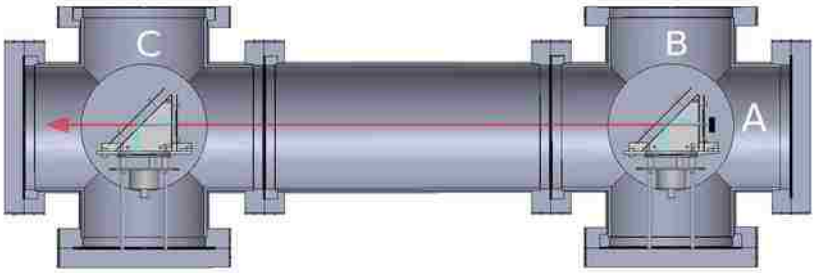

Figure 40: A) 1.67 Ci ^{239}Pu α-particle source. B) Time 1 (start)/MCP 1. C) Time 2 (stop)/MCP 2.

The dominant particle from ^{239}Pu has a discrete energy of 5.156 MeV, with a branching ratio of 73.3%. This correlates to an expected TOF of 63.5 ns at a distance of 1 m. Figure 41 shows the results of the TOF alpha resolution tests.

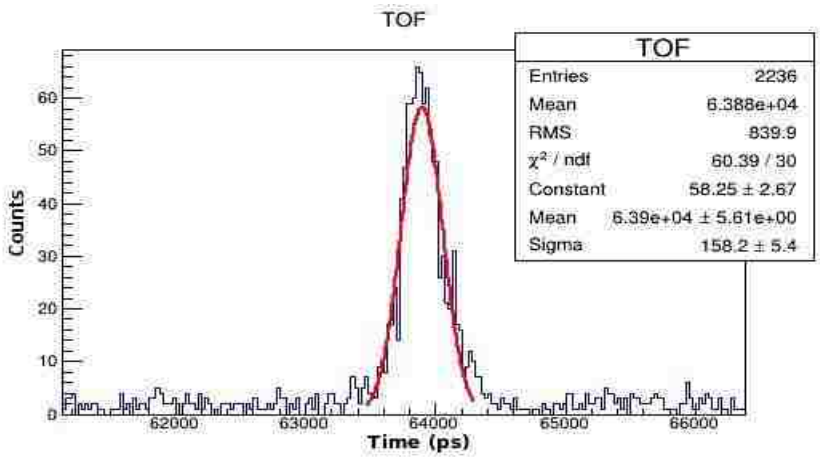

Figure 41: ^{239}Pu particle TOF Results.

We see from Figure 41 that the mean time-of-flight results (63.9 ± 5.6 ns) agree well with the expected value of 63.5 ns. Another significant quantity to obtain a mass resolution 1 amu, is the error associated with the time measurement. The α-particle test returned a σ = 158.2 ± 5.4 ps or 371.8 ps FWHM. A 315 ps FWHM in the timing measurement is necessary to obtain the stated mass resolution of 1 amu given the energy resolution of the IC is 1%. Widening of the

peak can partially be attributed to the lower percentage α-particle branching ratios from the ^{239}Pu, as well as the age, and thus possible surface dirtiness, and deposition method of the ^{239}Pu source.

New measurements were performed to evaluate the improvements made to the timing system and improved transmission materials by me and MS student Shelby Fellows [9]. Though the distance was decreased from 100 cm to 50 cm to improve efficiency and statistics, which has the effect of decreasing t and thus increasing the proportional uncertainty, $\delta t/t$, we were able to improve the proportional timing resolution. Incorporating fast-timing Ortec VT120 pre-amplifiers, fast-timing Phillips 715 CFD and thinner carbon foils has provided improved timing properties for the system and more than compensated for the shorter TOF chamber length. These updated quantities were very important for the final assessment of mass uncertainty for the ^{235}U and ^{252}Cf measurements as it is the identical electronics and chamber setup used for those experiments as shown in Figure 42. Signals from the CFD and VT120 pre-amplifier are shown in Figure 43.

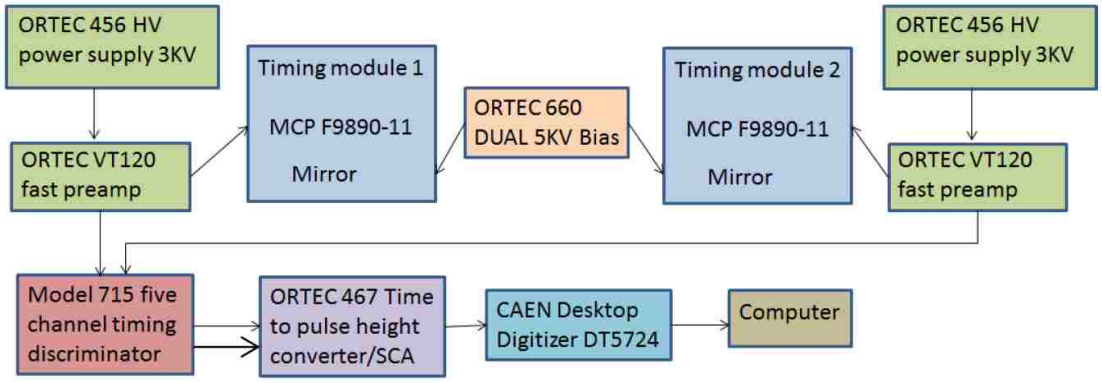

Figure 42: Experimental setup for improved timing resolution measurements [9].

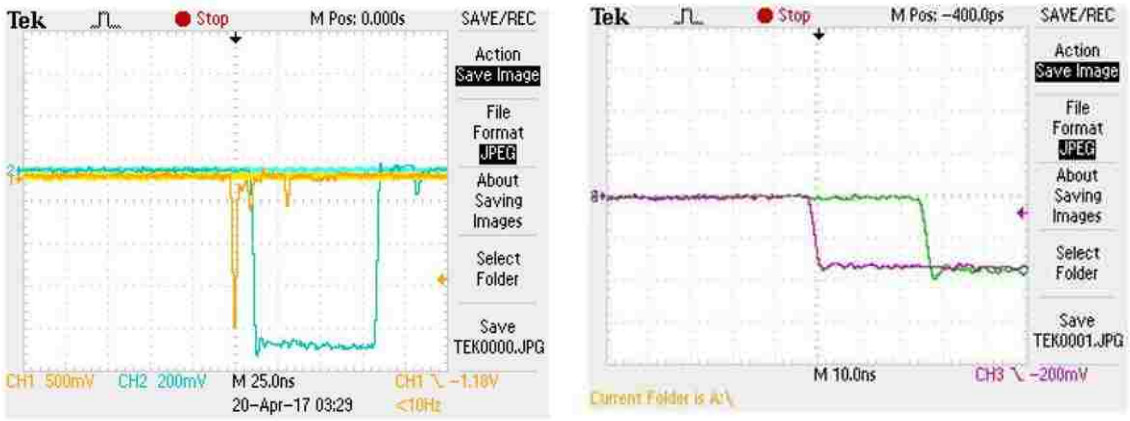

Figure 43: MCP/VT120 and CFD signal output (left) CFD output signals (right) for a ^{239}Pu α-particle.

Timing resolution measurements were performed using the same ^{239}Pu α-particle source for foil thicknesses of 20, 55 and 100 µg/cm^2 carbon foils in the TOF setup provided from our Los Alamos collaborators. The resulting FWHM of the timing distributions are provided in Figure 44 and detailed results in Tables 6, 7 and 8.

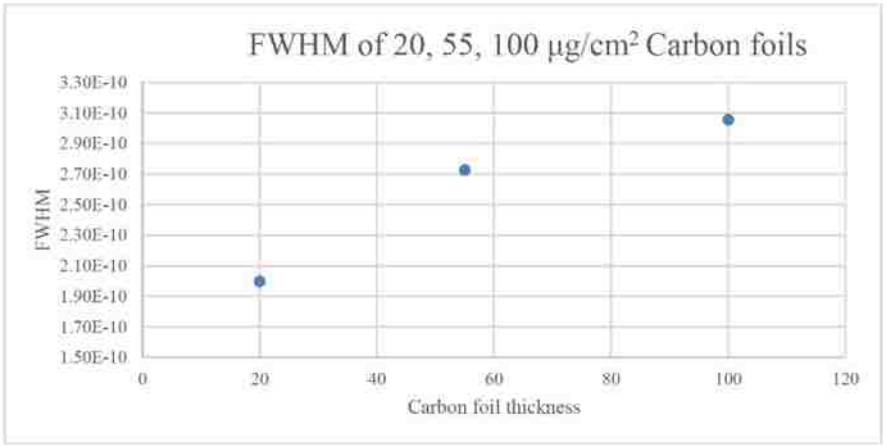

Figure 44: Time resolution results for 20, 55, 100 µg/cm^2 carbon foils Fellows [9].

Table 6: Detailed timing resolution results for 100 µg/cm2 carbon transmission foil Fellows [9].

	Energy after foil	Time (50cm)	5/18	5/22	5/29
Alpha1	5.076	3.195E-08	4730	4696	3560
Alpha2	5.064	3.199E-08	4742	4707	3571
Alpha3	5.025	3.211E-08	4781	4742	3606
Run Time (hr)			48	48	69
Sigma			120	100	130
Amplitude			900	740	5500

Table 7: Detailed timing resolution results for 55 µg/cm2 carbon transmission foil Fellows [9].

	Energy after foil	Time (50cm)	4/20	4/21	4/24	4/25	4/27	4/28
Alpha1	5.112	3.184E-08	5000	4901	4815	2880	2890	2902
Alpha2	5.100	3.188E-08	5012	4913	4826	2887	2897	2909
Alpha3	5.061	3.200E-08	5053	4953	4866	2910	2920	2933
Run Time (hr)			24.61	19.9	71.7	0.4004	25.5	19.5
Sigma (ps)			250	120	120	120	116	116
Amplitude			75	30	75	35	800	700

Table 8: Detailed timing resolution results for 20 µg/cm2 carbon transmission foil Fellows [9].

	Energy after foil	Time (50cm)	5/10	5/12	With center blocker 6/10
Alpha1	5.140	3.175E-08	3868	4655	3855
Alpha2	5.128	3.179E-08	3877	4666	3864
Alpha3	5.089	3.191E-08	3909	4704	3896
Run Time (hr)			1.7	48	67
Sigma (ps)			95	85	85
Amplitude			145	430	110

The 55 µg/cm^2 carbon foil results are the most important, as these are close to the foil thickness (50 µg/cm^2) used in the FPY mass measurements performed in this evaluation. As reported by Fellows [9], there were some initial issues with the signal acceptance in the CAEN ADC, however, these problems were resolve post-4/20/17 and began returning proper results of

$\sigma \sim 116 – 120$ ps, or 272.6 – 282 ps FWHM. We have only very recently been successful in mounting 20 μg/cm^2 carbon foils in a reliable way, however this method of mounting was done after our mass measurements using ^{235}U and ^{252}Cf. Going forward, we should see even further improvements in our timing data by the implementation of the 20 μg/cm^2 carbon foils to our system.

3.1.2 Energy Detector

The UNM mass spectrometer features a parallel plate, axial ionization chamber. The chamber is comprised of an annular copper cathode that is electrically connected to an aluminum housing for the silicon nitride (SiN) window, 15 copper guard rings, a gold-plated tungsten wire Frisch grid, and a solid copper anode disk, based on work by Oed et al. [7]. The ionization chamber was modified with an active cathode configuration, based on the work of Sanami et al. [11], capable of measuring the particle energy and range of penetration, from which charge information can be inferred. Figure 45 provides a simplified diagram for the ion chamber. A more in-depth description of the physical and operational parameters of the ion chamber can be found in the thesis of former students James Cole and Lena Heffern [34, 32].

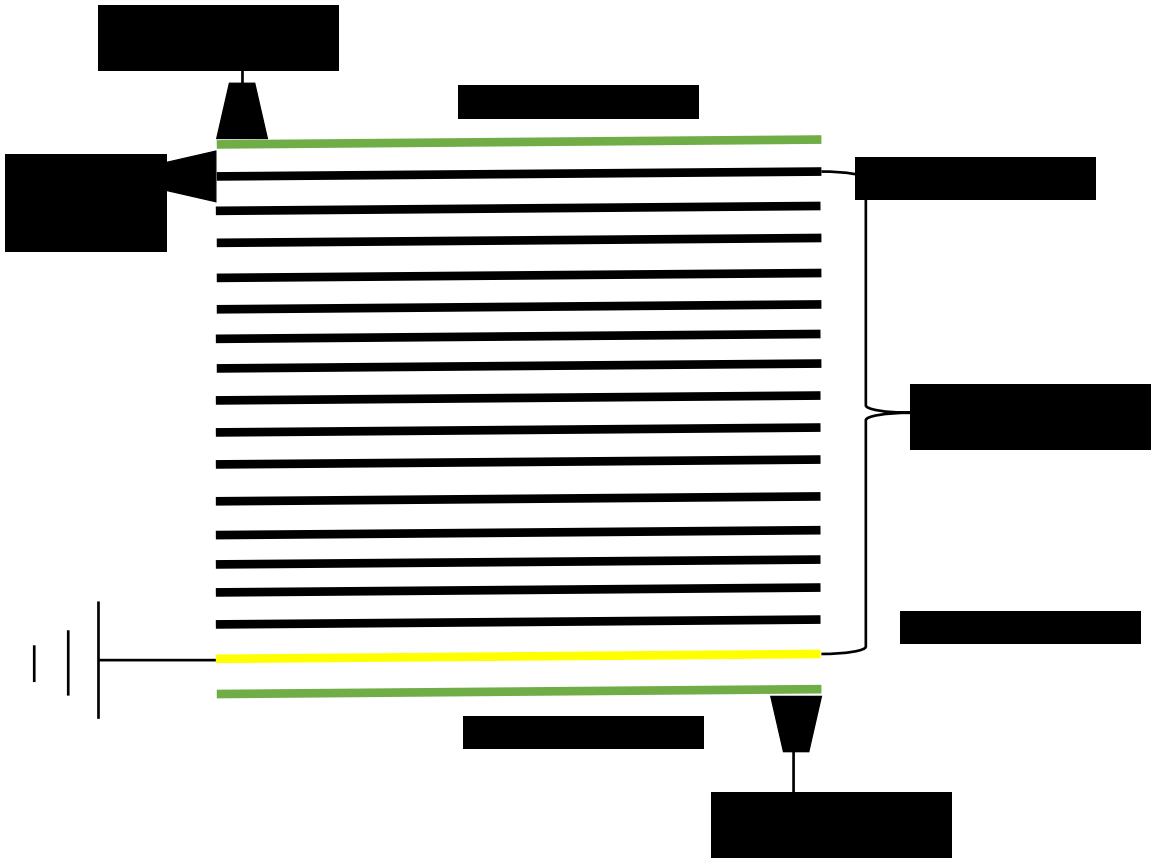

Figure 45: Simplified schematic of the ion chamber.

The ion chamber accurately determines the amount of energy deposited in the gas by ionizing radiation. As the particle loses its kinetic energy primarily ionizing the gas, the particle's energy can then be determined due to the linear proportionality between the amount of energy deposited within the gas and the height of the pulse measured, on the order of 10s of eV per ion pair produced for most gasses.

The guard rings smoothly transition the voltage from the cathode to the Frisch grid, so the electric field lines are basically parallel within most of the IC volume, so the IC is acts as a time projection chamber. When a charged particle enters the ion chamber, it ionizes the detector gas, liberating electrons. Under the electric field in the IC, the electrons immediately begin to accelerate towards the Frisch grid and anode. This charge movement induces a pulse on the

cathode that can be measured as the start time of the electron drift in the IC. The Frisch grid isolates the different E-field regions between the cathode-to-Frisch grid region and the Frisch grid-to-anode region. Once the electrons have pass the Frisch grid, a pulse is induced on the anode. This pulse acts as both an energy reading and a second time signal. The time difference between the induced pulses on the cathode and anode is directly related to the particle range, *R*.

The range, and thus the stopping power of the atom in the gas, is a function of the atomic number, Z, or rather the effective Z due to incomplete ionization. Though there is charge exchange with the gas and thus a range of charge states, with the energy and mass extracted, used with the range, Z information can be extracted. Figure 46 gives a description of the range determination methodology for an active cathode ionization chamber.

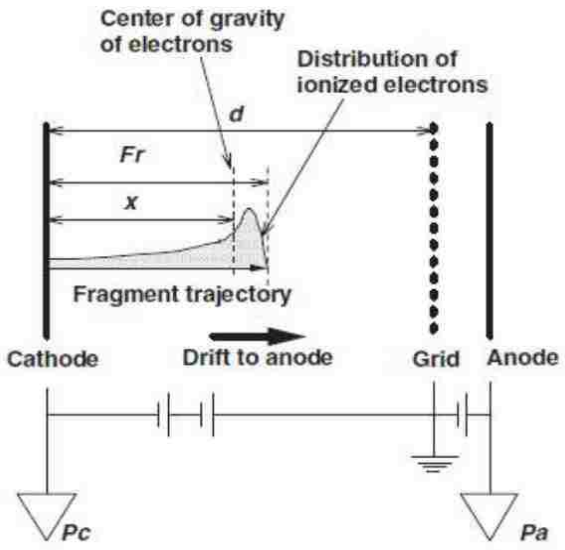

Figure 46: Active cathode configuration to determine particle range, shown with a light ion that produces a Bragg peak in the gas. [11]

3.1.3.1 Energy Resolution Test

The IC energy resolution has been determined directly for α-particles, from which we than infer the energy resolution for heavy ions in the mass range of fission products by statistical theory based on the number of charge carriers which is dependent on the particle incoming energy [48]:

$$ER = \frac{2.35\sqrt{f}}{\sqrt{n_o}} = \frac{2.35\sqrt{fW}}{\sqrt{E_{in}}} \quad \text{[Eq. 20]}$$

Where *f* is the fano-factor of the fill gas, *W* is the average energy lost by the incoming particle per ion pair formed, and n_o is the number of charge carriers which is directly proportional to the particle incoming energy, E_{in}. It is not possible to calibrate the ionization chamber energy response sharply for a broad fission fragment distribution, but we were able to do this for alpha particles. Comparing the alpha particle resolution, with energy about 5 MeV, with fission product energy resolution, with light and heavy product mean energy about 100 MeV and 70 MeV, respectively, we have about 14-20 times the energy and thus - ignoring recombination and thus pulse height defect - about 20 times the charge carriers and thus approximately $\sqrt{20}$ = 4.5 times improvement in resolution, δE/E for light products and $\sqrt{14}$ = 3.75 for heavy. An IC returning an energy resolution of 1.18% for α-particles should in theory produce an energy resolution of ~0.22% to 0.26% for a representative light and heavy fission products, respectively, again ignoring a small pulse height defect.

To determine the α-particle energy resolution of the UNM fission spectrometer IC, a 0.0318 μCi Tri-nuclide source consisting of ^{239}Pu (5156 keV primary alpha particle energy), ^{241}Am (5486 keV) and ^{244}Cm (5805 keV) was placed ~1 cm from the IC SiN entrance window.

Figure 47 provides a histogram with the measured energy resolution for each α-particle, with gaussian fits to the main alpha peak and several branches from each nuclide.

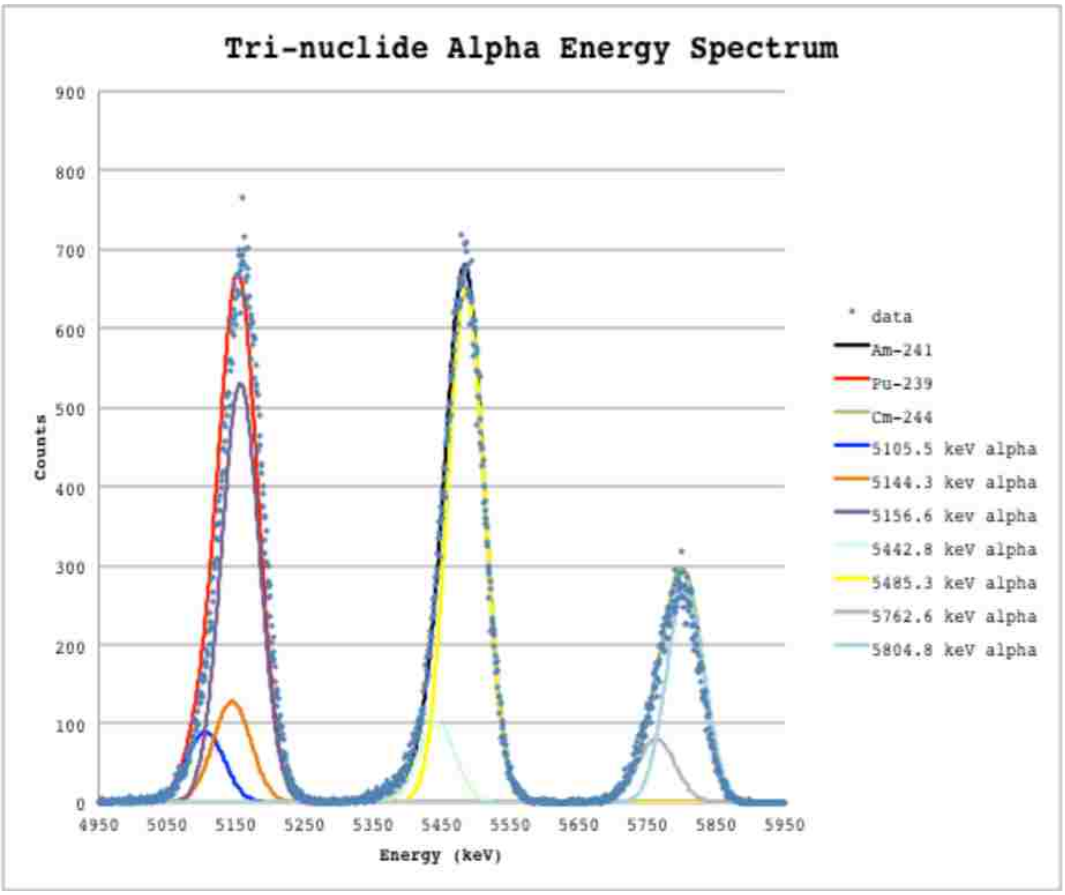

Figure 47: Ion chamber α-particle energy resolution results Cole [24].

The α-particle energy resolution tests returned reasonable results of 1.25%, 1.18% and 1.11% for the respective nuclides for an average energy resolution of 1.18%. From the heavy ion energy resolution relation above, we can approximate the average light and heavy fission product energy resolution to be ~0.26% - 0.31% or an expected FWHM ~ 260 keV for light products and FWHM ~ 217 keV for heavy products.

3.1.3.2 Ion Chamber Range Tests

To convert cathode vs. anode timing in the ionization chamber to range of the incident particle, the time projection in a time projection chamber, the electron drift velocity should be well characterized. The terminal electron drift velocity, v_{dr}, in isobutane is directly related to the IC reduced electric field, or *E/P*. The electron drift velocity plateaus at an *E/*P value of ~ 3.2 for isobutane [49], which is the primary factor when determining the IC operating conditions. The drift velocity is determined by the relationship of v_{dr} and *E/P* developed by James Cole [34] for a given pressure, an example is given in Figure 48.

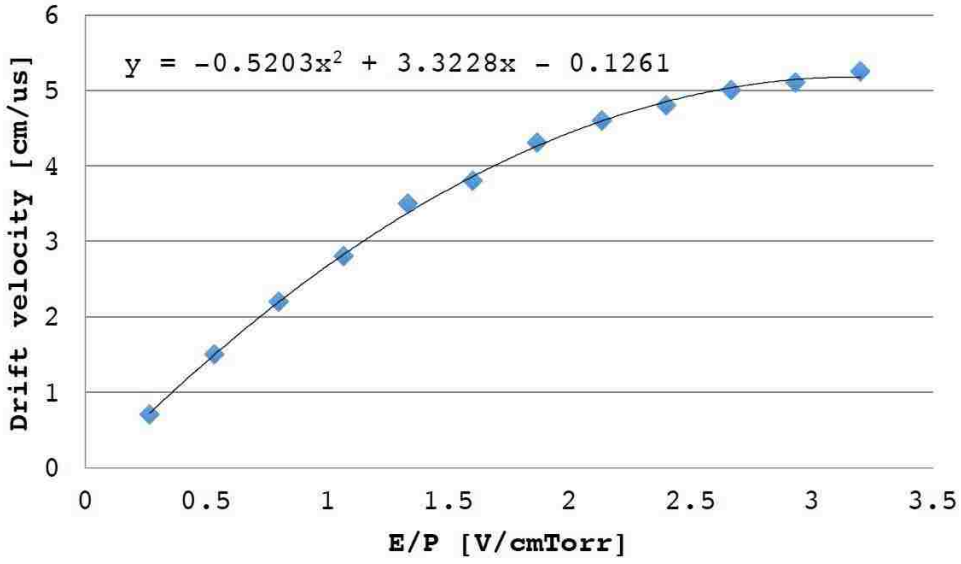

Figure 48: Drift velocity relation for isobutane Cole [34].

The range of a particle is determined by the equation

$$R = L - Dv_{dr} \qquad \text{[Eq. 21]}$$

where L is the active length of the chamber, D is the measured time difference, and v_{dr} is the drift velocity of the electrons under a constant electric field [12]. Figure 49 shows a typical anode and cathode signal, with a clear time difference between the anode and cathode signals.

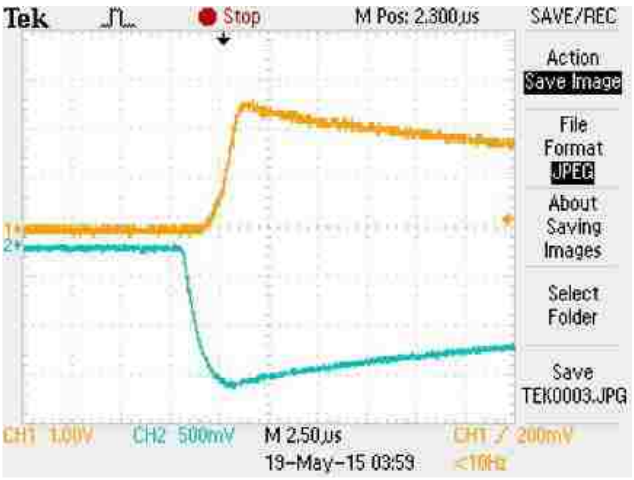

Figure 49: IC anode signal (orange) and cathode signal (blue), time difference between cathode and anode produces D

The α-particle range measurements were made with a 1 μCi ^{252}Cf (6118 keV) source with P-10 acting as the IC fill gas. Table 1 shows the measured range results at various pressures and their comparison to SRIM values.

Table 9: Cf-252 α-particle range comparison in P-10 Cole [34]

Pressure	Measured Range [cm]	SRIM Range [cm]
260	9.8 ± 0.3	15.0
340	9.2 ± 0.2	11.6
400	8.1 ± 0.2	9.8

The α-particle range was tested at three various pressure points. At 260 torr, the α-particle range exceeds the length of the ion chamber and should return a $\Delta t = 0$; however there seems to be a minimum time difference achievable, slightly above zero. At 340 torr, the α-particle should stop at or near the Frisch grid, leading to a Δt of 0 or slightly greater. At 400 torr, the SRIM predicted range is determined to be 9.8 cm, therefore we would expect a $\Delta t \sim 400$ ns. The measured α-particle range results are consistently lower than SRIM predictions by 1.7-2.4 cm.

Chapter 4: Mass Measurements & Data Analysis

In this chapter, I will be discussing the experimental setup for the full spectrometer system as well as methodology concerning calibration and energy loss accounting (energy addback) which ultimately leads to the determination of the initial mass of the fission products post scission. FPY distributions and associated uncertainties will then be presented for ^{252}Cf and then for ^{235}U.

4.1 Fission Product Yield Measurements

In this section, a step-by-step description of the data collection, calibration, energy correction and correlation methods for ultimately calculating FPY is discussed. At UNM, a 1 μCi ^{252}Cf source was typically used for benchmarking and testing purposes. Due to the low activity of the ^{252}Cf source and adjustments made to electronics for optimization purposes, total combined counts for the mass distributions are roughly ¼ of the ^{235}U mass distributions. For ^{235}U measurements; the UNM spectrometer was fielded on the thermal neutron beamline at the LANSCE facility within Los Alamos National Laboratories, shown in figure 50.

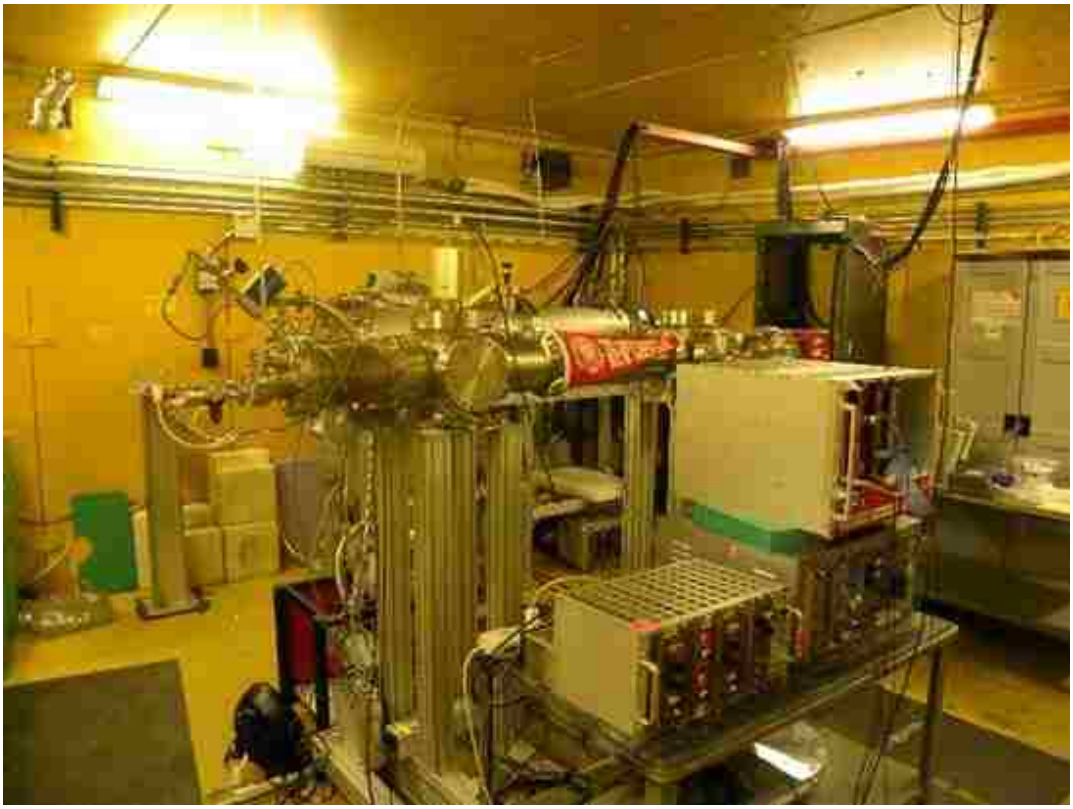

Figure 50: UNM Spectrometer setup at the LANSCE Lujan Center.

4.2 Experimental Setup

4.2.1 Chamber & Pressure System

Figure 51 provides a Solidworks [50] schematic of the chamber design. Letters above each modular piece are provided as a guide for the following paragraph of the chamber description.

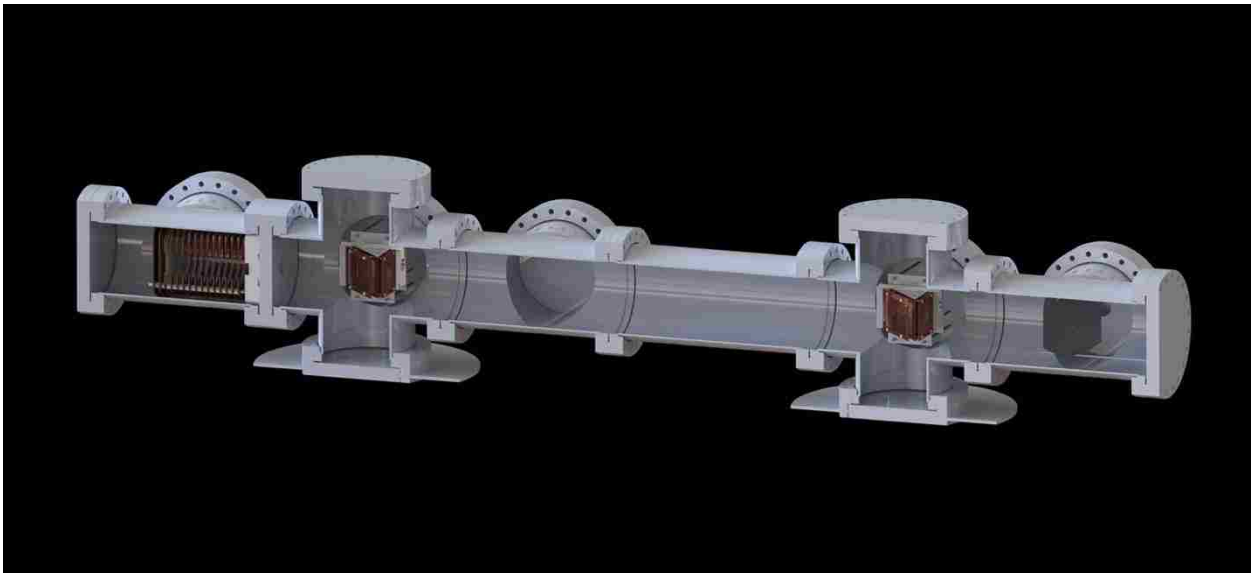

Figure 51: Solidworks schematic of the spectrometer chamber design.

The vacuum chamber design consists 5 main, stainless-steel pipe sections with a 6th optional 50 cm straight pipe, D, that can be added to increase the time of flight region of the chamber from 50 cm to 1 m. The pipes are standard ConFlat (CF) fittings with 8" flange diameter, referred to simply as 8" ConFlat. In this schematic, the fission fragments that are measured travel from right (F) to left (A). The target chamber (F) is a 28 cm x 28 cm 4-way cross. The neutron beam comes in normal to the plate facing into the page, with a target holder adjusted to a 45^{o} angle to the beam, and thus also the spectrometer axis. For a spontaneous fission source, the source faces the spectrometer axis. The MCP chambers (B & E) consist of two, 28 cm x 28 cm x 28 cm, 6-way crosses. The drift region comprises of (C) a 22 cm length three-way cross for the Pfeiffer Hi-Cube turbo pump to attach on the side, which sets the centers of the 6-way crosses (B & E) at 50 cm distance and thus the TOF detectors at 50 cm center-to-center. A 50 cm straight pipe (D) can also be added for a full time-of-flight path of 1 m, as mentioned previously.

The IC section (A) is comprised of a 28 cm length three-way cross. The IC and 2nd MCP chambers (A & B) are separated by thin (200 nm), 1 cm x 1 cm Silicon Nitride (SiN) entrance windows, either singly or arranged in a 7 window grid as in Figure 52, to provide separation of the ultra-high vacuum ($<10^{-6}$ torr) TOF region and the gas filled IC region (~70-80 torr). The SiN grids used for the separation of pressurized and vacuum regions are shown in Figure 52.

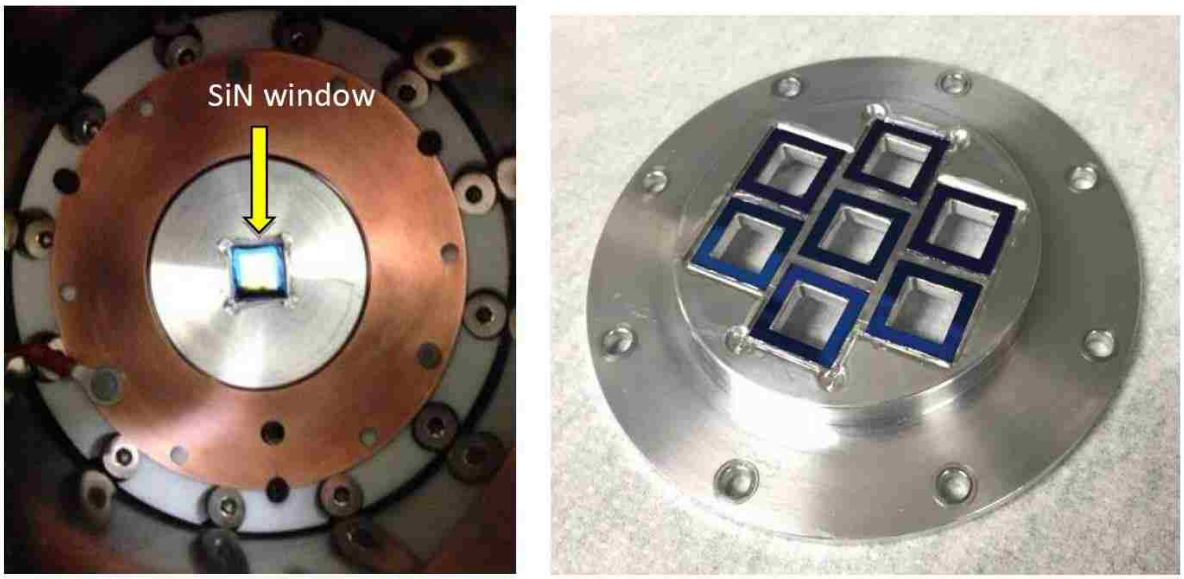

Figure 52: (left) single and (right) grid of 7 SiN IC entrance windows.

The pressure system for the spectrometer is broken up into two regions, the time-of-flight drift region and the IC region. The time-of-flight region needs to be at a constant ultra-high vacuum ($<10^{-6}$ Torr) for proper ion drift and operation of the MCPs. This is achieved by initially pumping down the entire system, both the TOF and IC regions, with an Edwards XDS 10 roughing pump to a pressure of approximately 10^{-2} Torr. The IC system is then isolated and sealed off from the roughing pump by closing of a Lesker bellows control valve, while a Pfeiffer Hi-Cube turbo pump is activated to bring the time-of-flight region down to a pressure of $< 10^{-6}$ Torr, typically achieving a vacuum pressure of 3×10^{-8} Torr. Once the time-of-flight region

reaches appropriate vacuum conditions, the IC chamber is then slowly filled with isobutane gas to a pressure of 70-80 Torr using a MKS 250 flow controller. A MKS 246 outflow controller, connected to a MKS 2159B mass flow controller, regulates the exhaust of the isobutane gas to maintain a constant flow of fresh gas, with a refresh rate of the full IC chamber volume once every 2 hours. Figure 53 provides a schematic of the gas flow and vacuum system.

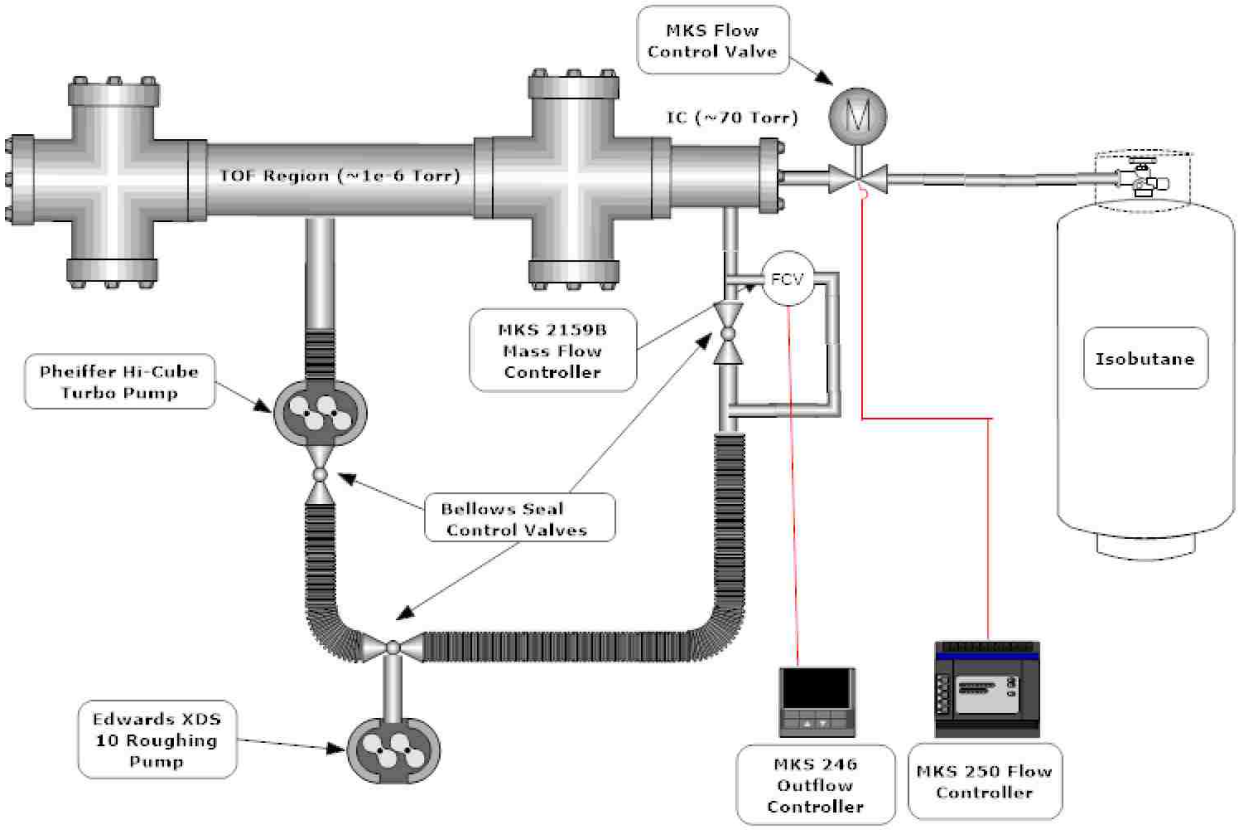

Figure 53: Pressure system schematic for IC and TOF regions.

4.2.2 Electronics and Data Acquisition System

Much like the pressure system, the electronics setup currently employed to collect mass data can effectively be broken up into two separate systems, the TOF and the IC. The TOF section consists of two MCPs for a start (*time 1*) and stop (*time 2*) signal. A positive high voltage of 2500V is applied to MCPs via a simple voltage division circuit by two separate Ortec 456 3-

kV power supplies. An Ortec 660 5-kV Dual power supply provides a negative high voltage of -2500V to each of the electron reflection mirrors. The output signals from each MCP is carried via a RG-58 coaxial BNC cable and fed into Ortec VT120 fast timing pre-amplifiers. Each timing signal from the VT120s are then independently connected via RG-174 cables with LEMO connections to a 5 channel Phillips 715 constant fraction discriminator (CFD) with a 2 ns shaping delay, specifically designed for fast timing signals to minimize discriminator walk. The CFD output signals are then connected via RG-174 LEMO cables to an Ortec 566 time-to-amplitude converter (TAC) with the timing range set to 100 ns. The final TOF output signal from the analog TAC is fed into the CAEN DT5724 desktop digitizer analog-to-digital converter (ADC). The digital signal is then sent to the personal computer (PC) for processing with the CAEN Digital Post-Processing Pulse Height Analysis (DPP-PHA) software. CAEN recently released a more complete post-processing software package, CAEN MC^2 Anlayzer, which provides more functionality, however this update was provided post mass measurements. All cables for each timing setup are of identical length to not add cable delay differences in the TOF time comparison measurement.

The IC electronics setup is a bit complex with both an anode and the active cathode design providing an independent cathode signal. This allows for not only an energy measurement but also a timing measurement between the cathode and anode signals. Voltage to the IC is provided by three independent Ortec 659 power supplies. The independent cathode (2500-3000V) and anode (500-600V) biases feed through Ortec 142A pre-amplifiers via RG-59 SHV cables. The guard ring (2240-2800V) voltage is provided directly from an Ortec 659 power supply connected with RG-59 SHV cables. The output signals for both the cathode and anode are fed to the CFD with RG-174 LEMO cables to produce logic signals for the start and stop signals

for the Ortec 467 time-to-pulse height converter (TPHC). The anode vs cathode timing signal from the TPHC is then connected to the CAEN DT5724 ADC, then to the PC for processing. The 142A pre-amplifiers each provide two, identical signal outputs. For the anode, one of the output signals is connected directly to the DT 5724 ADC for the energy deposition measurement and the other signal for the mentioned anode vs. cathode timing. As with the MCP timing setup, all IC timing cables are of equal length to preserve timing integrity. A diagram of the electronics setup used for the full spectrometer system is provided in Figure 54.

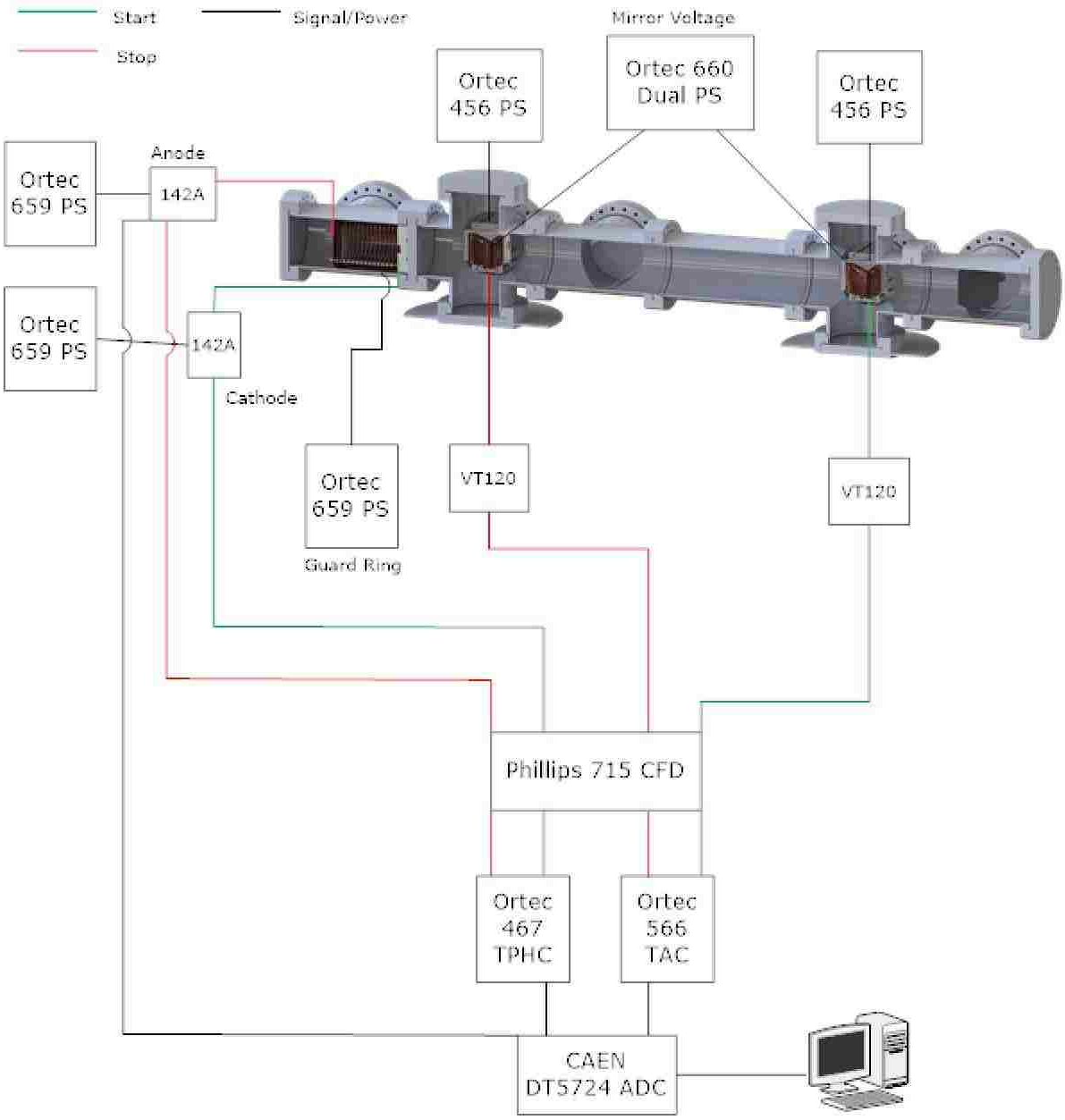

Figure 54: Electronics setup for IC and TOF detection systems

4.3 Calibration and Energy Addback Methodology

In the simplest case, the particle velocity is determined from the TOF reading, the ionization chamber value gives the energy, and the mass is extracted from $E=\frac{1}{2}mv^2$. Everything must be calibrated, there is energy loss in the system between the TOF measurement region and the E measurement region, and table values of E are known for E directly from the

sources, not E after foils and windows. Without an absolute heavy ion beam calibration available, we rely on previous published values and TRIM simulations [42] for timing and energy calibration at fission product mass and energies. The energy calibration begins by evaluating the published yield and energy values from previous experiments. For this assessment, published energy data from Schmitt *et al* [10] is the starting point. Beginning with the published values for kinetic energy of the average light and heavy products, shown as E_i, in Table 10, we perform a TRIM calculation to determine energy lost in the source/target, carbon foils and ion chamber entrance window.

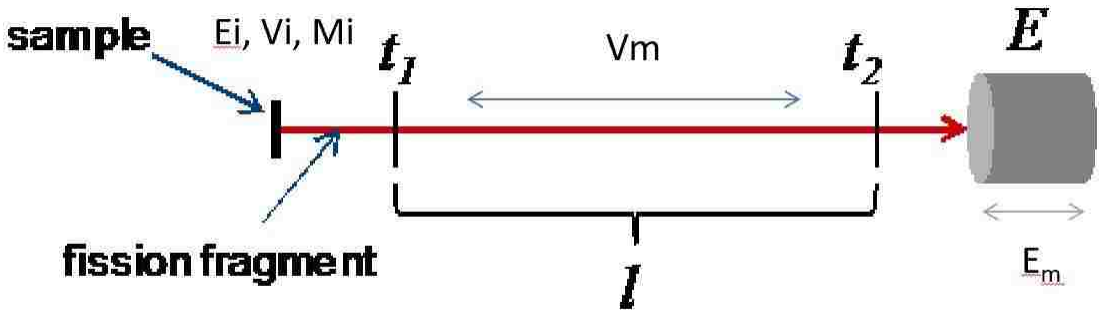

Figure 55: Methodology for determining calibration timing and energy.

The energy measured, E_m in Figure 55, is determined by running mean mass ions from representative light and heavy fission product groups through a TRIM simulation through all transmission materials and source/target. The TOF calibration is determined by the velocity, V_m in Table 10 and 11, of the same representative fission products, but only through the source/target and the first carbon foil.

Table 10: Published and calibrated values used for energy and timing calibration of ^{252}Cf.

Z	A	Ei (MeV)	E Calibrated	TOF Calibrated
42	106	103.8	93.605	37.159
56	142	79.4	70.101	49.372

Table 11: Published and calibrated values used for energy and timing calibration of ^{235}U

Z	A	Ei (MeV)	E Calibrated	TOF Calibrated
36	96	101.560	90.339	36.053
54	139	70.340	57.709	53.182

The peak channels in the data are found by the user and a simple linear fit is performed converting channel to energy and time. While the energy distributions are not actually gaussian distributions, they are remarkably gaussian in shape and so gaussian fits to data are used to assist in analysis. Figure 56, 57, 58 & 59 give the gaussian fitting procedure for ^{252}Cf and ^{235}U applied to the TOF and energy data with associated fitting parameter and goodness of fit, *b1* and *b2* are the calibration quantities used for calibration. These values are used for all individual runs for consistency and limitation of free parameters.

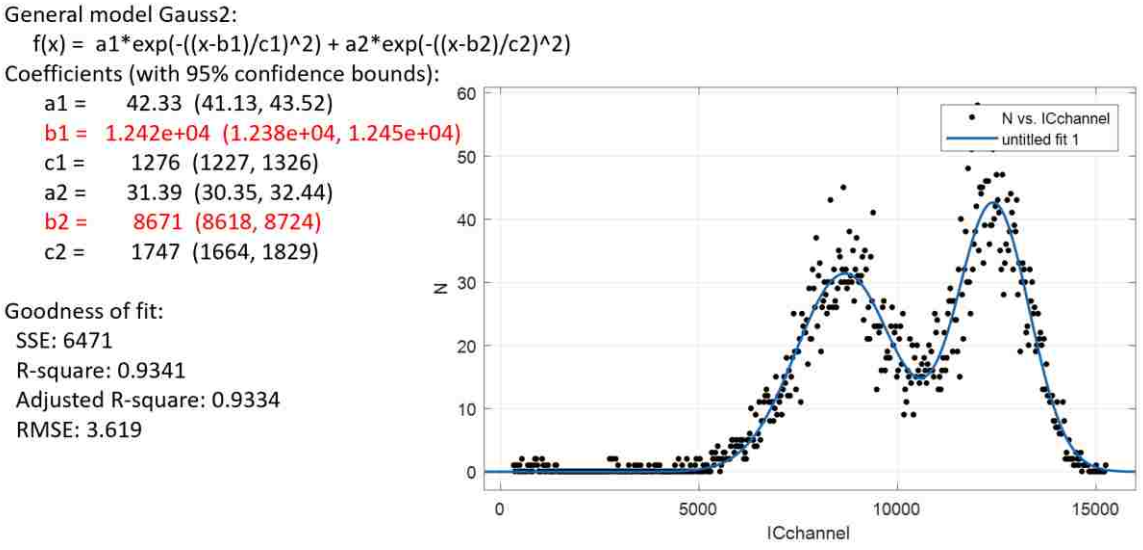

Figure 56: Energy calibration gaussian fits and associated parameters for ^{252}Cf.

General model Gauss2:
f(x) = a1*exp(-((x-b1)/c1)^2) + a2*exp(-((x-b2)/c2)^2)
Coefficients (with 95% confidence bounds):
a1 = 51.68 (50.4, 52.97)
b1 = 6611 (6593, 6629)
c1 = 867.2 (841.4, 893)
a2 = 25.52 (24.61, 26.42)
b2 = 1.055e+04 (1.05e+04, 1.061e+04)
c2 = 1791 (1714, 1867)

Goodness of fit:
SSE: 4852
R-square: 0.9473
Adjusted R-square: 0.9468
RMSE: 3.134

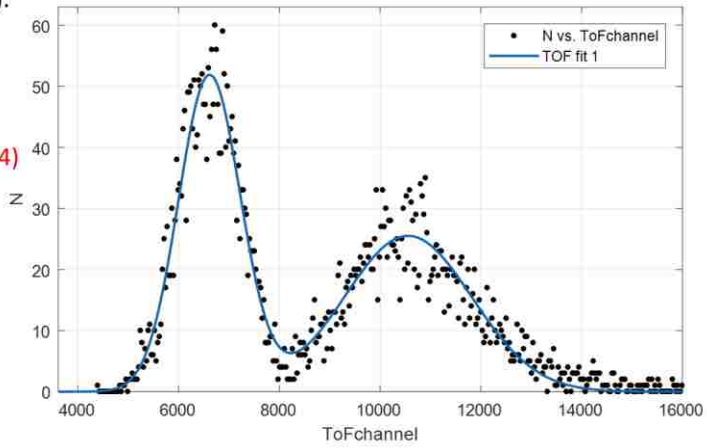

Figure 57: TOF calibration gaussian fits and associated parameters for ^{252}Cf.

General model Gauss2:
f(x) = a1*exp(-((x-b1)/c1)^2) + a2*exp(-((x-b2)/c2)^2)
Coefficients (with 95% confidence bounds):
a1 = 106.1 (103.8, 108.4)
b1 = 1.231e+04 (1.229e+04, 1.233e+04)
c1 = 1096 (1069, 1124)
a2 = 82.99 (81.09, 84.89)
b2 = 7560 (7530, 7589)
c2 = 1580 (1537, 1622)

Goodness of fit:
SSE: 3.077e+04
R-square: 0.9433
Adjusted R-square: 0.9428
RMSE: 7.892

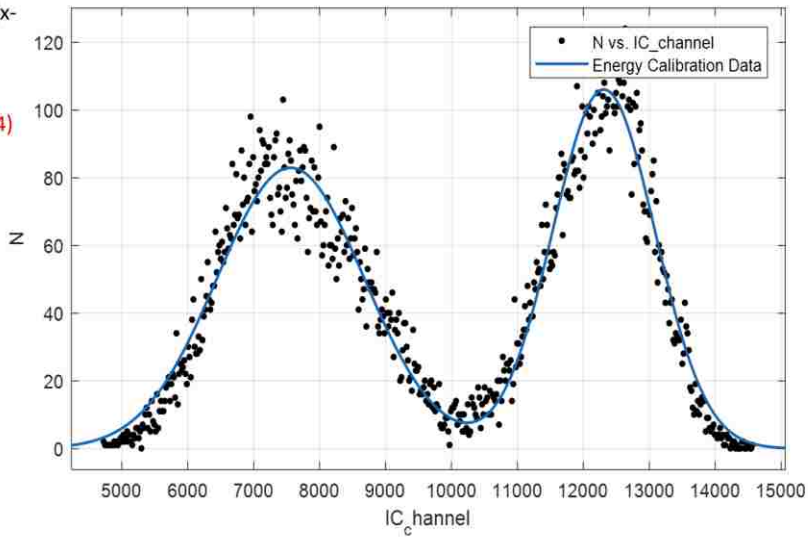

Figure 58: Energy calibration gaussian fits and associated parameters for ^{235}U

General model Gauss2:
f(x) = a1*exp(-((x-b1)/c1)^2) + a2*exp(-((x-b2)/c2)^2)
Coefficients (with 95% confidence bounds):
a1 = 109.1 (107.5, 110.8)
b1 = 5897 (5889, 5905)
c1 = 622.8 (612.2, 633.4)
a2 = 41.83 (40.88, 42.77)
b2 = 1.105e+04 (1.101e+04, 1.108e+04)
c2 = 1819 (1771, 1866)

Goodness of fit:
SSE: 3.042e+04
R-square: 0.9567
Adjusted R-square: 0.9565
RMSE: 5.532

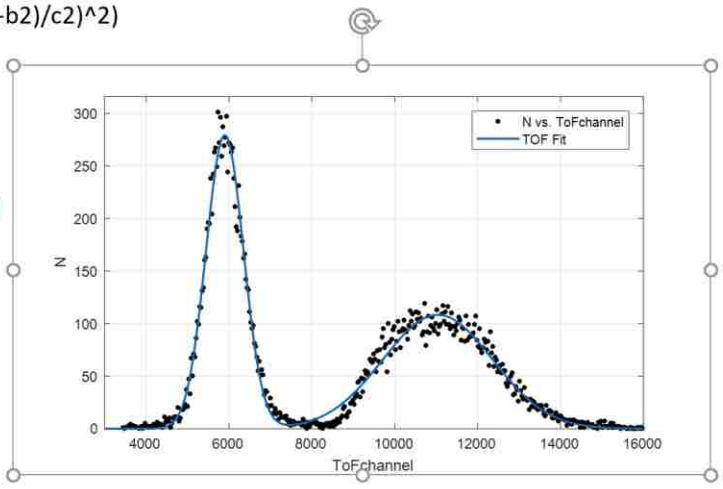

Figure 59: Time-of-flight calibration gaussian fits and associated parameters ^{235}U.

At this point we have the ion chamber calibrated to E_m and V_m from Figure 56 and 58. To get the value of the initial energy, E_i, and initial velocity, V_i. An energy correction "addback" needs to be made for the energy lost in the source/target and the transmission materials. To compare with table values, the addback is taken to reconstruct energy values in the ^{235}U target or ^{252}Cf source. The assessment starts by taking the highest yield element, Z, for a given mass, A, value in the yield distribution for four nuclides in each peak. The initial energies assigned for selected masses from the light and heavy mass peaks is determined by pulling the average product energy previously measured by Schmitt *et al.* [10] shown in Figure 60. Table 12 provides the selected mass, Z and initial energies from each of the light and heavy representative products for ^{252}Cf while table 13 shows values for ^{235}U.

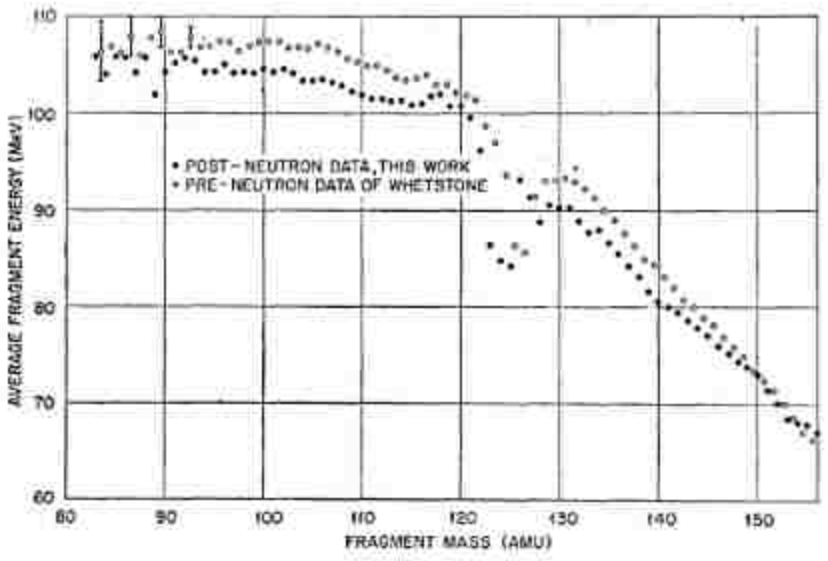

Figure 60: Average fragment energy as a function of fragment mass [10].

Table 12: Initial values used for representative ^{252}Cf fission products.

Light				*Heavy*			
A	**Z**	**Element**	**Ei(MeV)**	**A**	**Z**	**Element**	**Ei (MeV)**
101	40	Zr	107.6	130	50	Sn	93.5
106	42	Mo	107.3	134	52	Te	90.1
111	45	Rh	105.5	141	55	Cs	83.0
118	48	Cd	103.3	150	59	Pr	72.9

Table 13: Initial values used for representative ^{235}U fission products.

Light				*Heavy*			
A	**Z**	**Element**	**Ei(MeV)**	**A**	**Z**	**Element**	**Ei (MeV)**
88	35	Br	101.5	130	50	Sn	81.2
95	38	Sr	101.9	134	52	Te	77.9
100	40	Zr	102.0	138	54	Xe	72.2
104	42	Mo	101.0	143	56	Ba	66.0

These values are then used as the input to the TRIM calculation to be run through the transmission materials to develop a functionality of energy lost to be applied as energy added back to the energy measured in the IC, E_m, to obtain E_i, the original energy of the fragments in the target or source, before interacting with any foils or windows. The transmission materials

differ slightly depending on the source/target. The ^{252}Cf source has a 100 µg/cm^2 gold cover which equates to a thickness of 5.18x 10^{-6} cm of gold to be accounted for in the TRIM calculation. The UF_4 target used in the LANSCE measurements is 159.4 µg/cm^2, which is a thickness of 2.38 x 10^{-5} cm. To remain conservative with the TRIM calculation, the entire thickness of the U source is used, despite fission occurring at various points within the target material. The remainder of the transmission materials remain the same for both sources, two 50 µg/cm^2 carbon foils and the IC entrance window of 200 nm SiN. Total energy losses for each representative product are given in Tables 14 and 15.

Table 14: Total energy lost through ^{252}Cf source and transmission materials.

Light				***Heavy***			
A	**Z**	**Element**	**ΔE(MeV)**	**A**	**Z**	**Element**	**ΔE(MeV)**
101	40	Zr	9.31	130	50	Sn	9.93
106	42	Mo	10.26	134	52	Te	9.79
111	45	Rh	10.51	141	55	Cs	9.49
118	48	Cd	10.52	150	59	Pr	8.91

Table 15: Total energy lost through ^{235}U source and transmission materials

Light				***Heavy***			
A	**Z**	**Element**	**ΔE(MeV)**	**A**	**Z**	**Element**	**ΔE(MeV)**
88	35	Br	10.9	130	50	Sn	11.3
95	38	Sr	11.6	134	52	Te	11.1
100	40	Zr	11.1	138	54	Xe	12.7
104	42	Mo	12.1	143	56	Ba	10.3

The energy loss of all materials is then summed and compared to each representative product as a function of the TOF calculated in the TOF region, which is after the source/target and first carbon foil. Figures 61 and 62 show the relationships for energy addback and TOF.

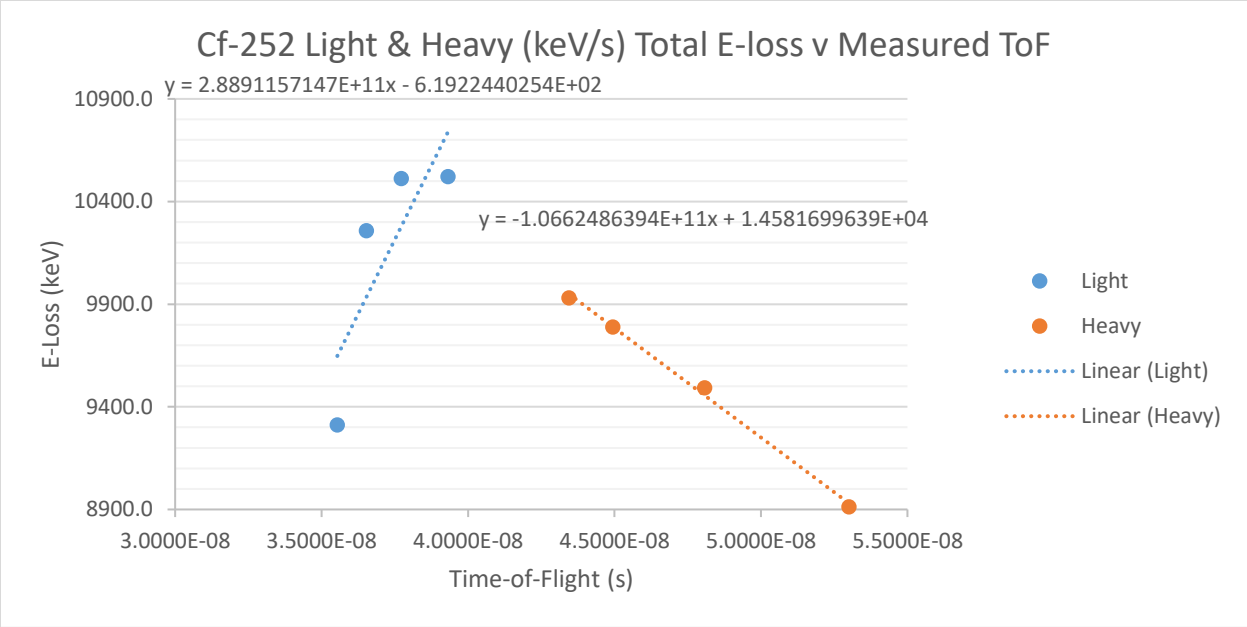

Figure 61: linear fits used in energy correction for ^{252}Cf.

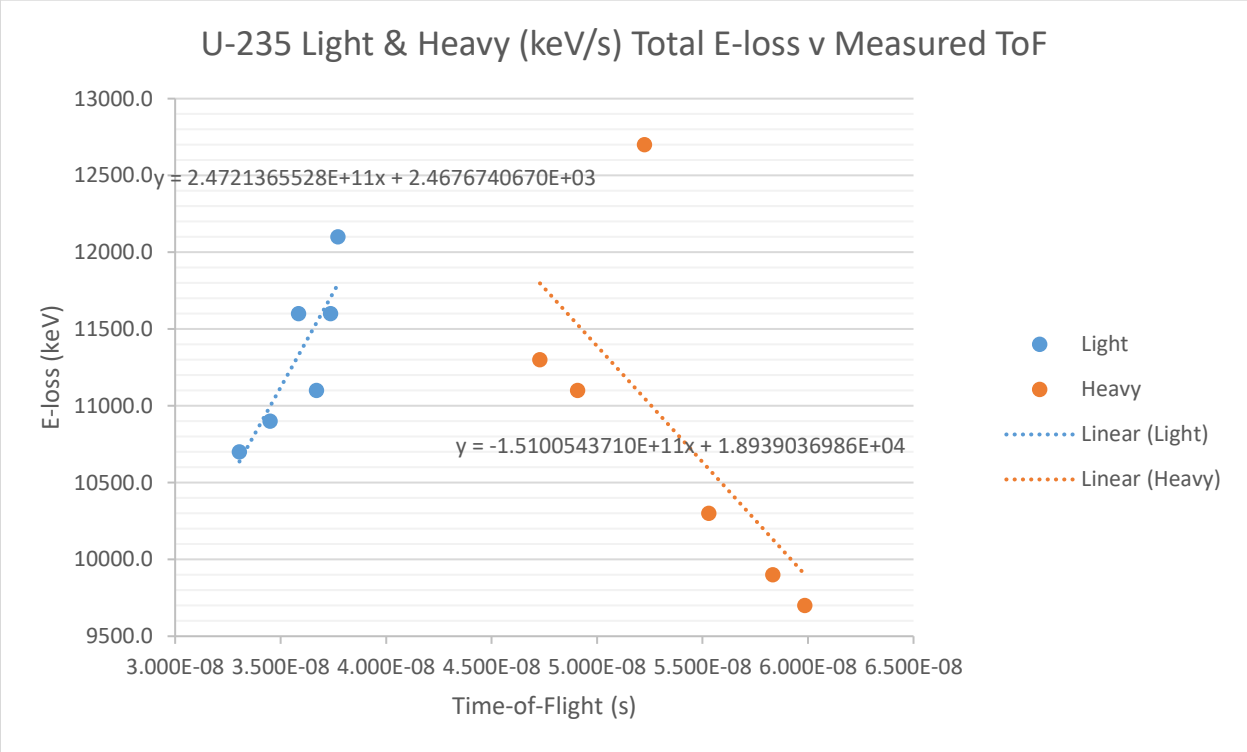

Figure 62: linear fits used in energy correction for ^{235}U.

The velocity measured is then corrected back to the initial velocity with a similar methodology, in this application using the mean energies of light and heavy products to determine the initial velocities for a simple two-point re-calibration to obtain V_i. Converting the TOF calculated for the mean light and heavy products in the TOF region to velocity, for the 50 cm drift region between carbon foil 1 and carbon foil 2, we relate those values directly to the initial velocity, based on the initial energy. Tables 16 and 17 provide values for measured and initial velocity for ^{252}Cf and ^{235}U, respectively.

Table 16: Initial and TOF region calculated velocities for ^{252}Cf.

	Z	A	Vi (m/s)	V measured (m/s)
Light	42	106	1.374E+07	1.345E+07
Heavy	56	142	1.039E+07	1.012E+07

Table 17: Initial and TOF region calculated velocities for ^{235}U.

	Z	A	Vi (m/s)	V TOF (m/s)
Light	36	96	1.429E+07	1.387E+07
Heavy	54	139	9.882E+06	9.402E+06

Figure 63 and 64 shows the re-calibration function generated to convert V_m *to* V_i for ^{252}Cf and ^{235}U.

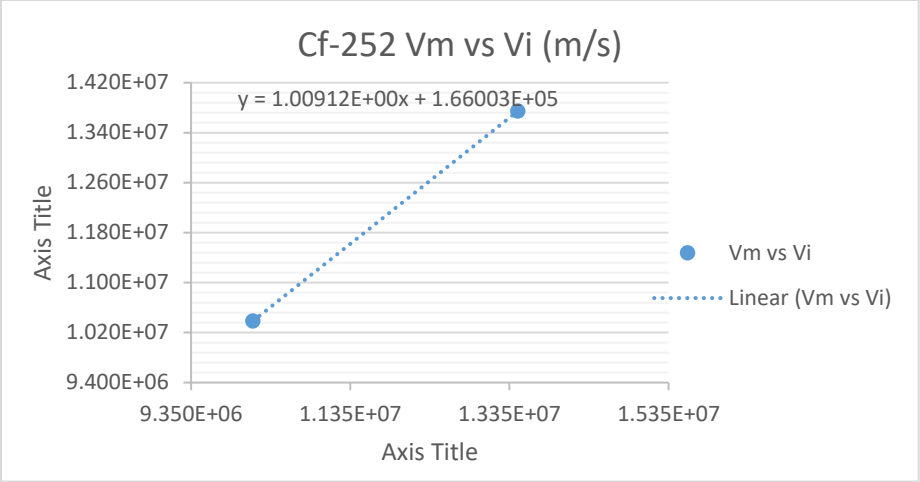

Figure 63: linear correction of initial velocity for ^{252}Cf.

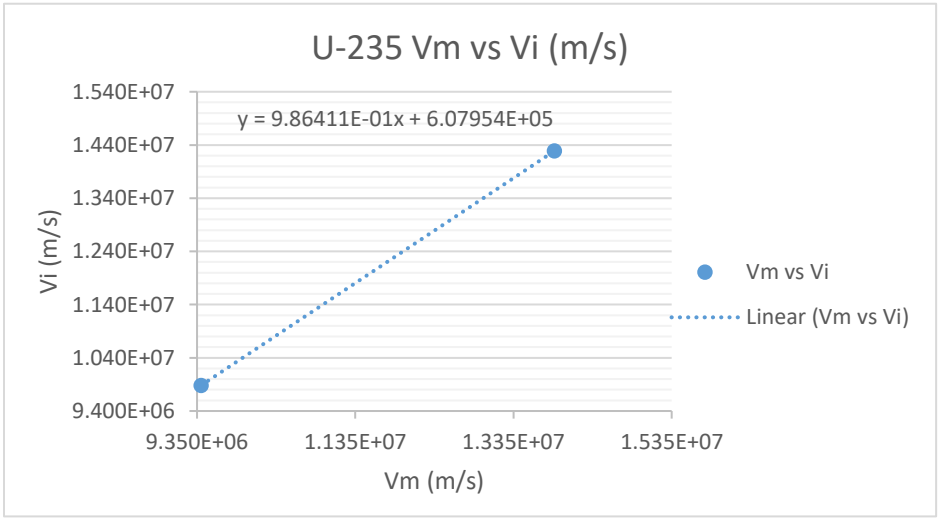

Figure 64: linear correction of initial velocity for ^{235}U.

With these corrections to the measured TOF and E we have all quantities necessary, Ei and Vi, to properly calculate the initial mass, Mi, from the classical kinetic energy equation

$$E_i = \frac{1}{2} M_i v_i^2 \qquad \text{restated as} \qquad M_i = \frac{2E_i}{v_i^2} \qquad \text{[Eq. 22]}$$

4.4 Spontaneous Fission (s.f.) of ^{252}Cf FPY Distribution

The ^{252}Cf data is relatively sparse compared to the ^{235}U data due to the ^{252}Cf's primary use for testing and optimization, as well as the low activity and small branching (3%) for spontaneous fission. However, several individual runs consisting of approximately 6,000 total counts each have been combined for statistically significant results shown in Figure 65 and 66.

As we are gathering quasi-prompt data within 50-100 ns of fission, more closely related to independent yields than cumulative yields in ENDF table data, we compare our results with ENDF data by summing ENDF independent yield data for each nuclide for a given mass. This is done for all our mass yield comparisons, for both ^{252}Cf and ^{235}U. On the question of beta delayed neutrons changing decaying fission products between isobar chains, on slow measurements this is only a small difference, and our measurement time scale is shorter than most fragment beta decay, so beta-delayed neutron emission changing product mass is not considered when comparing our data with independent yield tables.

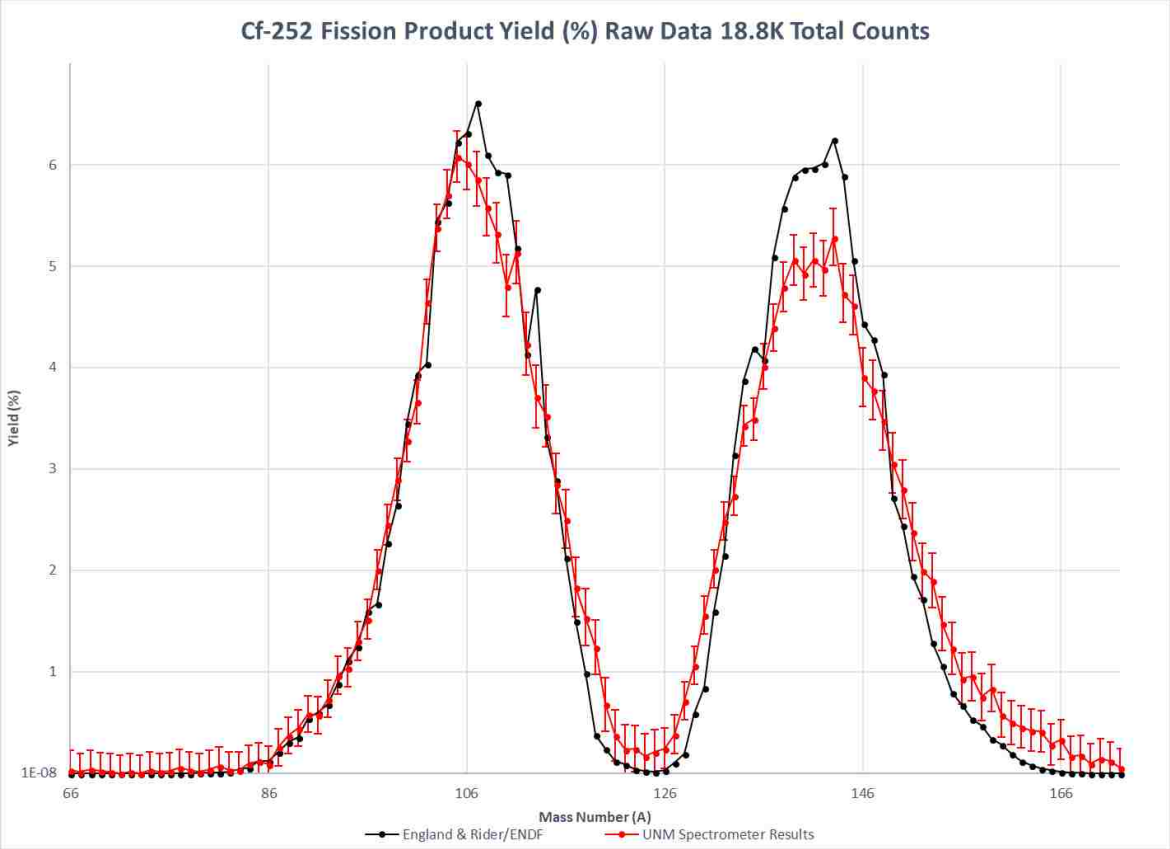

Figure 65: FPY for ^{252}Cf, ENDF/B-VII.1 [51] and UNM spectrometer results.

Taking a closer look at the FPY in logarithmic scale, we clearly see divergence from ENDF/B-VII.1 yields values in the edges of the light and heavy peaks as well as the “valley” region between light and heavy products.

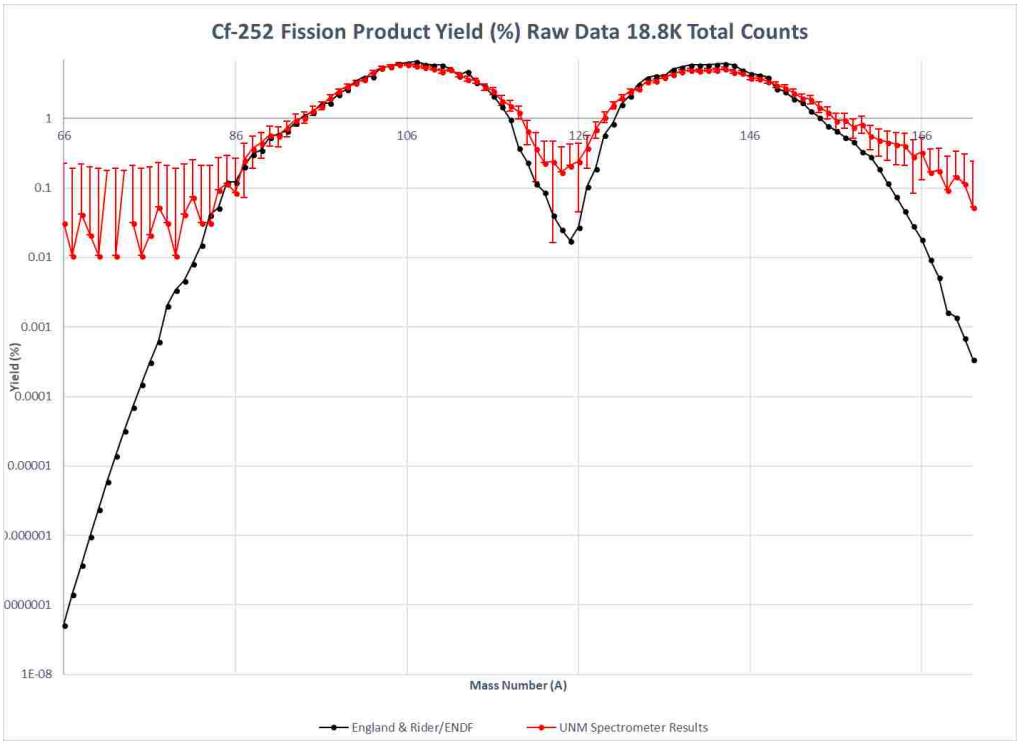

Figure 66: Logarithmic scale FPY for ^{252}Cf, ENDF/B-VII.1 [51] and UNM results.

A major reason for divergence between our data and table values can more than likely be attributed to scattering in the system. This will be discussed in more detail later in the ^{235}U FPY results section. Looking at the average kinetic energy per mass, we see decent agreement with previous experiments done by Schmitt [10].

Our data for average kinetic energy as a function of mass is presented in Figure 67 and shows a consistent underestimation vs table values, which can potentially be attributed to an underestimation of energy loss relying on TRIM simulations. Experiments to better understand heavy ion energy loss are currently being devised and tested to increase our understanding of the discrepancies and benchmark these experiments with simulation.

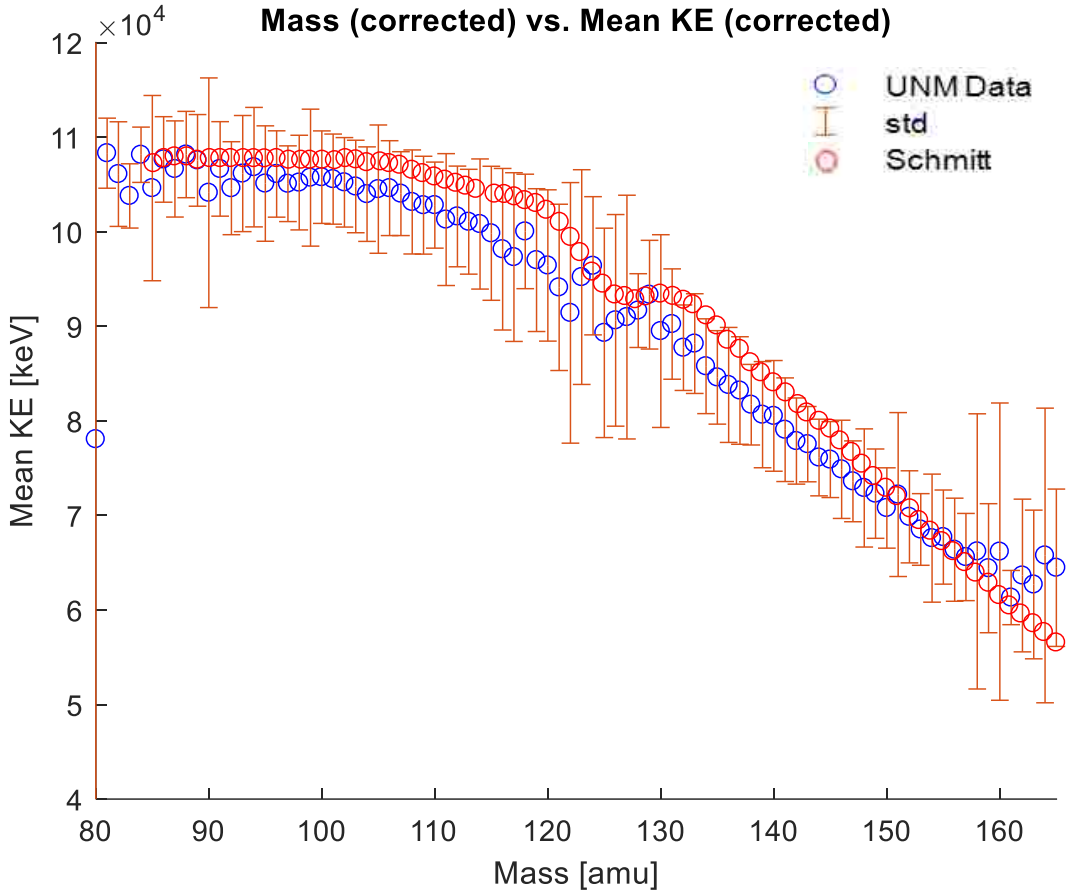

Figure 67: Average kinetic energy per fission product mass for ^{252}Cf. "std" is the standard deviation of the mean.

4.5 Thermal Neutron-Induced Fission ^{235}U FPY Distribution

The UNM spectrometer was fielded successfully on the low energy neutron beamline at the LANSCE accelerator facility in Los Alamos, NM for the past three run cycles. The first run cycle was highly successful considering the lower resolution and high energy loss in the original system (P-10 as an IC fill gas and Mylar entrance window). The second run cycle was relatively unsuccessful as the ion chamber suffered consistent electrical breakdown issues as we re-designed to an active cathode configuration. The electrical breakdown issues were resolved before the winter 2016/7 run cycle, which led to our best run cycle yet.

The latest data (winter 2016/7) taken at the LANSCE facility was our largest in terms of total counts and most sophisticated given the amount of improvements made between the first run cycle for our spectrometer and the latest. Since the first run cycle we made improvements, including thinner time-of-flight transmission foils (from 100 $\mu g/cm^2$ to 50 $\mu g/cm^2$), introduction of the SiN entrance window instead of thick mylar, for decreased energy loss, as well as successful implementation of the active cathode ion chamber configuration for range and thus Z determination. With the improvements this is the best data set and thus the accumulated data for the latest data, utilizing thermal neutron-induced fission of a ^{235}U target, will be presented here. A more recent run (winter 2017/8) was begun on ^{239}Pu but due to window breaking and arcing of the MCPs that measurement was stopped.

Starting by looking at all data, including obvious scattered data, we see reasonable agreement with published ENDF/B-VII.1 values as seen in Figure 68 and 69, where the full yield adds to 200% in binary fission. As seen in the ^{252}Cf FPY distributions, we see scattering contributing significantly to the peak edges and valley regions. Viewing the yield % variable in logarithmic terms shows the extent of the scattering more clearly. Despite the deviation between our data and table values for low yield masses, mean values of mass and energy for light and heavy peaks show good agreement with published values from Schmitt et al. [10] as shown in Table 18.

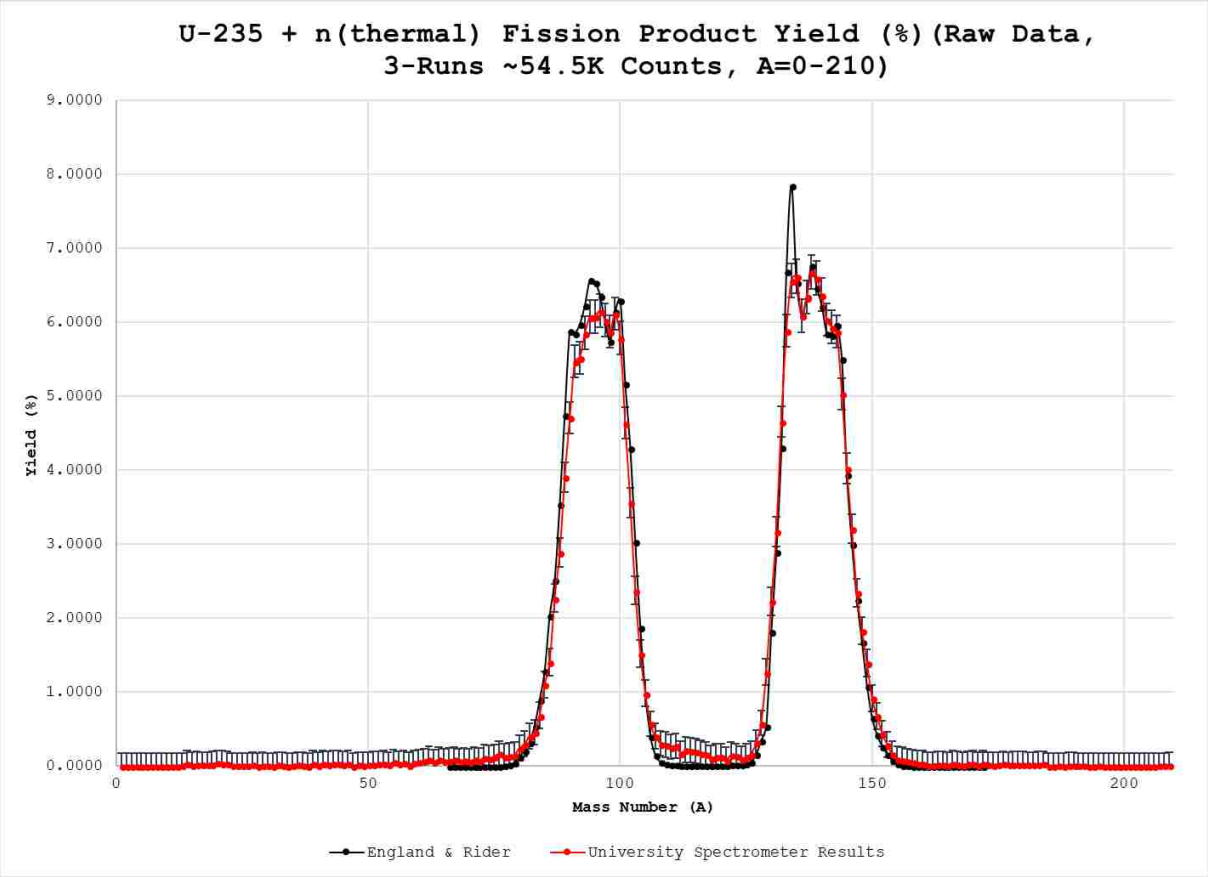

Figure 68: Full-range linear FPY for $U(n_{th}, f)X$.

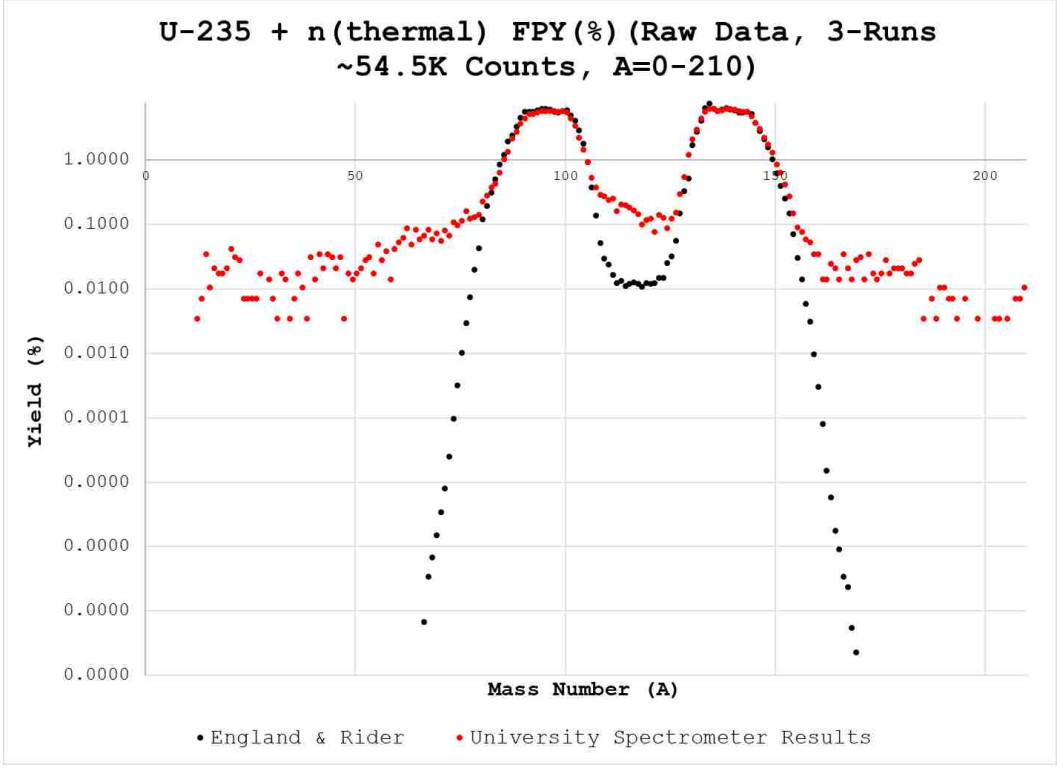

Figure 69: Full-range logarithmic FPY for U(n_{th}, f)X.

Table 18: Results for mean mass and energy for 235U.

This Work	**Mean E (MeV)**	**σ_{mean} E**	**Mean A (amu)**	**σ_{mean} A**
Light	98.76	0.06	94.35	0.05
Heavy	70.13	0.05	138.84	0.04
Schmitt				
Light	101.56	*N/A*	96.57	*N/A*
Heavy	70.34	*N/A*	139.53	*N/A*

Taking a closer look at the average kinetic energy as a function of mass of the full range (A = 1-210), seen in Figure 70, we know that a majority of the low-mass, low-yield detections are not realistic for the given fission reaction, nor the very high mass results.

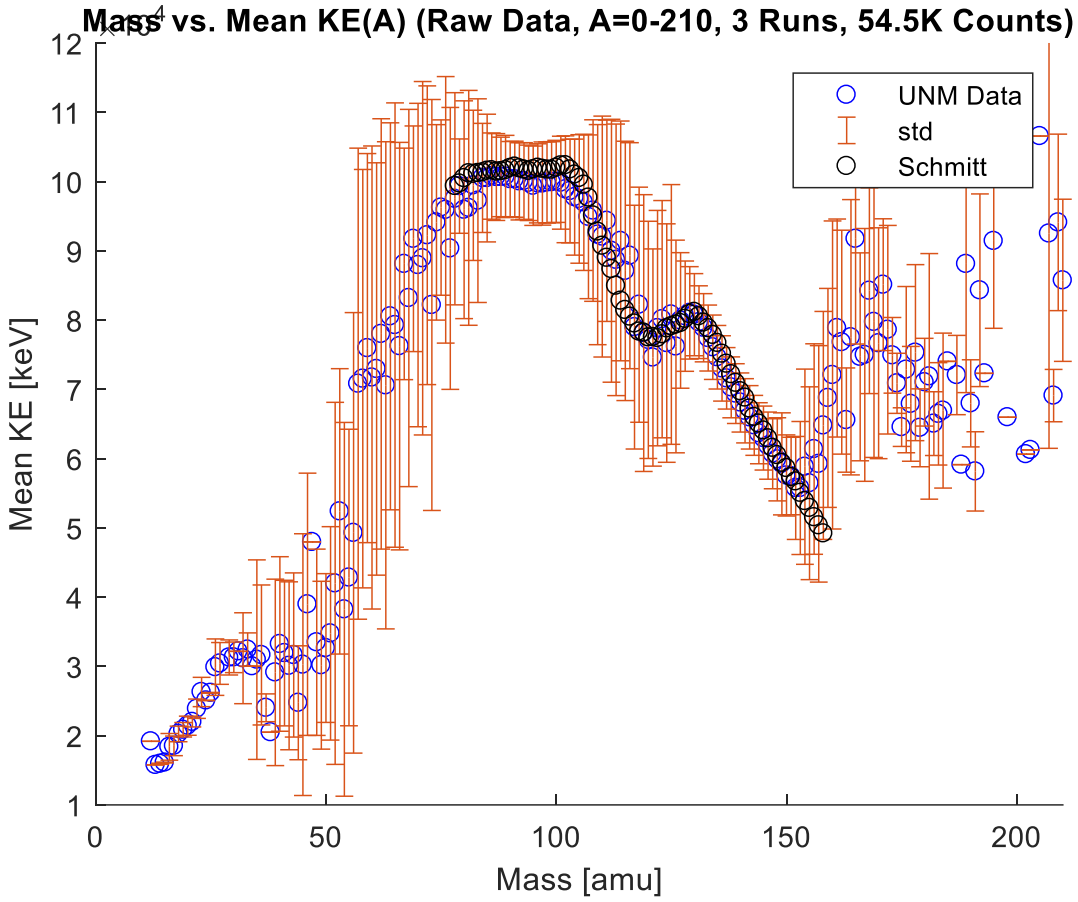

Figure 70: Average kinetic energy per fission product mass for ^{235}U.

For analysis purposes only, reducing the region of interest strictly to the mass region reported in the ENDF/B-VII data, A = 66 – 172, the UNM spectrometer results of the FPY distributions, Figure 71, begin to show good agreement with ENDF/B-VII data. While the light peak is slightly "condensed" this could potentially be from our energy addback procedures, but still agree well with ENDF/B-VII data. Peak shape artifacts are also present and show good agreement with previous assessment. The heavy peak looks very good when compared with ENDF/B-VII, outside of the obvious table data spike at mass 134.

It is difficult to know the mass yield uncertainty of the table values. Our quasi-prompt yield data more closely relates to table values of independent yields, and so independent yields

from the tables were summed over the isobars for each mass. Most published mass yield data is cumulative yield, and independent yields are worked out using models, meaning the uncertainties on each nuclide's independent yield are also following models and interrelationships between the different isobars. Simply summing the uncertainties in quadrature for the listed values for each nuclide's independent yield then clearly overstates the actual uncertainty for each mass as covariance is not considered. Values needed to determine the uncertainty reduction is unavailable and absent from the ENDF/B-VII presented here, however, overall uncertainty is not insignificant. An example of the uncertainties for different nuclides included in the ENDF table values we present for mass yields is presented in Figure 72 for ^{235}U and 73 for ^{252}Cf

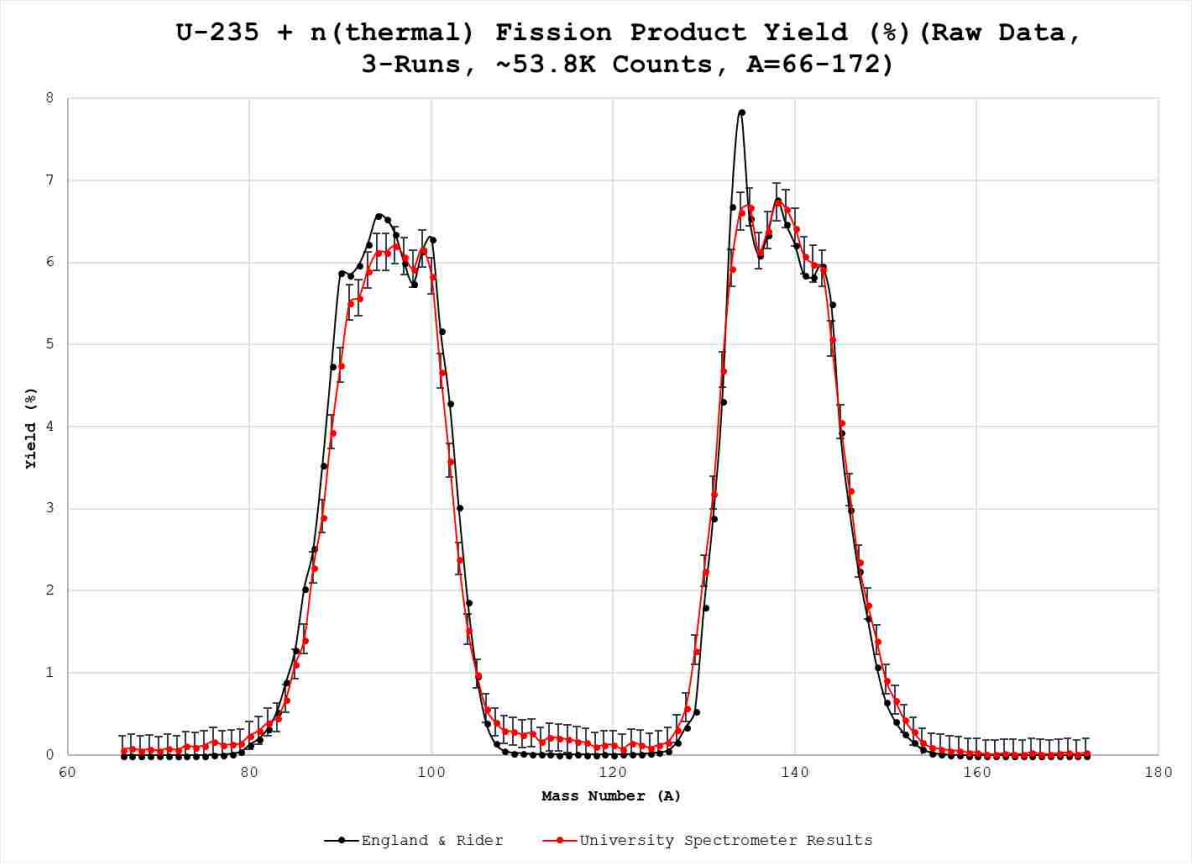

Figure 71: ^{235}U FPY distribution for mass region A = 66 – 172.

While the light peak is slightly "condensed" this could potentially be from our energy addback procedures, but still agree well with ENDF/B-VII data. Peak shape artifacts are also present and show good agreement with previous assessment. The heavy peak looks very good when compared with ENDF/B-VII, outside of the obvious spike at mass 134. Statistical uncertainties on the ENDF/B-VII data are difficult to assess, as uncertainties published are for all nuclides rather than one uncertainty for each mass. Simply adding these uncertainties in quadrature to find the uncertainty for each mass is not correct, as co-variance in the measurement can reduce the overall uncertainty significantly. Data needed to determine the uncertainty reduction is unavailable and absent from the ENDF/B-VII presented here, however, overall uncertainty is not insignificant. The ENDF/B-VII independent FPY distributions for ^{235}U and ^{252}Cf are shown with uncertainties in Figure 72 and 73.

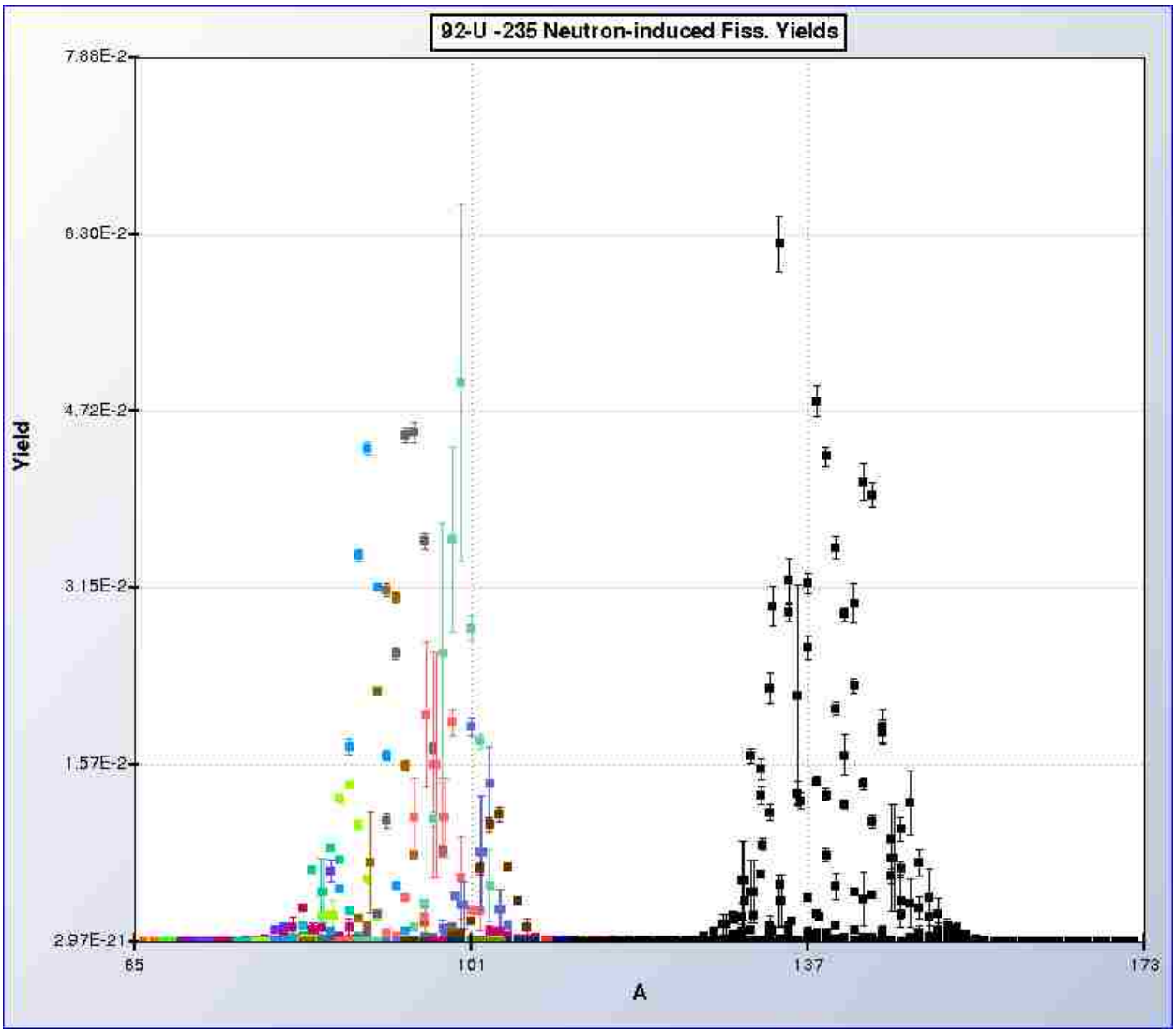

Figure 72: ENDEF/B-VII ^{235}U independent FPY with uncertainties. [51]

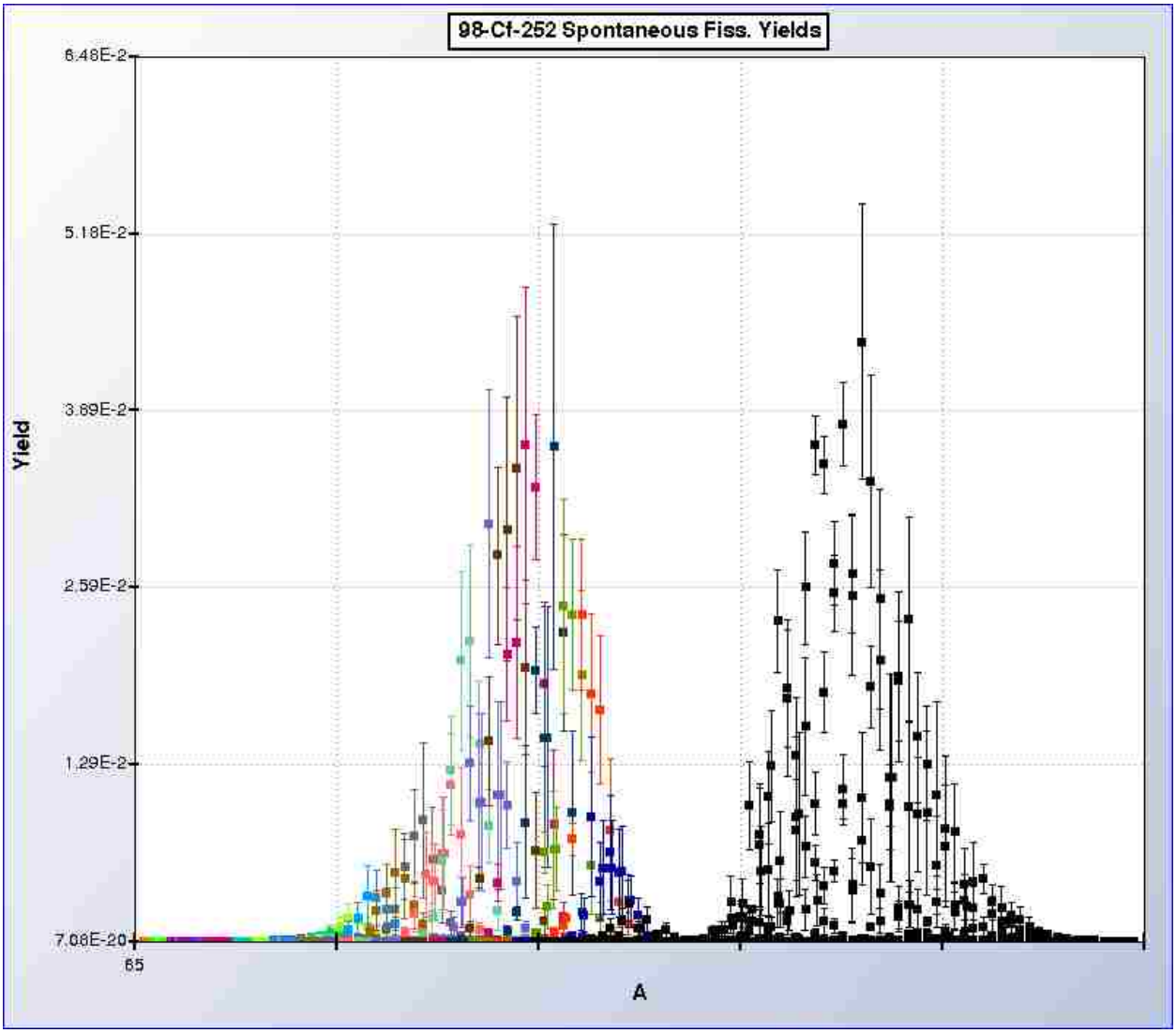

Figure 73: ENDEF/B-VII ^{252}Cf fission yield with uncertainties. [51]

As shown in Table 19, mean values for energy and mass change only slightly between this work and Schmitt et al. [10]. When a smaller mass region of interest is examined, the average kinetic energy as a function mass remains unchanged and in good agreement in the region of interest, particularly in the high-yield, peak regions. However, by examining a smaller mass region, the average kinetic energy as a function of mass plot becomes easier to assess, as seen in Figure 74.

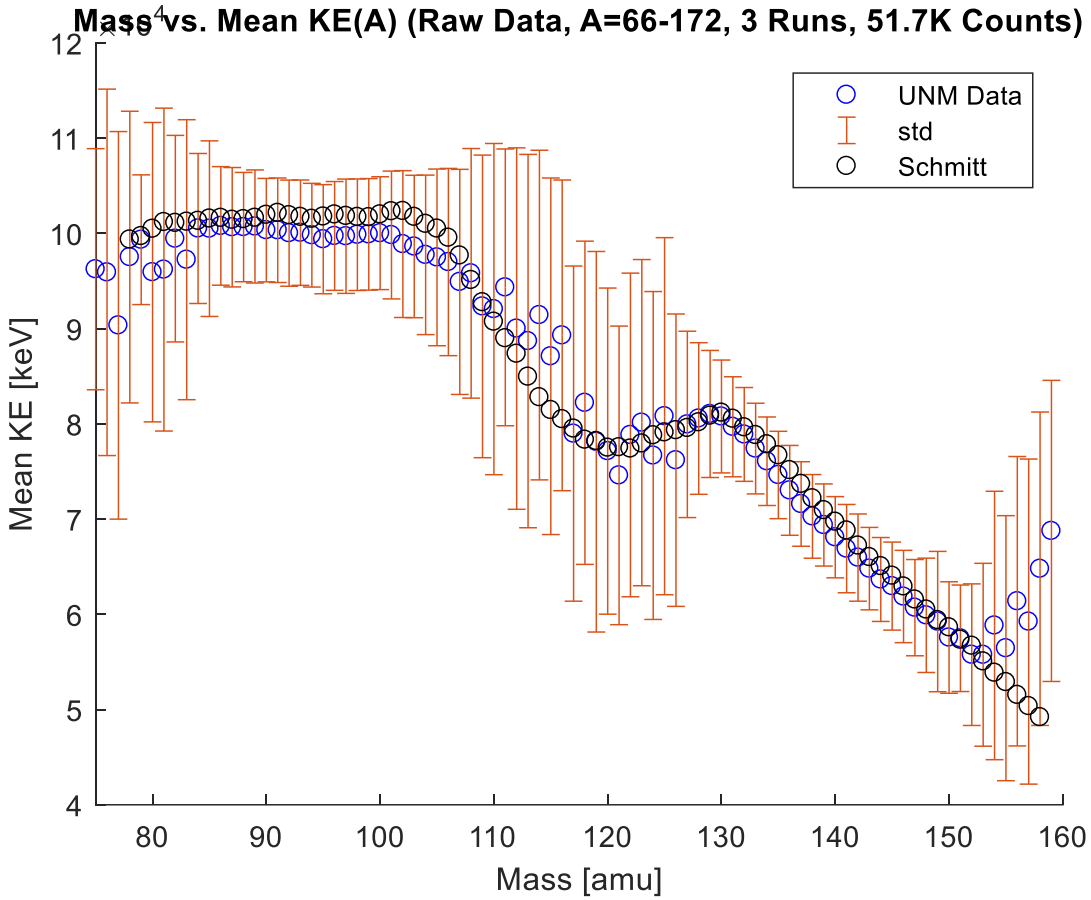

Figure 74: Average kinetic energy as a function of fission product mass for ^{235}U (A = 66 – 172).

Table 19: Results for mean mass and energy for ^{235}U (A = 66 – 172).

This Work (A= 66-172)	**Mean E (MeV)**	**σ_{mean} E**	**Mean A (amu)**	**σ_{mean} A**
Light	99.52	0.05	95.07	0.04
Heavy	70.12	0.05	138.67	0.04
Schmitt				
Light	101.56	*N/A*	96.57	*N/A*
Heavy	70.34	*N/A*	139.53	*N/A*

This is where a "second arm" of the detection system, i.e. an identical spectrometer setup positioned at 180°, becomes crucial. If a second arm was utilized in this experiment, an anti-coincidence conditional could be set on the coincidence mass data to determine whether the combined masses of the two detected products approximately adds up to the fissioning nucleus

(minus prompt neutrons), if not then these potentially scattered products could be validly excluded. However, since we do not have a second arm do this with complete confidence, despite the unrealistic nature of the product masses collected, we cannot exclude data. Instead a closer examination of the suspected scattered products was performed.

4.5.1 Uncertainty Accounting

4.5.1.1 Statistical Uncertainty

Statistical uncertainties assessed on the product yield is relatively straightforward. Simple bin counting statistics and normalization of the deviation is applied for the number of counts in each extracted mass bin as in equation 24, [52]

$$\sigma_{Nbin} = \sqrt{N} \quad \text{Eq. 24}$$

which for yield percent becomes

$$\sigma_{yield\%} = \frac{200*\sqrt{N}}{N_{total}} \quad \text{Eq. 25}$$

where the full yield from both products in binary fission adds up to 200%.

An additional uncertainty from scattering is added in quadrature. To get a reasonable assessment of the uncertainty in the number of counts due to scatter in to that mass bin, the difference in yield values in the valley portion (A = 108 – 126) of the distribution between ENDF/B-VII values and our data is noted. The amount of scatter is dependent on the region in the E/TOF plot but without a clear functional expression, the scatter into the region which is interpreted in the A=108-126 mass range is used as an average value, as in Figure 75. The range A=108-126 is chosen as table values are listed below 0.1%. The rms value of the differences over that range is used as the uncertainty due to scatter, as in

$$\sigma_{scatterring} = \frac{\sum_{i=108}^{18} d_i^2}{N} \quad \text{Eq. 26}$$

where d_i is the difference between the UNM spectrometer yield % data and the ENDF/B-VII yield % values. The total statistical uncertainty then becomes

$$\sigma_{total} = \sqrt{\sigma_{scattering}^2 + \sigma_{\%yield}^2} \quad \text{Eq. 27}$$

and dominates only in the very low yield regions.

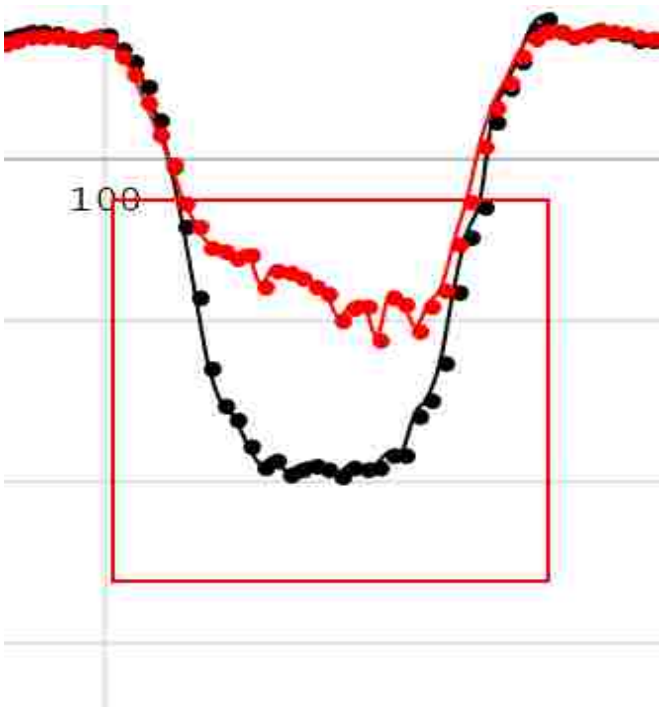

Figure 75: Example valley region in mass yield utilized to estimate scattering contribution to statistical uncertainty.

4.5.1.2 Estimating the Mass Uncertainty

The most direct way of measuring mass uncertainty of our system would be with known masses, as in a clean single mass beam in the fission fragment E and A range. Without the use of

a heavy ion beam, where an absolute mass uncertainty could be experimentally obtained, we are left with theoretical assessments of the overall mass uncertainty. The proportional distance uncertainty is negligible compared to the energy and time uncertainties. Simplifying slightly then from section 1.3, the mass uncertainty can be written as

$$\delta M = M\sqrt{\left(\frac{\delta E}{E}\right)^2 + \left(\frac{2\delta t}{t}\right)^2} \quad \text{Eq. 28}$$

again, discounting length uncertainty. Further, utilizing the energy resolution relationship for ion chambers from section 3.1.3.1;

$$ER = \frac{fwhm\ of\ E}{E_o} = \frac{2.35\sigma_E}{E_o} = \frac{2.35\sqrt{fW}}{\sqrt{E_{in}}} = 0.0118 \quad \text{Eq. 29}$$

Equation 29 is a statistical minimum of energy resolution for ion chambers, which does not account for other sources of uncertainty such as electronic noise. This will lead to an underestimation of the total uncertainty energy measurement, however, without a heavy ion beam for experimental measurement of uncertainty, this will at least serve as a minimum for fission fragment mass uncertainty. The resolution is dependent on the number of charges liberated in the IC gas (ignoring recombination and thus pulse height defect) with ER going as $1/\sqrt{N}$ and thus as $1/\sqrt{E}$. Using the average energy per product mass data generated, and the energy resolution found for the IC in section 3.1.3.1, we can estimate the energy uncertainty of fission fragments from by using the ratio of their energy to the

energy of alpha particles where we previously found the resolution, following equation 29, and so to find the energy resolution for fission products, ER_{FP},

$$ER_{FP} = ER_{\alpha}\sqrt{\frac{E_{\alpha}}{E_{FP}}} \quad \text{Eq. 30}$$

where E_{FP} is the energy of the fission product, ER_{α} is the energy resolution measured for the alpha particle in section 3.1.3.1, and E_{α} is the energy of alpha particle energy. This follows electron counting statistics only and must be corrected for the fission product pulse height defect, sightly broadening fission product energy resolution as compared with this equation.

The total time-of-flight value for each product mass is calculated from those same average kinetic energy per product mass data by determining the velocity using the classical kinetic energy equation. A flight distance of 50 cm is used to obtain an average time-of-flight value for each mass. The updated time resolution of 282 ps FWHM is used as a constant for the timing uncertainty. All information is available to make an estimated uncertainty assessment on the mass; however, this is an underestimation as stated previously as it is based off the statistical minimum for energy uncertainty. Figures 76 and 77 show the estimated uncertainty calculated for ^{252}Cf and ^{235}U, respectively, for each product mass.

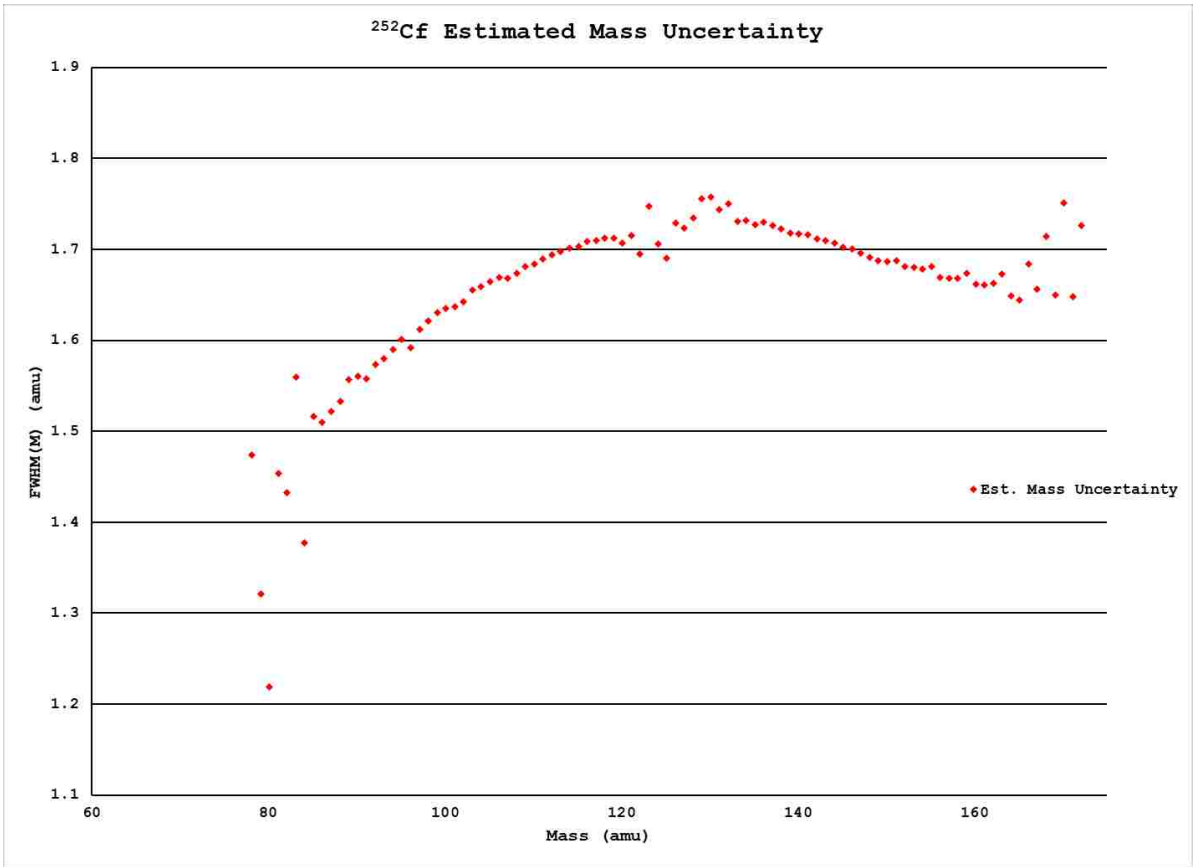

Figure 76: Estimated mass uncertainty for ^{252}Cf.

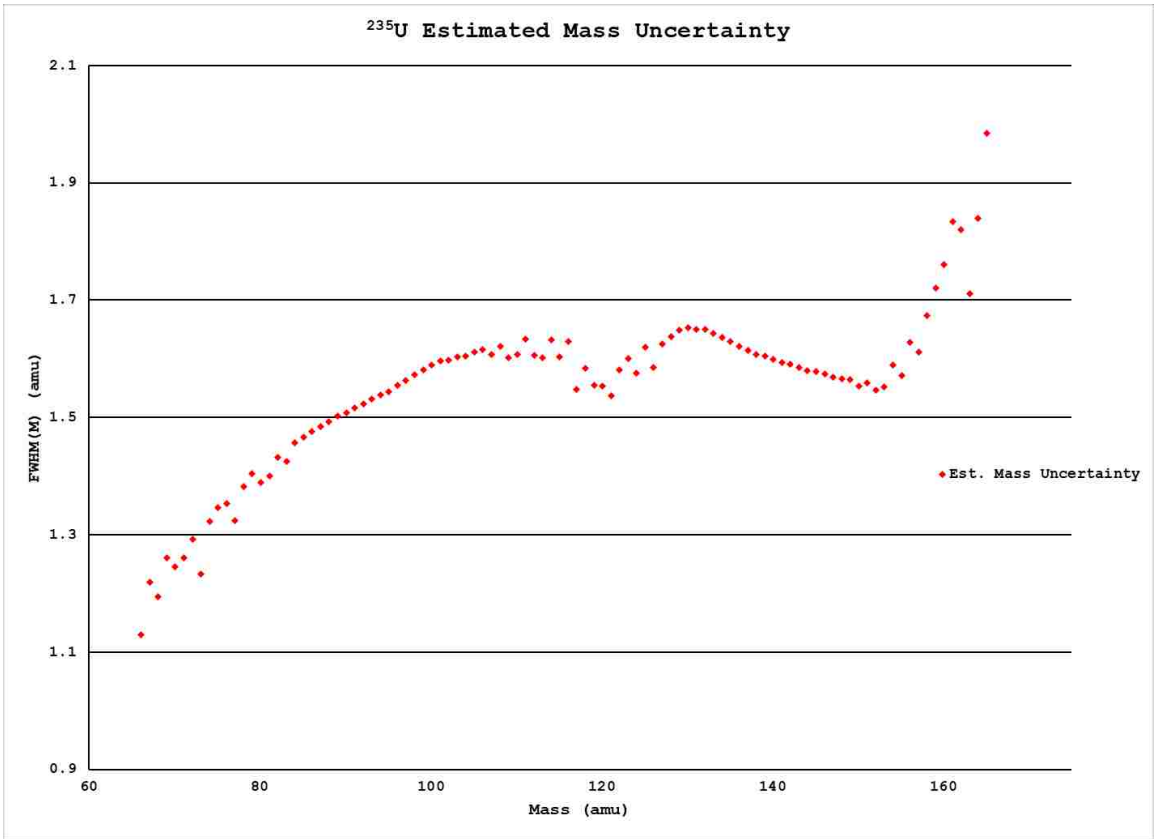

Figure 77: Estimated mass uncertainty for ^{235}U.

Utilizing the above method returns an underestimated resolution value. Based on similar, previous experiments with the availability of a heavy ion beam, we would expect FWHM values of approximately 385 keV and 510 keV [7] for light and heavy products, respectively. The statistical limit method in equation 30 returns average light and heavy FWHM values of 269 keV and 233 keV for ^{235}U, and 279 keV and 236 keV for ^{252}Cf, average light and heavy products, respectively.

4.5.2 Scattering

Masses are reconstructed using E and TOF data, but not all the data is valid, which may be due to scattering. This is clear in Figure 78, with energy and TOF for each measured particle presented point-by-point. The light and heavy mass data are tightly constrained within their

regions, but there are many points with E and TOF values, or combinations of values, that are clearly not within the range expected from fission fragments. Especially in the case of a fast TOF but a very low energy, meaning scattering occurred after the TOF measurement and before the energy measurement, it is understood there is scattering in the system.

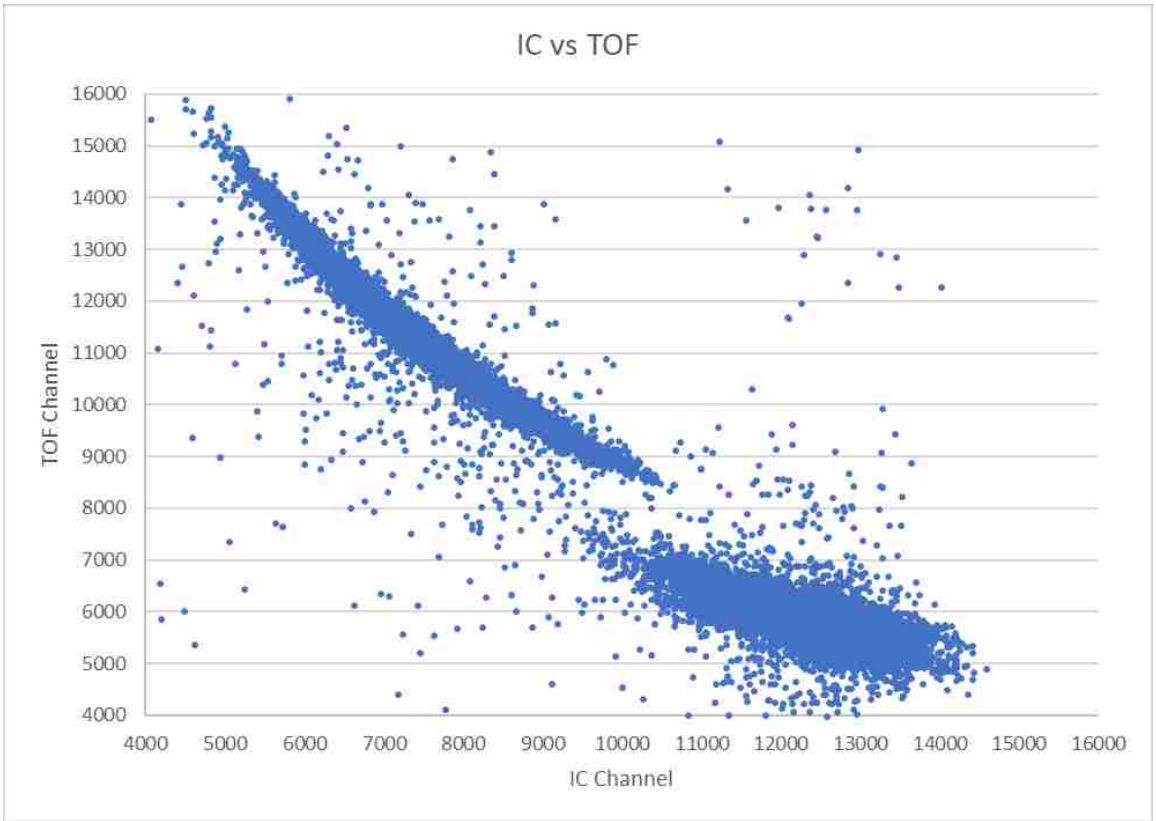

Figure 78: IC and TOF raw channel data for a single run for ^{235}U. The top left shape is slower, heavier products and the bottom right shape is faster, lighter products.

Scattering of fission fragments in the system can come from several different sources. The electron reflection grid wires, carbon foils and the foil holder frames, and the IC entrance window frames offer three of the most likely causes of potential ion scattering. Scattering can occur pre-TOF measurement, during TOF (scattering off the first electron reflection grid or first carbon foil) or post TOF (second electron grid and carbon foil or the IC entrance grid). This will

alter both the measured TOF and energy, or the energy measurement only, depending on where scattering occurs.

To provide some insight into what data is contributing to the scattering, we look at the IC vs TOF channel data as a function of individual mass. For this assessment, IC and TOF channel data for individual masses are superimposed in darker color onto the total IC vs TOF channel data for sample masses of A=95, A=115, and A=115 as representative of light, heavy, and mid-range masses, in Figures 79, 80, and 81, respectively for the $^{235}U(n_{th}, f)X$ reaction. All masses from A=66 through A=171 are presented in Figures 82 - 88.

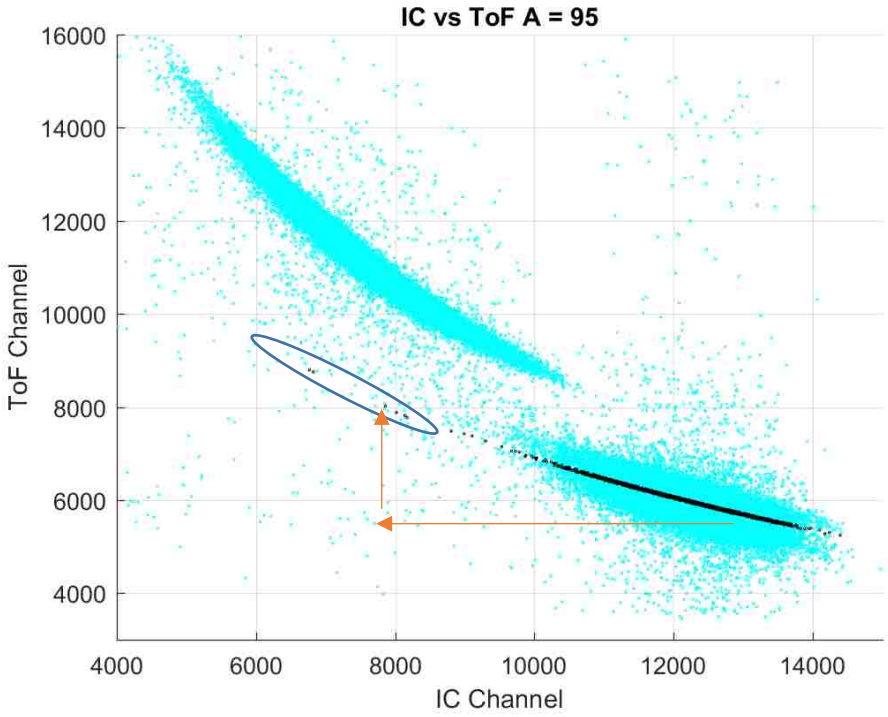

Figure 79: IC vs TOF channel as a function of mass for ^{235}U (A = 95).

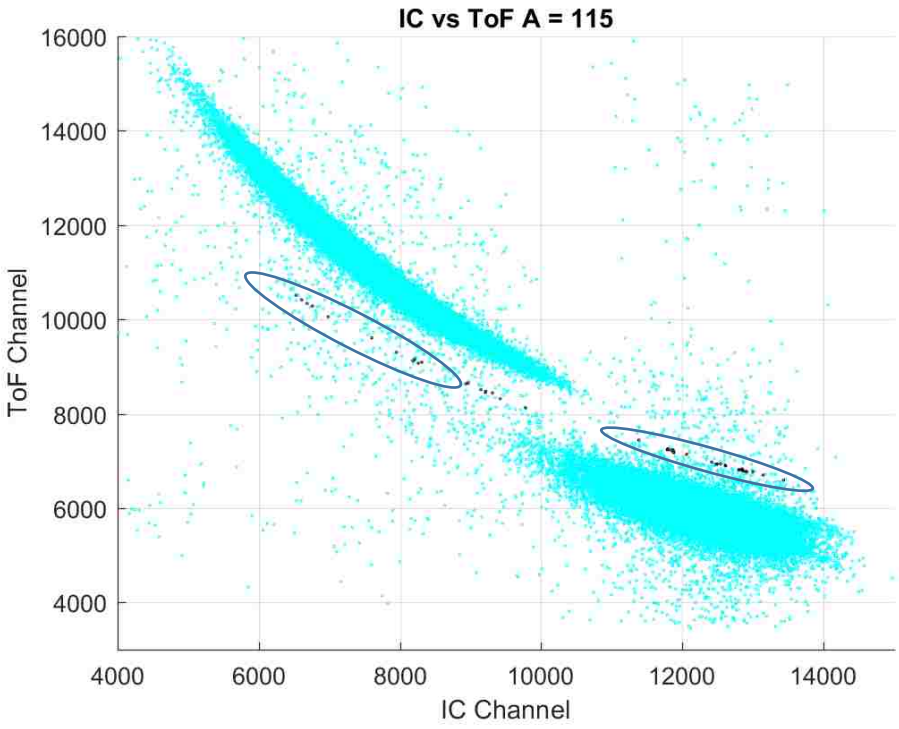

Figure 80: IC vs TOF channel as a function of mass for ^{235}U (A = 115).

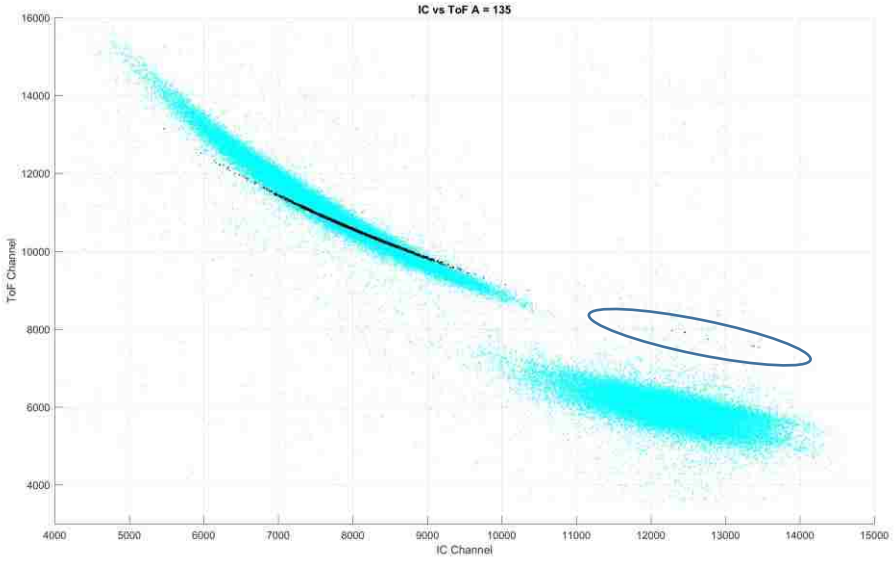

Figure 81: IC vs TOF channel as a function of mass for ^{235}U (A = 135).

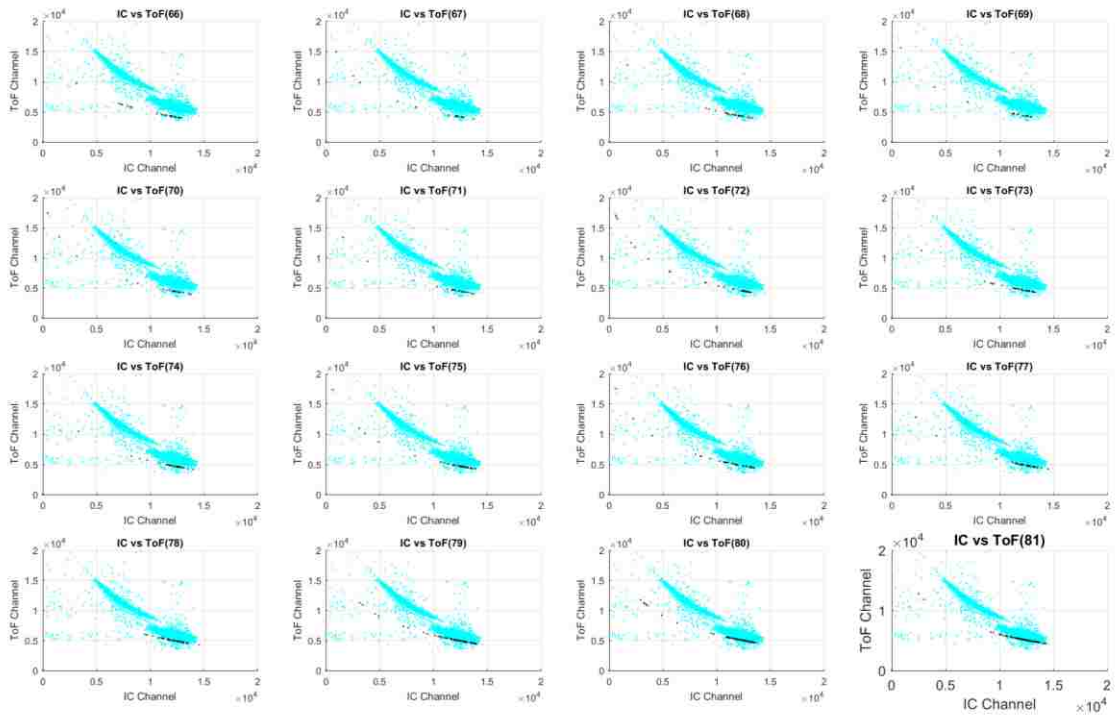

Figure 82: IC vs TOF channel as a function of mass for ^{235}U (A = 66 – 81).

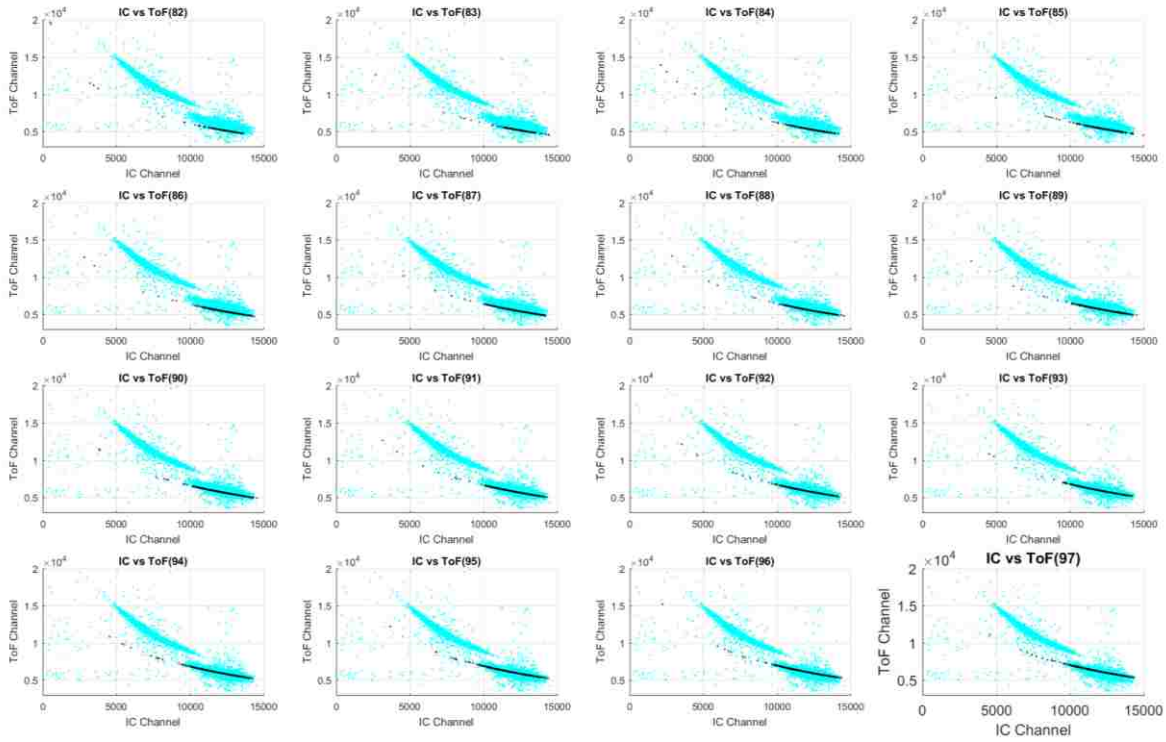

Figure 83: IC vs TOF channel as a function of mass for ^{235}U (A = 82 – 97).

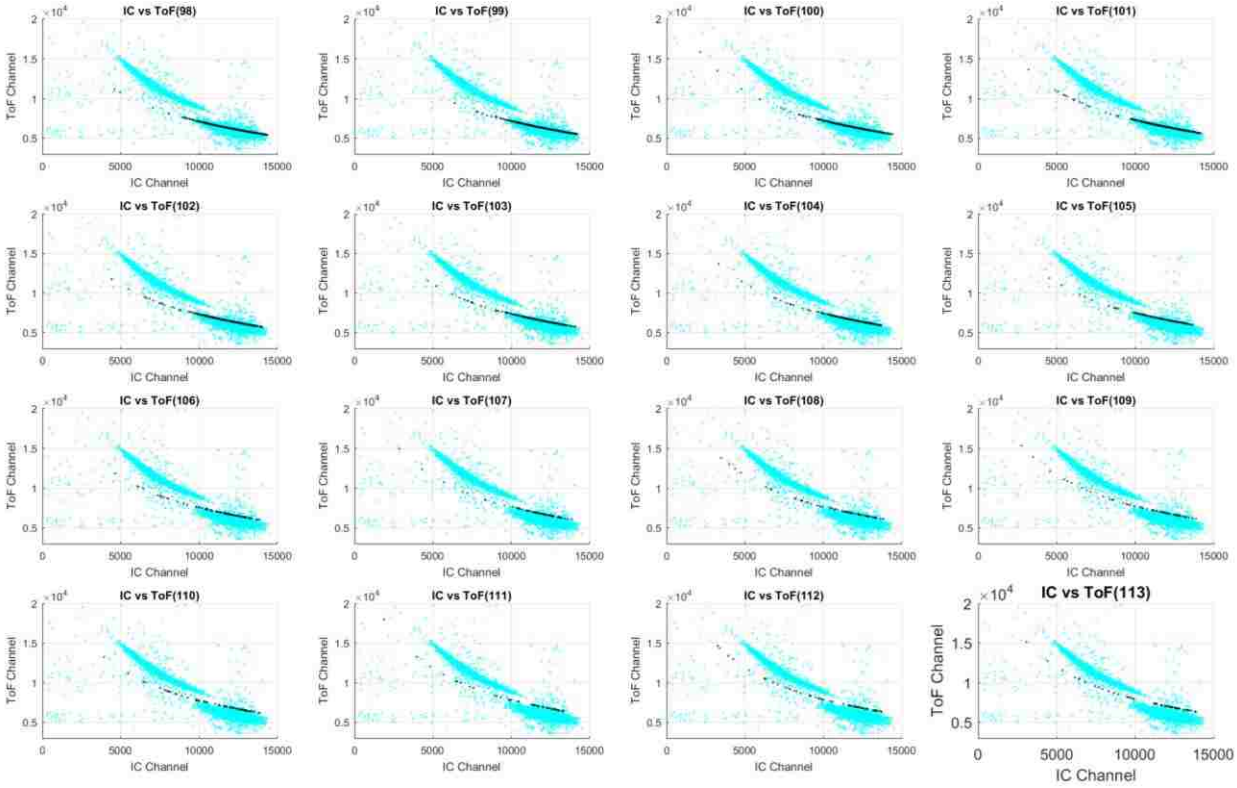

Figure 84: IC vs TOF channel as a function of mass for ^{235}U (A = 98 – 113).

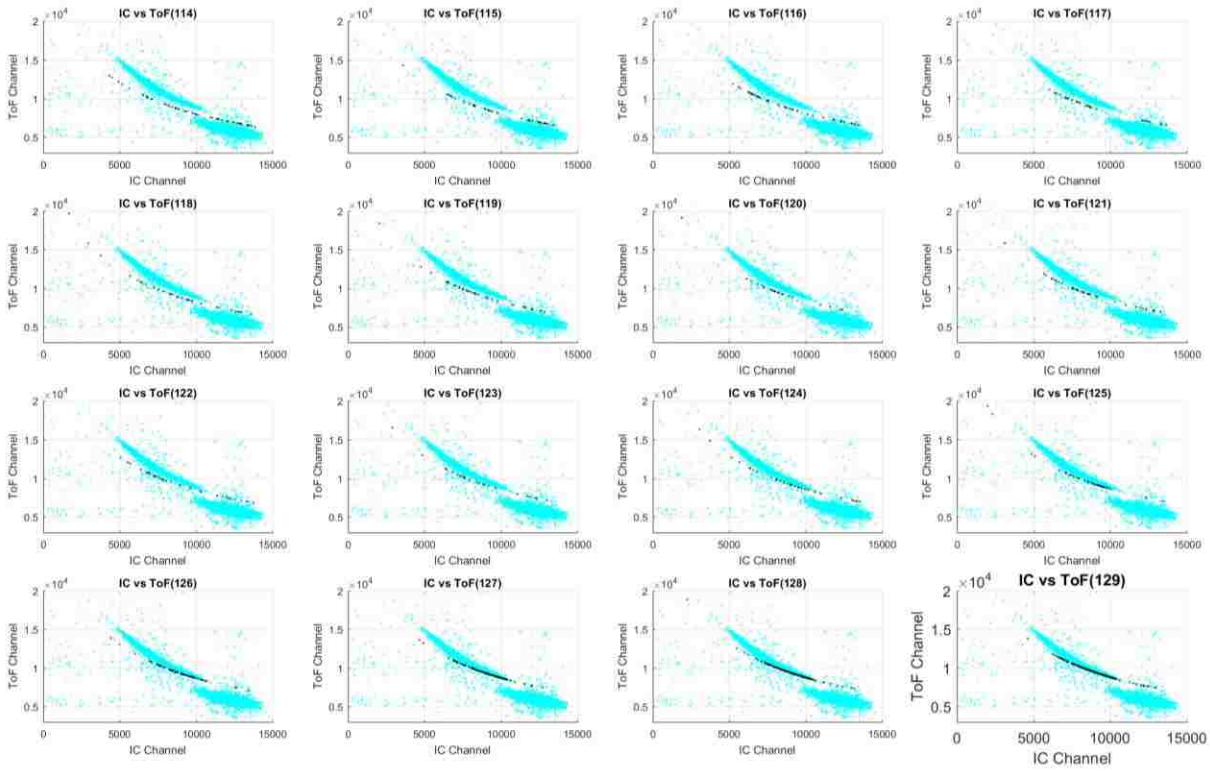

Figure 85: IC vs TOF channel as a function of mass for ^{235}U (A = 114 – 129).

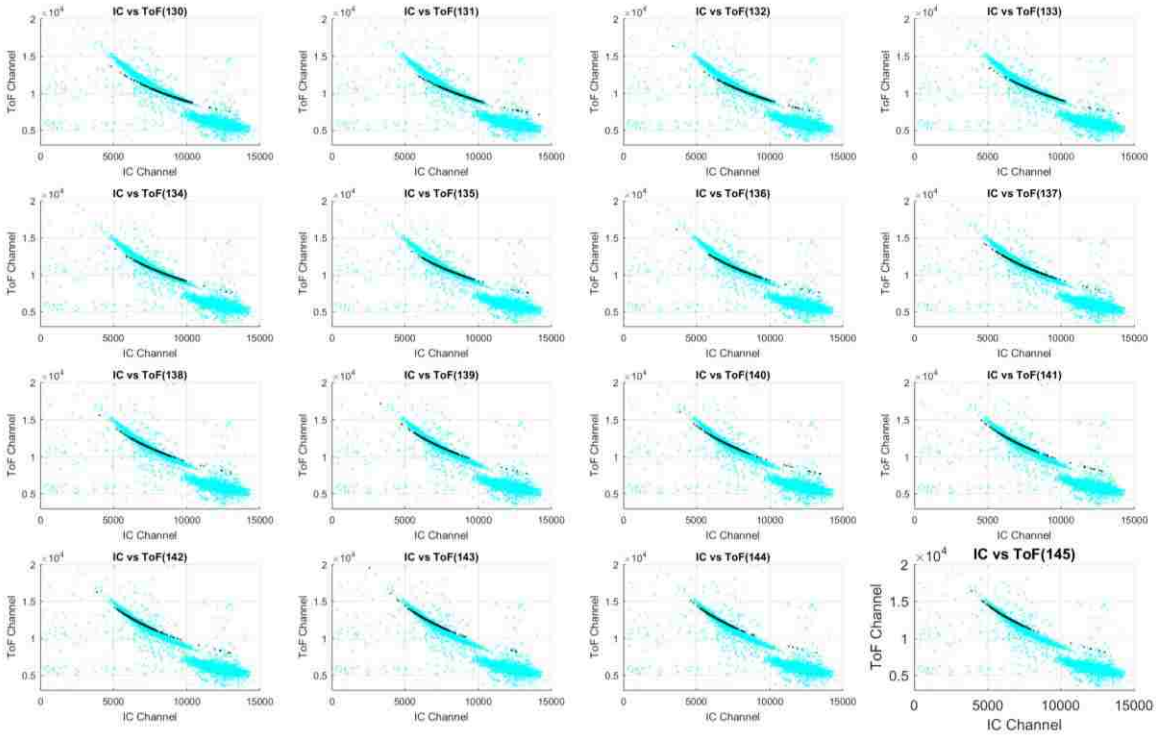

Figure 86: IC vs TOF channel as a function of mass for ^{235}U (A = 130 – 145).

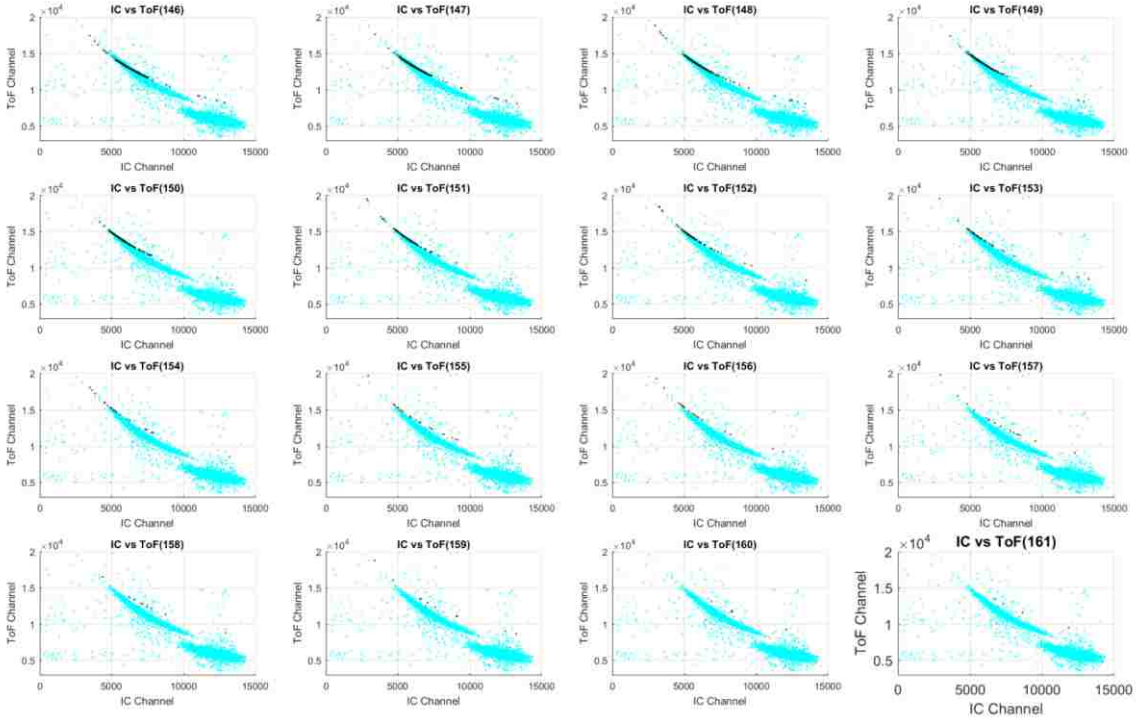

Figure 87: IC vs TOF channel as a function of mass for ^{235}U (A = 146 – 161).

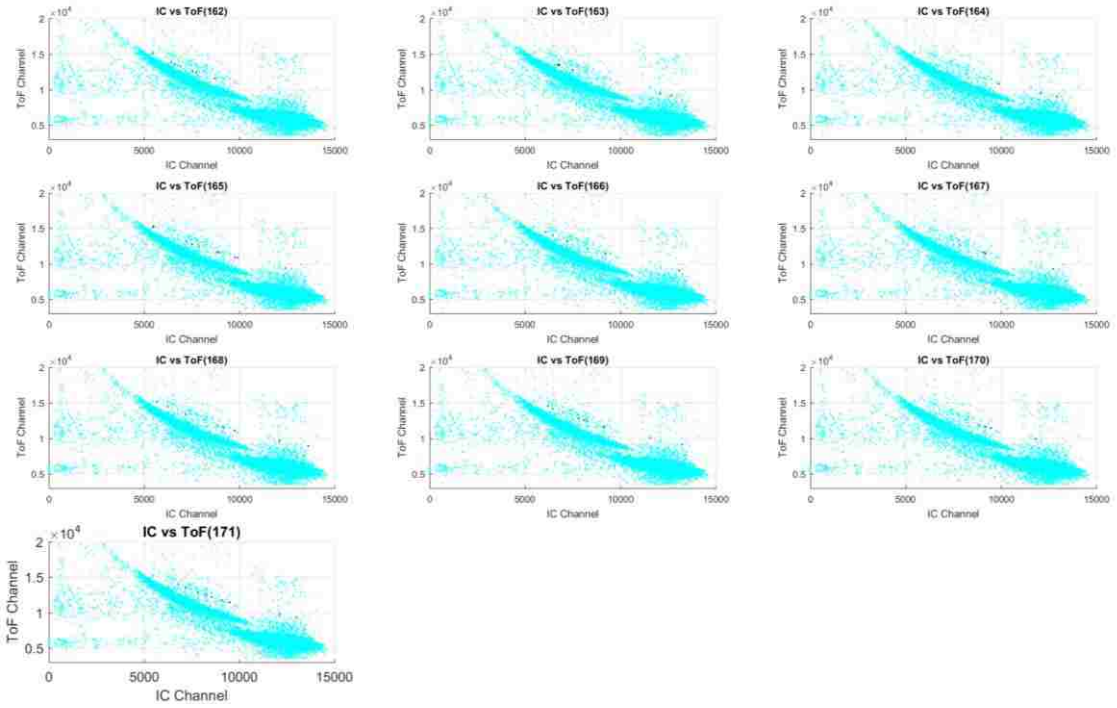

Figure 88: IC vs TOF channel as a function of mass for ^{235}U (A = 162 – 171).

Figures 82 – 88 show the results for all masses in the region of interest. Long tails can be seen in some of the mass results at combinations of energy and TOF that would be unlikely in a fission event. For example, Figure 79 shows results for A = 95. Alow energy, high TOF mass 95, circled in Figure 79, is an unlikely outcome of the $^{235}U(n_{th}, f)X$ reaction. This is more than likely a high energy, light product scattered in the electron reflection grid as indicated by the arrows in Figure 79. Figure 80 shows how down scatter also contributes from the increase in the valley portion of the fission peaks. This is the symmetric fission region where the spread in the TOF and energy should be minimal given the reaction in question. High energy, light products and low energy heavy products scattering in the electron reflection grids seem to be adding to the

increased yields in the valley region. In Figure 81, we see circled high energy particles that are unusually slow circled slow particles with long TOF like heavy products though they have the higher energy of lighter products. Since products are slowed in the system either after the TOF and before the E detector, and thus have a short TOF and small E, or before both, and thus a long TOF and small E, that combination with a long TOF and high E is harder to explain. In that vein, scattering expectations, the data point circled in Figure 89 are more than likely light and heavy products heavily scattering off the IC entrance window.

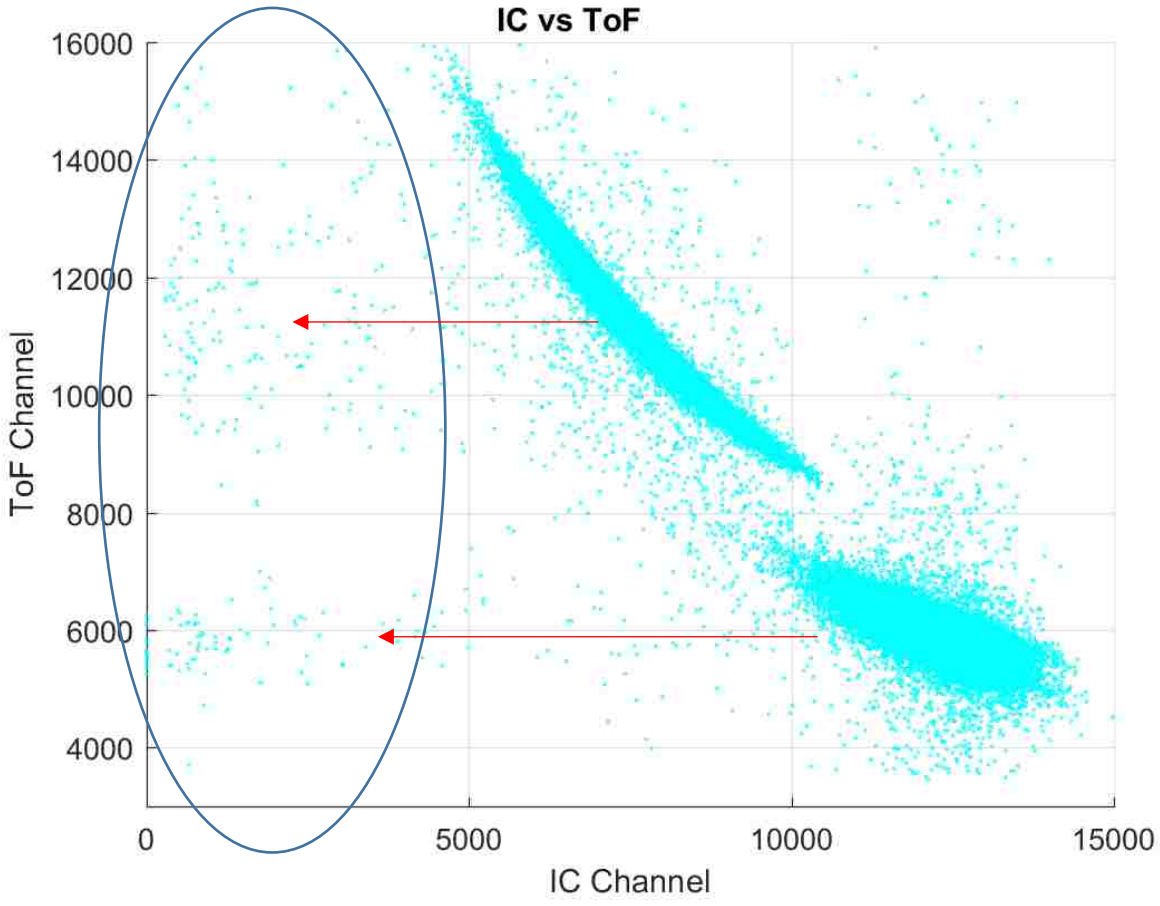

Figure 89: IC vs TOF channel as a function of mass for ^{235}U, likely large scattering events at the IC entrance window.

It is important to estimate the uncertainty due to scatter. Scatter is not homogenous over all extracted masses but without reducing scattering we must at least estimate. In regions with scatter where we expect data to be very low (for example, 0.1% or lower expected yield between peaks) the difference between our data and table values we may assume represent an average quantity of scatter, as represented in Figure 75. The average difference is used as the estimated scatter uncertainty and is added in quadrature to the other uncertainties in our mass values, and is approximately 0.18 % yield for ^{252}Cf and 0.166 % yield for ^{235}U. Using this scatter uncertainty uniformly gives the noticeable uncertainty values, even far from data points, though there is no clear alternative mode of analysis. Improvements in statistical uncertainties can come from reducing scatter. To account for the scattering contribution to the FPY distributions, the scattering variable assessed in this section has been added to the statistical uncertainty of all FPY distribution data using the root-mean-square method.

With the information on what appears to be scatter as a function of E and TOF, an attempt to make cuts on the data to "clean up" the mass distributions were performed. This process was performed simply for analysis purposes. Figure 90 shows an example of cut boundaries, or "banana gates", applied to the raw IC and TOF data.

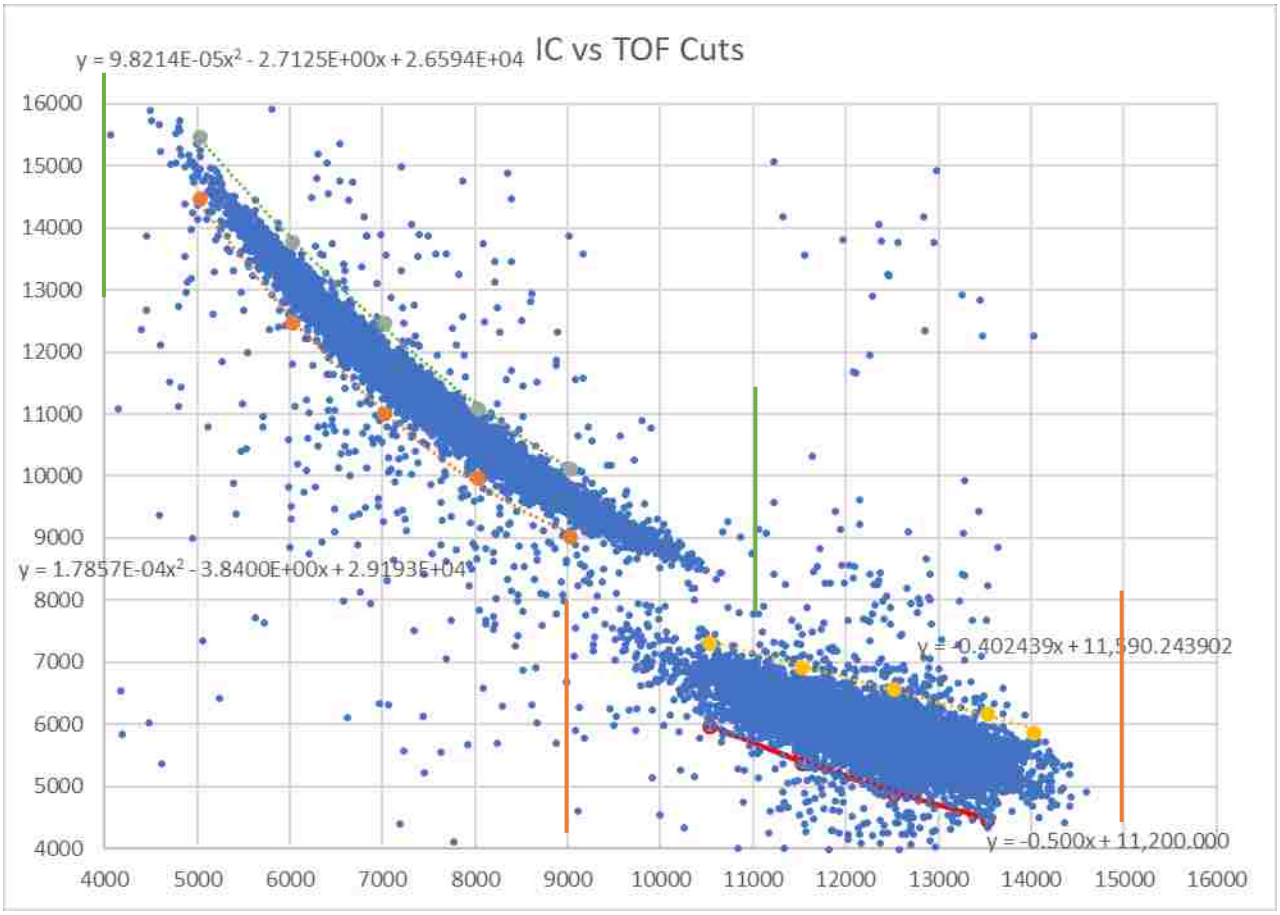

Figure 90: Cut boundaries on TOF and IC channel data. Horizontal cuts light (orange bars), heavy (green).

This process was performed simply for analysis purposes, unfortunately the very low yields (<0.001%) in the valley and peak edges reduce to 0. This isn't statistically impossible as this is approximately equal to a single count in the given bins of < 0.001% yield. The resultant yield for ^{235}U is shown in Figure 91 and 92. Without scattering taking some of the yield % from the data near the peaks, the fit to ENDF data is much better.

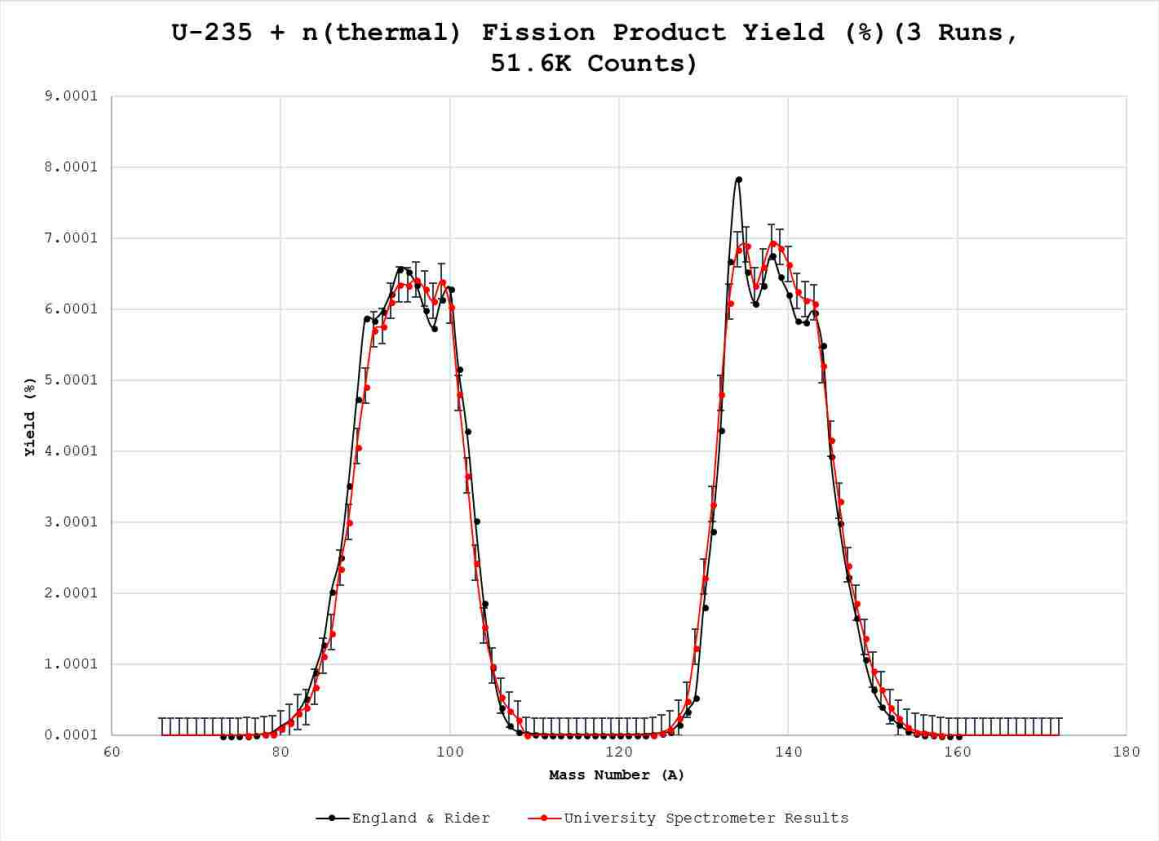

Figure 91: Linear FPY for ^{235}U cut data.

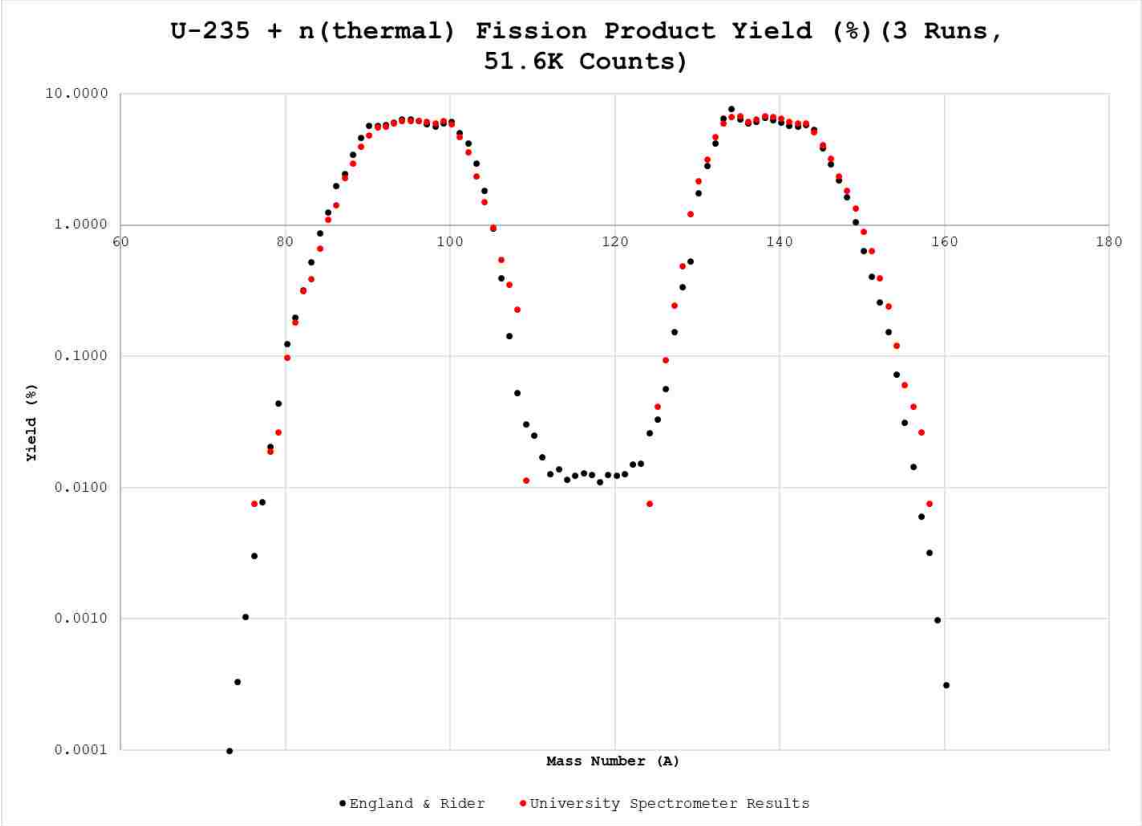

Figure 92: Logarithmic FPY for ^{235}U cut data.

Chapter 5: Range and Z Measurement Results

5.1 Range Determination

As discussed in section 3.1.3.2, the ionization chamber design functions as both an energy detector and a time projection chamber for depth of penetration measurements. The fission product ionizes the IC gas and, with appropriate gas pressure, stops within the region between the cathode and Frisch grid. The electrons immediately begin drifting towards the Frisch grid and the ions begin drifting towards the cathode, inducing a pulse in the cathode. The Frisch grid is grounded and blocks those moving electrons from inducing a pulse on the anode. Once the electrons pass the Frisch grid into the region between the Frisch grid and anode they begin to induce a pulse on the anode. By measuring the time difference between the cathode and anode signals and with known gas properties related to electron drift time in the IC, the fission product penetration range, R, can be determined following.

$$R = L - Dv_{dr} \quad \text{[Eq. 31]}$$

where L, is the length of the cathode to Frisch grid region, D is the time difference between cathode and anode signal and v_{dr}, the electron drift velocity determined section 3.1.3.2. This method is used to determine the range of ^{252}Cf and ^{235}U fission products

5.1.1 ^{252}Cf Range Determination Results

The cathode-anode time difference (ICΔt) measurements for ^{252}Cf at an IC pressure of 75 Torr and cathode voltage of 2620V show decent separation between light and heavy products, however, there is clear overlap, see Figure 93. The ICΔt is anti-correlated with the range, that is, a longer time difference corresponds to a shorter range. As expected, this also leads to an overlap of the range distribution. TRIM simulations were performed for mean light and heavy products

at the energies expected entering the IC, returning values of 7.09 cm ± 0.2 cm and 8.05 cm ± 0.16, respectively. The light products agree quite well with simulation, heavy products overestimate the range of simulation expectations by ~ 0.6 cm.

The data are correlated particle-by-particle for energy, TOF, as well as the IC time difference, so the IC time difference can be compared with energy. This makes the range or IC timing peaks much more clearly separated. The IC time difference is also compared with the measured energy, in Figure 93. Gaussian fitting parameters and associated mean values for ICΔt are shown in Figure 94.

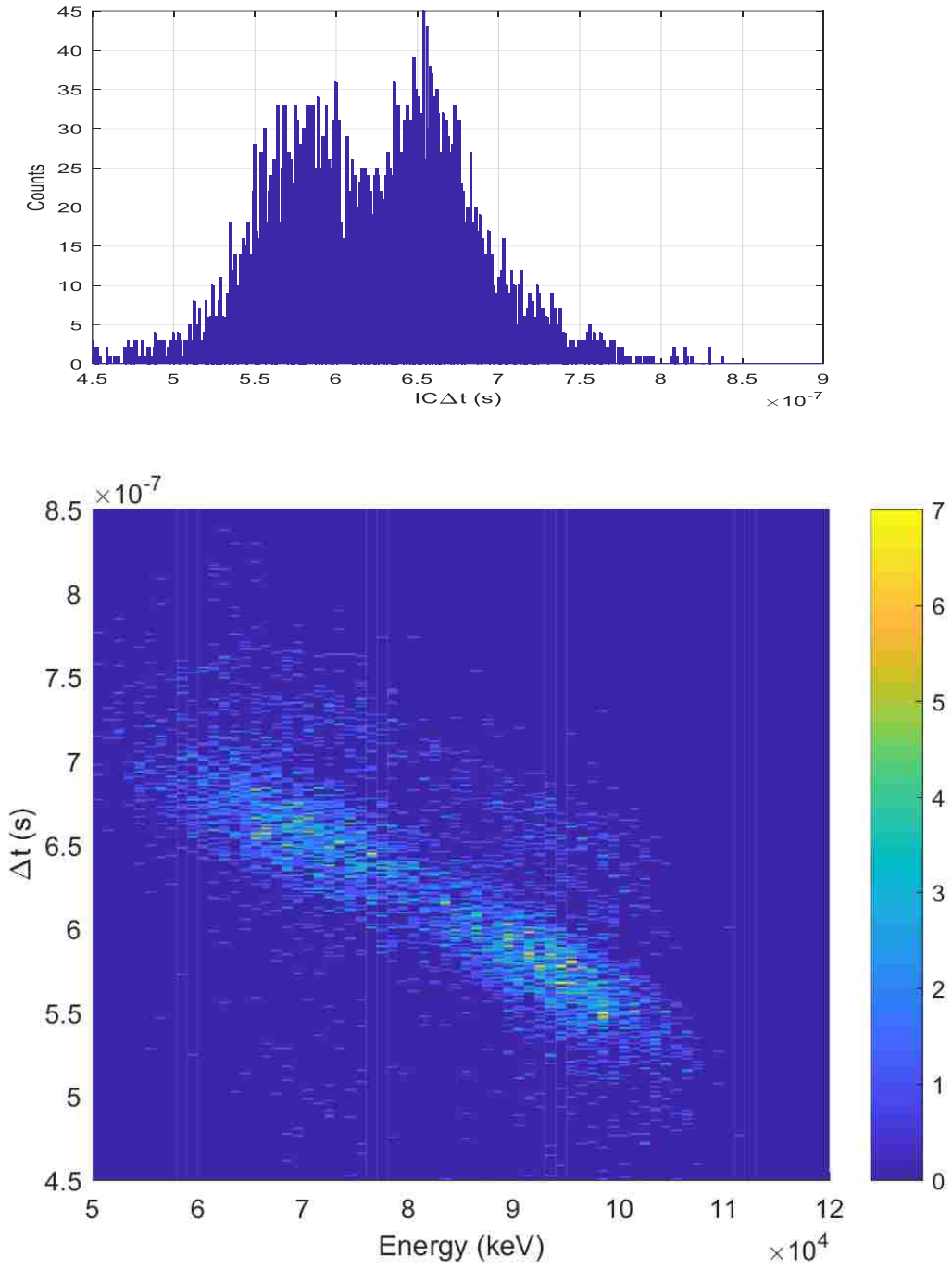

Figure 93: (top) Cathode-anode time difference distribution and (bottom) ICΔt vs E for ^{252}Cf.

General model Gauss2:

f(x) = a1*exp(-((x-b1)/c1)^2) + a2*exp(-((x-b2)/c2)^2)

Coefficients (with 95% confidence bounds):

a1 = 50.81 (49.27, 52.34)

b1 = 6.56e-07 (6.535e-07, 6.585e-07)

c1 = 4.652e-08 (4.356e-08, 4.949e-08)

a2 = 42.71 (40.85, 44.58)

b2 = 5.738e-07 (5.711e-07, 5.764e-07)

c2 = 4.077e-08 (3.775e-08, 4.379e-08)

Goodness of fit:

SSE: 5788

R-square: 0.9563

Adjusted R-square: 0.9558

RMSE: 3.423

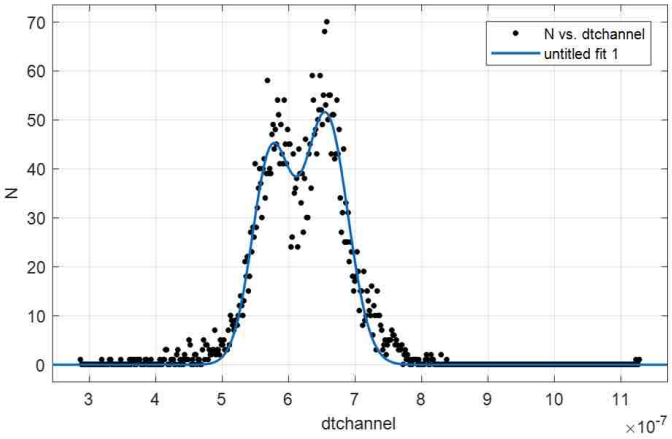

Figure 94: Gaussian fits for ICΔt timing ^{252}Cf and associated parameters.

The relationship between ICΔt and mass is expected to be directly correlated, an increase in mass should convert to lower energy and shorter range and thus an increased ICΔt. Mean values of ICΔt were extracted from the data as a function of mass shown in Figure 95.

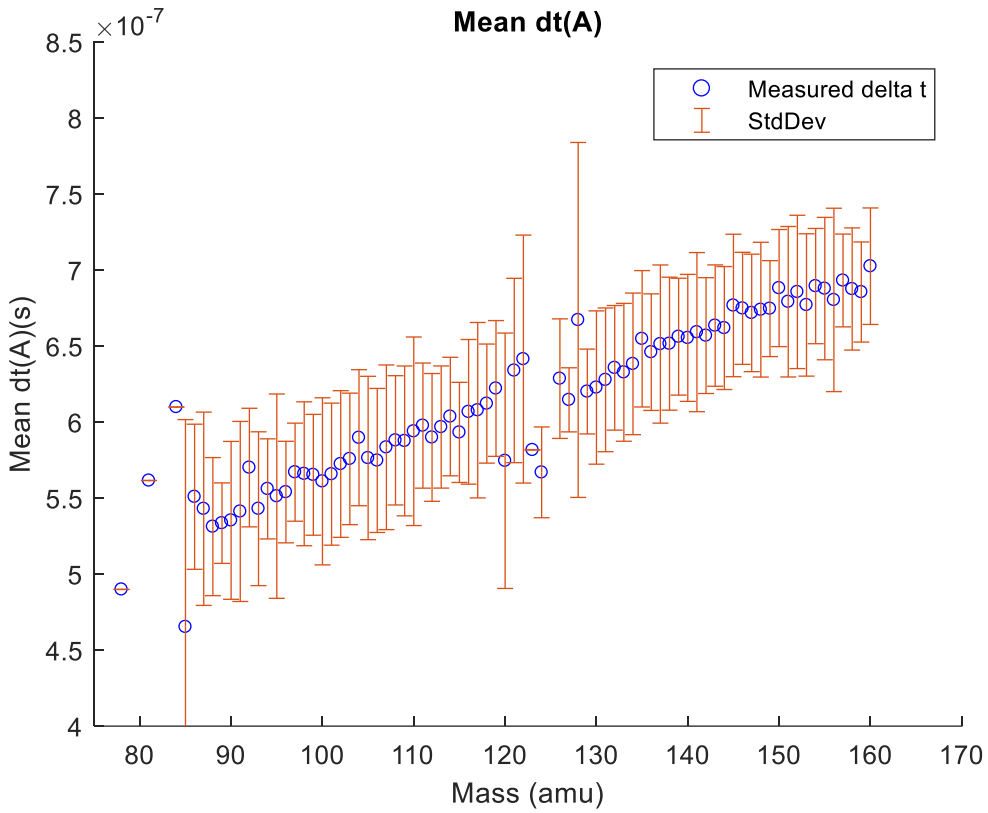

Figure 95: Mean ICΔt per product mass for ^{252}Cf

Gaussian fitting parameters and associated mean values for range are shown in Figure 96, where it can be seen it is essentially a mirror image of the ICΔt distribution as expected following the inverse relationship between range and ICΔt. This relationship can be seen in Figure 97 for the extracted values of mean range as a function mass compared with Figure 95. In Figure 97 TRIM simulated ranges are also included. While the data shows the relationship between range and mass behaves as expected, the mean range for light and heavy products are consistantly higher than the TRIM simulation results, with a larger difference for heavy products.

General model Gauss2:

f(x) = a1*exp(-((x-b1)/c1)^2) + a2*exp(-((x-b2)/c2)^2)

Coefficients (with 95% confidence bounds):

a1 = 51.79 (50.31, 53.27)

b1 = 8.258 (8.247, 8.268)

c1 = 0.231 (0.2176, 0.2445)

a2 = 44.22 (42.55, 45.88)

b2 = 8.685 (8.674, 8.697)

c2 = 0.2078 (0.1938, 0.2218)

Goodness of fit:

SSE: 5526

R-square: 0.9583

Adjusted R-square: 0.9578

RMSE: 3.345

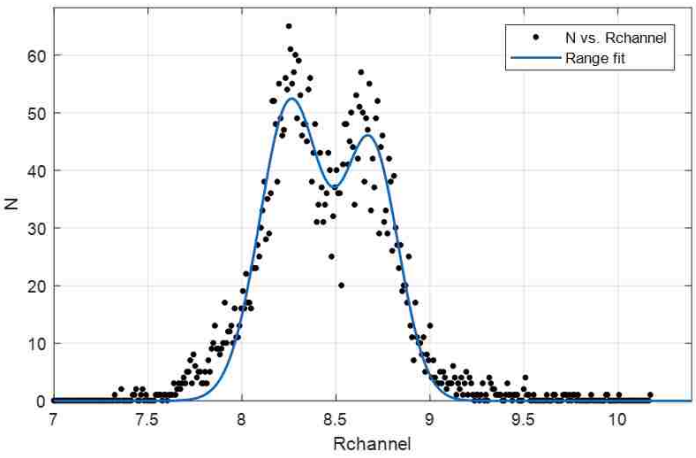

Figure 96: Range gaussian fits and means with associated uncertainties.

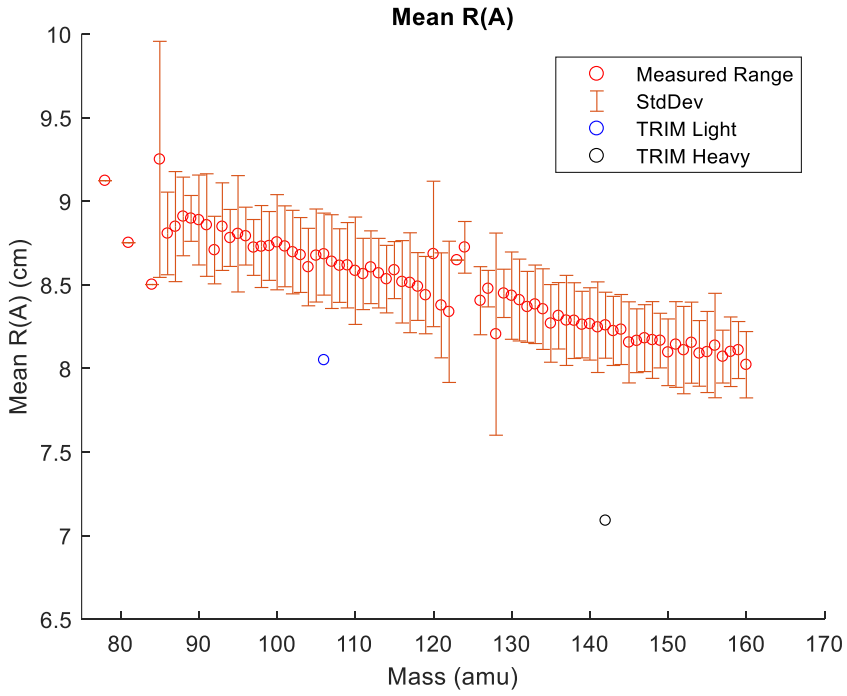

Figure 97: Mean R(A) for ^{252}Cf with mean light and heavy TRIM values.

With a total of 4,573 data points, the ^{252}Cf range experimental data suffers from large statistical uncertainties. While changing pressure, voltages, and other parameters on the IC affects the mass data only slightly, it has larger effects on the range and Z results. Since these parameters changed heavily during testing and optimization, no combined data is available, so each individual run needs to be assessed independently.

5.1.2 ^{235}U Range Determination Results

The ^{235}U ICΔt and range data show similar trends to what was seen in the ^{252}Cf timing and range analysis. Light products agree better with simulation results, in this case much better, while the heavy products tend to show a longer mean range experimentally than TRIM simulations would suggest. One difference is seen between the Cf and U ICΔt distribution, which is a more distinct peak-to-peak separation of the light and heavy products. The contour plot of ICΔt as a function of measured energy also shows more isolation between light and heavy peaks. These two results are shown in Figure 98.

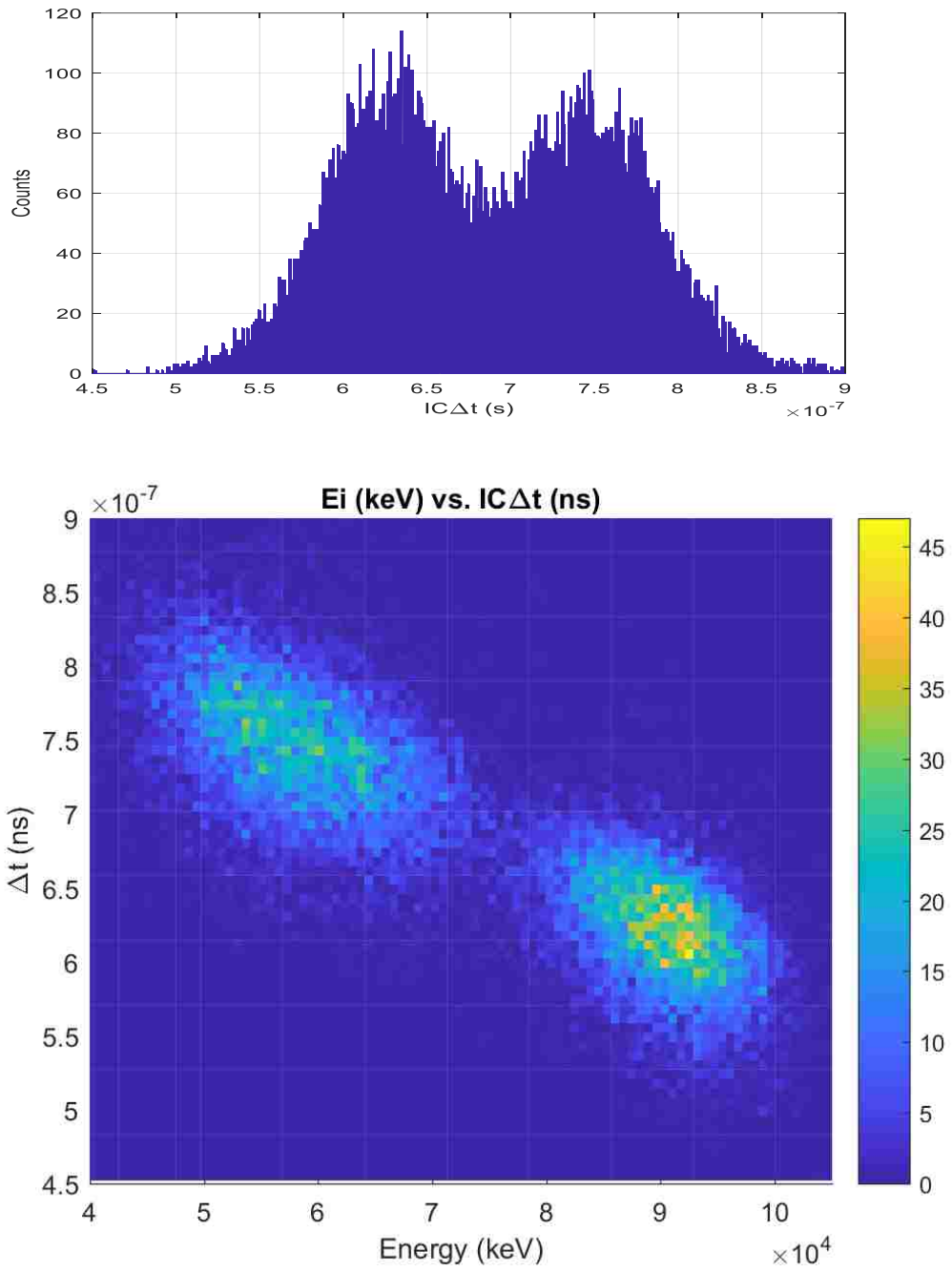

Figure 98: (top) Cathode-anode time difference, ICΔt distribution and (bottom) contour distribution for IC energy vs ICΔt (right) for ^{235}U.

The pressure was only slightly lower, 70 torr for ^{235}U as opposed to 75 torr for ^{252}Cf, but there is more separation between light and heavy ICΔt peaks. The peak-to-peak time separation

for ^{252}Cf ICΔt distributions is ~ 83 ns, while peak-to-peak time separation for ^{235}U ICΔt distributions is ~ 123 ns as seen in Figure 99. The improved timing separation should result in improved resolving power of the extracted Z values, which is the ultimate goal of the range determination.

General model Gauss2:
f(x) = a1*exp(-((x-b1)/c1)^2) + a2*exp(-((x-b2)/c2)^2)
Coefficients (with 95% confidence bounds):
a1 = 110.8 (108.9, 112.8)
b1 = 6.259e-07 (6.246e-07, 6.272e-07)
c1 = 5.743e-08 (5.563e-08, 5.922e-08)
a2 = 105.4 (103.5, 107.3)
b2 = 7.484e-07 (7.47e-07, 7.498e-07)
c2 = 5.946e-08 (5.75e-08, 6.141e-08)

Goodness of fit:
SSE: 1.751e+04
R-square: 0.9803
Adjusted R-square: 0.9801
RMSE: 5.953

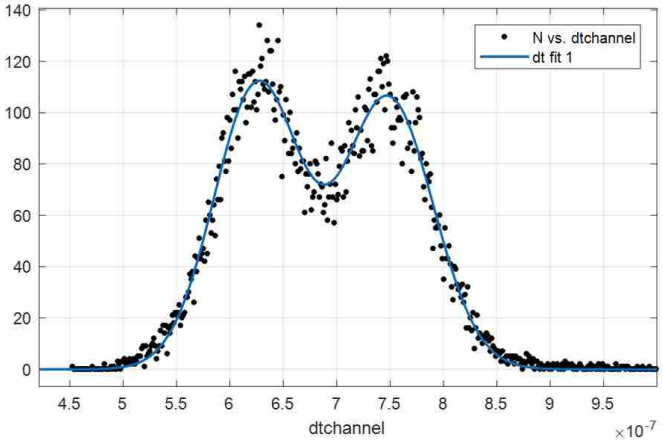

Figure 99: Gaussian fits for cathode-anode timing ^{235}U and associated parameters.

The relationship between average ICΔt as a function mass continues to behave as expected, though the slope is slightly increased with the ^{235}U data as shown in Figure 100.

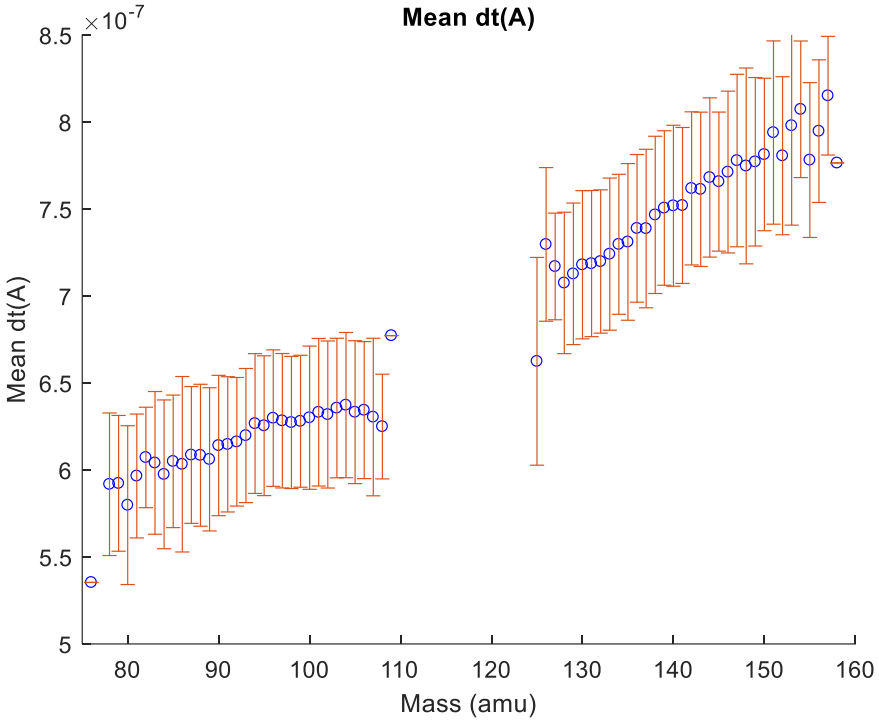

Figure 100: Mean ICΔt as a function of mass product mass for ^{235}U.

A steady increase in ICΔt with an increase in mass is seen with clear separation between light and heavy products ICΔt. This should lead to well separated range distribution as shown in Figure 101, with gaussian fitting parameters and mean values extracted in Figure 102.

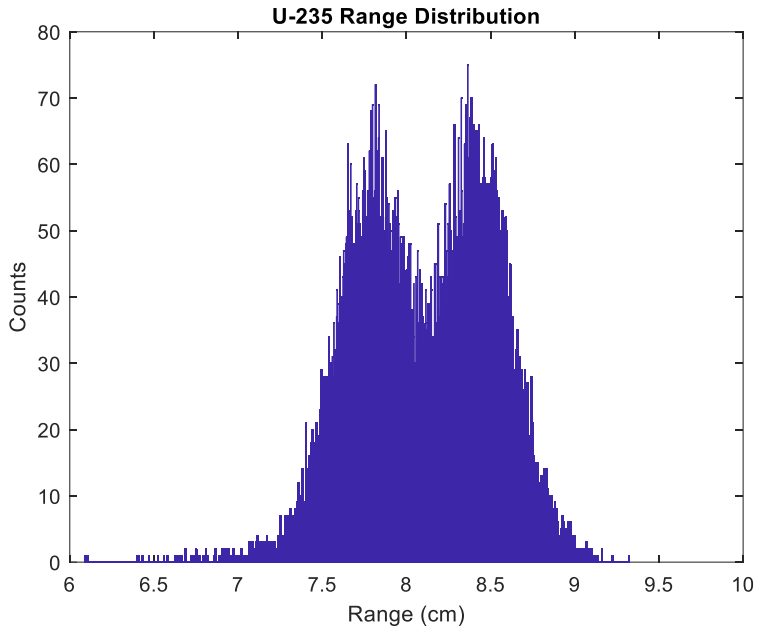

Figure 101: ^{235}U fission product range distribution at an IC pressure of 70 torr and cathode voltage of 2500V.

General model Gauss2:
f(x) = a1*exp(-((x-b1)/c1)^2) + a2*exp(-((x-b2)/c2)^2)
Coefficients (with 95% confidence bounds):
a1 = 112.8 (110.7, 114.9)
b1 = 8.427 (8.42, 8.434)
c1 = 0.2855 (0.2763, 0.2946)
a2 = 106.7 (104.6, 108.7)
b2 = 7.792 (7.785, 7.8)
c2 = 0.3077 (0.2973, 0.318)

Goodness of fit:
SSE: 2.013e+04
R-square: 0.9774
Adjusted R-square: 0.9772
RMSE: 6.384

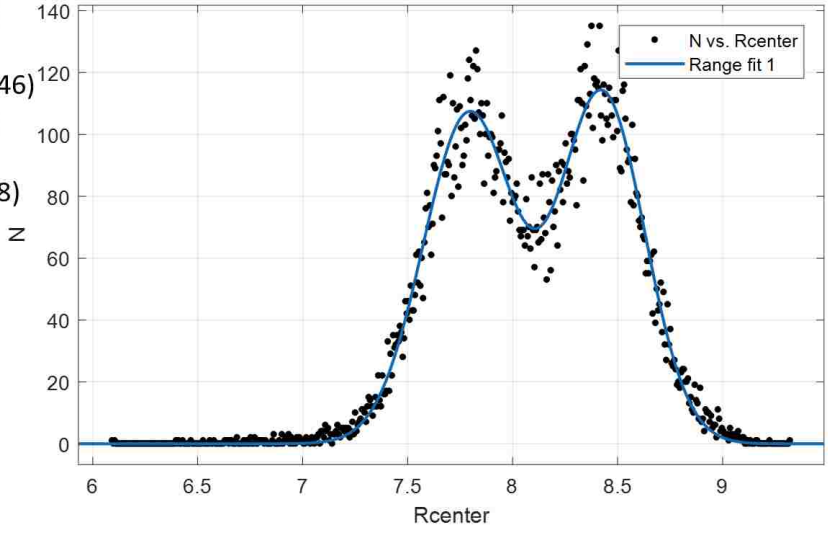

Figure 102: Gaussian fits for ^{235}U fission product range distribution and associated parameters.

TRIM simulations were performed for mean light and heavy products at the expected energies for ^{235}U fission products entering the IC, returning values of 7.41 ± 0.2 cm and 8.53 ± 0.15 cm, respectively. This is shown in Figure 103, with the mean light or heavy fragments calculated in TRIM each represented by a single point, presented against the measured values.

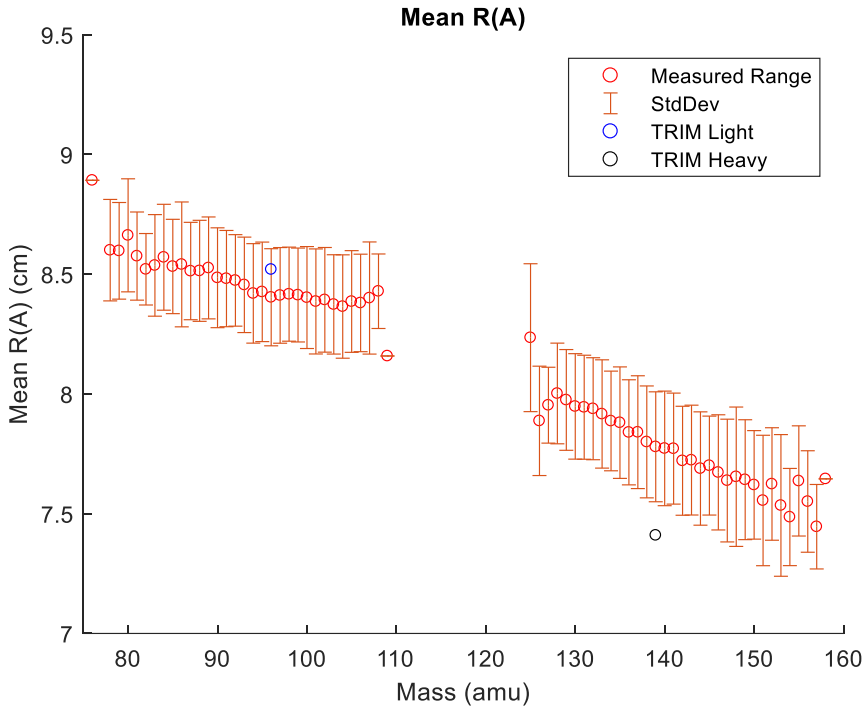

Figure 103: Mean range as a function of product mass for ^{235}U.

Mean range values as a function of mass follow the trend that we would expect, as mass increases energy and velocity decreases, leading to negative slope in the data. Like the ^{252}Cf data, the timing measurement for heavy products for ^{235}U show a higher range than expected from the TRIM calculation. Figures 104 – 107 show the range distributions for each individual mass, A.

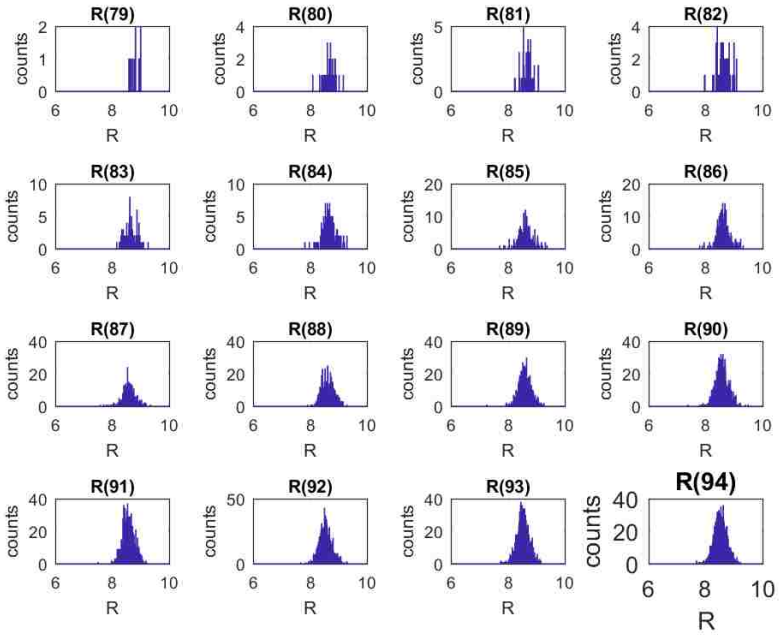

Figure 104: Range distribution as a function of product mass for ^{235}U (A = 79-94).

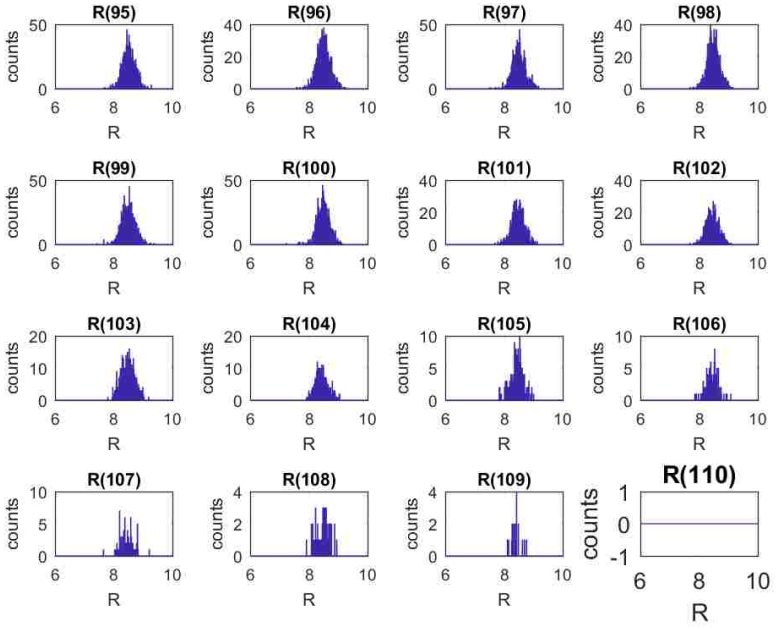

Figure 105: Range distribution as a function of product mass for ^{235}U (A = 95-110).

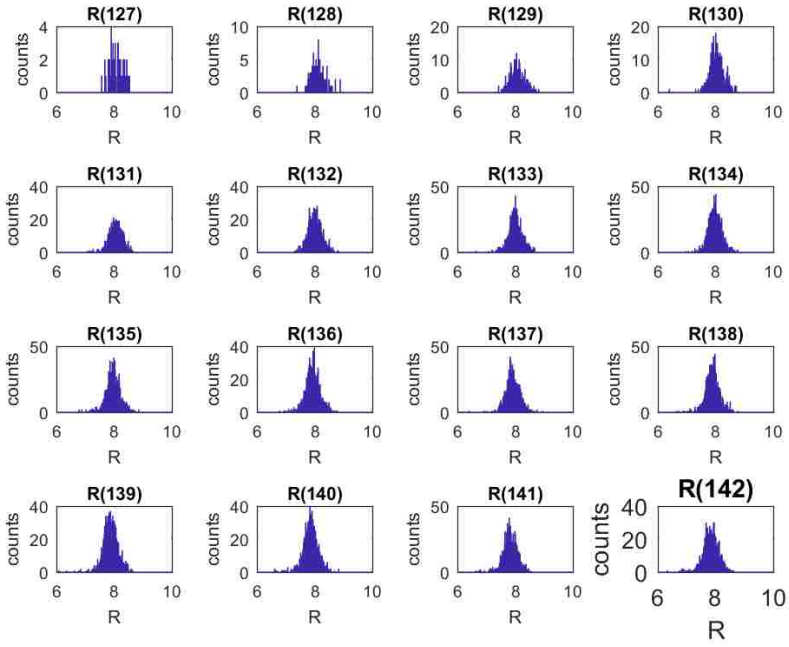

Figure 106: Range distribution as a function of product mass for ^{235}U (A = 127-142).

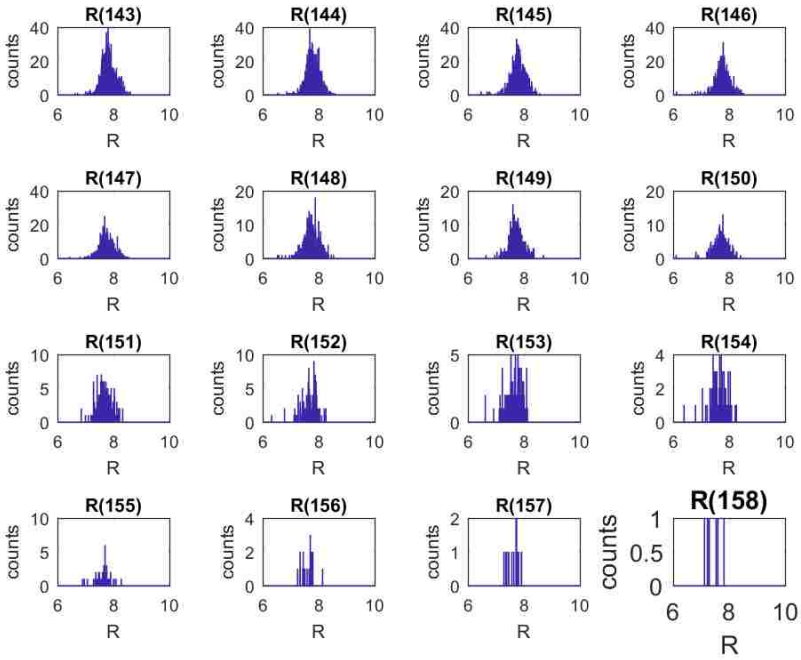

Figure 107: Range distribution as a function of product mass for ^{235}U (A = 143-158).

Similar to the ^{252}Cf range data, we see experimentally in Figure 103 the heavy products penetrating deeper into the IC than expected in TRIM simulation, though the light fragments are a closer match. There are several reasons contributing to the cause. For the same atomic number Z TRIM may calculate a different atomic charge state, and thus stopping power, then seen experimentally. Alpha particles are very well characterized and modeled in TRIM, though there is much less data to guide the models for fission products. It could also have to do with pulse shape differences between heavy and light products and their resultant time pick-offs in the CFD.

The ^{235}U range and timing data were taken at a lower pressure of 70 torr and cathode voltage of 2500V than the ^{252}Cf data taken at a pressure of 75 torr and 2620V. The lower pressure seems to lead to a better separation of timing and range peaks, this should be taken into consideration for future run cycles. With ~ 3 cm to spare in the cathode to Frisch grid region, the pressure could be lowered further to gain increased peak separation. Lower pressure would allow for more distance separation between high penetrating and low penetrating fragments. The electric field to pressure ratio, E/P, is kept somewhat constant, ~3.49 to 3.57, so the accelerating field would be lower which would reduce the drift velocity, but there is less resistance to motion in a lower pressure chamber which may increase that drift velocity. More work in this area is needed to fully understand the relationship between IC timing and range, especially for heavy products.

5.3 Z determination

A new method of Z identification was employed for the determination of the fission product atomic number. To remain consistent with our previous simulation comparisons, TRIM was used to draw a relation between E, A, Z, and R. While E, A, and R could be determined through measurement, Z could perhaps be extracted through relationships between those

variables. TRIM simulations were performed to extract relationships. Central values of E, A, and Z were chosen to represent light fragments, noted as E_0, A_0, and Z_0, and the associated range, noted as R_0. This was repeated for heavy fragments. One variable was varied while the others were held at their central value and the range, or rather the difference from R_0, as a function of that free variable was extracted. In Figure 108 for ^{252}Cf, results with a variation in A, Z, and E from the central values are presented on the x axes, and the resulting change in R from the central value presented on the y axes. This is repeated for ^{235}U in Figure 109. The spreads in A, Z, and E values, represented in the spreads in dA, dZ, and dE values, cover most of the spreads seen in table values.

The relationship between Z and R for a constant E and A (and thus starting velocity in the gas) makes sense, a higher Z should have a larger effective atomic charge going through the gas and interact more, leading to a shorter range. This also makes sense for the relationship between E and R, as a lower energy for the same Z and A should have a shorter range. The A results though are puzzling; for a constant Z and E, an increasing A (and thus decreasing velocity) appears to increase the range. This occurs for all the TRIM calculations presented in Figures 108 and 109. For consistency we stay with TRIM results, though this surely will affect Z determination. The solution, of course, is experimental calibration with a known beam with nuclides and energies similar to fission products but this was not possible for this project.

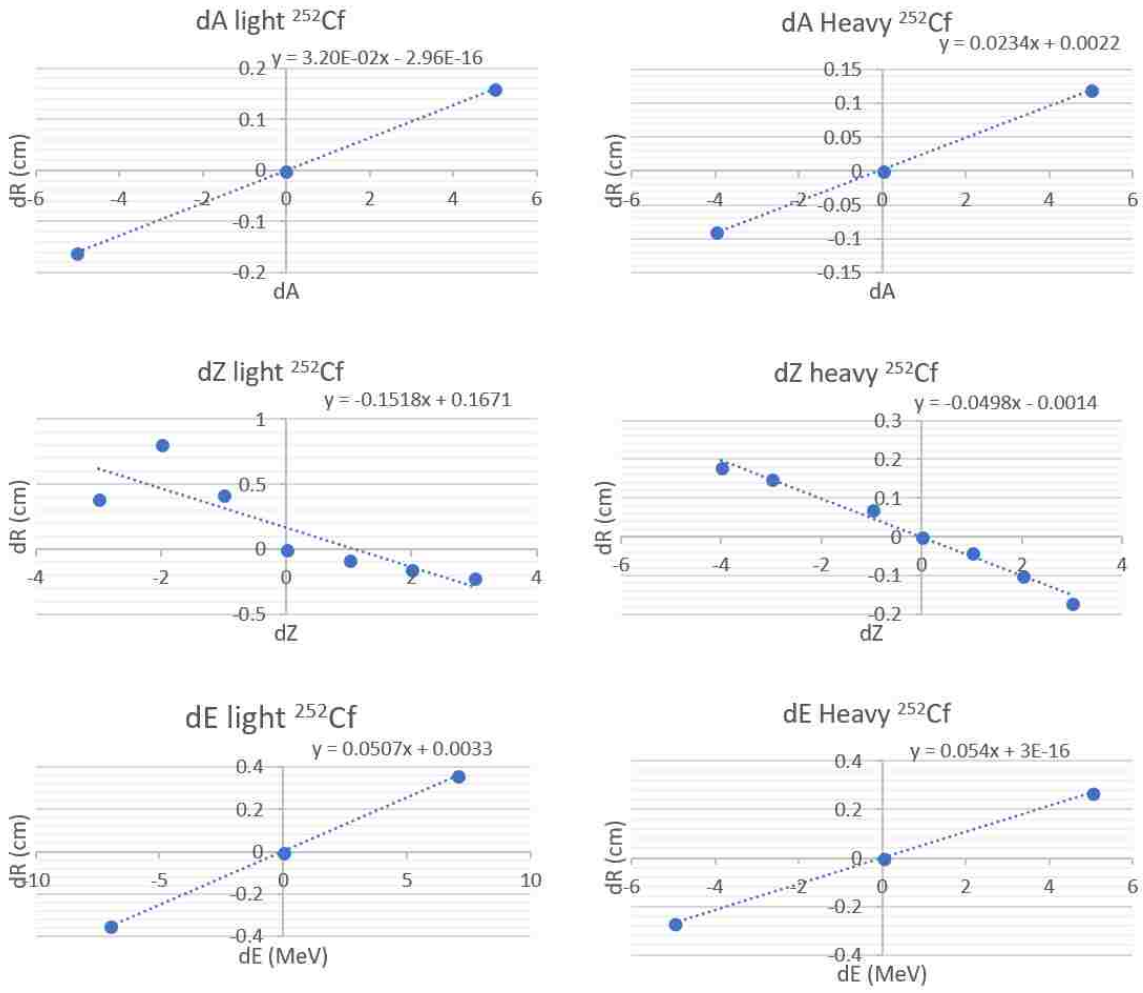

Figure 108: Functions relating perturbations of energy, mass and Z in relation to range for ^{252}Cf.

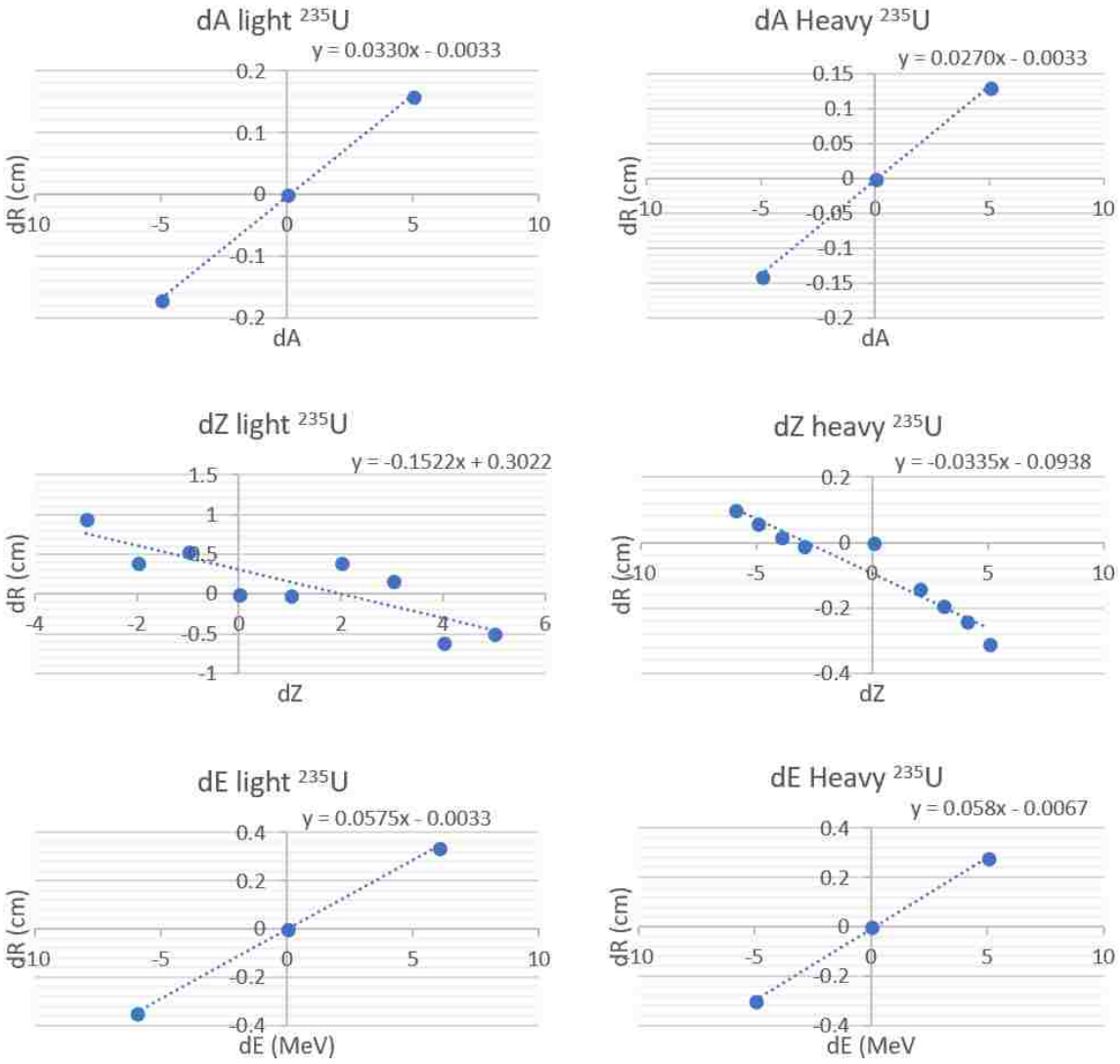

Figure 109: Functions relating perturbations of energy, mass and Z in relation to range for ^{235}U.

A relationship can then be formulated to determine the product Z based on how the values of detected products deviate from the mean. For simplicity we are using a linear relationship, which looks reasonable in the plots. We also assume independence between the variables and their effect on range. Using the linearly independent relationships gives us an equation relating the change of range with the perturbations in energy, mass and Z.

$$dR = C_1 dE + C_2 dZ + C_3 dA + C_4 \quad \text{Eq. 32}$$

where $C_{1\text{-}3}$ are the slope constants for each relation and C_4 is the summed intercepts. We can then solve for the above in terms of dZ.

$$dZ = \frac{dR - C_1 dE - C_3 dA - C_4}{C_2} \quad \text{Eq. 33}$$

Again, dR = R - R_0 and likewise for the other parameters. The Z value then is extracted as Z_0 + dZ for a given E, A, and R. This equation is unfortunately very sensitive, and small changes in constants can make extracted Z values change greatly. Separate relations are generated for light and heavy products based on the relations found in Figure 108 or 109 depending on the source.

For the perturbation method to work correctly, the means used need to line up well. Measured means for mass and energy line up well with expected values. However, the range for heavy products falls outside the expected mean, therefore we will use the measured range in this case for R_0. Light product ranges line up well with the expected mean range calculated from TRIM, thus the TRIM expected mean for light product range will still be used.

5.3.1 ^{252}Cf Z distribution

Applying the R, E, Z, A relations derived in section 5.3 for the ^{252}Cf data, we find fairly good agreement between measured Z distributions and published data from ENDF/B-VII, particularly for the light fragments. The raw Z distribution and gaussian fitting parameters are presented in Figure 110 and 111, respectively, and in relation to ENDF/B-VII yield values in Figure 112.

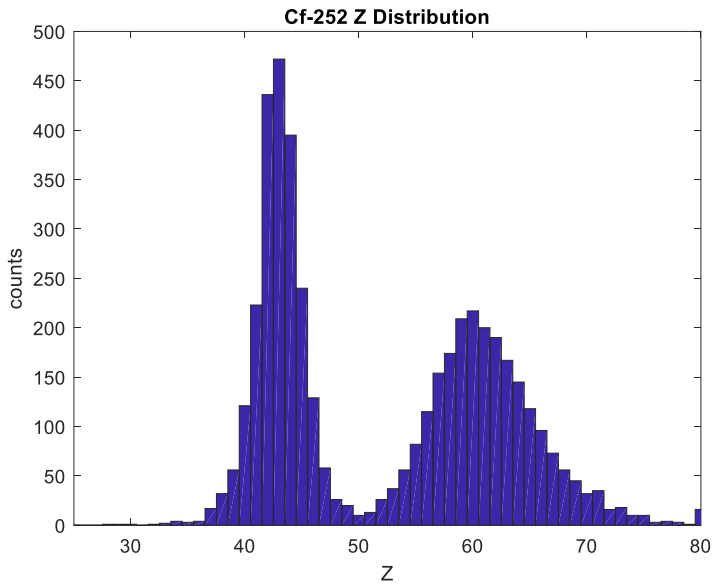

Figure 110: Raw Z distribution for ^{252}Cf.

General model Gauss2:
f(x) = a1*exp(-((x-b1)/c1)^2) + a2*exp(-((x-b2)/c2)^2)
Coefficients (with 95% confidence bounds):
a1 = 158.4 (156, 160.8)
b1 = 43 (42.97, 43.03)
c1 = 2.544 (2.499, 2.588)
a2 = 68.74 (67.21, 70.27)
b2 = 60.63 (60.52, 60.75)
c2 = 6.233 (6.073, 6.393)

Goodness of fit:
SSE: 4664
R-square: 0.9851
Adjusted R-square: 0.9849
RMSE: 3.073

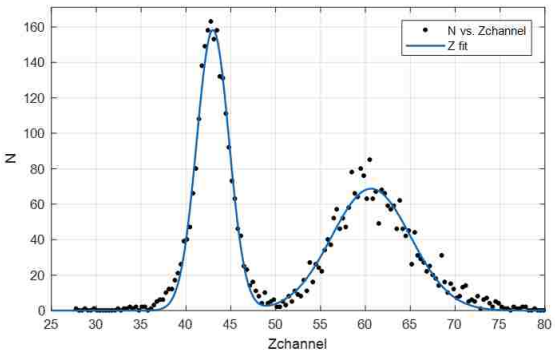

Figure 111: Z distribution gaussian fits with mean values calculated for ^{252}Cf Z distribution.

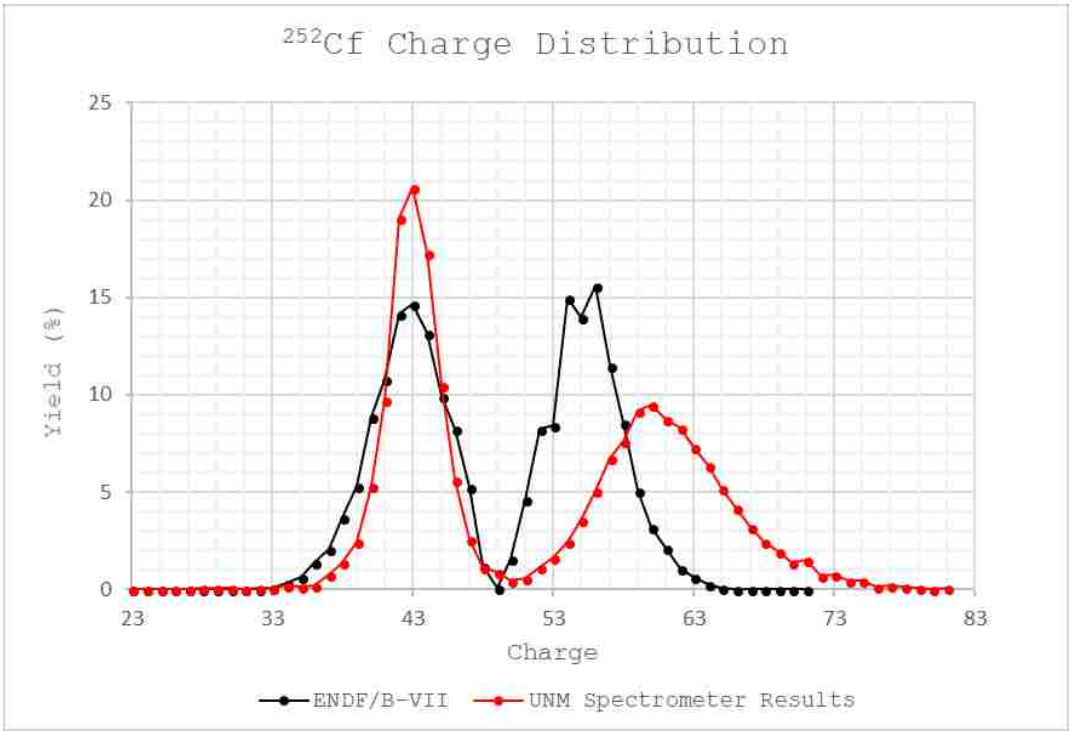

Figure 112: Measured Z distribution for ^{252}Cf compared with ENDF/B-VII.

The heavy product portion of the Z distribution is clearly broadened and shifted towards higher Z than expected as can be seen in Figure 112 when compared to ENDF/B-VII published values. Looking at the mean Z as a function of mass values offers more insight into what could potentially be contributing to the peak spreading and narrowing with the Z distributions. Looking at the Z, energy and mass relationships with range from Figure 108 and 109, we see that the energy has the largest effect on range, as seen in the largest slopes. Recalling the plot of kinetic energy as a function of mass, Figure 74, we notice that the light product average kinetic energy per mass stays relatively constant, while the heavy products exhibit large differences in average kinetic energy. The Z extracted is a sensitive function of the variables and this leads to a large change from the mean Z value for heavy products. On the other hand, the smaller spread of energy in the light product masses leads to a narrower extracted Z distribution in.

As mentioned, another surprising result from the TRIM simulations was the increase in range with the increase in mass. With an increase in mass and energy held constant, the velocity should decrease. This was expected to lead to a decrease in range. However, according to TRIM simulations, range decreases with mass. The increase to the range due to increased mass is the smallest contributor in our relation. However, it still seems to contribute to the broadening of the heavy product region of the Z distribution. Figure 113 shows the relation between mass and the extracted Z for the ^{252}Cf Products which consist of a spread of A, E, and Z. Even with the other variables, the inverse Z-A relation in the heavy fragments is still apparent in the downward slope of Z vs A for heavy fragments, and a reduction in upward slope for the light fragments.

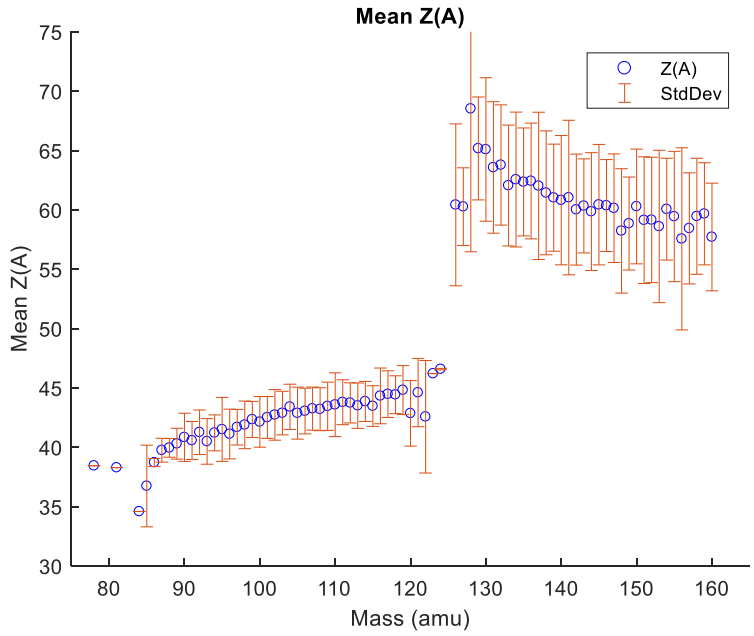

Figure 113: Mean Z as a function of mass values for ^{252}Cf.

As mentioned previously, the broad range of energies for the heavy products leads to an unexpected decrease in the mean Z per mass in the heavy product region of the distribution. This

effect of the perturbation method on the determination of Z distributions needs to be further investigated. Figures 114-116 show individual Z distributions for each mass.

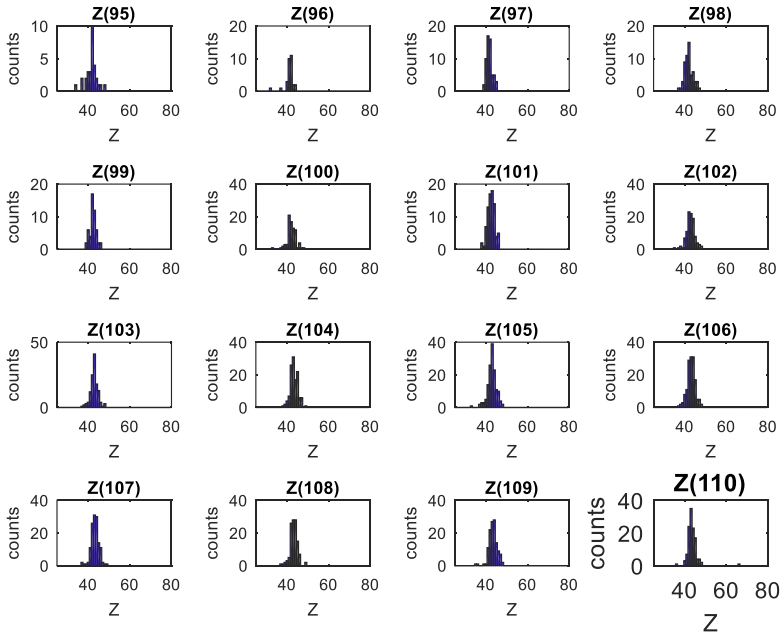

Figure 114: Z distributions for individual masses (A = 95 – 110) for ^{252}Cf.

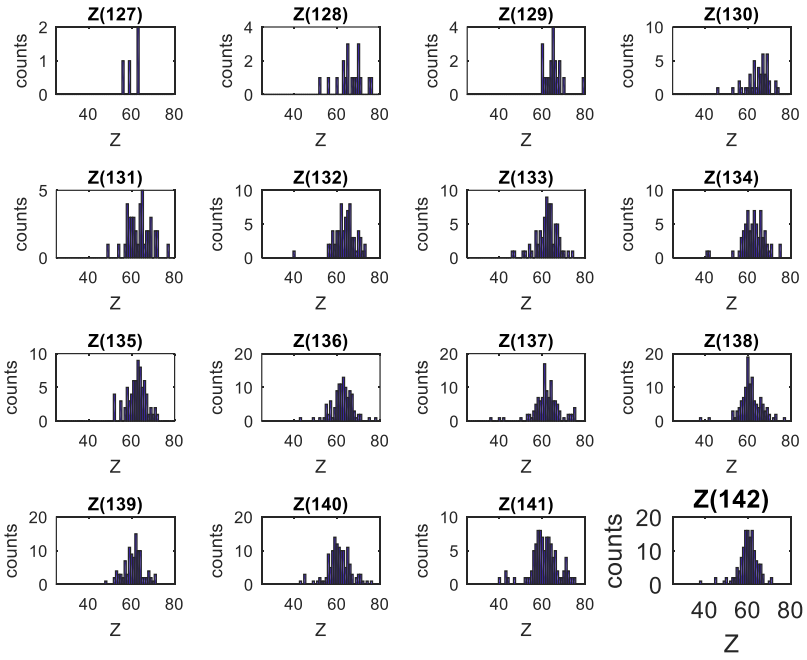

Figure 115: Z distributions for individual masses (A = 127 – 142) for ^{252}Cf.

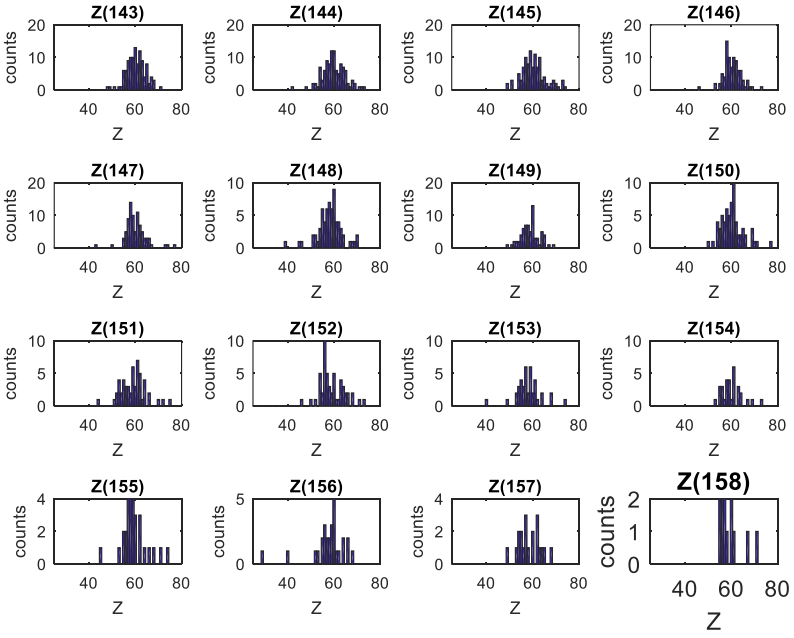

Figure 116: Z distributions for individual masses (A = 127 – 142) for ^{252}Cf.

The ^{252}Cf data suffers from low statistics; a total of 4,573 counts in the Z distribution leads to a large statistical uncertainty. The uncertainty in Z is not assessed in this work however, as can be seen in the Z distribution for each mass in Figures 114, 115 and 116, we see Z is quite broad, particularly for the heavy products. The number of neutrons can be determined after Z is determined, and contour plots illustrate clearly the spread of the heavy products in Figures 117 and 118 for N as a function of Z, N as a function of A, and Z as a function of A. The A/Z data is another representation of the information in Figure 113. Not only would the heavy product distribution benefit from a more sensible A-R relationship. A higher slope in the A/Z data for the light products, which may occur with more a sensible A-R relationship, would produce a more diagonal slope in the light products for the N/Z plot which is closer to ENDF data.

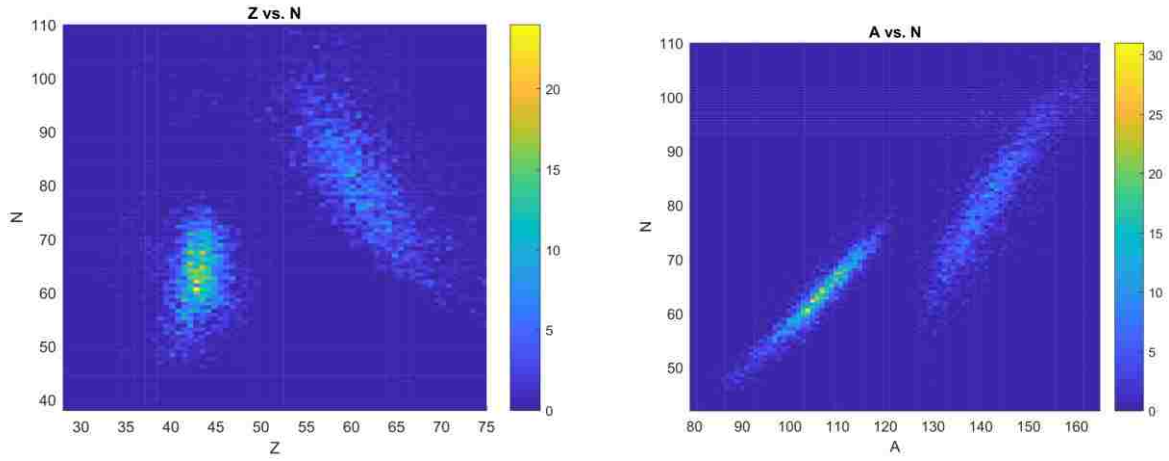

Figure 117: Calculated N/Z and A/N data for ^{252}Cf.

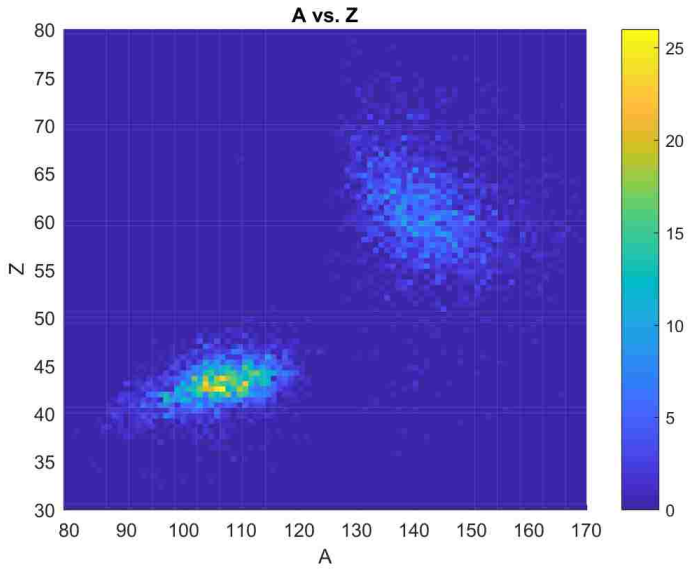

Figure 118: Measured A/Z data for ^{252}Cf.

5.3.2 ^{235}U Z distribution

Though the Z data is more statistically significant for ^{235}U, the Z distributions suffer from similar issues experienced with the ^{252}Cf Z distribution data. While the light product the Z distribution is similar to that from published data from ENDF/B-VII; the heavy product distribution shows the same broadening seen with the ^{252}Cf Z distribution data. The Z distribution for ^{235}U and gaussian fitting parameters are shown in Figure 119 and 120, respectively.

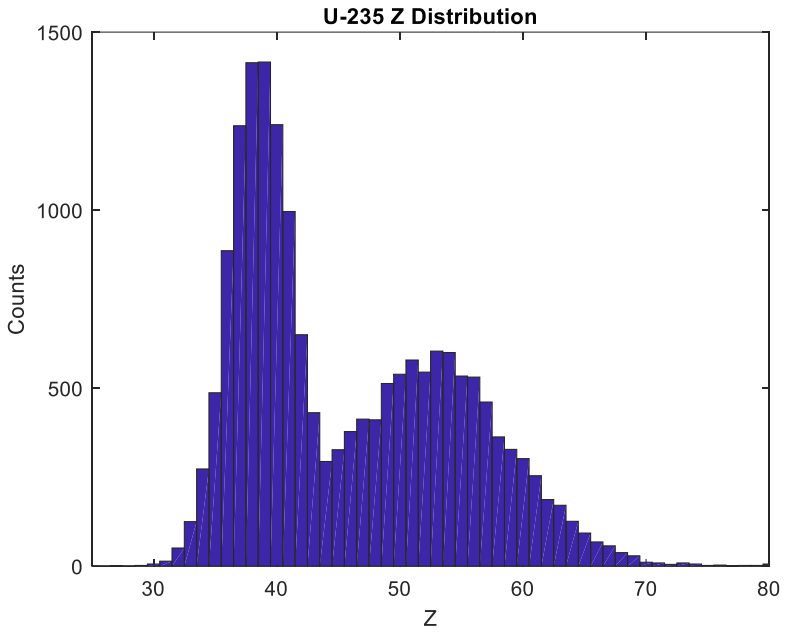

Figure 119: Raw Z distribution for ^{235}U.

General model Gauss2:
f(x) = a1*exp(-((x-b1)/c1)^2) + a2*exp(-((x-b2)/c2)^2)
Coefficients (with 95% confidence bounds):

a1 =	192.2	(189.6, 194.8)
b1 =	38.48	(38.44, 38.52)
c1 =	3.428	(3.37, 3.487)
a2 =	78.74	(77.15, 80.33)
b2 =	52.63	(52.46, 52.79)
c2 =	8.939	(8.678, 9.199)

Goodness of fit:
SSE: 1.673e+04
R-square: 0.9862
Adjusted R-square: 0.986
RMSE: 5.82

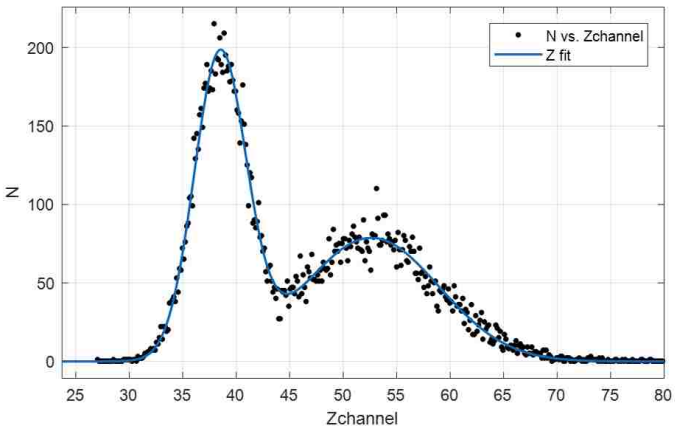

Figure 120: Z distribution gaussian fits with mean values calculated for ^{235}U Z distribution.

Average Z as a function of mass calculations for ^{235}U show similar issues found with the data on ^{252}Cf average Z for each mass. While the light product peak behaves as expected with a positive increase in average Z with increased mass, we see the opposite effect with the heavy

product average Z for each mass slope with increasing mass values as shown in Figure 121. This again is more than likely attributed to the substantial role deviations in energy perturb the Z value in our Z determination method. Effects on determination of Z follow, with an underestimation of Z leading to an overestimation of N for a given mass.

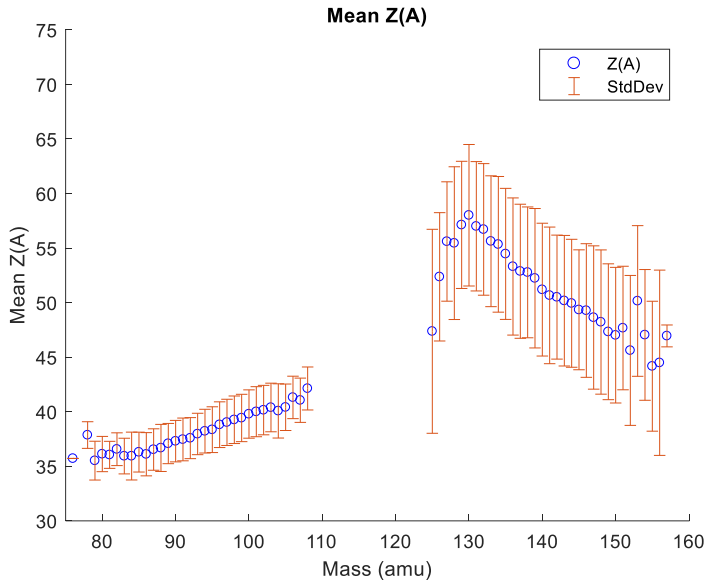

Figure 121: Mean Z for each mass value for ^{235}U.

Comparing the ^{235}U Z distribution to ENDF/B-VII values, we see in Figure 122 the light product peak in good agreement, but lacking details in the peak artifacts. The England and Rider data from ENDF/B-VII relys heavily on interpolation utilizing modelling based on Wahl [6], which leads to a large uncertainty in the published values.

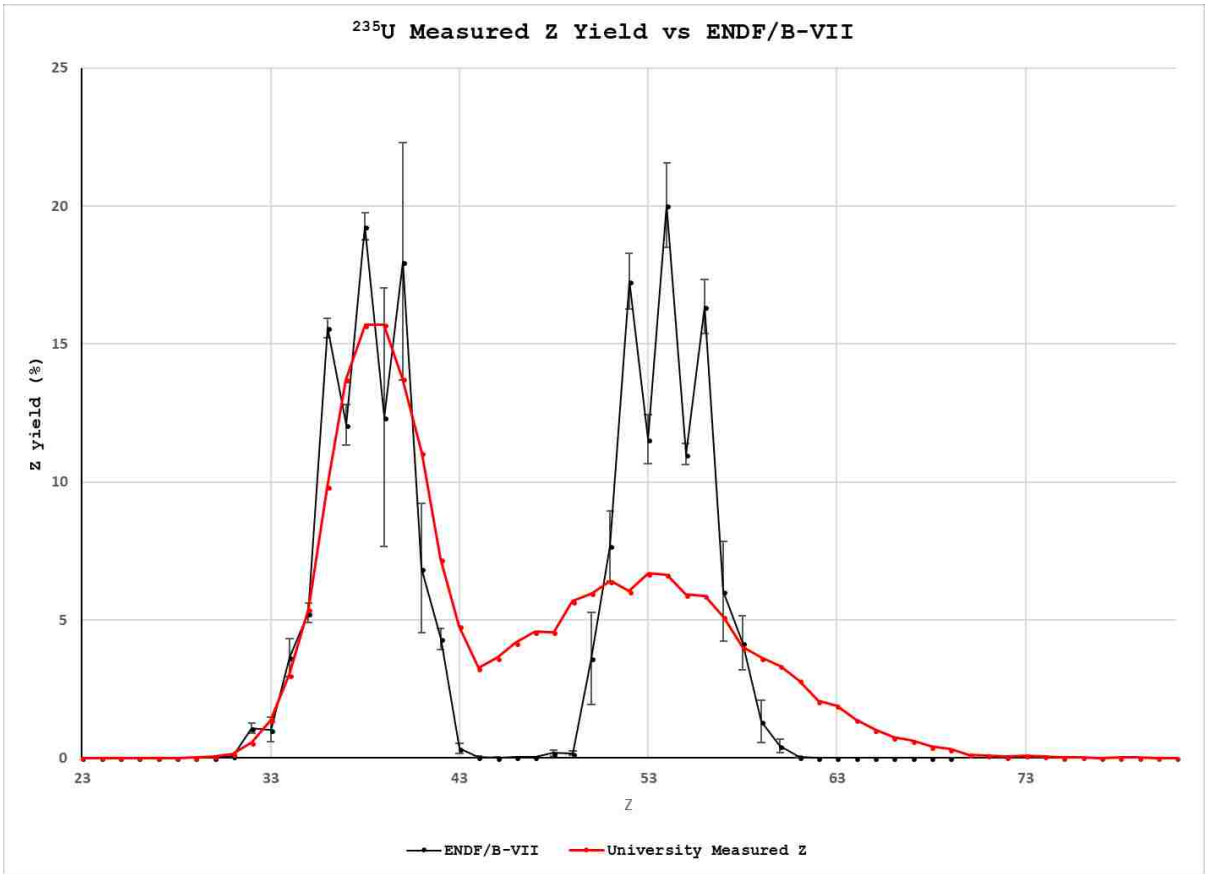

Figure 122: Measured Z distribution for ^{235}U compared with ENDF/B-VII.

Different run parameters were used for different experimental data acquisition periods to find an optimum. Combining the runs for mass determination is straightforward, but different IC pressures makes combining data sets difficult for Z determination. Longer runs, would be useful to smooth out our Z yield distribution for better assessment of peak widths. Since optimal operation parameters have primarily been determined, this can be a more primary focus of future LANSCE run cycles.

Prior work on Z determination was performed by Tyukavkin *et al*. [12] by extracting range in their ionization chamber, though they used an external detector as the start signal. Our mean Z values measured for ^{235}U agree well with previous work by Tyukavkin *et al* [12] and Lang *et al* [53] as seen in Table 20 and Figure 123.

Table 20: Mean Z value comparisons with previous experiments [12, 53].

	This Work	Tyukavkin 1	Tyukavkin 2	Lang
Mean Z Light	38.48	38.18	38.22	37.92
Mean Z Heavy	52.63	52.26	53.02	53.92

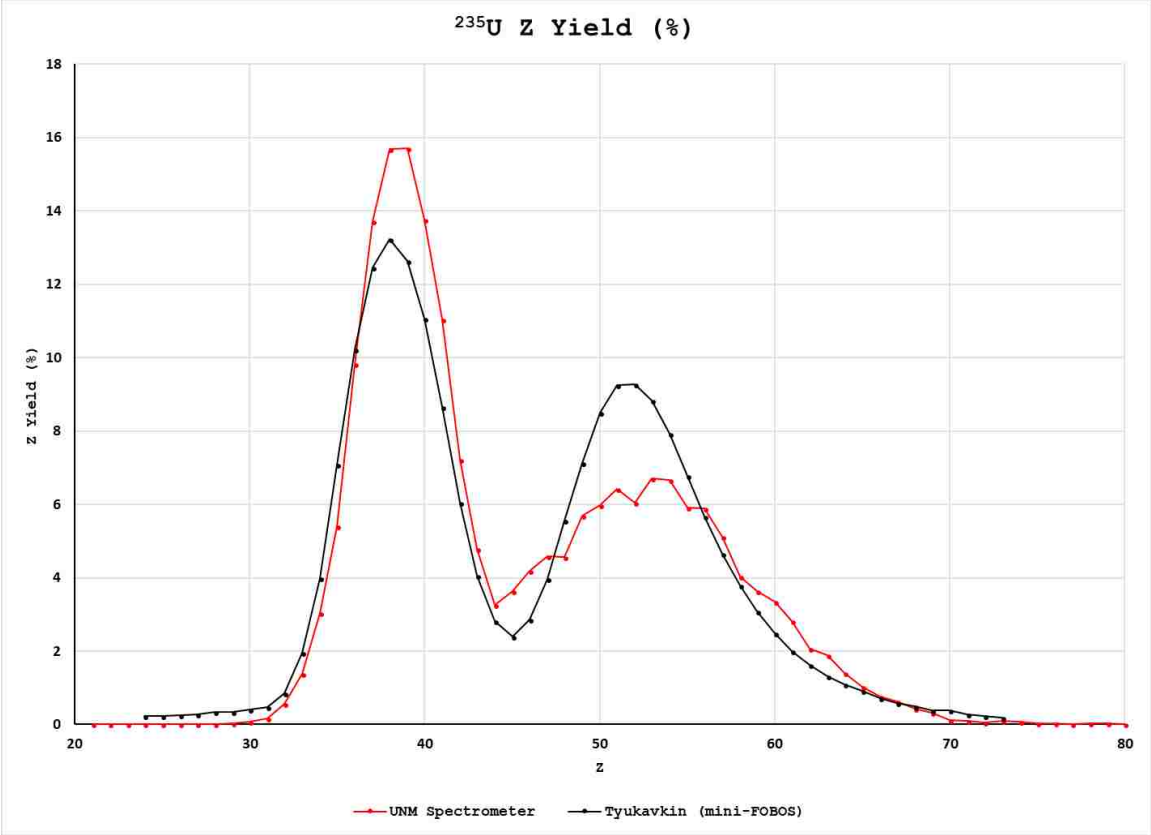

Figure 123: UNM measured Z distribution compared with Tyukavkin *et al*. [12].

Looking at the Z distributions for individual mass values, we again see expected increases in mean Z values and narrow widths in the light product region. The heavy products show the opposite, the lighter side of the heavy region ~ A = 128 relates to the highest Z values and decreases as mass increases. The heavy product Z distributions are quite broad, but the inverse trend of average Z decreasing as mass increases can clearly be seen. Figures 124 – 127 show Z distributions for each mass, A, for A=79 to 158.

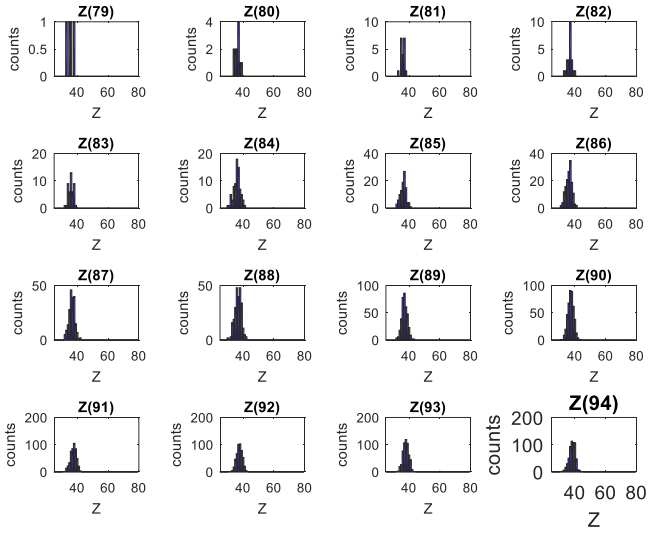

Figure 124: ^{235}U Z distributions for individual masses (A = 79 – 94).

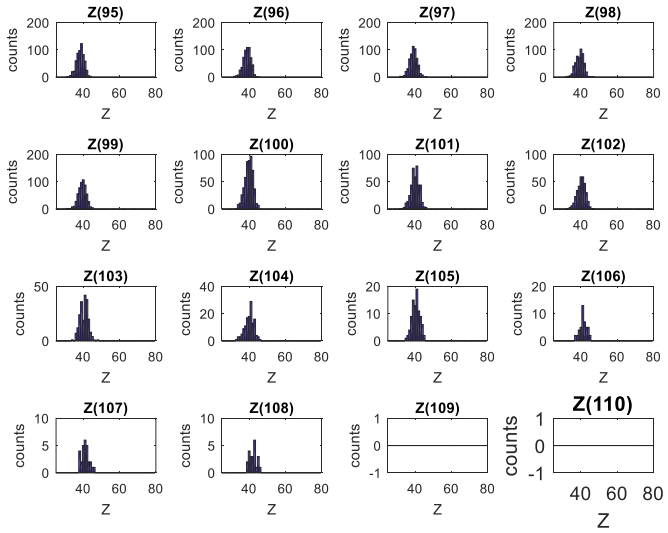

Figure 125: ^{235}U Z distributions for individual masses (A = 95 – 110).

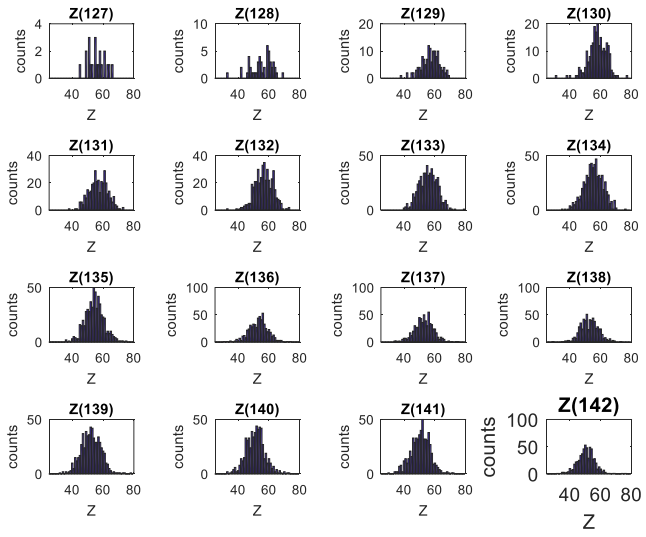

Figure 126: ^{235}U Z distributions for individual masses (A = 127 – 142).

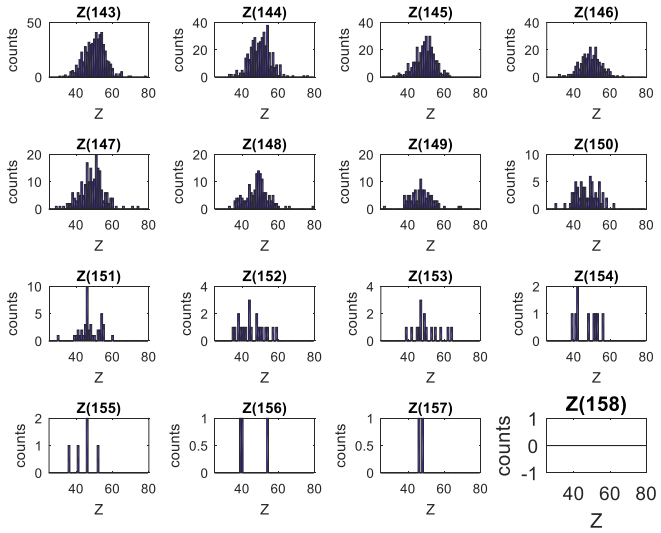

Figure 127: ^{235}U Z distributions for individual masses (A = 143 – 158).

Calculating the number of neutrons using the Z and mass data for each particle, shows the broad distribution of atomic numbers associated with heavy products. A more in-depth analysis regarding the treatment of Z determination for heavy products will be necessary. Light product Z

distributions align quite well with expectations, especially with the more statistically significant ^{235}U data. Contour plots for N vs Z, A vs N and A vs Z are shown in Figure 128 and 129.

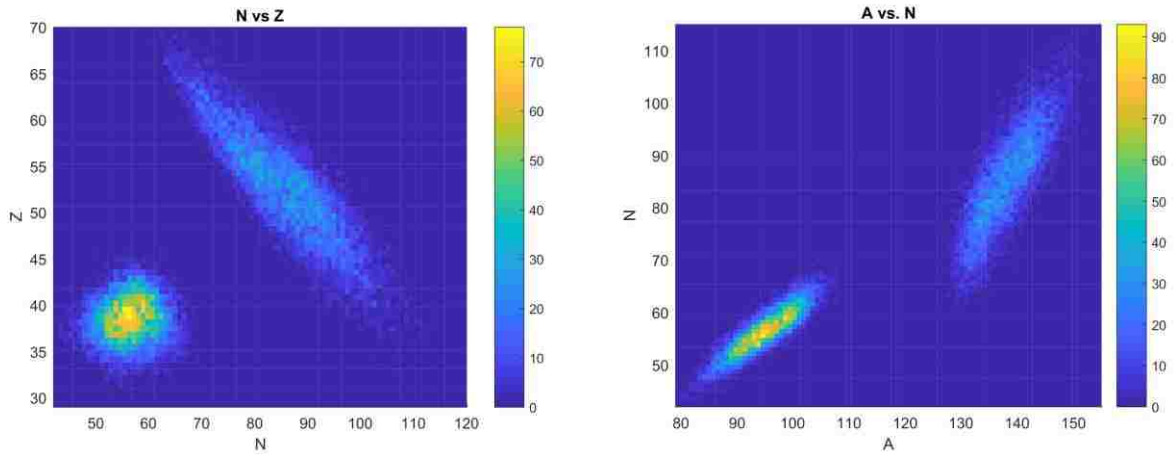

Figure 128: Calculated N/Z (left) and A/N (right) data for ^{235}U.

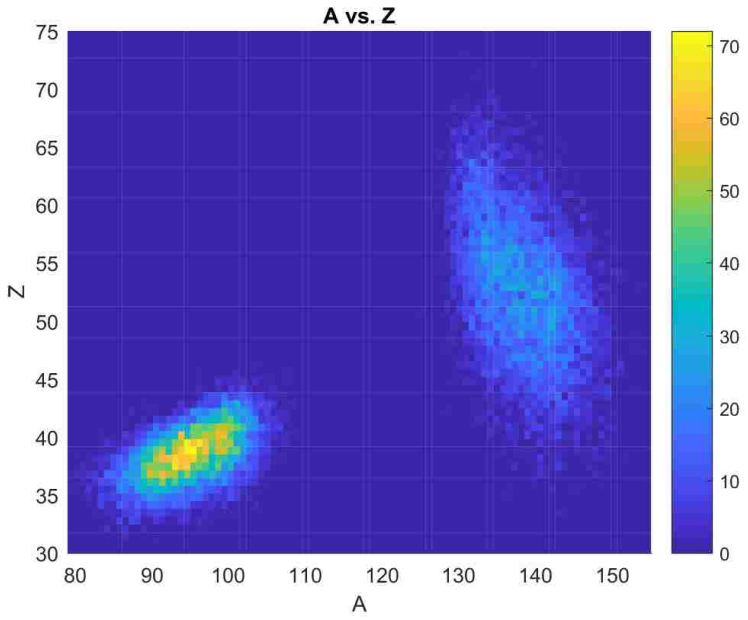

Figure 129: Measured A/Z data for ^{235}U.

Superimposing the light product N/Z data onto published N/Z data of stable nuclei, shows what we would expect. Light product N/Z from fission should fall “southeast” of the line of stable nuclides, towards the high N and low Z quadrant. That is what is seen in Figure 130 for

most of the light distribution, while the light products appearing to the "northwest" of the stable nuclides, towards the high Z and low N quadrant, show that there is still some analysis uncertainty.

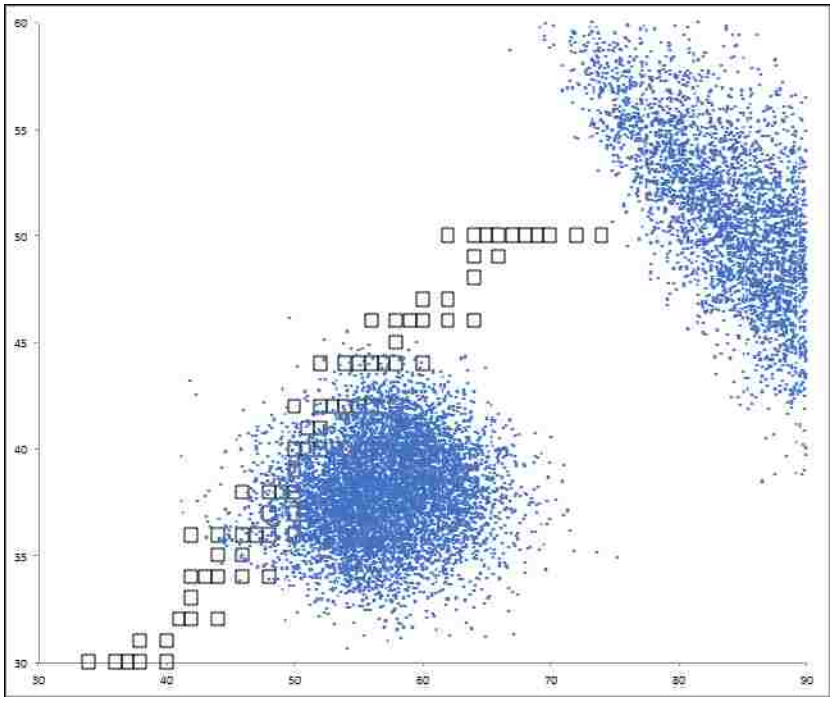

Figure 130: ^{235}U Z/N data superimposed on stable light elements.

While light products agree well with published and expected values for range and Z distributions, the heavy products require more investigation regarding the relationships between Z and range. Fielding the spectrometer at an accelerator facility that can provide a particle beam in this unique, high mass, low-energy per nucleon region would be highly beneficial toward better understanding this relationship.

Chapter 6: Conclusions

6.1 Conclusions on Mass Measurements

The fission product yield data collected using the UNM spectrometer for ^{252}Cf spontaneous fission and ^{235}U thermal neutron induced fission compared quite favorably with published ENDF/B-VII data files and previous experiments, particularly the ^{235}U dataset. Shown previously in chapter 4, Figures 131 and 132 show the results of ^{252}Cf and ^{235}U FPY distributions. The data are normalized to 200% yield total which means that intensity taken by scatter beyond the edges of the peaks or between the peaks reduces the intensity in the peaks. While the height of the ^{252}Cf peak data is lower, the data matches fairly well the shape of the ENDF values, again with scatter between the peaks and to the side taking some of the intensity. The ^{235}U data shows much less scatter and the height, the shape of the peak features, and the slope of the peak walls are in fairly good agreement with ENDF values. While not matching exactly, this data is highly correlated, with A, E, v, and Z information correlated particle-by-particle as opposed to simply a mass measurement. Additionally, this technique has been developed with comparisons to well-known data but can be applied to other, less well studied, fission parent nuclides.

Masses were extracted using energy and time-of-flight data, with corrections to the energy and velocity for energy loss in the system, through carbon foils and SiN windows and, for ^{252}Cf, through the gold source covering, with the corrections based on SRIM calculations. Data were calibrated to correspond with expected E and v values, though not for mass directly. Extracted values of mean mass values for ^{235}U light and heavy product peaks match well with previous experiments by Schmitt *et al*. [4], reiterated here in Table 21.

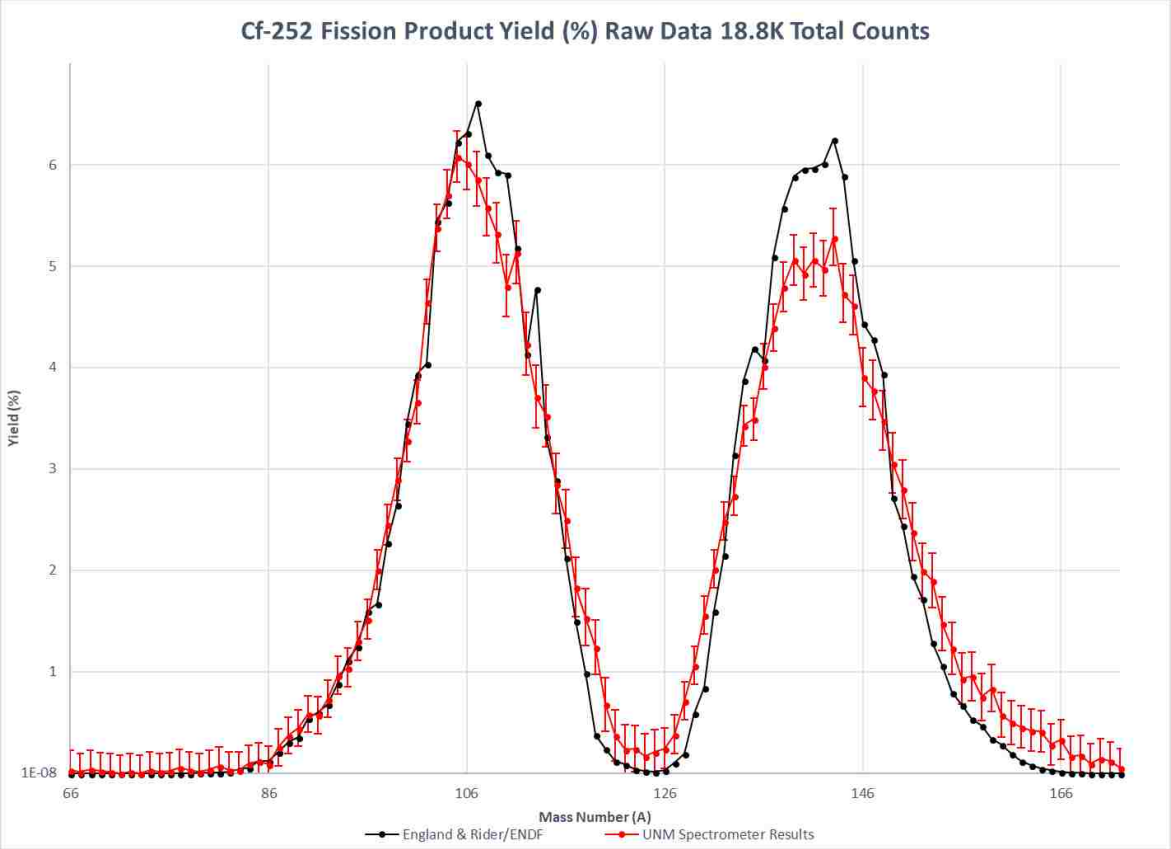

Figure 131: ^{252}Cf(s.f.) FPY distribution compared with ENDF/B-VII data file.

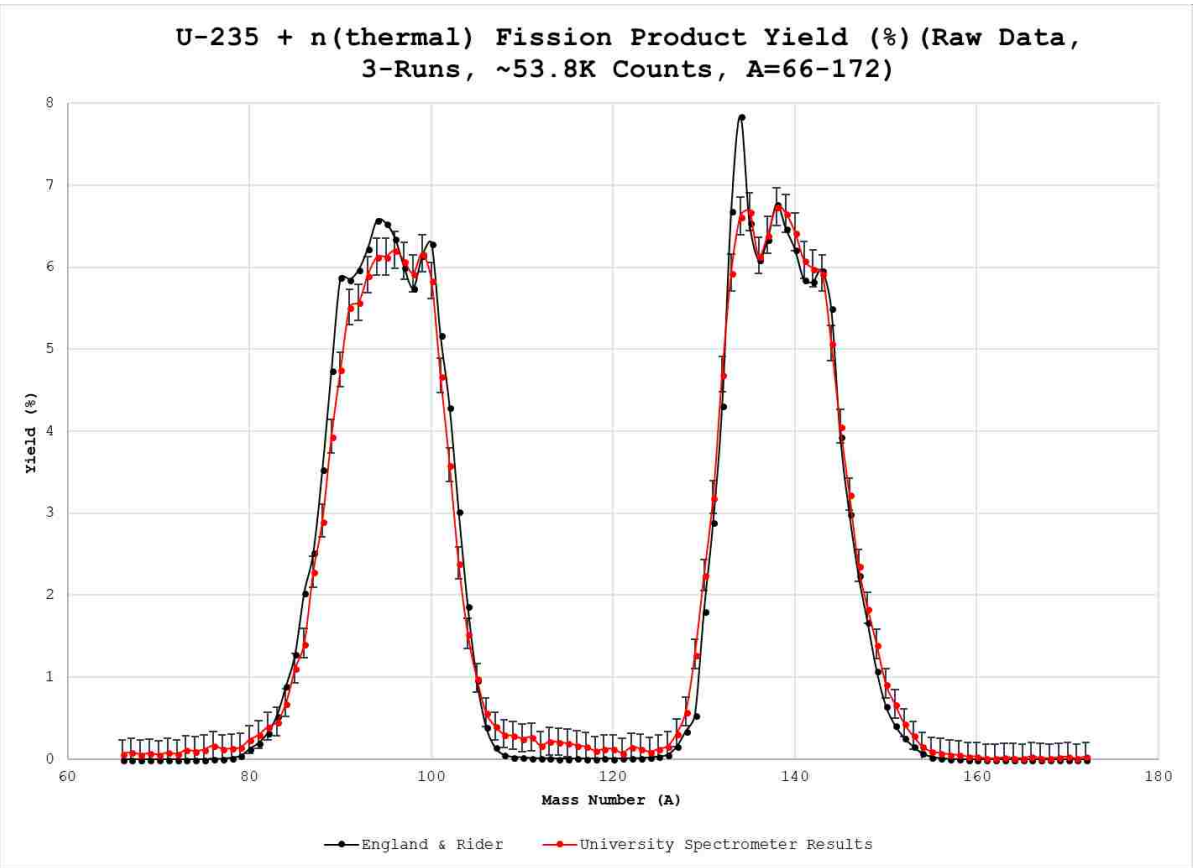

Figure 132: ^{235}U (n_{th}, f) FPY distribution compared with ENDF/B-VII data file.

Table 21: Results for mean mass and energy for ^{235}U (A = 66 – 172) compared with Schmitt *et al.* [4].

This Work (A= 66-172)	**Mean E (MeV)**	**σ_{mean} E**	**Mean A (amu)**	**σ_{mean} A**
Light	99.52	0.05	95.07	0.04
Heavy	70.12	0.05	138.67	0.04
Schmitt				
Light	101.56	*N/A*	96.57	*N/A*
Heavy	70.34	*N/A*	139.53	*N/A*

While mass uncertainty estimates remain above our stated goal of ≤ 1% mass resolution for the datasets analyzed, improvements in the transmission materials used, such as changing to 20 μg/cm^2 carbon foils for the timing modules, or lengthening the time-of-flight distance to increase t and so reduce δt/t, could potentially make the goal achievable. Both changes have been

implemented and tested, but not yet fielded for a statistically valid mass run. As shown previously, Figures 133 and 134 give an estimate of mass uncertainty for the 50 μg/cm^2 carbon transmission foils and 50 cm time-of-flight distance used in this dissertation work.

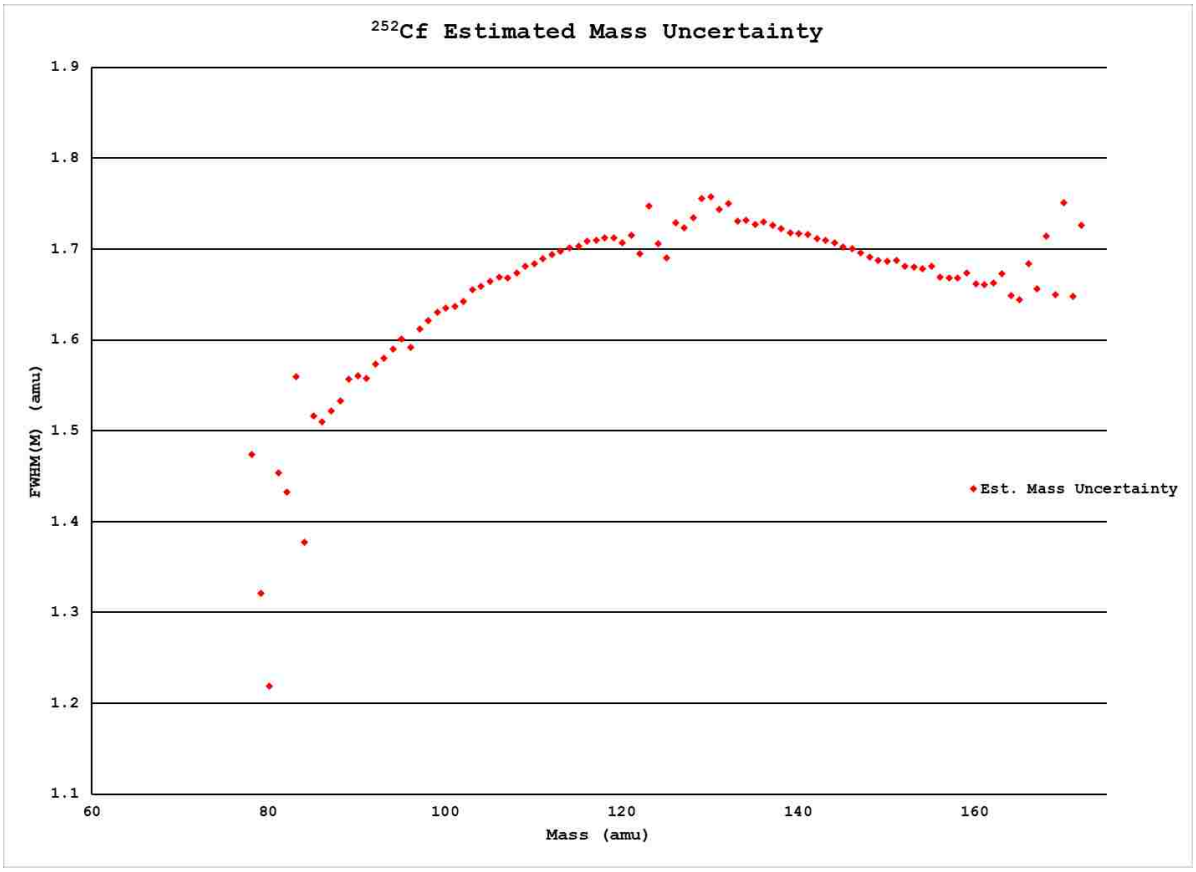

Figure 133: Estimated mass uncertainty for ^{252}Cf (s.f.).

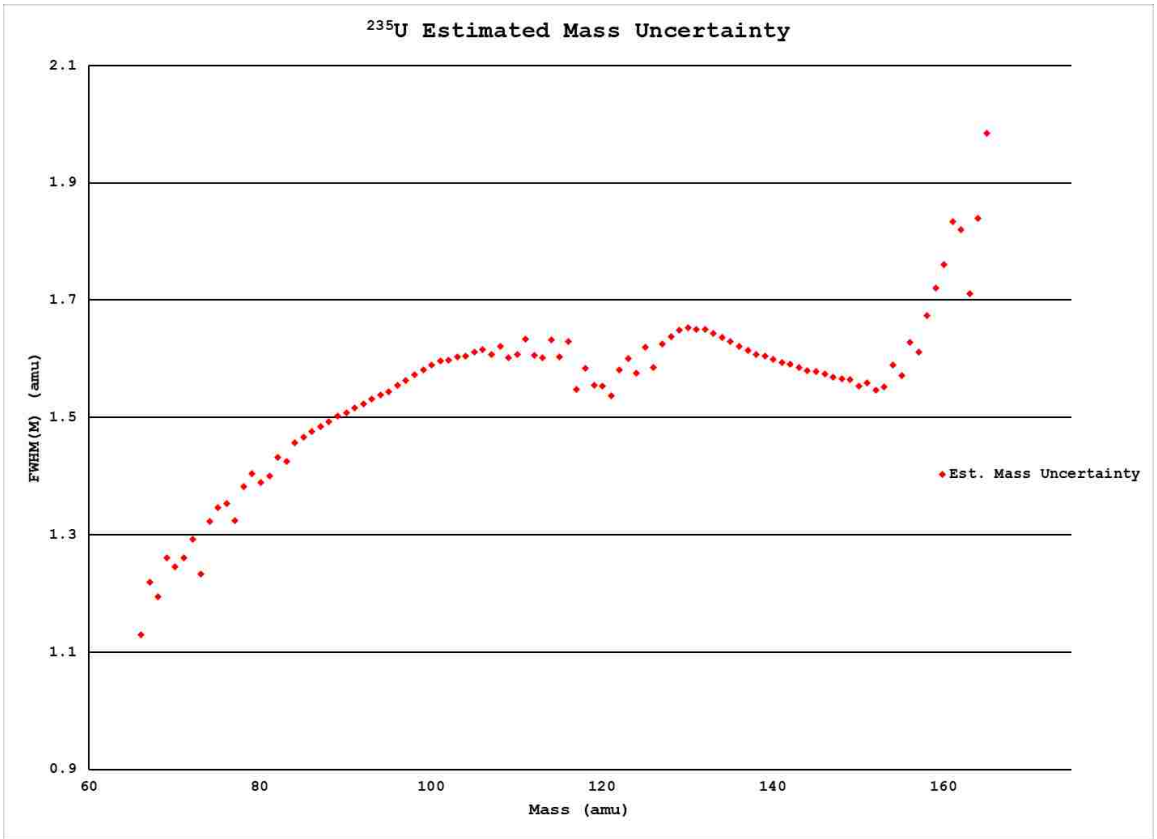

Figure 134: Estimated mass uncertainty for ^{235}U (n_{th}, f).

Analysis of sources of scattering and the statistical impact on the FPY distributions was discussed at length. An estimation of how much scattering adds statistical uncertainty from these sources was performed and found to be approximately 0.18% for the ^{252}Cf dataset and 0.17% for the ^{235}U dataset.

6.2 Range and Z Determination Conclusions

Range calculations based on the electron drift velocity in the IC and the time difference between cathode and anode signals and TRIM simulations agree well for light fission product ranges, while heavy product ranges are consistently underestimated in TRIM when compared to experiment. There are several possible reasons contributing to the cause. There is much less data on fission fragment stopping power than for alpha particles, and so simulations are expected to

be less refined for fission products. For the same atomic number, Z, TRIM may calculate incorrect atomic charge states, and thus different stopping power and range than seen experimentally. Another contribution to differences could have to do with pulse shape differences between heavy and light products, which could add differences in the time they trigger the CFD.

Z determination methodology employed in this work gave results that compared favorably to previous work. A comparison with results by Tyukavkin *et al.* [12] and Lang *et al.* [45] for ^{235}U, is shown in Table 22. The Z yield distributions are compared with ENDF/B-VII in Figure 135. There is reasonable agreement in the distribution for light fragments, less so for the heavy fragments.

Table 22: Mean Z value comparisons with previous experiments [12, 53].

	This Work	Tyukavkin 1	Tyukavkin 2	Lang
Mean Z Light	38.48	38.18	38.22	37.92
Mean Z Heavy	52.63	52.26	53.02	53.92

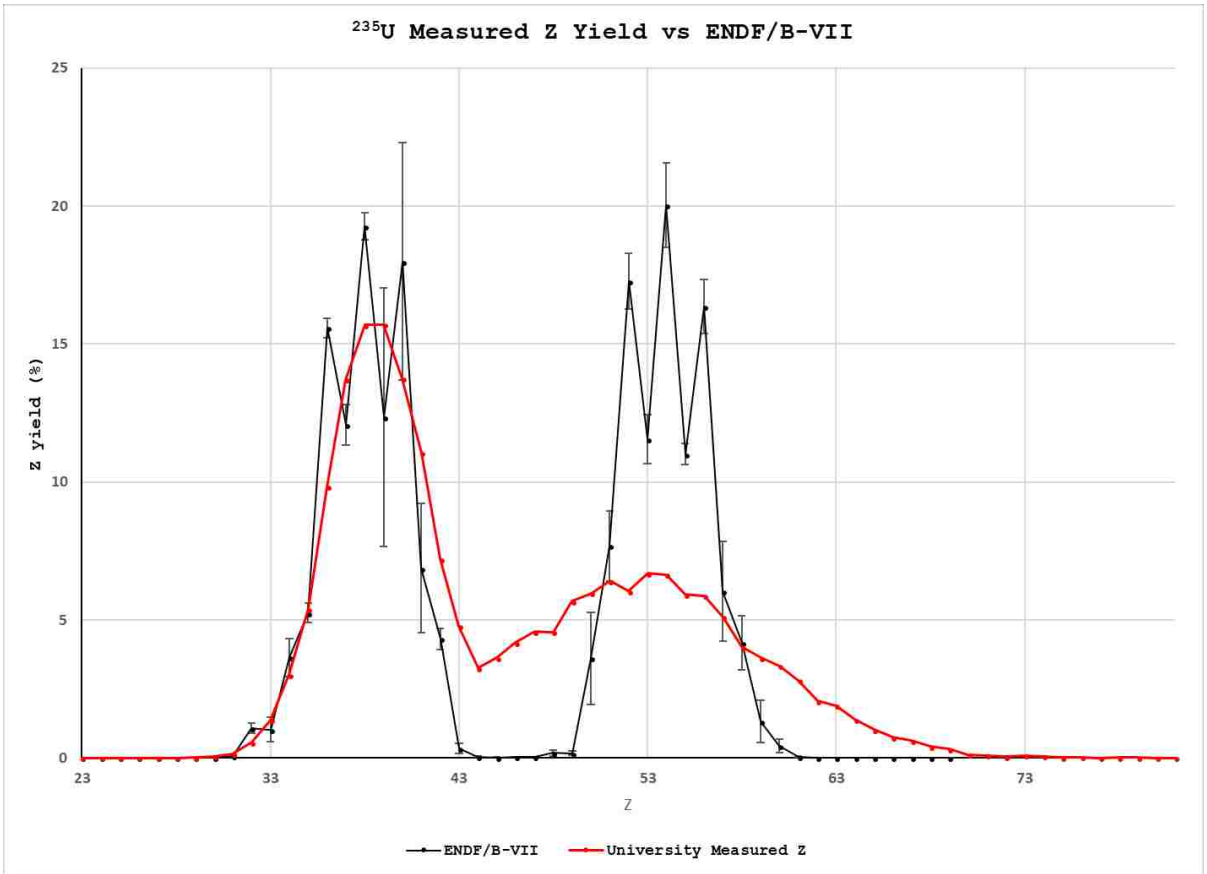

Figure 135: Measured Z distribution for ^{235}U compared with ENDF/B-VII.

The heavy product peak consistently suffers from broadening, which can potentially be attributed to the Z, energy, range and mass perturbation relationships developed using the TRIM code. The broadening effect of the heavy products potentially comes from the decreasing average energy as a function of mass for the mass products, while the light product average energy as a function of mass are relatively constant.

According to the TRIM simulation results, with a constant energy and Z, with an increase in mass, and thus a decrease in velocity, the range increases. This is counterintuitive and calibration data is needed in this energy, mass, and Z region. This may be the cause of why we extract an average Z as a function of mass for heavy products decreasing with increasing mass.

Chapter 7: Future Work

Several suggestions for future improvements will be presented in the following sections. From simple experiments we can undertake in the short-term to projects that rely heavily on funds available and re-design of parts of the detector itself.

7.1: Scattering Assessment Experiments

As noted in chapter 5, scattering plays a large role in the accuracy of yield measurements, particularly in the low-yield portion of the distribution. During our last run cycle at the LANSCE facility, attempting to obtain $^{239}Pu(n_{th}, f)X$ data, a SiN window failed during our initial run, filling the TOF region with isobutane and causing heavy damage to both MCPs as they arced in the gas. Since the MCPs are quite expensive, we have been unable to replace them as of this writing. With that in mind, we can still investigate the potential scattering of the system with a simple setup utilizing one or more silicon surface barrier detector(s) where the IC would sit within an empty ionization chamber as shown in Figure 136. Sources of potential scattering such as the IC entrance window frame and TOF foil holders and mirror wires can be removed entirely to get a benchmark measurement. Individual pieces can then be re-introduced one at a time to understand each component's contribution to scattering. As we would only have energy measurements, we would not be able to identify scattering as easily as when using the E/TOF plot. This could potentially yield useful information regarding rejection of scattered data in the spectrometer. An array of these detectors would be more efficient as most of the silicon surface barrier detectors have small solid angle acceptance.

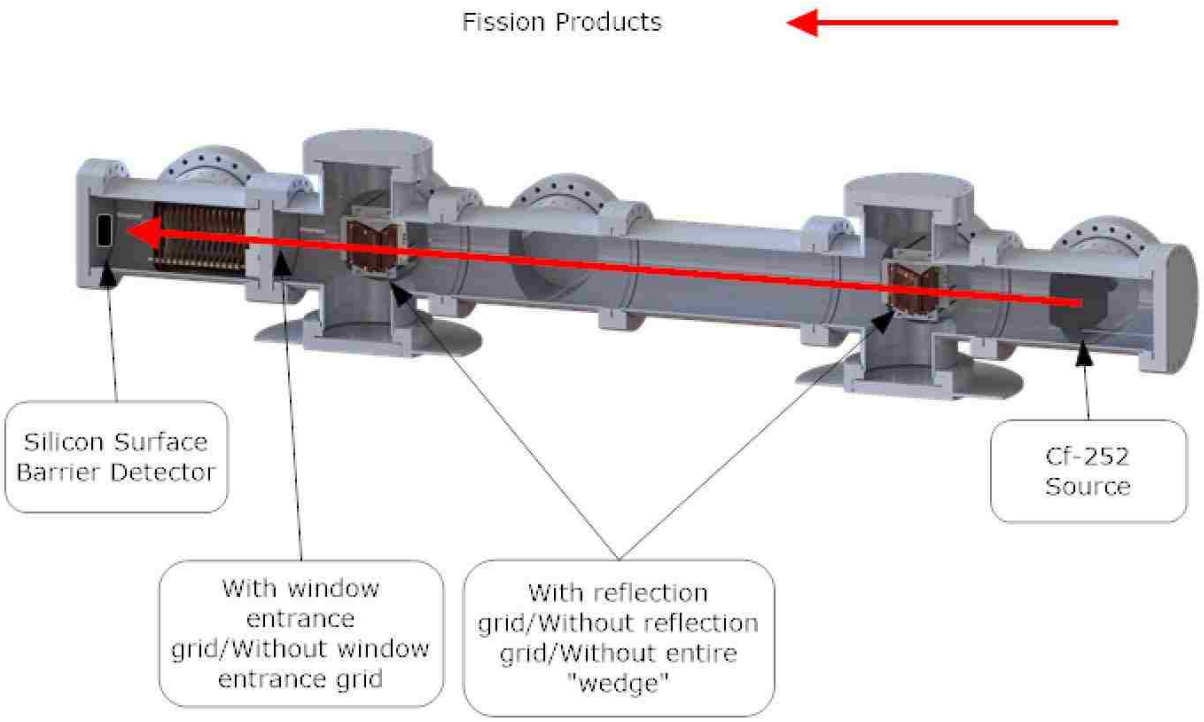

Figure 136: Potential experimental diagram for assessing scatter.

Peak-to-valley ratios in the energy distribution can be inspected, or perhaps the mass analysis using ^{252}Cf utilized by Fellows [9] based on Schmitt *et al.* [10] could yield useful information. An addition of a timing measurement would be useful for a distribution more like the IC based E/TOF plots once a new MCP becomes available.

7.2 Switch to All Digital Electronics

We currently are in possession of all the electronics necessary to make the switch to all digital electronics. A CAEN VME crate with associated CAEN CFD, Time to Digital Convertor (TDC), and Analog (pulse height) to Digital Convertor (ADC) are available for data acquisition. However, a large time investment is needed to write and troubleshoot the computer code for this endeavor. With the detector system currently in need of repair, this down time can create an opportunity to get this project achieved. A graduate student with a strong grasp of hardware and

coding could potentially implement this all digital data acquisition system for a master's project. This would open up several potential improvements, most importantly the ability to save all waveforms to potentially improve timing pick offs using post-processing methods.

7.3 Explore Other Simulation Packages

Exploring other simulation packages is another project that could be assessed during spectrometer down-time. Phoenix Baldez, who will be the senior graduate student on this project, has already began to investigate the implementation of detailed MCNP calculations to potentially replace TRIM. Other packages such as GEANT4 should also be considered, as GEANT4 offers high flexibility in application, it is also more geared towards heavy ion physics and interactions, however it does have a higher learning curve than "black box" codes such as TRIM or MCNP.

7.4 Decrease in IC Pressure

Examining a decrease in IC pressure and its effect on range measurements and resolution should be a relatively easy effort once the spectrometer is back in working condition. As was seen in the range portion of this work, we have ~3-4 cm to spare in the active IC region. We also see improved separation in the range and timing data with decreased pressure. This was going to be tested during the ^{239}Pu run cycle at LANSCE before the IC entrance window break.

7.5 Ion Beam Calibration

Fielding the entire detector on a dedicated ion beam with heavy ion energy per mass ranges of ~ 0.3 – 1.6 MeV/amu is crucial. This will allow for an absolute calibration of both the TOF and energy detectors as well as give definitive mass and time resolution quantities in the fission product mass and energy ranges. Experimental energy loss information in these energy/mass regions would also be highly useful for the energy addback methods employed rather than relying exclusively on simulation. This is a necessary step that needs to be done to

give increased validity to the overall yield distributions reported. Several locations have been investigated for this purpose, such as the Ion Beam Laboratory (IBL) at Sandia National Laboratories, shown in Figure 137, and the Notre Dame Nuclear Science Laboratory at the University of Notre Dame. Our collaborators at LANL have recently fielded their IC at NSL and are currently analyzing results.

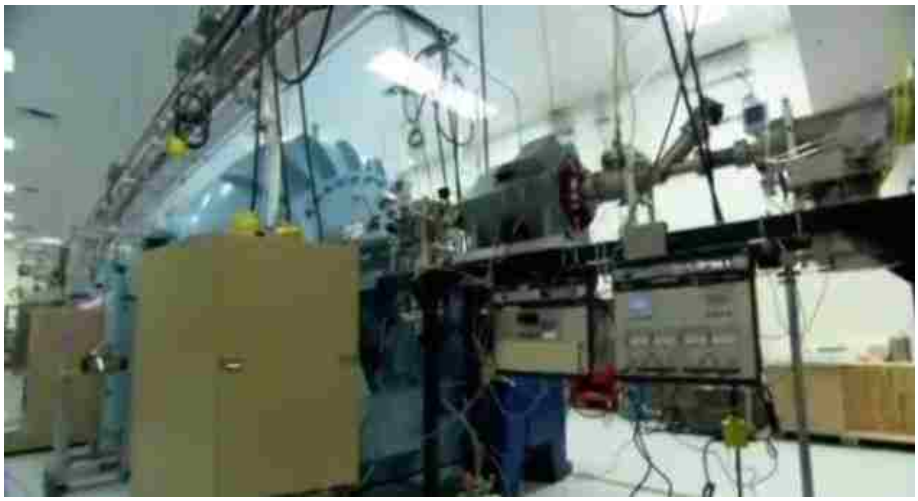

Figure 137: 6V Tandem accelerator at IBL.

7.6 2nd Spectrometer Arm

Constructing a second, identical spectrometer to field at 180° of the original, as shown in Figure 138, would also be highly useful in terms of gathering even more fission information such as TKE. Secondly, it would also provide a useful anti-coincidence purpose by rejecting scattered ions that occur within the detection system.

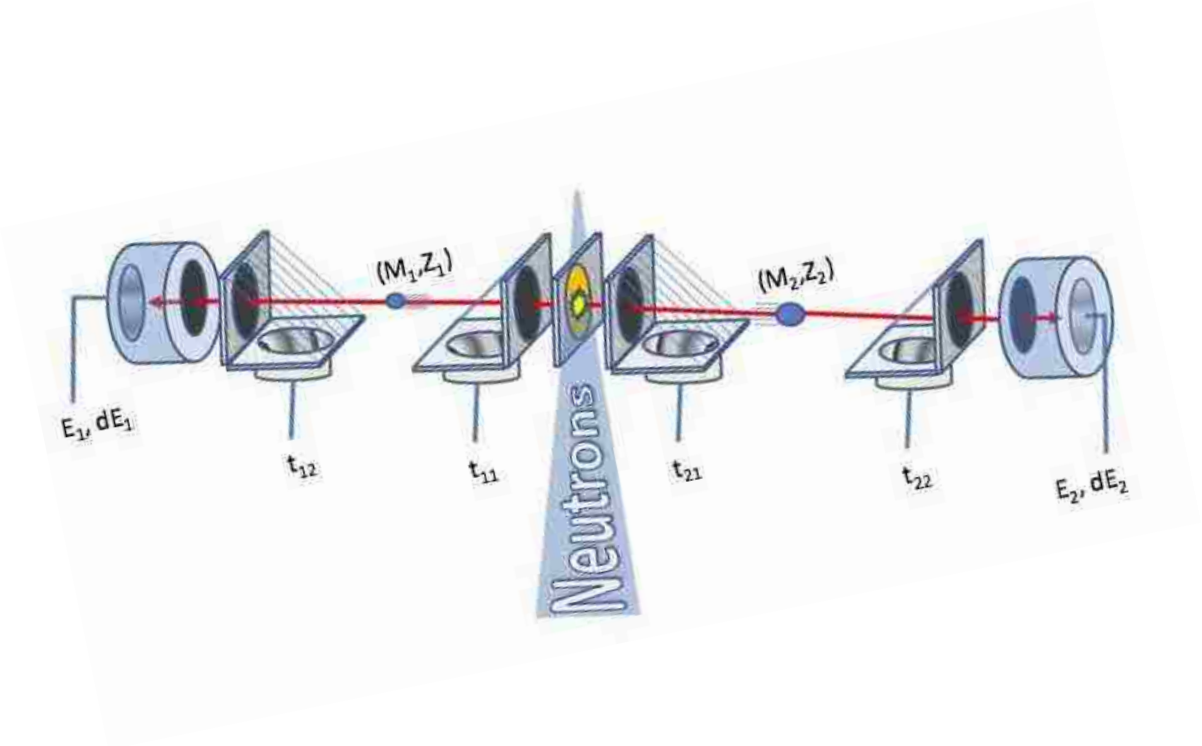

Figure 138: 2-arm, 2v-2E spectrometer diagram.

As noted previously, scattering potentially contributes in a significant way to the overall yield distribution, particularly in the valley and edges region of the distribution. Having coincidence information for Z of the opposite paired fission product would be useful in formulating a more accurate Z determination scheme as the total Z is known and is that of the fission parent.

References

[1] Hambusch, F. J; *et al; Fission Product Yields Data Current Status and Perspectives*, IAEA Technical Meeting, 2016

[2] Pomp, S. *et al; Accurate Fission Data for Nuclear Safety Final Report*, Uppsala University, 2015

[3] Rochman, D. *et al; Propagation of $^{235,236,238}U$ and ^{239}Pu Nuclear Data Uncertainties for a Typical PWR Fuel Element*, 2011

[4] H. W. Schmitt, J. H. Neiler, and F. J. Walter. *Fragment Energy Correlation Measurements for ^{252}Cf Spontaneous Fission and ^{235}U Thermal-Neutron Fission* Phys. Rev. 141, 1146 – Published 21 January 1966

[5] LBNL; *Nuclear Data Needs and Capabilities for Applications*, white paper, 2015

[6] Wahl, A. C; *Systematics of Fission-Product Yields*, LA-13928, May 2012

[7] Oed, A; *et al*; *High Resolution Axial Ionization Chamber for Fission Products*, Nuclear Instruments and Methods 205 (1983) 455-459

[8] Wagemans, C., 1991. *The Nuclear Fission Process.* 1st ed. Florida: CRC Press.

[9] Fellows, Shelby. *Time-Of-Flight And Energy Loss Analysis On The Unm Fission Fragment Spectrometer*, MS thesis, Department of Nuclear Engineering, University of New Mexico, Albuquerque, New Mexico, USA 2017. http://digitalrepository.unm.edu/ne_etds/64

[10] Schmitt, H. W; *et al*; *Precision Measurements of Correlated Energies and Velocities of ^{252}Cf Fission Fragments*, Physical Review, Vol 137, 48, 1965

[11] Sanami, T; *et al; A Bragg Curve Counter with an Active Cathode to Improve the Energy Threshold in Fragment Measurements*, Nuclear Instruments and Methods A, 589, 2008, 193-201

[12] Tyukavkin, A. N.; Pyatkov Yu. V.; *et al*., 2008. *Measuring the Nuclear Charge of Fission Fragments Using a Large Ionization Chamber – Part of the Double-Arm Time-of-Flight Spectrometer*. Instruments and Experimental Techniques, Volume 52, Number 4, pp. 508-518.;

[13] Hahn, O; Strassmann, F; *Concerning the Existence of Alkaline Earth Metals Resulting from Neutron Irradiation of Uranium*, Die Naturwissenschaften 27, 11-15, 1939.

[14] L. Meitner, F. Strassmann, and O. Hahn, Z. Physik 109**,** 538 (1938)

[15] Magee, 2001. [Online]. Available at:

http://lablemminglounge.blogspot.com/2011/03/why-fuel-rods-are-radioactive.html.

[16] World Nuclear Association. http://www.world-nuclear.org/nuclear-basics/how-does-a-nuclear-reactor-make-electricity.aspx

[17] H.D. Selby et al, *Fission Product Data Measured at Los Alamos for Fission Spectrum and Thermal Neutrons on Pu-239, U-235, and U-238,* Nuclear Data Sheets, 111, 2010

[18] Gook, A; Hambusch, F.-J; Vidali, M; *Prompt Neutron Multiplicity in Correlation with Fragments from Spontaneous Fission of ^{252}Cf,* Physical Review C, 90, 2014

[19] Boucheneb, N; *et al*; *High Resolution Measurements of Mass, Energy and Nuclear Charge Correlations for $^{229Th}(n,f)$ with the COSI FAN TUTTE Spectrometer*, Nuclear Physics A502, 1989, 261c-270c

[20] Meierbachtol, K; *et al*; *The SPIDER Fission Fragment Spectrometer for Fission Product Yield Measurements*, Nuclear Instruments and Methods Section A, Vol 788, 2015, 59-66

[21] Geltenbort, P; Gonnenwein, F; Oed, A; *Precision measurements of mean kinetic energy release in thermal-neutron-induced fission of ^{233}U, ^{235}U and ^{239}Pu*, Radiation Effects, 1986, Vol 93/1-4 57-60

[22] Romano, C; *et al*; *Fission Fragment Mass and Energy Distributions as a Function of Incident Neutron Energy Measured in a Lead Slowing-down Spectrometer*; Physical Review C 81, 2010

[23] Duke, D; *Fission Fragment Mass Distributions and Total Kinetic Energy Release of 235-Uranium and 238-Uranium in Neutron-Induced Fission at Medium and Fast Neutron Energies, LA-UR-15-28829,* Dissertation

[24] Institut Laue-Langevin, http://www.ill.eu/instruments-support/instruments-groups/instruments/pn1/, *Fission product spectrometer PN1, 2012*

[25] D.N. Poenaru, W. Greiner, *Experimental Techniques in Nuclear Physics*, de Gruyter, 1997

[26] M.C. White, *Advancing the Fundamental Understanding of Fission*, LANL Internal Document 2012077DR

[27] Oed, A; *et al; A Mass Spectrometer for Fission Fragments Based on Time-of-Flight and Energy Measurements*, Nuclear Instruments and Methods in Physics Research 219, 1984, 569-574

[28] *The SPIDER fission fragment spectrometer for fission product yield measurements*
K. Meierbachtol, F. Tovesson, D. Shields, C. Arnold, R. Blakeley, T. Bredeweg, M. Devlin,

A.A. Hecht, L.E. Heffern, J. Jorgenson, A. Laptev, D. Mader, J.M. O'Donnell, A. Sierk, M. White
Nuclear Instruments and Methods A 788, 58 (2015);
http://dx.doi.org/10.1016/j.nima.2015.02.032

[29] *Development of position-sensitive time-of-flight spectrometer for fission fragment research*
C.W. Arnold, F. Tovesson, K. Meierbachtol, T. Bredeweg, M. Jandel, H.J. Jorgenson, A. Laptev, G. Rusev, D.W. Shields, M. White, R.E. Blakeley, D.M. Mader, A.A. Hecht
Nuclear Instruments and Methods A 764, 53 (2014);
http://dx.doi.org/10.1016/j.nima.2014.07.001

[30] *Development of position-sensitive time-of-flight spectrometer for fission fragment research*
arXiv:1403.1573 [physics.ins-det]
http://arxiv.org/pdf/1403.1573v1.pdf

[31] *A high resolution ionization chamber for the SPIDER fission fragment detector*
K.C. Meierbachtol, F.K. Tovesson, C. Arnold, A.B. Laptev, T.A. Bredeweg, M. Jandel, R.O. Nelson, M.C. White, A.A. Hecht, D. Mader
Los Alamos publication LA-UR-13-20402 (2013)

[32] Heffern, L. *Ionization Chamber for Design, Development and Testing for the UNM Fission Fragment Spectrometer*, M.S. Thesis, Department of Nuclear Engineering, University of New Mexico, Albuquerque, New Mexico, USA 2015

[33] Mader, Drew. "An ionization chamber for fission fragment analysis." MS thesis, Department of Nuclear Engineering, University of New Mexico, Albuquerque, New Mexico, USA 2013. http://digitalrepository.unm.edu/ne_etds/33

[34] Cole, J. *An Ionization Chamber for High Resolution Fission Product Spectroscopy*, M.S. Thesis, Department of Nuclear Engineering, University of New Mexico, Albuquerque, New Mexico, USA 2016

[35] Blakeley, R. *A Time-of-Flight Spectrometer for Fission Fragment Identification*, M.S. Thesis, Department of Nuclear Engineering, University of New Mexico, Albuquerque, New Mexico, USA 2013

[36] Hamamatsu Technical Document, *MCP Assembly*, Hamamatsu Corporation, 2001

[37] J.W. Wiza, *Microchannel Plate Detector*, Nuclear Instruments and Methods, 162-587, 1979

[38] J. Adams and B.W. Manley. *The Mechanism of Channel Electron Multiplication*, IEEE Transactions on Nuclear Science, NS-13-88 1966

[39] K. Kosev. *A High-Resolution Time-of-Flight Spectrometer for Fission Fragments and Ion Beams*, Dissertation, Institute for Kern Physics, 2007

[40] K.C. Schmidt and C.F. Hendee. *Continuous Channel Electron Multiplier Operated in the Pulse Saturated Mode*, IEEE Trans. Nucl. Sci., NS-13-100, 1966

[41] W.R. Leo, *Techniques for Nuclear and Particle Physics Experiments*, Springer Verlag, 1993

[42] Ziegler, J.F., 2008. *Particle Interactions with Matter*. [Online]. Available at: www.SRIM.org

[43] G. D'Erasmo and V. Paticchio. *A Transmission Time Detector for Low Energy Light Ions*, Nucl. Instr. And Meth., A234 91-96, 1985

[44] N. Nankov et al. *Energy Distribution of Secondary Electrons by Swift Heavy Ions in Thin Foils*, Wissenschaftlich-Technische Berichte, FZR-442, 15, 2006

[45] K. Kosev et al. *A high-resolution time-of-flight spectrometer with tracking capabilities for fission fragments and beams of exotic nuclei*, Nuclear Instruments and Methods, A 594 2008 178-183

[46] RoentDek GmbH; http://www.roentdek.com

[47] ORTEC http://www.ortec-online.com, *Introduction to Amplifiers*, 2010

[48] Knoll, G. F. 2010. Radiation Detection and Measurement. 4th ed. New Jersey: John Wiley & Sons

[49] Buchriegler, J. 2013. Construction of a Multi-Anode Ionization Chamber for AMS at VERA, M.Sc. Thesis, University of Vienna, Austria.

[50] *SolidWorks: 3D CAD Design Software*, www.solidworks.com/sw/655_ENU_HTML.htm.

[51] T.R. England, B.F. Rider. *Evaluation And Compilation Of Fission-Product Yields*, 1992, ENDF-349

[52] Taylor, John R. *An Introduction to Error Analysis: The Study of Uncertainties in Physical Measurements* University Science Books 1997

[53] Lang, W., Clerc, H.-G., Wohlfarth, H., et al., Nucl. Phys. A, 1980, vol. 345, p. 34.

Appendix 1 – Matlab Data Analysis

```
%%%%%%%%%%%%%%%%%%%%%%%%%%%%%%%%%%%%%%%%%%%%%%%%%%%%%%%%%%%%%%%%
%%%%%%%%%%%
%%%%%%%%%%%%%%%%%%%%%%Importing Data From ToF, Energy &
ICToF%%%%%%%%%%%%
%%%%%%%%%%%%%%%%%%%%%%%%%%%%%%%%%%%%%%%%%%%%%%%%%%%%%%%%%%%%%%%%
%%%%%%%%%%%
clear;
clc;
%Loading CAEN Desktop ADC data for Ch1 (Anode), Ch2 (MCPToF),
Ch3 (ICToF)
ch1tmp =
load('C:\Users\Rick\Desktop\Data\LANL2017data\Jan23_2017LANLU235
_Full_C2500_A570_iso_70torr_007_ls_1.dat');
ch1tmp;
ch2tmp =
load('C:\Users\Rick\Desktop\Data\LANL2017data\Jan23_2017LANLU235
_Full_C2500_A570_iso_70torr_007_ls_2.dat');
ch2tmp;
ch0tmp =
load('C:\Users\Rick\Desktop\Data\LANL2017data\Jan23_2017LANLU235
_Full_C2500_A570_iso_70torr_007_ls_3.dat');
ch0tmp;
ch_ar_tmp =
load('C:\Users\Rick\Desktop\Data\LANL2017data\Jan23_2017LANLU235
_Full_C2500_A570_iso_70torr_007_ls_2.dat');
ch_ar_tmp;
%Loading Schmitt data for later comparison
schmittE =
load('C:\Users\Rick\Desktop\Data\50umdata\SchmittE.dat');
schmittE;
schmittM =
load('C:\Users\Rick\Desktop\Data\50umdata\SchmittM.dat');
schmittM;

%Comparing dataset length and making all correlated arrays the
same legnth
[N,M] = size(ch1tmp);
[S,T] = size(ch2tmp);
[U,V] = size(ch0tmp);
[W,X] = size(ch_ar_tmp);

if (N>S)
```

```
    ch2 =
load('C:\Users\Rick\Desktop\Data\LANL2017data\Jan23_2017LANLU235
_Full_C2500_A570_iso_70torr_007_ls_2.dat');
    ch2 = [ch1;zeros(N-S,T)];
    ch1 = ch1tmp;
else
    ch1 =
load('C:\Users\Rick\Desktop\Data\LANL2017data\Jan23_2017LANLU235
_Full_C2500_A570_iso_70torr_007_ls_1.dat');
    ch1 = [ch1;zeros(S-N,T)];
    ch2 = ch2tmp;
end
if (U>W)
    ch_ar =
load('C:\Users\Rick\Desktop\Data\LANL2017data\Jan23_2017LANLU235
_Full_C2500_A570_iso_70torr_007_ls_2.dat');
    ch_ar = [ch0;zeros(U-W,X)];
    ch0 = ch0tmp;
else
    ch0 =
load('C:\Users\Rick\Desktop\Data\LANL2017data\Jan23_2017LANLU235
_Full_C2500_A570_iso_70torr_007_ls_3.dat');
    ch0 = [ch0;zeros(W-U,X)];
    ch_ar = ch_ar_tmp;
end

%Assigns tof, anode pulse, and IC TPH pulse to matrix
m = length(ch1);
data_E_tof_delt = [ch1(1:m,1) ch1(1:m,2) ch2(1:m,1) ch2(1:m,2)
ch0(1:m,1) ch0(1:m,2)];
fprintf('Loading Complete \n')

%%
%%%%%%%%%%%%%%%%%%%%%%%%%%%%%%%%%%%%%%%%%%%%%%%%%%%%%%%%%%%%%%%%%%%%
%%%%%%%%%%
%%%%%%%%%%%%%%%%%Correlating ToF & Energy
Measurements%%%%%%%%%%%%%%%%%%%%%
%%%%%%%%%%%%%%%%%%%%%%%%%%%%%%%%%%%%%%%%%%%%%%%%%%%%%%%%%%%%%%%%%%%%
%%%%%%%%%%
% Sorts through anode (ch1) & MCPToF (ch2) for correlated data
points
tic
j = data_E_tof_delt(:,3);
d = data_E_tof_delt(:,1);
c = data_E_tof_delt(:,5);

k=0;
```

```
A=[];
n=1;
for i = (1:length(d));
    k=k+1;
    for h = (n:length(j));
        if((abs(j(h)-d(i))<95 && (data_E_tof_delt(i,2)>4500 &&
(data_E_tof_delt(h,4)<(9.8214E-05*data_E_tof_delt(i,2).^2 -
2.7125*data_E_tof_delt(i,2) + 2.6594E+04)) &&
(data_E_tof_delt(h,4)>(1.7857E-04*data_E_tof_delt(i,2).^2 -
3.8400E+00*data_E_tof_delt(i,2) + 2.9193E+04)) &&
data_E_tof_delt(i,2)<11000)) || (abs(j(h)-d(i))<95 &&
(data_E_tof_delt(i,2)>9000 && data_E_tof_delt(h,4)<(-
0.402439*data_E_tof_delt(i,2) + 11590.243902) &&
data_E_tof_delt(h,4)>(-0.500*data_E_tof_delt(i,2) + 11200) &&
data_E_tof_delt(i,2)<15000)));
            A(i,:) =
[data_E_tof_delt(i,1),data_E_tof_delt(i,2),data_E_tof_delt(h,3),
data_E_tof_delt(h,4)];
            break
        end
    end
    if (k == 100)
        k = 0;
        (i/length(d))*100
    end
end
fprintf('Correlating Data Complete 1\n')

loc1 = find(A(:,1)==0);
A(loc1,:) = [];
toc
%dlmwrite('RawChannelDataLANL20172500V70TorrRun4UF4Raw.txt',A);
%% Summing Data
RawChannelDataRun7 =
load('C:\Users\Rick\Documents\MATLAB\RawChannelDataLANL20172500V
70TorrRun7UF4Raw.txt');
RawChannelDataRun6 =
load('C:\Users\Rick\Documents\MATLAB\RawChannelDataLANL20172500V
70TorrRun6UF4Raw.txt');
RawChannelDataRun4 =
load('C:\Users\Rick\Documents\MATLAB\RawChannelDataLANL20172500V
70TorrRun4UF4Raw.txt');
RawChannelDataSUM
=vertcat(RawChannelDataRun7,RawChannelDataRun6,RawChannelDataRun
4);
dlmwrite('CumulativeRawChannelDataUF4Raw.txt',RawChannelDataSUM)
;
```

```
%%
A = RawChannelDataSUM;
%% Fitting gaussians to light & heavy peaks to produce fit
parameters for calibration
%h1=hist(A(:,2),5000);
[N, edges] = histcounts(A(:,2),500);
ICchannel = (edges(1:end-1) + edges(2:end))./2; %histcounts
gives the bin edges, but we want to plot the bin centers
plot(ICchannel,N,'ko');
title('Plotted as points');
ylabel('Frequency');
%% Fitting gaussians to light & heavy ToF peaks to produce fit
parameters for calibration
%h1=hist(A(:,2),5000);
[N, edges] = histcounts(A(:,4),1000);
ToFchannel = (edges(1:end-1) + edges(2:end))./2; %histcounts
gives the bin edges, but we want to plot the bin centers
plot(ToFchannel,N,'ko');
title('Plotted as points');
ylabel('Frequency');
xlim([3000,16000])
%% (Optional)
%h1=hist(A(:,2),5000);
[N, edges] = histcounts(ToFTruncheavy,100);
ToFchannel = (edges(1:end-1) + edges(2:end))./2; %histcounts
gives the bin edges, but we want to plot the bin centers
plot(ToFchannel,N,'ko');
title('Plotted as points');
ylabel('Frequency');
%% (Optional) Plot to check data
scatter(A(:,2),A(:,4),1,'b')%timing(:,4)
title('IC (ch) vs. ToF (ch)')
ylim([3000,16000])
ylabel('ToF Channel')
xlim([3000,16000])
xlabel('IC Channel')
grid()
%% (Optional) Removing non peak data/Seperating Heavy & Light
Energy Peaks for Fitting
%
i=0;
for i = (1:length(ch1));
    if (ch1(i,2)>3500) && (ch1(i,2)<10000);
        ETruncheavy(i,1) = ch1(i,2);
    end
    if (ch1(i,2)>10201) && (ch1(i,2)<15000);
        ETrunclight(i,1) = ch1(i,2);
```

```
    end
end
loc2 = find(ETruncheavy(:,1)==0);
ETruncheavy(loc2,:) = [];
loc3 = find(ETrunclight(:,1)==0);
ETrunclight(loc3,:) = [];
%% (Optional) Removing non peak data/Seperating Heavy & Light
ToF Peaks for Fitting
%
i=0;
for i = (1:length(A(:,4)));
    if (A(i,4)>3000) && (A(i,4)<8000);
        ToFTrunclight(i,1) = A(i,4);
    end
    if (A(i,4)>8001) && (A(i,4)<16000);
        ToFTruncheavy(i,1) = A(i,4);
    end
end
loc4 = find(ToFTruncheavy(:,1)==0);
ToFTruncheavy(loc4,:) = [];
loc5 = find(ToFTrunclight(:,1)==0);
ToFTrunclight(loc5,:) = [];

%%
%%%%%%%%%%%%%%%%%%%%%%%%%%%%%%%%%%%%%%%%%%%%%%%%%%%%%%%%%%%%%%%%
%%%%%%%%%%%
%%%%%%%%%%%%%%%%%%%%%%Calibration of ToF & Energy
measurement%%%%%%%%%%%%%%
%%%%%%%%%%%%%%%%%%%%%%%%%%%%%%%%%%%%%%%%%%%%%%%%%%%%%%%%%%%%%%%%
%%%%%%%%%%%
fignum = 1;
%Looks at raw data of TOF and anode pulse to determine peaks for
%calibration and mass calculations
figure(fignum)
fignum = fignum+1;
subplot(1,2,1)
hist(A(:,2),500)
title('Ion Chamber')
xlabel('Channel #')
ylabel('Counts')
grid()
subplot(1,2,2)

hist(A(:,4),1000)
title('TOF')
xlabel('Channel #')
ylabel('Counts')
```

```
grid()


heavy_frag_E = input('Centroid channel of heavy fragment energy
peak:');
light_frag_E = input('Centroid channel of light fragment energy
peak:');

light_frag_t = input('Centroid channel of light fragment timing
peak:');
heavy_frag_t = input('Centroid channel of heavy fragment timing
peak:');

%Energy calibration parameters
x3 = [heavy_frag_E light_frag_E];
hf1eng2 = 57709; %Calibration heavy product energy for IC
lf1eng2 = 90339; %Calibration light product energy for IC
% Above values are E-loss corrected from SRIM calcs
y3 = [hf1eng2 lf1eng2];
% Applying the linear fit
p3 = polyfit (x3,y3,1);
yfit = polyval(p3,x3);
energy = A;
energy(:,2) = p3(1)*A(:,2) + p3(2); %first order fit for FF only
countseng = length(data_E_tof_delt);
counts2eng = length(energy(:,2));

%Timing calibration parameters
x2 = [light_frag_t heavy_frag_t];
lf1time = 3.60529e-8; % seconds
hf1time = 5.31819e-8; % seconds
y2 = [lf1time hf1time];
% Applying the fit
p2 = polyfit(x2,y2,1);
y2fit = polyval(p2,x2);
timing = [A];
timing (:,4) = p2(1)*A(:,4) + p2(2); %first order fit for timing
countstime = length(data_E_tof_delt);
counts2time = length(timing(:,4));

% (Optional) Calibration with Pulser 25,50 & 100 ns
%timing = [A];
%timing (:,4) = 5.048676813159e-12*A(:,4) + 1.770866310304e-8;

% Applying energy equation to obtian mass distribution
% E = (1/2)mv^2 ----> 2E/(v^2) = m ---> 2E*(dT/dX)^2 = m
```

```
%%%%%%%%%%%%%%%%%%%%%%%%%%%%%%%%%%%%%%%%%%%%%%%%%%%%%%%%%%%%%%%%%
%%%%%%%%%%%
%%%%%%%%%%%%%%%%%%%%%%Calculating Mass
Parameters%%%%%%%%%%%%%%%%%%%%%%%%%%
%%%%%%%%%%%%%%%%%%%%%%%%%%%%%%%%%%%%%%%%%%%%%%%%%%%%%%%%%%%%%%%%%
%%%%%%%%%%%
KE = energy(:,2); % keV
KER = energyR(:,2);
dT = timing(:,4); % seconds
dX = 0.5; % meters
v = dX./dT;
vi = 9.86411E-01*v + 6.07954E+05;%9.85517E-01*v + 5.96662E+05;
fprintf('Calibration Complete \n')

%%
%%%%%%%%%%%%%%%%%%%Liner Heavy/Light split Addback
jj = timing(:,4);
KEadd = KE;

for i3 = (1:length(jj));
    if (timing(i3,4)<4.2e-8);
        KEadd(i3)= KE(i3) + 2.0721365528E+11*timing(i3,4) +
2.9676740670E+03;%2.4721365528E+11*timing(i3,4) +
2.4676740670E+03  DECENT VALUES 2.0721365528E+11*timing(i3,4) +
2.9676740670E+03;
    else
        KEadd(i3)= KE(i3) + (-7.6100543710E+10)*timing(i3,4) +
1.5939036986E+04;%(-1.5100543710E+11)1.8939036986E+04   DECENT
VALUES CUTS (-7.6100543710E+10)*timing(i3,4) + 1.5939036986E+04
    end
end
fprintf('Energy Addback Complete \n')
KEadd_t = [A(:,3),KEadd];
KE_t = [A(:,3),KE];
KER_t = [A(:,3),KER];
vi_t = [A(:,3),vi];
%%%%%%%%%%%%%%%%%%%%%%%%%%%%%%%%%%%%%%%%%%%%%%%%%%%%%%%%%%%%%%%%%
%%%%%%%%%%%
%%%%%%%%%%%%%%%%%%%%%%Calculating Final
Mass%%%%%%%%%%%%%%%%%%%%%%%%%%%%%%%
%%%%%%%%%%%%%%%%%%%%%%%%%%%%%%%%%%%%%%%%%%%%%%%%%%%%%%%%%%%%%%%%%
%%%%%%%%%%%
mass = 2.*KE./(v.^2); % in keVs^2/m^2
amu = 9.64853365*10^10; %conversion factor --> to amu
mass_un = mass*amu;
% Corrected mass
mass_c = (2.*KEadd./(vi.^2))*amu; %With E corrections
```

```
mass_c_t = [A(:,3),mass_c];
% Making Matrices With Important Data to be Used Later
Mass_KEadd = [mass_c,KEadd];
Mass_KEadd_vi = [mass_c,KEadd,vi];
%% (Optional)
% Writing important individual run matrices to files
dlmwrite('MassLANL20172500V70TorrRun4UF4Raw.txt',mass_c);
dlmwrite('Mass_KEadd_viRun4UF4Raw.txt',Mass_KEadd_vi);
dlmwrite('Mass_KEaddRun4UF4Raw.txt',Mass_KEadd);
%% (Optional) Summing mass data
MassRun7 =
load('C:\Users\Rick\Documents\MATLAB\MassLANL20172500V70TorrRun7
UF4Raw.txt');
MassRun6 =
load('C:\Users\Rick\Documents\MATLAB\MassLANL20172500V70TorrRun6
UF4Raw.txt');
MassRun4 =
load('C:\Users\Rick\Documents\MATLAB\MassLANL20172500V70TorrRun4
UF4Raw.txt');
MassSUM =vertcat(MassRun7,MassRun6,MassRun4);
%% (Optional) Writing sum mass to file
dlmwrite('CumulativeMassUF4Raw.txt',MassSUM);
%% (Optional) Summing mass, KE and initial velocity matrices to
file
Mass_KEadd_viRun7 =
load('C:\Users\Rick\Documents\MATLAB\Mass_KEadd_viRun7UF4Raw.txt
');
Mass_KEadd_viRun6 =
load('C:\Users\Rick\Documents\MATLAB\Mass_KEadd_viRun6UF4Raw.txt
');
Mass_KEadd_viRun4 =
load('C:\Users\Rick\Documents\MATLAB\Mass_KEadd_viRun4UF4Raw.txt
');
Mass_KEadd_viSUM
=vertcat(Mass_KEadd_viRun7,Mass_KEadd_viRun6,Mass_KEadd_viRun4);
%% (Optional) Writing Sum mass, KE and initial velocity matrices
to file
dlmwrite('CumulativeMass_KEadd_viRaw.txt',Mass_KEadd_viSUM);
%% (Optional) Summing mass and KE matrices to file
Mass_KEaddRun7 =
load('C:\Users\Rick\Documents\MATLAB\Mass_KEaddRun7UF4Raw.txt');
Mass_KEaddRun6 =
load('C:\Users\Rick\Documents\MATLAB\Mass_KEaddRun6UF4Raw.txt');
Mass_KEaddRun4 =
load('C:\Users\Rick\Documents\MATLAB\Mass_KEaddRun4UF4Raw.txt');
Mass_KEaddSUM
=vertcat(Mass_KEaddRun7,Mass_KEaddRun6,Mass_KEaddRun4);
```

```
%% (Optional) Writing Sum mass and KE matrices to file
dlmwrite('CumulativeMass_KEaddCut.txt',Mass_KEaddSUM);
%% (Optional) Plot Checking Corrected KE
%KE vs TOF
%subplot(2,2,2)
scatter(timing(:,4),KEadd,1,'b')
title('KEi (corrected) vs. Vi')
ylim([3.5e4,12e4])
ylabel('KEi [keV]')
xlim([2.8e-8,6.0e-8])
xlabel('Vi [m/s]')
grid()
%% (Optional) Plotting
%%%%%%%%%%%%%%%%%%%%%%%%%%%%%%%%%%%%%%%%%%%%%%%%%%%%%%%%%%%%%%%%
%%%%%%%%%%%
%%%%%%%%%%%%%%%%%%%%%%Mass, Energy & ToF
Plots%%%%%%%%%%%%%%%%%%%%%%%%%%%%%
%%%%%%%%%%%%%%%%%%%%%%%%%%%%%%%%%%%%%%%%%%%%%%%%%%%%%%%%%%%%%%%%
%%%%%%%%%%%
figure
scatter(mass_c(:),KEadd(:),1,'b')
title('Mass (corrected) vs. KE (corrected)')
xlim([75,165])
ylim([4e4,12e4])
grid()
hold on
%Schmitt E vs M Data (keV/amu)
scatter(schmittM(:),schmittE(:),'r')
xlabel('Mass [amu]')
ylabel('KE [keV]')
xlim([75,165])
ylim([4e4,12e4])
legend('UNM Data','Schmitt (AVG)')
grid()
%% Calculate mean mass from light/heavy peaks (Sum data,
remember to change region of interest)
i2=0;
countslight = 0;
countsheavy = 0;
mass_light = MassSUM;
mass_light(mass_light >= 1) =0;
mass_heavy = MassSUM;
mass_heavy(mass_heavy >= 1) =0;
for i2 = (1:length(MassSUM));
    if (MassSUM(i2) >= 66 && MassSUM(i2) <= 116);
        countslight = countslight + 1;
        mass_light(i2) = MassSUM(i2);
```

```
    end
    if (MassSUM(i2) >= 116 && MassSUM(i2) <= 172);
        countsheavy = countsheavy + 1;
        mass_heavy(i2) = MassSUM(i2);
    end
end
loc6 = find(mass_light(:,1)==0);
mass_light(loc6,:) = [];
loc7 = find(mass_heavy(:,1)==0);
mass_heavy(loc7,:) = [];
mean_light = mean(mass_light);
mean_heavy = mean(mass_heavy);
SMasslight = std(mass_light(:))/sqrt(countslight);
SMassheavy = std(mass_heavy(:))/sqrt(countsheavy);
countslight;
countsheavy;
fprintf('Mean Mass Calculation Complete \n')
%% Calculating mean energy for light/heavy
i3=0;
countslight = 0;
countsheavy = 0;
KE_light = MassSUM;
KE_light(KE_light >= 1) =0;
KE_heavy = MassSUM;
KE_heavy(KE_heavy >= 1) =0;
for i2 = (1:length(MassSUM));
    if (Mass_KEaddSUM(i2,1) >= 66 && Mass_KEaddSUM(i2,1) <=
116);
        countslight = countslight + 1;
        KE_light(i2) = Mass_KEaddSUM(i2,2);
    end
    if (Mass_KEaddSUM(i2,1) >= 116 && Mass_KEaddSUM(i2,1) <=
172);
        countsheavy = countsheavy + 1;
        KE_heavy(i2) = Mass_KEaddSUM(i2,2);
    end
end
loc8 = find(KE_light(:,1)==0);
KE_light(loc8,:) = [];
loc9 = find(KE_heavy(:,1)==0);
KE_heavy(loc9,:) = [];
meanKE_light = mean(KE_light);
meanKE_heavy = mean(KE_heavy);
SKElight = std(KE_light(:))/sqrt(countslight);
SKEheavy = std(KE_heavy(:))/sqrt(countsheavy);
countslight;
countsheavy;
```

```
fprintf('Mean KE Calculation Complete \n')
%% Calculates average kinetic energy per mass KE(A) (individual
runs)
i = 0;
i2=0;
KEA = zeros(length(Mass_KEadd),100);
KEAavg = zeros(100,3);
for i = (1:100)
   for i2 = (1:length(Mass_KEadd))
    if (Mass_KEadd(i2,1) > (i + 59 - 0.5) && Mass_KEadd(i2,1) <
(i + 59 + 0.5))
        KEA(i2,i) = Mass_KEadd(i2,2);
    end
   end
   loc8 = find(KEA(:,i)==0);
   KEA(loc8,:) = [];
   KEAavg(i,1) = i+59;
    KEAavg(i,2) = mean(KEA(:,i));
    KEAavg(i,3) = std(KEA(:,i));
end
err=KEAavg(:,3);
fprintf('KE(A) Calculation Complete \n')
%% Calculates average kinetic energy per mass KE(A) (SUM runs, A
= 66-172 Region)
i = 0;
i2=0;
KEA = zeros(length(Mass_KEaddSUM),110);
KEAavg = zeros(110,3);
for i = (1:110)
   for i2 = (1:length(Mass_KEaddSUM))
    if (Mass_KEaddSUM(i2,1) > (i + 65 - 0.5) &&
Mass_KEaddSUM(i2,1) < (i + 65 + 0.5))
        KEA(i2,i) = Mass_KEaddSUM(i2,2);
    end
   end
   loc8 = find(KEA(:,i)==0);
   KEA(loc8,:) = [];
   KEAavg(i,1) = i+65;
    KEAavg(i,2) = mean(KEA(:,i));
    KEAavg(i,3) = std(KEA(:,i));
end
err=KEAavg(:,3);
fprintf('KE(A) Calculation Complete \n')
%% Calculates average kinetic energy per mass KE(A) (SUM runs, A
= 0-210 Region)
i = 0;
i2=0;
```

```
KEA = zeros(length(Mass_KEaddSUM),210);
KEAavg = zeros(210,3);
for i = (1:210)
   for i2 = (1:length(Mass_KEaddSUM))
    if (Mass_KEaddSUM(i2,1) > (i - 0.5) && Mass_KEaddSUM(i2,1) <
(i + 0.5))
        KEA(i2,i) = Mass_KEaddSUM(i2,2);
    end
   end
   loc8 = find(KEA(:,i)==0);
   KEA(loc8,:) = [];
   KEAavg(i,1) = i;
    KEAavg(i,2) = mean(KEA(:,i));
    KEAavg(i,3) = std(KEA(:,i));
end
err=KEAavg(:,3);
fprintf('KE(A) Calculation Complete \n')
%% KE(A) vs Mass Plot w/ Schmitt Comparison
figure
scatter(KEAavg(:,1),KEAavg(:,2),'b')
hold on
errorbar(KEAavg(:,1),KEAavg(:,2),err,'LineStyle','none')
title('Mass vs. Mean KE(A) (Raw Data, A=0-210, 3 Runs, 54.5K
Counts)')
xlim([60,170])
ylim([4e4,12e4])
grid()
hold on
%Schmitt E vs M Data (keV/amu)
scatter(schmittM(:),schmittE(:),'k')
xlabel('Mass [amu]')
ylabel('Mean KE [keV]')
xlim([0,210])
ylim([1e4,12e4])
legend('UNM Data','std','Schmitt')
grid()
%% Various individual plots IC v ToF Channel Per A
i=0;
i2=0;
RawToFDataA = zeros(length(RawChannelDataSUM),106);
RawKEDataA = zeros(length(RawChannelDataSUM),106);
for i = (1:16)
   for i2 = (1:length(RawChannelDataSUM))
    if (Mass_KEaddSUM(i2,1) > (i + 66 - 0.5) &&
Mass_KEaddSUM(i2,1) < (i + 66 + 0.5))
        RawToFDataA(i2,i) = RawChannelDataSUM(i2,4);
        RawKEDataA(i2,i) = RawChannelDataSUM(i2,2);
```

```
     end
    end
    figure(1)
    set(gca,'FontSize',7)
    subplot(4,4,i)
    scatter(A(:,2),A(:,4),1,'c')
    hold on
    scatter(RawKEDataA(:,i),RawToFDataA(:,i),1,'k')%timing(:,4)
    title('IC (ch) vs. ToF (ch)')
    ylim([0,20000])
    ylabel('ToF Channel')
    xlim([0,20000])
    xlabel('IC Channel')
    grid()
    aa=i+65;
    title(['IC vs ToF(' num2str(aa) ')'])
end

for i = (17:32)
    for i2 = (1:length(RawChannelDataSUM))
     if (Mass_KEaddSUM(i2,1) > (i + 66 - 0.5) &&
Mass_KEaddSUM(i2,1) < (i + 66 + 0.5))
         RawToFDataA(i2,i) = RawChannelDataSUM(i2,4);
         RawKEDataA(i2,i) = RawChannelDataSUM(i2,2);
     end
    end
    figure(2)
    set(gca,'FontSize',7)
    subplot(4,4,i-16)
    scatter(A(:,2),A(:,4),1,'c')
    hold on
    scatter(RawKEDataA(:,i),RawToFDataA(:,i),1,'k')%timing(:,4)
    title('IC (ch) vs. ToF (ch)')
    ylim([3000,20000])
    ylabel('ToF Channel')
    xlim([0,15000])
    xlabel('IC Channel')
    grid()
    aa=i+65;
    title(['IC vs ToF(' num2str(aa) ')'])
end
for i = (33:48)
    for i2 = (1:length(RawChannelDataSUM))
     if (Mass_KEaddSUM(i2,1) > (i + 66 - 0.5) &&
Mass_KEaddSUM(i2,1) < (i + 66 + 0.5))
         RawToFDataA(i2,i) = RawChannelDataSUM(i2,4);
         RawKEDataA(i2,i) = RawChannelDataSUM(i2,2);
```

```
     end
    end
    figure(3)
    set(gca,'FontSize',7)
    subplot(4,4,i-32)
    scatter(A(:,2),A(:,4),1,'c')
    hold on
    scatter(RawKEDataA(:,i),RawToFDataA(:,i),1,'k')%timing(:,4)
    title('IC (ch) vs. ToF (ch)')
    ylim([3000,20000])
    ylabel('ToF Channel')
    xlim([0,15000])
    xlabel('IC Channel')
    grid()
    aa=i+65;
    title(['IC vs ToF(' num2str(aa) ')'])
end
for i = (49:64)
    for i2 = (1:length(RawChannelDataSUM))
     if (Mass_KEaddSUM(i2,1) > (i + 66 - 0.5) &&
Mass_KEaddSUM(i2,1) < (i + 66 + 0.5))
         RawToFDataA(i2,i) = RawChannelDataSUM(i2,4);
         RawKEDataA(i2,i) = RawChannelDataSUM(i2,2);
     end
    end
    figure(4)
    set(gca,'FontSize',7)
    subplot(4,4,i-48)
    scatter(A(:,2),A(:,4),1,'c')
    hold on
    scatter(RawKEDataA(:,i),RawToFDataA(:,i),1,'k')%timing(:,4)
    title('IC (ch) vs. ToF (ch)')
    ylim([3000,20000])
    ylabel('ToF Channel')
    xlim([0,15000])
    xlabel('IC Channel')
    grid()
    aa=i+65;
    title(['IC vs ToF(' num2str(aa) ')'])
end
for i = (65:80)
    for i2 = (1:length(RawChannelDataSUM))
     if (Mass_KEaddSUM(i2,1) > (i + 66 - 0.5) &&
Mass_KEaddSUM(i2,1) < (i + 66 + 0.5))
         RawToFDataA(i2,i) = RawChannelDataSUM(i2,4);
         RawKEDataA(i2,i) = RawChannelDataSUM(i2,2);
     end
```

```
    end
    figure(5)
    set(gca,'FontSize',7)
    subplot(4,4,i-64)
    scatter(A(:,2),A(:,4),1,'c')
    hold on
    scatter(RawKEDataA(:,i),RawToFDataA(:,i),1,'k')%timing(:,4)
    title('IC (ch) vs. ToF (ch)')
    ylim([3000,20000])
    ylabel('ToF Channel')
    xlim([0,15000])
    xlabel('IC Channel')
    grid()
    aa=i+65;
    title(['IC vs ToF(' num2str(aa) ')'])
end
for i = (81:96)
    for i2 = (1:length(RawChannelDataSUM))
     if (Mass_KEaddSUM(i2,1) > (i + 66 - 0.5) &&
Mass_KEaddSUM(i2,1) < (i + 66 + 0.5))
         RawToFDataA(i2,i) = RawChannelDataSUM(i2,4);
         RawKEDataA(i2,i) = RawChannelDataSUM(i2,2);
     end
    end
    figure(6)
    set(gca,'FontSize',7)
    subplot(4,4,i-80)
    scatter(A(:,2),A(:,4),1,'c')
    hold on
    scatter(RawKEDataA(:,i),RawToFDataA(:,i),1,'k')%timing(:,4)
    title('IC (ch) vs. ToF (ch)')
    ylim([3000,20000])
    ylabel('ToF Channel')
    xlim([0,15000])
    xlabel('IC Channel')
    grid()
    aa=i+65;
    title(['IC vs ToF(' num2str(aa) ')'])
end

for i = (97:106)
    for i2 = (1:length(RawChannelDataSUM))
     if (Mass_KEaddSUM(i2,1) > (i + 66 - 0.5) &&
Mass_KEaddSUM(i2,1) < (i + 66 + 0.5))
         RawToFDataA(i2,i) = RawChannelDataSUM(i2,4);
         RawKEDataA(i2,i) = RawChannelDataSUM(i2,2);
     end
```

```
    end
    figure(7)
    set(gca,'FontSize',7)
    subplot(4,3,i-96)
    scatter(A(:,2),A(:,4),1,'c')
    hold on
    scatter(RawKEDataA(:,i),RawToFDataA(:,i),1,'k')%timing(:,4)
    title('IC (ch) vs. ToF (ch)')
    ylim([3000,20000])
    ylabel('ToF Channel')
    xlim([0,15000])
    xlabel('IC Channel')
    grid()
    aa=i+65;
    title(['IC vs ToF(' num2str(aa) ')'])
end
%% Some Individual Plots of IC v ToF Channel Per A
figure
scatter(RawChannelDataSUM(:,2),RawChannelDataSUM(:,4),1,'c')
    hold on
    scatter(RawKEDataA(:,70),RawToFDataA(:,70),1,'k')%timing(:,4)
    title('IC (ch) vs. ToF (ch)')
    ylim([3000,16000])
    ylabel('ToF Channel')
    xlim([0,15000])
    xlabel('IC Channel')
    grid()
    aa=i+65;
    title(['IC vs ToF A = 135'])
%% Light Mass IC vs ToF Channel per Mass, 66-114 (every other
mass)
cc=jet(50);
figure(8)
hold on
i4=0;
for i4 =(1:2:50)
scatter(RawKEDataA(:,i4),RawToFDataA(:,i4),1,cc(i4,:))%timing(:,
4)
    title('IC (ch) vs. ToF (ch) Light Peak (single mass)')
    ylim([4000,8000])
    ylabel('ToF Channel')
    xlim([10000,15000])
    xlabel('IC Channel')
    grid()
    aa=i4+65;
    legendInfo{i4} = ['Mass = ' num2str(i4+65)];
end
```

```
emptyCells = cellfun('isempty', legendInfo);
legendInfo(emptyCells) = [] ;
   legend(legendInfo)
   %% Light Mass IC vs ToF Channel per Mass, 67-116 (every other
mass)
cc=jet(50);
figure(9)
hold on
i4=0;
for i4 =(2:2:50)
scatter(RawKEDataA(:,i4),RawToFDataA(:,i4),1,cc(i4,:))%timing(:,
4)
   title('IC (ch) vs. ToF (ch) Light Peak (everyother mass 67-
116)')
   ylim([4000,8000])
   ylabel('ToF Channel')
   xlim([10000,15000])
   xlabel('IC Channel')
   grid()
   aa=i4+65;
   legendInfo{i4} = ['Mass = ' num2str(i4+65)];

end
emptyCells = cellfun('isempty', legendInfo);
legendInfo(emptyCells) = [] ;
   legend(legendInfo)
   %% Light Mass IC vs ToF Channel per Mass, 66-115 (every mass)
cc=jet(50);
figure(10)
hold on
i4=0;
for i4 =(1:50)
scatter(RawKEDataA(:,i4),RawToFDataA(:,i4),1,cc(i4,:))%timing(:,
4)
   title('IC (ch) vs. ToF (ch) Light Peak (everyother mass 66-
115)')
   ylim([4000,8000])
   ylabel('ToF Channel')
   xlim([10000,15000])
   xlabel('IC Channel')
   grid()
   aa=i4+65;
   legendInfo{i4} = ['Mass = ' num2str(i4+65)];
end
emptyCells = cellfun('isempty', legendInfo);
legendInfo(emptyCells) = [] ;
legend(legendInfo,'FontSize',6)
```

```
%% Heavy Mass IC vs ToF Channel per Mass, 115-172 (every other
mass)
cc=jet(56);
figure(11)
hold on
i4=0;
for i4 =(1:2:56)
scatter(RawKEDataA(:,i4+50),RawToFDataA(:,i4+50),1,cc(i4,:))%tim
ing(:,4)
   title('IC (ch) vs. ToF (ch) Heavy Peak (everyother mass 116-
170)')
   ylim([7000,16000])
   ylabel('ToF Channel')
   xlim([4000,11000])
   xlabel('IC Channel')
   grid()
   aa=i4+115;
   legendInfo{i4} = ['Mass = ' num2str(i4+115)];
end
emptyCells = cellfun('isempty', legendInfo);
legendInfo(emptyCells) = [] ;
   legend(legendInfo)
   %% Heavy Mass IC vs ToF Channel per Mass, 116-171 (every
other mass)
cc=jet(56);
figure(11)
hold on
i4=0;
for i4 =(2:2:56)
scatter(RawKEDataA(:,i4+50),RawToFDataA(:,i4+50),1,cc(i4,:))%tim
ing(:,4)
   title('IC (ch) vs. ToF (ch) Heavy Peak (everyother mass 117-
171)')
   ylim([7000,16000])
   ylabel('ToF Channel')
   xlim([4000,11000])
   xlabel('IC Channel')
   grid()
   aa=i4+115;
   legendInfo{i4} = ['Mass = ' num2str(i4+115)];
end
emptyCells = cellfun('isempty', legendInfo);
legendInfo(emptyCells) = [] ;
   legend(legendInfo)
   %% Heavy Mass IC vs ToF Channel per Mass, 66-115 (every mass)
cc=jet(56);
myMap = rand(56, 3);
```

```
figure(11)
hold on
i4=0;
for i4 =(1:56)
scatter(RawKEDataA(:,i4+50),RawToFDataA(:,i4+50),1,myMap(i4,:))%
timing(:,4)
   title('IC (ch) vs. ToF (ch) Heavy Peak (all masses 116-171)')
   ylim([7000,16000])
   ylabel('ToF Channel')
   xlim([4000,11000])
   xlabel('IC Channel')
   grid()
   aa=i4+115;
   legendInfo{i4} = ['Mass = ' num2str(i4+115)];
end
emptyCells = cellfun('isempty', legendInfo);
legendInfo(emptyCells) = [] ;
legend(legendInfo,'FontSize',6)

%% Plotting the calibration fits for verification purposes.
fignum = 1;
figure(fignum);
fignum = fignum+1;
subplot(1,2,1)
scatter(x,y)
title('Ion Chamber Calibration')
xlabel('Channel #')
ylabel('Energy [keV]')
grid()
hold on
plot(x,yfit)
hold off

subplot(1,2,2)
scatter(x2,y2)
title('TOF Calibration')
xlabel('Channel #')
ylabel('Time [s]')
grid()
hold on
plot(x2, y2fit)
hold off
%% Plot calibrated data
figure(fignum)
fignum = fignum+1;
%%subplot(2,2,1)
%hist(energy(:,2),2000)
```

```
histogram(KE(:),500,'EdgeColor','b','FaceColor','b')
title('KE Initial & Corrected')
xlim([40000,112000])
xlabel('Energy [keV]')
ylabel('Counts')
grid()
hold on
histogram(KEadd(:),500,'EdgeColor','r','FaceColor','r')
%title('KE Corrected')
xlim([40000,112000])
xlabel('Energy [keV]')
ylabel('Counts')
grid()
legend('Initial','Post-Addback')
%%
%subplot(2,2,2)
hist(KEadd(:),1999)
title('IC Calibrated (FF)')
xlim([40000,120000])
xlabel('Energy [keV]')
ylabel('Counts')
grid()
%%
%subplot(2,2,3)
hist(timing(:,4),1000)
title('TOF Calibrated')
xlabel('Time (s)')
ylabel('Counts')
grid()
%%
%subplot(2,2,4)
hist(timing(:,4),200)
title('TOF Calibrated (FF)')
xlim([3.0e-8,6.5e-8])
xlabel('Time (s)')
ylabel('Counts')
grid()
%% Various "final" energy corrected plots (Mass, KE vs. TOF,
Mass vs. KE, ect...)
fignum = 15;
figure(fignum)
fignum = fignum+1;
% FF ROI
%subplot (1,2,1)
edges = [0:1:210];
hist(mass_c,edges)
xlim([0,210])
```

```
xlabel('Mass (amu)')
ylabel('Counts')
title('U235+n(th) Corrected Mass Distribution')
grid()
%%
%KE vs TOF
%subplot(2,2,2)
scatter(Mass_KEadd_viSUM(:,3),Mass_KEadd_viSUM(:,2),1,'b')%timin
g(:,4)
title('vi vs. KEi')
ylim([4e4,12e4])
ylabel('KEi [keV]')
xlim([7.5e6,1.7e7])
xlabel('Vi [m/s]')
grid()
%%
%Mass vs TOF
%subplot(2,2,3)
figure
scatter(Mass_KEadd_viSUM(:,1),Mass_KEadd_viSUM(:,3),1)
title('Mass vs. Vi')
xlim([75,165])
xlabel('Mass [amu]')
ylim([7.5e6,1.7e7])
ylabel('Vi [m/s]')
%ylim([2e-8,7e-8])
%ylabel('TOF [s]')
grid()

%Mass vs KE
%%
%subplot(1,2,2)
figure
scatter(Mass_KEadd_viSUM(:,1),Mass_KEadd_viSUM(:,2),1,'b')
title('Mass (corrected) vs. KE (corrected)')
xlim([75,165])
ylim([4e4,12e4])
grid()
hold on
%Schmitt E vs M Data (keV/amu)
scatter(schmittM(:),schmittE(:),'r')
xlabel('Mass [amu]')
ylabel('KE [keV]')
xlim([75,165])
ylim([4e4,12e4])
legend('UNM Data','Schmitt (AVG)')
grid()
```

```
%% Starting Range calculations
a = [data_E_tof_delt(:,5),data_E_tof_delt(:,6)];
b = KE_t;%changing from KE to KEadd 12/21
f = mass_c_t;

[O,P]= size(a);
[Q,R]= size(b);
[B,D]= size(f);

if (O>Q)
    b1 = b;
     b1 = [b;zeros(O-Q,R)];
     a1 = a;
end

if (O>B)
    f1 = f;
    f1 = [f;zeros(O-B,D)];
    a2 = a;
end

IC_E = b1;
tph = a1;
mass_c = f1;


%%
tic
shape = 1000

k3 = 0
C = []
z = length(tph);
for o = (1:z);
    k3 = k3+1;
    for e = (n:length(IC_E));
        tph_ICE = tph(o,1)-IC_E(e,1);
        if(abs(tph_ICE)<shape);
            sorteddata(o,:) =
[tph(o,1),tph(o,2),IC_E(e,1),IC_E(e,2)];
            break
        end
    end
    if (k3 == 100)
        k3 = 0;
        (o/z)*100
```

```
    end
end

loc4 = find(sorteddata(:,1) == 0);
sorteddata(loc4,:) = [];

k4 = 0;
for o2 = (1:z);
    k4 = k4+1;
    for ee = (n:length(mass_c))
        tph_mass = tph(o2,1)-mass_c(ee,1);
        if(abs(tph_mass)<shape)
            sort_tph_mass(o2,:) =
[tph(o2,1),tph(o2,2),mass_c(ee,1),mass_c(ee,2)];
            break
        end
    end
end


loc5 = find(sort_tph_mass(:,1) == 0);
sort_tph_mass(loc5,:) = [];

toc
fprintf('Complete 2\n')

%%
i=0;
peaks = sorteddata(:,4);
tph_time_energy = sorteddata(:,2); %seconds
KEICMeV = sorteddata(:,4)*1e-3;
tph_time_mass = sort_tph_mass(:,4);
tph_time_energyCal =  7.0026E-11*tph_time_energy + 1.1769E-
11;%seconds
%%
figure(1)
%Energy Plot
subplot(1,2,2)
hist(peaks(:),1000)
xlabel('Energy (keV)')
ylabel('Counts')
xlim([50000,130000])
grid()
subplot(1,2,1)
%%
edges = [0:1e-9:10e-7];
hist(tph_time_energyCal(:),edges)
```

```
xlabel('IC\Deltat (s)')
ylabel('Counts')
xlim([4.5e-7,9e-7])
grid()
%% Fitting gaussians to dt data
%h1=hist(A(:,2),5000);
[N, edges] = histcounts(tph_time_energyCal(:),500);
dtchannel = (edges(1:end-1) + edges(2:end))./2; %histcounts
gives the bin edges, but we want to plot the bin centers
plot(dtchannel,N,'ko');
title('Plotted as points');
xlim([3e-7,9e-7])
ylabel('Frequency');
%%
figure(2)
scatter(peaks(:),tph_time_energyCal(:),1)
ylabel('IC\Deltat (s)')
xlabel('Energy (keV)')
title('Ei (keV) vs. IC\Deltat (ns)')
grid ()
xlim([40000,120000])
ylim([4.5e-7,9e-7])
%%
% Contour time vs. energy plot
figure(3)
a = [peaks(:),tph_time_energyCal(:)];
hist3(a,[100 100])
set(get(gca,'child'),'FaceColor','interp','CDataMode','auto','Li
neStyle','none');
view([0 90]);
title('Ei (keV) vs. IC\Deltat (ns)')
ylabel('\Deltat (ns)')
xlabel('Energy (keV)')
xlim([40000,105000])
ylim([4.5e-7,9e-7])
colorbar
%% Range Calculation

L = 11.66; % distance in cm
Volt = input('Enter Cathod Voltage'); % Enter CATHODE voltage in
command window
Pressure = input('Enter Operating Pressure'); % Enter operating
voltage in command window
E = Volt/L; % electric field
E_P = E/Pressure;
mu_0_e = 10E4; %[cm^2/Vs] from publication
mu_0_i = 1; %[cm^2/Vs]
```

```
v_dr = ((-.5203*(E_P)^2)+(3.3228*E_P)-.1261)*10^6; %drift
velocity of electrons [cm/s*torr]
%v_dr = 10^6;
D = tph_time_energyCal;%tph_time_energy*1e-9; %(sorteddata(:,1)-
sorteddata(:,3))/100;%[s]
Dvr = D.*v_dr;
R = L-(D.*v_dr); % range of ff [cm]
%RCal = 1.75*R - 6.3975;
R_t = [R,tph_time_energyCal(:,1)];
R_Mass_KEadd = [R,tph_time_mass,KEICMeV];
dlmwrite('RLANL20172500V70TorrRun7UF4.txt',R);
%% Fitting gaussians to range data
%h1=hist(A(:,2),5000);
[N, edges] = histcounts(R(:),500);
Rcenter = (edges(1:end-1) + edges(2:end))./2; %histcounts gives
the bin edges, but we want to plot the bin centers
plot(Rcenter,N,'ko');
title('Plotted as points');
ylabel('Frequency');
%%
RRun7 =
load('C:\Users\Rick\Documents\MATLAB\RLANL20172500V70TorrRun7UF4
.txt');
RRun6 =
load('C:\Users\Rick\Documents\MATLAB\RLANL20172500V70TorrRun6UF4
.txt');
RRun4 =
load('C:\Users\Rick\Documents\MATLAB\RLANL20172500V70TorrRun4UF4
.txt');
RSUM =vertcat(RRun7,RRun6,RRun4);
dlmwrite('CumulativeRUF4.txt',RSUM);
%%
%SRIM Z Determination
Zi=R;
Z=R;
i4=0;
for i4 = (1:length(R));
    if (R_Mass_KEadd(i4,2)<117);
        Zi(i4) = (-0.033*(R_Mass_KEadd(i4,2)-
96)+(R_Mass_KEadd(i4,1)-8.53)-0.0575*(R_Mass_KEadd(i4,3)-
90.337)-0.2956)/(-.1522);%2.2656753205E+11*timing(i3,4)
        Z(i4) = Zi(i4)+38;
    else
        Zi(i4) = (-0.027*(R_Mass_KEadd(i4,2)-
139)+(R_Mass_KEadd(i4,1)-7.41)-0.058*(R_Mass_KEadd(i4,3)-
57.709)+0.1038)/(-.0335);%(-9.9672636783E+10)57.975
        Z(i4) = Zi(i4)+53;
```

```
    end
end
fprintf('Z Calculation Complete \n')
edges_z = [20:1:80];
hist(Z,edges_z)
xlim([20,80])
R_Mass_KEadd_Z = [R,tph_time_mass,KEICMeV,Z];
%(Optional)
%dlmwrite('ZLANL20172500V70TorrRun7UF4.txt',Z);
%dlmwrite('R_Mass_KEadd_ZLANL20172500V70TorrRun7UF4.txt',R_Mass_
KEadd_Z);
%%
%SRIM Z Determination Old Version
Zi=zeros(length(R),1);
Z=zeros(length(R),1);
i4=0;
for i4 = (1:length(R));
    if (R_Mass_KEadd(i4,2)<117);
        Zi(i4) = -7.04225*(R_Mass_KEadd(i4,1)-
8.52)+0.23592*(R_Mass_KEadd(i4,2)-
95)+0.416197*(R_Mass_KEadd(i4,3)-90.339)+0.16507;
        Z(i4) = Zi(i4)+38;
    else
         Zi(i4) = -22.8311*(R_Mass_KEadd(i4,1)-
7.71)+.609589*(R_Mass_KEadd(i4,2)-
134)+1.324201*(R_Mass_KEadd(i4,3)-57.709)-
.39269;%2.2656753205E+11*timing(i3,4)
         Z(i4) = Zi(i4)+52;
    end
end
fprintf('Z Calculation Complete \n')
R_Mass_KEadd_Z = [R,tph_time_mass,KEICMeV,Z];
%(Optional)
%dlmwrite('ZLANL20172500V70TorrRun4.txt',Z);
%dlmwrite('R_Mass_KEadd_ZLANL20172500V70TorrRun7252.txt',R_Mass_
KEadd_Z);
%%
%SRIM Z Determination Old Version (Normal)
Zi=zeros(length(R),1);
Z=zeros(length(R),1);
i4=0;
for i4 = (1:length(R));
    if (R_Mass_KEadd(i4,2)<117);
        Zi(i4) = -7.04225*(R_Mass_KEadd(i4,1)-
8.52)+0.23592*(R_Mass_KEadd(i4,2)-
95)+0.416197*(R_Mass_KEadd(i4,3)-
90.339)+0.16507;%2.10704;%2.2656753205E+11*timing(i3,4)
```

```
        Z(i4) = Zi(i4)+38;
    else
         Zi(i4) = -22.8311*(R_Mass_KEadd(i4,1)-
7.41)+.609589*(R_Mass_KEadd(i4,2)-
134)+1.324201*(R_Mass_KEadd(i4,3)-57.709)-
.39269;%2.2656753205E+11*timing(i3,4)
         Z(i4) = Zi(i4)+52;
    end
end
fprintf('Z Calculation Complete \n')
R_Mass_KEadd_Z = [R,tph_time_mass,KEICMeV,Z];
%dlmwrite('ZLANL20172500V70TorrRun4.txt',Z);
%dlmwrite('R_Mass_KEadd_ZLANL20172500V70TorrRun7252.txt',R_Mass_
KEadd_Z);
%%
%SRIM Z Determination Old Version (trying new)
Zi=zeros(length(R),1);
Z=zeros(length(R),1);
i4=0;
for i4 = (1:length(R));
    if (R_Mass_KEadd(i4,2)<117);
         Zi(i4) = -6.5703*(R_Mass_KEadd(i4,1)-
8.53)+0.21682*(R_Mass_KEadd(i4,2)-
95)+0.3779*(R_Mass_KEadd(i4,3)-
90.339)+1.94218;%2.10704;%2.2656753205E+11*timing(i3,4)
         Z(i4) = Zi(i4)+38;
    else
         Zi(i4) = -29.8507*(R_Mass_KEadd(i4,1)-
7.41)+.80497*(R_Mass_KEadd(i4,2)-
139)+1.73134*(R_Mass_KEadd(i4,3)-57.709)-
3.0985;%2.2656753205E+11*timing(i3,4)
         Z(i4) = Zi(i4)+52;
    end
end
fprintf('Z Calculation Complete \n')
R_Mass_KEadd_Z = [R,tph_time_mass,KEICMeV,Z];
%dlmwrite('ZLANL20172500V70TorrRun4.txt',Z);
%dlmwrite('R_Mass_KEadd_ZLANL20172500V70TorrRun7252.txt',R_Mass_
KEadd_Z);
%% (Optional)
R_Mass_KEadd_ZRun7 =
load('C:\Users\Rick\Documents\MATLAB\R_Mass_KEadd_ZLANL20172500V
70TorrRun7UF4.txt');
R_Mass_KEadd_ZRun6 =
load('C:\Users\Rick\Documents\MATLAB\R_Mass_KEadd_ZLANL20172500V
70TorrRun6UF4.txt');
```

```
R_Mass_KEadd_ZRun4 =
load('C:\Users\Rick\Documents\MATLAB\R_Mass_KEadd_ZLANL20172500V
70TorrRun4UF4.txt');
R_Mass_KEadd_ZSUM
=vertcat(R_Mass_KEadd_ZRun7,R_Mass_KEadd_ZRun6,R_Mass_KEadd_ZRun
4);
dlmwrite('CumulativeR_Mass_KEadd_ZUF4.txt',R_Mass_KEadd_ZSUM);
%% (Optional)
ZRun7 =
load('C:\Users\Rick\Documents\MATLAB\ZLANL20172500V70TorrRun7UF4
.txt');
ZRun6 =
load('C:\Users\Rick\Documents\MATLAB\ZLANL20172500V70TorrRun6UF4
.txt');
ZRun4 =
load('C:\Users\Rick\Documents\MATLAB\ZLANL20172500V70TorrRun4UF4
.txt');
ZSUM =vertcat(ZRun7,ZRun6,ZRun4);
dlmwrite('CumulativeZUF4.txt',ZSUM);
%%
edges_z = [20:1:80];
hist(Z,edges_z)
title('U-235 Z Distribution');
ylabel('Counts')
xlabel('Z')
xlim([25,80])
%% Fitting gaussians to Z data
%h1=hist(A(:,2),5000);
[N, edges] = histcounts(Z(:),500);
Zchannel = (edges(1:end-1) + edges(2:end))./2; %histcounts gives
the bin edges, but we want to plot the bin centers
plot(Zchannel,N,'ko');
title('Plotted as points');
xlim([25,85])
ylabel('Frequency');
%%
hist(R,1000)
xlim([6,10])
title('U-235 Range Distribution');
ylabel('Counts')
xlabel('Range (cm)')
%% TPH plots
%Mass and TPH
edges_mass = {(60:1:180),(0:2e-9:10e-7)};
figure(12)
scatter(sort_tph_mass(:,4),tph_time_energyCal(:),5)
ylabel('\Deltat (s)')
```

```
xlabel('Mass (amu)')
grid ()
xlim([60,172])
ylim([4.5e-7,9e-7])
figure(13)
a = [sort_tph_mass(:,4),tph_time_energyCal(:)];
hist3(a,'Edges',edges_mass)
set(get(gca,'child'),'FaceColor','interp','CDataMode','auto','Li
neStyle','none');
view([0 90]);
ylabel('\Deltat (s)')
xlabel('Mass (amu)')
xlim([60,172])
ylim([4.5e-7,9e-7])
colorbar
%%

%TPH and Energy (NEED TO RE-DO WITH KEadd_t)
figure(14)
edges_energy = {(40000:1000:110000),(0:10e-9:10e-7)};
scatter(sorteddata(:,4),tph_time_energyCal(:),5)
ylabel('\Deltat (s)')
xlabel('Energy (keV)')
grid ()
xlim([50000,120000])
ylim([4.5e-7,8.5e-7])
figure(15)
a = [sorteddata(:,4),tph_time_energyCal(:)];
hist3(a,'Edges',edges_energy)
set(get(gca,'child'),'FaceColor','interp','CDataMode','auto','Li
neStyle','none');
view([0 90]);
ylabel('\Deltat (s)')
xlabel('Energy (keV)')
xlim([40000,110000])
ylim([4.5e-7,8.5e-7])
colorbar
%%

%Mass and Range
figure(16)
edges_range = {(60:1:180),(0:.025:11)};
scatter(R_Mass_KEadd_Z(:,2),R_Mass_KEadd_Z(:,1),5)
title('Mass (A) vs. Range (cm)')
ylabel('Range (cm)')
xlabel('Mass (amu)')
grid ()
```

```
xlim([60,172])
ylim([7,9.5])

figure(17)
a = [R_Mass_KEadd_Z(:,2),R_Mass_KEadd_Z(:,1)];
hist3(a,'Edges',edges_range)
set(get(gca,'child'),'FaceColor','interp','CDataMode','auto','Li
neStyle','none');
view([0 90]);
title('Mass (A) vs. Range (cm)')
ylabel('Range (cm)')
xlabel('Mass (amu)')
xlim([60,172])
ylim([7, 9.5])
colorbar
%% Z determination Tyuk Method
Energy_IC = [sorteddata(:,4)];%*1.6022e-16; % Energy in Joulse
Mass = [sort_tph_mass(:,4)];%*1.66054e-27;% mass in kg
Range = [RCal];%/100; % Range in m
%Beta = 1*exp(-4);
Beta = 0.033;%.034
Sqr_root_EM = (Energy_IC.*Mass).^(1/2);
Z = real(((Beta.*Sqr_root_EM)./(Range)).^(3/2));
Z_corr= Z*1.5-20;
edges_z = [20:1:80];
hist(Z,edges_z)
xlim([20,80])
MassZ_corr = [Mass,Z_corr];
R_Mass_KEadd_Z = [RCal,tph_time_mass,KEICMeV,Z];
%%

% Contour time vs. energy plot (NEED TO RE-DO WITH KEadd_t)
figure(3)
a = [R_Mass_KEadd_Z(:,2),R_Mass_KEadd_Z(:,4)];
hist3(a,[100 100])
set(get(gca,'child'),'FaceColor','interp','CDataMode','auto','Li
neStyle','none');
view([0 90]);
title('Mass vs. Charge')
ylabel('Z')
xlabel('Mass')
xlim([78,158])
ylim([29,70])
colorbar
%%
figure(3)
b = [R_Mass_KEadd_Z(:,1),R_Mass_KEadd_Z(:,4)];
```

```
hist3(b,[100 100])
set(get(gca,'child'),'FaceColor','interp','CDataMode','auto','Li
neStyle','none');
view([0 90]);
title('Range (cm) vs. Charge')
ylabel('Charge')
xlabel('Range (cm)')
xlim([7,9.3])
ylim([29,75])
colorbar
%%
figure
scatter(R_Mass_KEadd_Z(:,3),R_Mass_KEadd_Z(:,4),1)
xlabel('Energy (MeV)')
ylabel('Z')
ylim([20,80])
xlim([50,120])
figure
scatter(tph_time_mass,Z,1)
xlabel('Mass (amu)')
ylabel('Z')
ylim([20,80])
xlim([60,172])
figure
scatter(R,Z,1)
xlabel('Range (cm)')
ylabel('Z')
ylim([20,80])
xlim([7,10])
%% Average Z(A) Calculation
i3=0;

ZA_light = R_Mass_KEadd_ZSUM;
ZA_light(ZA_light >= 1) =0;
ZA_heavy = R_Mass_KEadd_ZSUM;
ZA_heavy(ZA_heavy >= 1) =0;
for i2 = (1:length(R_Mass_KEadd_ZSUM));
    if (R_Mass_KEadd_ZSUM(i2,2) >= 70 && R_Mass_KEadd_ZSUM(i2,2)
<= 117);

        ZA_light(i2) = R_Mass_KEadd_ZSUM(i2,4);
    end
    if (R_Mass_KEadd_ZSUM(i2,2) >= 117 &&
R_Mass_KEadd_ZSUM(i2,2) <= 160);

        ZA_heavy(i2) = R_Mass_KEadd_ZSUM(i2,4);
    end
```

```
end


loc8 = find(ZA_light(:,1)==0);
ZA_light(loc8,:) = [];
loc9 = find(ZA_heavy(:,1)==0);
ZA_heavy(loc9,:) = [];
meanZA_light = mean(ZA_light);
meanZA_heavy = mean(ZA_heavy);
fprintf('Mean Z Light/Heavy Calculation Complete \n')
%% Mean Z(A)
i = 0;
i2=0;
ZA = zeros(length(R_Mass_KEadd_Z),101);
ZAavg = zeros(100,3);
for i = (1:101)
   for i2 = (1:length(R_Mass_KEadd_Z))
    if (R_Mass_KEadd_Z(i2,2) > (i + 59 - 0.5) &&
R_Mass_KEadd_Z(i2,2) < (i + 59 + 0.5))
        ZA(i2,i) = R_Mass_KEadd_Z(i2,4);
    end
   end
   loc8 = find(ZA(:,i)==0);
   ZA(loc8,:) = [];
   ZAavg(i,1) = i+59;
    ZAavg(i,2) = mean(ZA(:,i));
    ZAavg(i,3) = std(ZA(:,i));
end
err1=ZAavg(:,3);
fprintf('Mean Z(A) Calculation Complete \n')
%%
figure(1)
scatter(ZAavg(:,1),ZAavg(:,2),20,'b')
hold on
errorbar(ZAavg(:,1),ZAavg(:,2),err1,'LineStyle','none')
xlabel('Mass (amu)')
ylabel('Mean Z(A)')
title('Mean Z(A)')
ylim([30,75])
xlim([75,160])
legend('Z(A)','StdDev')
%% Mean dt(A)
i = 0;
i2=0;
dtA = zeros(length(R),101);
dtavg = zeros(102,3);
for i = (1:101)
```

```
   for i2 = (1:length(R))
    if (R_Mass_KEadd_Z(i2,2) > (i + 59 - 0.5) &&
R_Mass_KEadd_Z(i2,2) < (i + 59 + 0.5))
        dtA(i2,i) = D(i2);
    end
   end
   loc8 = find(dtA(:,i)==0);
   dtA(loc8,:) = [];
   dtAavg(i,1) = i+59;
    dtAavg(i,2) = mean(dtA(:,i));
    dtAavg(i,3) = std(dtA(:,i));
end
err3=dtAavg(:,3);
fprintf('Mean dt(A) Calculation Complete \n')
%%
figure(2)
scatter(dtAavg(:,1),dtAavg(:,2),20,'b')
hold on
errorbar(dtAavg(:,1),dtAavg(:,2),err3,'LineStyle','none')
xlabel('Mass (amu)')
ylabel('Mean dt(A)')
title('Mean dt(A)')
ylim([5e-7,8.5e-7])
xlim([75,160])
%% Mean R(A)
i = 0;
i2=0;
RA = zeros(length(R),101);
RAavg = zeros(102,3);
for i = (1:101)
   for i2 = (1:length(R_Mass_KEadd_Z))
    if (R_Mass_KEadd_Z(i2,2) > (i + 59 - 0.5) &&
R_Mass_KEadd_Z(i2,2) < (i + 59 + 0.5))
        RA(i2,i) = R_Mass_KEadd_Z(i2,1);
    end
   end
   loc8 = find(RA(:,i)==0);
   RA(loc8,:) = [];
   RAavg(i,1) = i+59;
    RAavg(i,2) = mean(RA(:,i));
    RAavg(i,3) = std(RA(:,i));
end
err2=RAavg(:,3);
fprintf('Mean R(A) Calculation Complete \n')
RSRIMLight = [96 8.52];
RSRIMHeavy = [139 7.41];
%%
```

```
figure(3)
scatter(RAavg(:,1),RAavg(:,2),20,'r')
hold on
errorbar(RAavg(:,1),RAavg(:,2),err2,'LineStyle','none')
xlabel('Mass (amu)')
ylabel('Mean R(A) (cm)')
title('Mean R(A)')
ylim([7,9.5])
xlim([75,160])
hold on
scatter(RSRIMLight(1,1),RSRIMLight(1,2),20,'b')
scatter(RSRIMHeavy(1,1),RSRIMHeavy(1,2),20,'k')
legend('Measured Range','StdDev','TRIM Light','TRIM Heavy')
%% Various individual plots (Z(A), R(A), R(Z), etc
i=0;
i2=0;
ZA = zeros(49897,81);
for i = (1:16)
   for i2 = (1:length(R))
    if (R_Mass_KEadd_Z(i2,2) > (i + 78 - 0.5) &&
R_Mass_KEadd_Z(i2,2) < (i + 78 + 0.5))
        ZA(i2,i) = R_Mass_KEadd_Z(i2,4);
    end
   end
   figure(1)
   set(gca,'FontSize',7)
   edges_ZA = [0:1:100];
   subplot(4,4,i)
   hist(ZA(:,i),edges_ZA)
   xlabel('Z')
   ylabel('counts')
   xlim([25,80])
   aa=i+78;
   title(['Z(' num2str(aa) ')'])
end

for i = (17:32)
   for i2 = (1:length(R))
    if (R_Mass_KEadd_Z(i2,2) > (i + 78 - 0.5) &&
R_Mass_KEadd_Z(i2,2) < (i + 78 + 0.5))
        ZA(i2,i) = R_Mass_KEadd_Z(i2,4);
    end
   end
   figure(2)
   set(gca,'FontSize',7)
   edges_ZA = [0:1:100];
   subplot(4,4,i-16)
```

```
   hist(ZA(:,i),edges_ZA)
   xlabel('Z')
   ylabel('counts')
   xlim([25,80])
   aa=i+78;
   title(['Z(' num2str(aa) ')'])
end
for i = (33:48)
   for i2 = (1:length(R))
    if (R_Mass_KEadd_Z(i2,2) > (i + 78 - 0.5) &&
R_Mass_KEadd_Z(i2,2) < (i + 78 + 0.5))
        ZA(i2,i) = R_Mass_KEadd_Z(i2,4);
    end
   end
   figure(3)
   set(gca,'FontSize',7)
   edges_ZA = [0:1:100];
   subplot(4,4,i-32)
   hist(ZA(:,i),edges_ZA)
   xlabel('Z')
   ylabel('counts')
   xlim([25,80])
   aa=i+78;
   title(['Z(' num2str(aa) ')'])
end
for i = (49:64)
   for i2 = (1:length(R))
    if (R_Mass_KEadd_Z(i2,2) > (i + 78 - 0.5) &&
R_Mass_KEadd_Z(i2,2) < (i + 78 + 0.5))
        ZA(i2,i) = R_Mass_KEadd_Z(i2,4);
    end
   end
   figure(4)
   set(gca,'FontSize',7)
   edges_ZA = [0:1:100];
   subplot(4,4,i-48)
   hist(ZA(:,i),edges_ZA)
   xlabel('Z')
   ylabel('counts')
   xlim([25,80])
   aa=i+78;
   title(['Z(' num2str(aa) ')'])
end
for i = (65:80)
   for i2 = (1:length(R))
    if (R_Mass_KEadd_Z(i2,2) > (i + 78 - 0.5) &&
R_Mass_KEadd_Z(i2,2) < (i + 78 + 0.5))
```

```
        ZA(i2,i) = R_Mass_KEadd_Z(i2,4);
    end
   end
   figure(5)
   set(gca,'FontSize',7)
   edges_ZA = [0:1:100];
   subplot(4,4,i-64)
   hist(ZA(:,i),edges_ZA)
   xlabel('Z')
   ylabel('counts')
   xlim([25,80])
   aa=i+78;
   title(['Z(' num2str(aa) ')'])
end

fprintf('Z(A) Calculation Complete \n')
%%
i=0;
i2=0;
RA = zeros(49897,81);
for i = (1:16)
   for i2 = (1:length(RSUM))
    if (R_Mass_KEadd_ZSUM(i2,2) > (i + 78 - 0.5) &&
R_Mass_KEadd_ZSUM(i2,2) < (i + 78 + 0.5))
        RA(i2,i) = R_Mass_KEadd_ZSUM(i2,1);
    end
   end
   figure(1)
   set(gca,'FontSize',7)
   edges_RA = [0:.01:10];
   subplot(4,4,i)
   hist(RA(:,i),edges_RA)
   xlabel('R')
   ylabel('counts')
   xlim([6,10])
   aa=i+78;
   title(['R(' num2str(aa) ')'])
end

for i = (17:32)
   for i2 = (1:length(RSUM))
    if (R_Mass_KEadd_ZSUM(i2,2) > (i + 78 - 0.5) &&
R_Mass_KEadd_ZSUM(i2,2) < (i + 78 + 0.5))
        RA(i2,i) = R_Mass_KEadd_ZSUM(i2,1);
    end
   end
   figure(2)
```

```
    set(gca,'FontSize',7)
    edges_RA = [0:.01:10];
    subplot(4,4,i-16)
    hist(RA(:,i),edges_RA)
    xlabel('R')
    ylabel('counts')
    xlim([6,10])
    aa=i+78;
    title(['R(' num2str(aa) ')'])
end
for i = (33:48)
    for i2 = (1:length(RSUM))
     if (R_Mass_KEadd_ZSUM(i2,2) > (i + 78 - 0.5) &&
R_Mass_KEadd_ZSUM(i2,2) < (i + 78 + 0.5))
         RA(i2,i) = R_Mass_KEadd_ZSUM(i2,1);
     end
    end
    figure(3)
    set(gca,'FontSize',7)
    edges_RA = [0:.01:10];
    subplot(4,4,i-32)
    hist(RA(:,i),edges_RA)
    xlabel('R')
    ylabel('counts')
    xlim([25,80])
    aa=i+78;
    title(['R(' num2str(aa) ')'])
end
for i = (49:64)
    for i2 = (1:length(RSUM))
     if (R_Mass_KEadd_ZSUM(i2,2) > (i + 78 - 0.5) &&
R_Mass_KEadd_ZSUM(i2,2) < (i + 78 + 0.5))
         RA(i2,i) = R_Mass_KEadd_ZSUM(i2,1);
     end
    end
    figure(4)
    set(gca,'FontSize',7)
    edges_RA = [0:.01:10];
    subplot(4,4,i-48)
    hist(RA(:,i),edges_RA)
    xlabel('R')
    ylabel('counts')
    xlim([6,10])
    aa=i+78;
    title(['R(' num2str(aa) ')'])
end
for i = (65:80)
```

```
   for i2 = (1:length(RSUM))
    if (R_Mass_KEadd_ZSUM(i2,2) > (i + 78 - 0.5) &&
R_Mass_KEadd_ZSUM(i2,2) < (i + 78 + 0.5))
        RA(i2,i) = R_Mass_KEadd_ZSUM(i2,1);
    end
   end
   figure(5)
   set(gca,'FontSize',7)
   edges_RA = [0:.01:10];
   subplot(4,4,i-64)
   hist(RA(:,i),edges_RA)
   xlabel('R')
   ylabel('counts')
   xlim([6,10])
   aa=i+78;
   title(['R(' num2str(aa) ')'])
end

fprintf('R(A) Calculation Complete \n')
%% N-Z Plots

Neu = R;
i=0;
for i = (1:length(R_Mass_KEadd_Z))
   Neu(i) = R_Mass_KEadd_Z(i,2) - R_Mass_KEadd_Z(i,4);
end

figure(1)
b = [Neu,R_Mass_KEadd_Z(:,4)];
hist3(b,[100 100])
set(get(gca,'child'),'FaceColor','interp','CDataMode','auto','Li
neStyle','none');
view([0 90]);
title('N vs Z')
xlabel('N')
ylabel('Z')
xlim([42,120])
ylim([29,70])
colorbar
fprintf('N Calculation Complete \n')
%%
figure(1)
b = [R_Mass_KEadd_Z(:,2),Neu];
hist3(b,[100 100])
set(get(gca,'child'),'FaceColor','interp','CDataMode','auto','Li
neStyle','none');
view([0 90]);
```

```
title('A vs. N')
ylabel('N')
xlabel('A')
ylim([42,115])
xlim([79,155])
colorbar
%%
figure(1)
b = [R_Mass_KEadd_Z(:,2),Z];
hist3(b,[100 100])
set(get(gca,'child'),'FaceColor','interp','CDataMode','auto','Li
neStyle','none');
view([0 90]);
title('A vs. Z')
ylabel('Z')
xlabel('A')
ylim([30,75])
xlim([79,155])
colorbar
%%
tic
B = [];
b = [R_t(:,2)];
f = [mass_c_t(:,2)];
l = [KEadd_t(:,2)];
k2=0
for i2 = (1:length(l));
 k2=k2+1;
 for g = (n:length(f))
 if (abs(f(g)-b(i2))<300)
 B(i2,:)=[R_t(i2,1),R_t(i2,2),mass_un(g,1),mass_un(g,2)];
 break
 end
 end
 if (k2 == 100)
 k2 = 0;
 (i2/length(f))*100
 end
end
fprintf('Complete\n')
toc
loc = find(B(:,1)==0);
B(loc,:) = [];
%%
tic
F = [];
k4 = 0
```

```
for i3 = (1:length(l));
 k4 = k4+1;
 for q = (n:length(f))
 if (abs(f(q)-l(i3))<300)

F(i3,:)=[KEadd_t(i3,1),KEadd_t(i3,2),mass_c_t(q,1),mass_c_t(q,2)
];
 break
 end
 end
 if (k4 == 100)
 k4=0;
 (i3/length(f))*100
 end
end
fprintf('Complete\n')
toc
loc2 = find(F(:,1)==0);
F(loc2,:) = [];
%%
F_tmp = F;
B_tmp = B;
[N1,M1] = size(B_tmp);
[S1,T1] = size(F_tmp);
if (N1>S1)
 F1 = F;
 F1 = [B1;zeros(N1-S1,T1)];
 B1 = B_tmp;
else
 B1 = B;
 B1 = [B1;zeros(S1-N1,T1)];
 F1 = F_tmp;
end
%%
E_mass_range = [F1,B1(:,1),B1(:,2)];
%%
fignum = 25;
figure(fignum)
fignum = fignum+1;
subplot(2,2,1)
scatter(E_mass_range(:,3),E_mass_range(:,1),1) % energy vs. mass
xlim([0,200])
xlabel('Mass (amu)')
ylabel('KE (keV)')
grid()
subplot(2,2,2)
```

```
scatter(E_mass_range(:,1),E_mass_range(:,5),1) % energy vs.
range
%xlim([50000,130000])
ylim([7,9.5])
xlabel('KE (keV)')
ylabel('Range (cm)')
grid()
subplot(2,2,3)
scatter(E_mass_range(:,3),E_mass_range(:,5),1) % mass vs. range
ylim([7,9.5])
%xlim([0,200])
xlabel('Mass (amu)')
ylabel('Range (cm)')
grid()
%subplot(2,2,4)
%scatter(timingdat(:),E_mass_range(:,3),1)
```